REPORT DOCUMENTATION PAGE

Form Approved OMB NO. 0704-0188

1. REPORT DATE (DD-MM-YYYY)	2. REPORT TYPE	3. DATES COVERED (From - To)
02-08-2016	Final Report	1-Aug-2010 - 31-Jan-2016

4. TITLE AND SUBTITLE
Final Report: Scalable Quantum Information Processing (SQIP) with Trapped Ions

5a. CONTRACT NUMBER
W911NF-10-1-0284

5b. GRANT NUMBER

5c. PROGRAM ELEMENT NUMBER
411359

6. AUTHORS
Rainer Blatt

5d. PROJECT NUMBER

5e. TASK NUMBER

5f. WORK UNIT NUMBER

7. PERFORMING ORGANIZATION NAMES AND ADDRESSES
Universitat Innsbruck
Institut fur Experimentalphysik
Technikerstrasse 25
-

8. PERFORMING ORGANIZATION REPORT NUMBER

9. SPONSORING/MONITORING AGENCY NAME(S) AND ADDRESS (ES)
U.S. Army Research Office
P.O. Box 12211
Research Triangle Park, NC 27709-2211

10. SPONSOR/MONITOR'S ACRONYM(S)
ARO

11. SPONSOR/MONITOR'S REPORT NUMBER(S)
58104-PH-MOC.41

12. DISTRIBUTION AVAILIBILITY STATEMENT
Approved for Public Release; Distribution Unlimited

13. SUPPLEMENTARY NOTES
The views, opinions and/or findings contained in this report are those of the author(s) and should not contrued as an official Department of the Army position, policy or decision, unless so designated by other documentation.

14. ABSTRACT
The following report outlines the progress that has been made within the “Scalable Quantum Information Processing (SQIP) with Trapped Ions” program. In particular it will emphasis on ☼ the two setups maintained and installed at the University of Innsbruck (UIBK) in Austria, lead by Rainer Blatt, focusing on quantum information processing - in particular the realization of quantum algorithms, the team around Ferdinand Schmidt-Kaler at the University of Mainz (UMZ) working on distributed entanglement within an ion-trap via splitting and shuttling of ions without excess heating of the motional state, the group of Issac Chuang at the MIT in Boston working both on

15. SUBJECT TERMS
quantum processing, ion traps, qubic measurement

16. SECURITY CLASSIFICATION OF:			17. LIMITATION OF ABSTRACT	15. NUMBER OF PAGES	19a. NAME OF RESPONSIBLE PERSON
a. REPORT	b. ABSTRACT	c. THIS PAGE			Rainer Blatt
UU	UU	UU	UU		19b. TELEPHONE NUMBER 004-351-2507

Report Title

Final Report: Scalable Quantum Information Processing (SQIP) with Trapped Ions

ABSTRACT

The following report outlines the progress that has been made within the “Scalable Quantum Information Processing (SQIP) with Trapped Ions” program. In particular it will emphasis on ♊ the two setups maintained and installed at the University of Innsbruck (UIBK) in Austria, lead by Rainer Blatt, focusing on quantum information processing - in particular the realization of quantum algorithms, the team around Ferdinand Schmidt-Kaler at the University of Mainz (UMZ) working on distributed entanglement within an ion-trap via splitting and shuttling of ions without excess heating of the motional state, the group of Issac Chuang at the MIT in Boston working both on quantum algorithms as well as an ion-photon interface to connect distant ion-traps, supplemented by the team at the University of Berkeley/California (UCB), supervised by Hartmut Haffner, aiming at understanding and overcoming detrimental effects in surface trap based quantum computation.

Enter List of papers submitted or published that acknowledge ARO support from the start of the project to the date of this printing. List the papers, including journal references, in the following categories:

(a) Papers published in peer-reviewed journals (N/A for none)

Received		Paper
03/15/2017	38	Esteban A Martinez, Thomas Monz, Daniel Nigg, Philipp Schindler, Rainer Blatt. Compiling quantum algorithms for architectures with multi-qubit gates, New Journal of Physics, ( ): 063029. doi: 1,013,535.00
07/18/2016	1	Philipp Schindler, Julio T. Barreiro,Thomas Monz, Volckmar Nebendahl, Daniel Nigg, Michael Chwalla, Markus Hennrich, Rainer Blatt. Experimental Repetitive Quantum Error Correction, Science, ( ): 1059. doi: 1,012,755.00
07/18/2016	4	Shannon X. Wang, Guang Hao Low, Nathan S. Lachenmyer, Yufei Ge, Peter F. Herskind, Isaac L. Chuang. Laser-induced charging of microfabricated ion traps, Journal of Applied Physics, ( ): 104901. doi: 1,012,763.00
07/18/2016	3	A. Walther, U. Poschinger, K. Singer, F. Schmidt-Kaler. Precision measurements in ion traps using slowly moving standing waves, Applied Physics B, ( ): 1061. doi: 1,012,760.00
07/18/2016	2	Tony Hyun Kim, Peter F. Herskind, Isaac L. Chuang. Surface-electrode ion trap with integrated light source, Applied Physics Letters, ( ): 214103. doi: 1,012,757.00
08/01/2016	14	T. Karin, I. Le Bras, A. Kehlberger, K. Singer, N. Daniilidis, H. Häffner. Transport of charged particles by adjusting rf voltage amplitudes, Applied Physics B, ( ): 117. doi: 1,013,427.00
08/01/2016	11	N Daniilidis, S Narayanan, S A Möller, R Clark, T E Lee, P J Leek, A Wallraff, St Schulz, F Schmidt-Kaler, H Häffner. Corrigendum: Fabrication and heating rate study of microscopic surface electrode ion traps, New Journal of Physics, ( ): 079504. doi: 1,013,420.00
08/01/2016	12	Daniel Nigg, Thomas Monz, Philipp Schindler, Esteban A Martinez, Markus Hennrich, Rainer Blatt, Matthew F Pusey, Terry Rudolph, Jonathan Barrett. Can different quantum state vectors correspond to the same physical state? An experimental test, New Journal of Physics, ( ): 013007. doi: 1,013,425.00
08/01/2016	13	H A Fürst, M H Goerz, U G Poschinger, M Murphy, S Montangero, T Calarco, F Schmidt-Kaler, K Singer, C P Koch. Controlling the transport of an ion: classical and quantum mechanical solutions, New Journal of Physics, ( ): 075007. doi: 1,013,426.00
08/01/2016	5	Amira M. Eltony, Dorian Gangloff, Molu Shi, Alexei Bylinskii, Vladan Vuleti?, Isaac L. Chuang. Technologies for trapped-ion quantum information systems, Quantum Information Processing, ( ): 1. doi: 1,013,410.00
08/01/2016	6	D. Nigg, M. Muller, E. A. Martinez, P. Schindler, M. Hennrich, T. Monz, M. A. Martin-Delgado, R. Blatt. Quantum computations on a topologically encoded qubit, Science, ( ): 302. doi: 1,013,411.00
08/01/2016	7	H Kaufmann, T Ruster, C T Schmiegelow, F Schmidt-Kaler, U G Poschinger. Dynamics and control of fast ion crystal splitting in segmented Paul traps, New Journal of Physics, ( ): 073012. doi: 1,013,414.00

08/01/2016 8 Julio T. Barreiro, Jean-Daniel Bancal, Philipp Schindler, Daniel Nigg, Markus Hennrich, Thomas Monz, Nicolas Gisin, Rainer Blatt. Demonstration of genuine multipartite entanglement with device-independent witnesses,
Nature Physics, ( ): 559. doi:
1,013,416.00

08/01/2016 9 Philipp Schindler, Daniel Nigg, Thomas Monz, Julio T Barreiro, Esteban Martinez, Shannon X Wang, Stephan Quint, Matthias F Brandl, Volckmar Nebendahl, Christian F Roos, Michael Chwalla, Markus Hennrich, Rainer Blatt. A quantum information processor with trapped ions,
New Journal of Physics, ( ): 123012. doi:
1,013,418.00

08/01/2016 10 J. Welzel, A. Bautista-Salvador, C. Abarbanel, V. Wineman-Fisher, C. Wunderlich, R. Folman, F. Schmidt-Kaler. Designing spin-spin interactions with one and two dimensional ion crystals in planar micro traps,
The European Physical Journal D, ( ): 285. doi:
1,013,419.00

08/01/2016 15 Guang Hao Low, Peter F. Herskind, Isaac L. Chuang. Finite-geometry models of electric field noise from patch potentials in ion traps,
Physical Review A, ( ): . doi:
1,013,465.00

08/01/2016 17 Amira M. Eltony, Shannon X. Wang, Gleb M. Akselrod, Peter F. Herskind, Isaac L. Chuang. Transparent ion trap with integrated photodetector,
Applied Physics Letters, ( ): 054106. doi:
1,013,470.00

08/01/2016 18 Daniel Nigg, Julio T. Barreiro, Philipp Schindler, Masoud Mohseni, Thomas Monz, Michael Chwalla, Markus Hennrich, Rainer Blatt. Experimental Characterization of Quantum Dynamics Through Many-Body Interactions,
Physical Review Letters, ( ): . doi:
1,013,472.00

08/01/2016 19 Shannon X. Wang, Yufei Ge, Jaroslaw Labaziewicz, Eric Dauler, Karl Berggren, Isaac L. Chuang. Superconducting microfabricated ion traps,
Applied Physics Letters, ( ): 1. doi:
1,013,475.00

08/01/2016 20 Peter F. Herskind, Shannon X. Wang, Molu Shi, Yufei Ge, Marko Cetina, Isaac L. Chuang. Microfabricated surface ion trap on,
OPTICS LETTERS, ( ): 3045. doi:
1,013,476.00

08/01/2016 21 Julio T. Barreiro, Philipp Schindler, Otfried Gühne, Thomas Monz, Michael Chwalla, Christian F. Roos, Markus Hennrich, Rainer Blatt. Experimental multiparticle entanglement dynamics induced by decoherence,
Nature Physics, ( ): 943. doi:
1,013,477.00

08/01/2016 22 T. Ruster, C. Warschburger, H. Kaufmann, C. T. Schmiegelow, A. Walther, M. Hettrich, A. Pfister, V. Kaushal, F. Schmidt-Kaler, U. G. Poschinger. Experimental realization of fast ion separation in segmented Paul traps,
Physical Review A, ( ): . doi:
1,013,478.00

08/01/2016 23 F Ziesel, T Ruster, A Walther, H Kaufmann, S Dawkins, K Singer, F Schmidt-Kaler, U G Poschinger. Experimental creation and analysis of displaced number states,
Journal of Physics B: Atomic, Molecular and Optical Physics, ( ): 104008. doi:
1,013,479.00

08/01/2016 24 U. Poschinger, A. Walther, M. Hettrich, F. Ziesel, F. Schmidt-Kaler. Interaction of a laser with a qubit in thermal motion and its application to robust and efficient readout,
Applied Physics B, ( ): 1159. doi:
1,013,480.00

08/01/2016 25 A. Stute, B. Casabone, P. Schindler, T. Monz, P. O. Schmidt, B. Brandstätter, T. E. Northup, R. Blatt. Tunable ion–photon entanglement in an optical cavity,
Nature, ( ): 482. doi:
1,013,481.00

08/01/2016 26 Xiao-Jing Lu, J. G. Muga, Xi Chen, U. G. Poschinger, F. Schmidt-Kaler, A. Ruschhaupt. Fast shuttling of a trapped ion in the presence of noise,
Physical Review A, ( ): . doi:
1,013,482.00

08/01/2016 27 A. Walther, F. Ziesel, T. Ruster, S. T. Dawkins, K. Ott, M. Hettrich, K. Singer, F. Schmidt-Kaler, U. Poschinger. Controlling Fast Transport of Cold Trapped Ions,
Physical Review Letters, ( ): . doi:
1,013,483.00

08/01/2016 28 G. Huber, F. Ziesel, U. Poschinger, K. Singer, F. Schmidt-Kaler. A trapped-ion local field probe,
Applied Physics B, ( ): 725. doi:
1,013,484.00

08/01/2016 29 Philipp Schindler, Thomas Monz, Daniel Nigg, Julio T. Barreiro, Esteban A. Martinez, Matthias F. Brandl, Michael Chwalla, Markus Hennrich, Rainer Blatt. Undoing a Quantum Measurement,
Physical Review Letters, ( ): . doi:
1,013,485.00

08/01/2016 30 P. Schindler, M. Müller, D. Nigg, J. T. Barreiro, E. A. Martinez, M. Hennrich, T. Monz, S. Diehl, P. Zoller, R. Blatt. Quantum simulation of dynamical maps with trapped ions,
Nature Physics, ( ): 361. doi:
1,013,487.00

08/01/2016 31 A. Walther, U. Poschinger, F. Ziesel, M. Hettrich, A. Wiens, J. Welzel, F. Schmidt-Kaler. Single ion as a shot-noise-limited magnetic-field-gradient probe,
Physical Review A, ( ): . doi:
1,013,488.00

08/01/2016 32 Thomas Monz, Philipp Schindler, Julio T. Barreiro, Michael Chwalla, Daniel Nigg, William A. Coish, Maximilian Harlander, Wolfgang Hänsel, Markus Hennrich, Rainer Blatt. 14-Qubit Entanglement: Creation and Coherence,
Physical Review Letters, ( ): . doi:
1,013,489.00

08/01/2016 33 J. S. Pedernales, R. Di Candia, P. Schindler, T. Monz, M. Hennrich, J. Casanova, E. Solano. Entanglement measures in ion-trap quantum simulators without full tomography,
Physical Review A, ( ): . doi:
1,013,490.00

08/01/2016 34 Tobias Moroder, Matthias Kleinmann, Philipp Schindler, Thomas Monz, Otfried Gühne, Rainer Blatt. Certifying Systematic Errors in Quantum Experiments,
Physical Review Letters, ( ): . doi:
1,013,493.00

08/01/2016 35 Philipp Schindler, Dylan J Gorman, Nikos Daniilidis, Hartmut Häffner. Polarization of electric-field noise near metallic surfaces,
Physical Review A, ( ): . doi:
1,013,494.00

08/02/2016 36 T. Monz, D. Nigg, E. A. Martinez, M. F. Brandl, P. Schindler, R. Rines, S. X. Wang, I. L. Chuang, R. Blatt. Realization of a scalable Shor algorithm,
Science, ( ): 1068. doi:
1,013,521.00

08/02/2016 37 M. F. Brandl, P. Schindler, T. Monz, R. Blatt. Cryogenic resonator design for trapped ion experiments in Paul traps,
Applied Physics B, ( ): . doi:
1,013,523.00

08/02/2016 39 M Palmero, S Martínez-Garaot, U G Poschinger, A Ruschhaupt, J G Muga. Fast separation of two trapped ions,
New Journal of Physics, ( ): 093031. doi:
1,013,537.00

08/02/2016 40 I. Talukdar, D. J. Gorman, N. Daniilidis, P. Schindler, S. Ebadi, H. Kaufmann, T. Zhang, H. Häffner. Implications of surface noise for the motional coherence of trapped ions,
Physical Review A, ( ): . doi:
1,013,538.00

TOTAL: **39**

Number of Papers published in peer-reviewed journals:

(b) Papers published in non-peer-reviewed journals (N/A for none)

Received	Paper

TOTAL:

Number of Papers published in non peer-reviewed journals:

(c) Presentations

Number of Presentations: 0.00

Non Peer-Reviewed Conference Proceeding publications (other than abstracts):

Received	Paper	
08/01/2016	16	Peter F. Herskind, Shannon X. Wang, Molu Shi, Yufei Ge, Marko Cetina, Isaac L. Chuang. Microfabricated Surface Trap for Scalable Ion-Photon Interfaces, Quantum Electronics and Laser Science Conference. 01-OCT-11, Baltimore, Maryland. : ,

TOTAL: **1**

Number of Non Peer-Reviewed Conference Proceeding publications (other than abstracts):

Peer-Reviewed Conference Proceeding publications (other than abstracts):

Received	Paper

TOTAL:

Number of Peer-Reviewed Conference Proceeding publications (other than abstracts):

(d) Manuscripts

Received Paper

TOTAL:

Number of Manuscripts:

Books

Received Book

TOTAL:

Received Book Chapter

TOTAL:

Patents Submitted

Patents Awarded

Awards

Graduate Students

NAME	PERCENT_SUPPORTED

FTE Equivalent:
Total Number:

Names of Post Doctorates

NAME	PERCENT_SUPPORTED

FTE Equivalent:
Total Number:

Names of Faculty Supported

NAME	PERCENT_SUPPORTED

FTE Equivalent:
Total Number:

Names of Under Graduate students supported

NAME	PERCENT_SUPPORTED

FTE Equivalent:
Total Number:

Student Metrics

This section only applies to graduating undergraduates supported by this agreement in this reporting period

The number of undergraduates funded by this agreement who graduated during this period: 0.00
The number of undergraduates funded by this agreement who graduated during this period with a degree in science, mathematics, engineering, or technology fields:..... 0.00
The number of undergraduates funded by your agreement who graduated during this period and will continue to pursue a graduate or Ph.D. degree in science, mathematics, engineering, or technology fields:..... 0.00
Number of graduating undergraduates who achieved a 3.5 GPA to 4.0 (4.0 max scale):..... 0.00
Number of graduating undergraduates funded by a DoD funded Center of Excellence grant for Education, Research and Engineering:..... 0.00
The number of undergraduates funded by your agreement who graduated during this period and intend to work for the Department of Defense 0.00
The number of undergraduates funded by your agreement who graduated during this period and will receive scholarships or fellowships for further studies in science, mathematics, engineering or technology fields: 0.00

Names of Personnel receiving masters degrees

NAME

Total Number:

Names of personnel receiving PHDs

NAME

Total Number:

Names of other research staff

NAME PERCENT_SUPPORTED

FTE Equivalent:
Total Number:

Sub Contractors (DD882)

Inventions (DD882)

Scientific Progress

See attached.

Technology Transfer

See attached.

BAA #: IARPA-BAA-09-06

PROJECT #: W911NF-10-1-0284

Scalable Quantum Information Processing (SQIP) With Trapped Ions

Final report

Principal Investigator:	Rainer BLATT
Phone:	0043 512 507 524 50
Fax:	0043 512 507 524 91
email:	rainer.blatt@uibk.ac.at
Institution:	Institute for Experimental Physics University of Innsbruck, Austria
Institution address:	Technikerstr. 25/4 6020 Innsbruck, Austria
Other Institutions:	Universität Mainz, Germany University of Berkeley, California, USA Massachussets Institute of Technology, USA

Reporting Period:	Aug 2010 - July 2015
Agency & Point of Contact:	IARPA, Dr. David Moehring

Contents

1 Introduction

The following report outlines the progress that has been made within the "Scalable Quantum Information Processing (SQIP) with Trapped Ions" program. In particular it will emphasis on

- the two setups maintained and installed at the University of Innsbruck (UIBK) in Austria, lead by Rainer Blatt, focusing on quantum information processing - in particular the realization of quantum algorithms ,
- the team around Ferdinand Schmidt-Kaler at the University of Mainz (UMZ) working on distributed entanglement within an ion-trap via splitting and shuttling of ions without excess heating of the motional state,
- the group of Issac Chuang at the MIT in Boston working both on quantum algorithms as well as an ion-photon interface to connect distant ion-traps,
- supplemented by the team at the University of Berkeley/California (UCB), supervised by Hartmut Häffner, aiming at understanding and overcoming detrimental effects in surface-trap based quantum computation.

Starting with an introduction into ion-trap based quantum computing, systems employed in the program will be explained in Sec. 2. Subsequently, Sec. 3 will describe various hardware components and accompanying procedures - in particular various 3D and surface ion-traps, as well as cleaning processes for these. Sec. 4 complements our efforts on hardware development with software specifically aimed at quantum information processing with trapped ions. Finally, Sec. 5 will explain various algorithms and procedures that have been successfully derived and implemented within the SQIP consortium. Most prominently among these is the realization of a scalable Shor algorithm for ion-trap based quantum computers.

2 Quantum Information Processing with Trapped Ions

Within the consortium, we are mainly working with Calcium and Strontium ions. Both species are well established, have similar mass (making them decent candidates for sympathetic cooling, if loaded within the same trap) and the respective transitions have similar wavelengths. The wavelengths for Ca/Sr are at 497/422 nm for Doppler cooling, around 729/674 nm for the quadrupole transition, and around 800 nm (respectively 1000 nm) as repump transitions for Ca/Sr. All of these wavelengths are commercially readily available.

The following subsections will address the 3D linear Paul trap in Innsbruck, used as "Commercial-of-the-shelf" (COTSS) system, a surface-ion-trap chamber based on a flow cryostat to represent the "Scalable System" (SS) approach, a segmented 3D-trap system in Mainz, a specially assembled surface-science chamber in Berkeley, and, finally, a ion-photon interface at the MIT.

2.1 Innsbruck I: Commercial off-the-shelf system QIP system

2.1.1 The qubit - $^{40}Ca^{+}$

A crucial choice for any QC implementation is the encoding of a qubit in a physical system. In ion trap based QCs, two distinct types of qubits have been explored: (i) Ground-state qubits where the information is encoded in two hyperfine or Zeeman sublevels of the ground state [1], and (ii) Optical qubits where the information is encoded in the ground state and an optically accessible metastable excited state [2]. The two types of qubits require distinct experimental techniques where ground-state qubits are manipulated with either two-photon Raman transitions or by direct microwave excitation [1]. In contrast, operations on optical qubits are performed via a resonant light field provided by a laser [2, 3]. Measuring the state of the qubits in a register is usually performed via the electron shelving method using an auxiliary short-lived state for both qubit types [1]. In the presented setup we use $^{40}Ca^{+}$ ions, which contain both, an optical qubit for state manipulation and a ground-state qubit for a quantum memory. Figure 1a) shows a level scheme of the $^{40}Ca^{+}$ ions including all relevant energy levels. Our standard qubit is encoded in the $4S_{1/2}$ ground state and the $3D_{5/2}$ metastable state where the natural lifetime of the $3D_{5/2}$ state ($t_1 = 1.1s$) provides an upper limit to the storage time of the quantum information. The $4S_{1/2}$ state consists of two Zeeman sublevels ($m = \pm 1/2$) whereas the $3D_{5/2}$ state has six sublevels ($m = \pm 1/2, \pm 3/2 \pm 5/2$). This leads to ten allowed optical transitions given the constraint that only $\Delta m = 0, 1, 2$ are possible on a quadrupole transition. The coupling strength on the different transitions can be adjusted by varying the polarization of the light beam and its angle of incidence with respect to the quantization axis set by the direction of the applied magnetic field. Usually we choose the $4S_{1/2}(m_j = 1/2) = |S\rangle = |1\rangle$ and the $3D_{5/2}(m_j = 1/2) = |D\rangle = |0\rangle$ as the computational basis states because the transition connecting them is the least sensitive to fluctuations in the magnetic field. Furthermore it is possible to store quantum information in the two Zeeman substates

noindent of the $4S_{1/2}$ ground-state which are not subject to spontaneous decay ($4S_{1/2}(m_j = 1/2) = |1\rangle_Z$ and $4S_{1/2}(m_j = +1/2) = |0\rangle_Z$).

The projective measurement of the qubit in the computational basis is performed via the $4S_{1/2} \leftrightarrow 4P_{1/2}$ transition at a wavelength of 397nm. If the qubit is in a superposition of the qubit states, shining in a near resonant laser at the detection transition projects the ions state either in the $4S_{1/2}$ or the $3D_{5/2}$ state. If the ion is projected into the $4S_{1/2}$ state, a closed cycle transition is possible and the

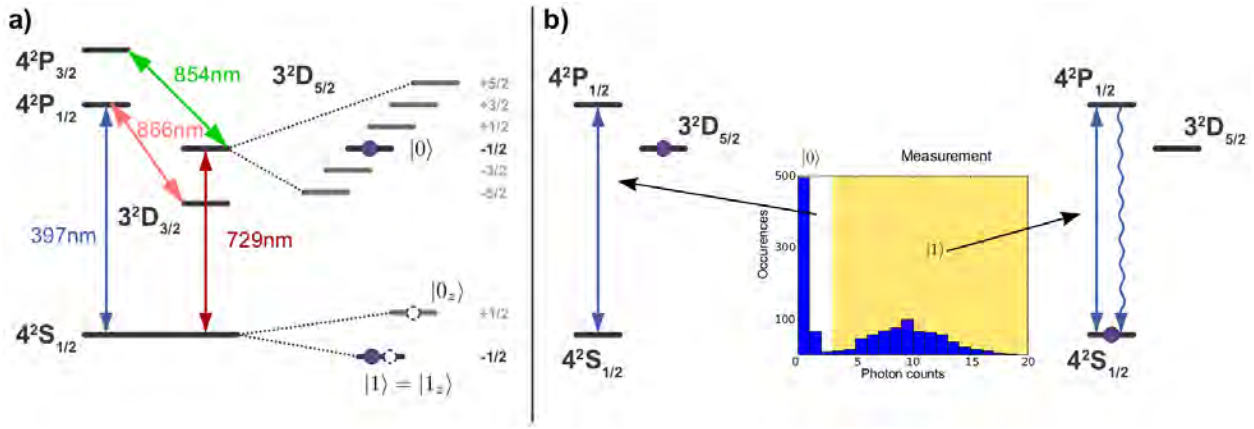

Figure 1: (a) Level scheme of $^{40}Ca^{+}$. Solid circles indicate the usual optical qubit ($4S_{1/2}(m_j = 1/2) = |1\rangle$ and $3D_{5/2}(m_j = 1/2) = |0\rangle$). Open circles indicate the ground state qubit that avoids spontaneous decay $4S_{1/2}(m_j = 1/2) = |1\rangle_Z$ and $4S_{1/2}(m_j = +1/2) = |0\rangle_Z$. (b) Schematic representation of electron shelving detection. The histogram shows the detected photon counts from projections onto both states during the detection interval. It can be seen that it is possible to distinguish the two different outcomes. The highlighted area illustrates the threshold whether the stat is detected as $|0\rangle$ or $|1\rangle$.

ion will fluoresce as sketched in figure 1(b). It is however still possible that the decay from $4P_{1/2}$ leads to population being trapped in the $4D_{3/2}$ state that needs to be pumped back to the $4P_{1/2}$ with light at 866nm. Fluorescence is then collected with high numerical aperture optics and single-photon counting devices. If the ion is projected into the $3D_{5/2}$ state though, it does not interact with the light field and no photons are scattered. Thus the absence or presence of scattered photons can be interpreted as the two possible measurement outcomes which can be clearly distinguished as shown in the histogram in figure 1b). In order to measure the probability $p_{|1\rangle}$ to find the qubit in $4S_{1/2}$, this measurement needs to be performed on multiple copies of the same state. In ion-trap QCs these multiple copies are produced by repeating the experimental procedure N times yielding the probability $p_{|1\rangle} = n(|1\rangle)/N$ where $n(|1\rangle)$ is the number of bright outcomes. This procedure has a statistical uncertainty given by the projection noise $\Delta p|1\rangle = p_{|1\rangle}(1-p_{|1\rangle})/N$ [3]. Depending on the required precision, the sequence is therefore executed between 50 and 5000 times.

Preparing the qubit register in a well defined state is a crucial prerequisite of any quantum computer. In our system this means (i) preparing the qubit in one of the two Zeeman levels of the ground state and (ii) cooling the motional state of the ion string in the trap to the ground state. The well established technique of optical pumping is used to prepare each ion in the $m_j = 1/2$ state of the $4S_{1/2}$ state [2]. In our setup two distinct methods for optical pumping are available: (i) Polarization dependent optical pumping by a circularly polarized laser beam resonant on the $4S_{1/2} \leftrightarrow 4P_{1/2}$ transition as shown in figure 2a) and (ii) frequency selective optical pumping via the Zeeman substructure of the $3D_{5/2}$ state as depicted in figure 2b). Here, the transfer on the qubit transition at 729nm is frequency selective. Selection rules ensure that depletion of the $3D_{5/2}(m_j = 3/2)$ level via the $4P_{3/2}$ effectively pumps the population into the $4S_{1/2}(m_j = -1/2)$ state. The second part of the initialization procedure prepares the ion string into the motional

ground state which requires multiple laser-cooling techniques.

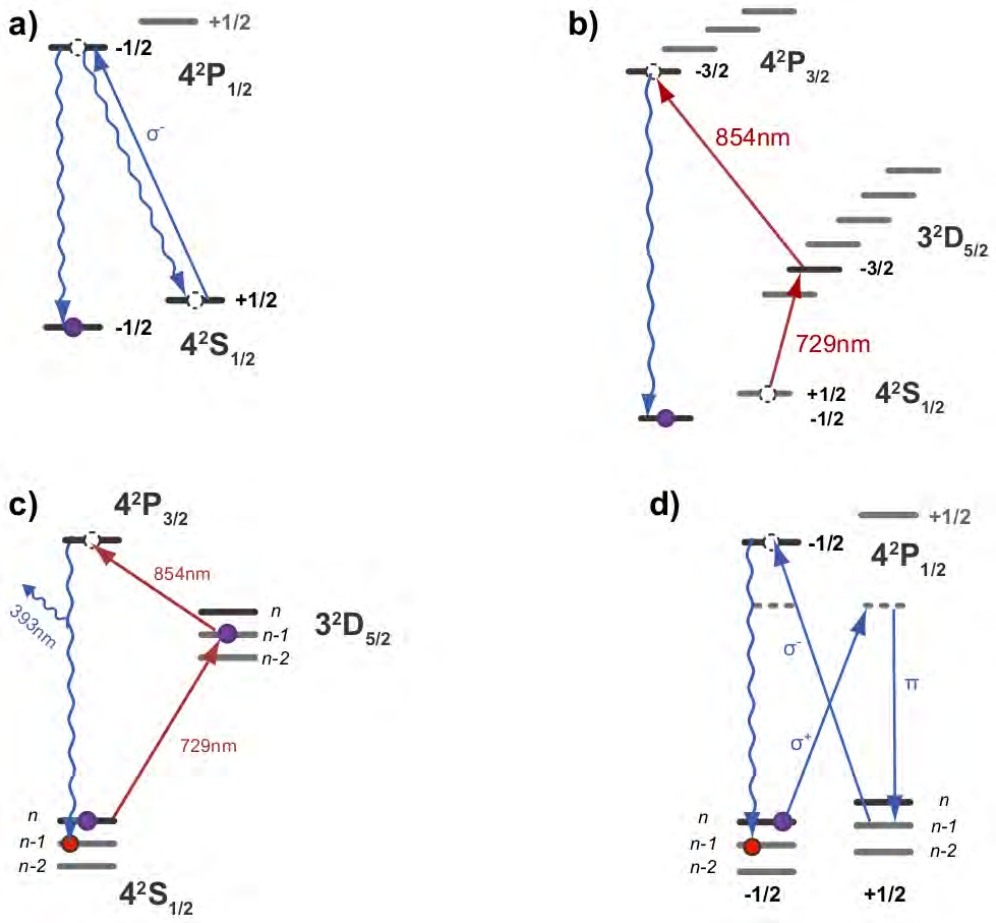

Figure 2: Schematic view of optical pumping which is (a) polarization selective and (b) frequency selective (c) Sideband cooling on the qubit transition. The light resonant with the $3D_{5/2} \leftrightarrow 4P_{3/2}$ transition is used to tune the effective linewidth of the excited state leading to an adiabatic elimination of the $3D_{5/2}$ state. (d) Scheme for sideband cooling utilizing a Raman transition. Here, the σ^- light performs optical pumping which corresponds to the spontaneous decay on the optical transition.

We use a two-step process where the first step consists of Doppler cooling on the $4S_{1/2} \leftrightarrow 4P_{1/2}$ transition that leads to a mean phonon number of $\bar{n} \approx 10$. The motional ground state is subsequently reached with sideband cooling techniques [4]. In our system, the necessary two-level system can be either realized on the narrow qubit transition [5] or as a Raman process between the two ground states via the $4P_{1/2}$ level [1, 2]. A crucial parameter, determining the cooling rate, is the linewidth of the actual cooling transition [4]. When cooling on the long-lived optical transition, the excited state lifetime needs to be artificially shortened in order to adjust the effective linewidth of the transition. This is realized by repumping population from the $3D_{5/2}$ state to the $4S_{1/2}$ state via the $4P_{3/2}$ level with light at 854nm, as outlined in figure 2c) [4]. The procedure using the Raman transition is outlined in figure 2d). Here, the spontaneous decay is replaced by

optical pumping as used for state preparation [1, 6]. In principle, this cooling technique allows for faster cooling rates as the coupling strength to the motional mode, described by the Lamb-Dicke parameter, increases for smaller wavelengths. More importantly, it has the advantage that it can be applied within a quantum algorithm without disturbing the quantum state of idling qubits when the population of the $4S_{1/2}$ state is transferred to a Zeeman substate of the excited state that is outside the computational basis, for example $3D_{5/2}(m_j = 5/2) = |D\rangle$ [7].

2.1.2 The universal set of gates

With a universal set of gates at hand, every unitary operation acting on a quantum register can be implemented [8]. The most prominent example for such a set consists of arbitrary single-qubit operations and the controlled NOT (CNOT) operation. However, depending on the actual physical system, the CNOT operation may be unfavorable to implement and thus it may be preferable to choose a different set of gates. In current ion trap systems, entangling operations based on the ideas of Mølmer and Sørensen have achieved the highest fidelities [9, 10, 11] which, in conjunction with single-qubit operations, form a universal set of gates. In order to implement all necessary operations, we use a wide laser beam that illuminates the entire register uniformly and a second, tightly focused, laser beam to address each ion. Interferometric stability between the two beams would be required, if arbitrary single-qubit operations were performed with this addressed beam in addition to the global MS operations. To circumvent this demanding requirement, the addressed beam is only used for inducing localized phase shifts caused by the AC-Stark effect. Using an off-resonant light field causing AC-Stark shifts has the advantage that the phase of the light field does not affect the operations and thus no interferometric stability is needed. The orientation of the two required laser beams is shown in figure 3a).

Applying an off-resonant laser light with Rabi frequency Ω and detuning Δ onto a the j-th ion modifies its qubit transition frequency by an AC-Stark shift of $\delta_{AC} = \frac{\Omega^2}{2\Delta}$. This energy shift causes rotations around the Z axis of the Bloch sphere and the corresponding operations on ion j can be expressed as

$$S^{(j)}_{(z)}(\theta) = e^{-i\theta\sigma_z^j/2}$$

where the rotation angle $\theta = \delta_{AC}t$ is determined by the AC-Stark shift and the pulse duration. As the $^{40}Ca^+$ ion is not a two-level system, the effective frequency shift originates from AC-Stark shifts on multiple transitions. We choose the laser frequency detuning from any $4S_{1/2} \leftrightarrow 3D_{5/2}$ transition to be 20MHz. There, the dominating part of the AC-Stark shift originates from coupling the far off-resonant transitions from $4S_{1/2}$ to $4P_{1/2}$ and $4P_{3/2}$ as well as from $3D_{5/2}$ to $4P_{3/2}$ [12]. The second type of non-entangling operations are collective resonant operations using the global beam. They are described by

$$R_\phi(\theta) = e^{i\theta S_\phi/2}$$

where $S_\phi = \sum_{i=0}^{N}(\sigma_x^{(i)}\cos\phi + \sigma_y \sin\phi)$ is the sum over all single-qubit Pauli matrices $\sigma_{x,y}^{(i)}$ acting on qubit i. The rotation axis on the Bloch sphere ϕ is determined by the phase of the light field and the rotation angle $\theta = t\Omega$ is fixed by the pulse duration t and the Rabi frequency . Together with the single-qubit operations described above this allows us to implement arbitrary non-entangling operations on the entire register. The entangling MS gate operation completes the universal set of operations. The ideal action of the gate on an N-qubit register is described by

$$MS_\phi(\theta) = e^{-i\theta S_\phi^2/4}.$$

For any even number of qubits the operation $MS_\phi(\pi/2)$ maps the ground state $|00..0\rangle$ directly onto the maximally entangled GHZ state $1/2(|00..0\rangle - ie^{iN\phi}|11..1\rangle)$. For an odd number of ions the produced state is still a maximally GHZ-class entangled state which can be transferred to a GHZ state by an additional collective local operation $R_\phi(\pi/2)$. Implementing the MS gate requires the application of a bichromatic light field $E(t) = E_+(t) + E_-(t)$ with constituents $E = E_0 \cos((\omega_0(\omega_z + \delta))t)$ where ω_0 is the qubit transition frequency, ω_z denotes the frequency of the motional mode and δ is an additional detuning. The level scheme of the MS operation acting on a two-ion register is shown in figure 3b). Mølmer and Sørensen showed that if the detuning from the sideband δ equals the coupling strength on the sideband $\eta\Omega$ the operation $MS(\pi/2)$ is performed when the light field is applied for a duration $t = 2\pi/\delta$. However, implementing MS operations with rotation angles $\pi/2$ is not sufficient for universal quantum computation. Arbitrary rotation angles θ can be implemented with the same detuning δ by adjusting the Rabi frequency on the motional sideband to $\eta\Omega = \delta\sqrt{\theta/(\pi/2)}$. Due to this fixed relation between the rotation angle and the detuning, the gate operation needs to be optimized for each value of θ. In practice this optimization is a time-consuming task and thus the gate is optimized only for the smallest occurring angle in the desired algorithm. Gate operations with larger rotation angles are realized by a concatenation of multiple instances of the already optimized operation.

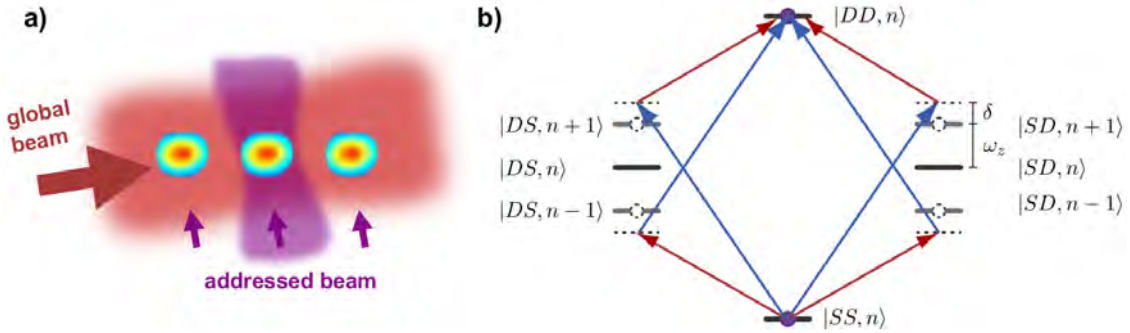

Figure 3: a) Schematic view of the laser beam geometry for qubit manipulation. b) Schematic level scheme of a Mlmer Srensen type interaction. The bichromatic light field couples the states $|SS,n\rangle$ with $|DD,n\rangle$ via the intermediate states $|SD,n\pm1\rangle$ and $|DS,n\pm1\rangle$ with a detuning δ.

If the physical system would consist of a two-level atom coupled to a harmonic oscillator the AC- Stark introduced by one off-resonant light field would be perfectly compensated by its counterpart in the bichromatic field. However, $^{40}Ca^+$ shows a rich level structure where due to the additional Zeeman levels and coupling to the other $4P$ states an additional AC-Stark shift is introduced [12]. This shift changes the transition frequency between the two qubit states which has the effect that the detuning from the sideband transition δ is not equal for both constituents of the bichromatic light field. This would degrade the quality of the operation drastically and thus the shift has to be compensated for which can be achieved by two distinct techniques [13]: (i) The center frequency of the bichromatic light field can be shifted or (ii) the light intensity of the two constituents can be unbalanced to induce a Stark shift on the carrier transition which compensates the unwanted Stark shift. Depending on the application, one compensation method is favorable over the other. Method (i) makes it easier to optimize the physical parameters to achieve very high gate fidelities but leads to an additional global rotation around σ_z which is tedious to

measure and compensate for in a complex algorithm. This can be avoided by method (ii) but the compensation is not independent of the motional state leading to a slightly worse performance [13]. Therefore, we generally choose method (i) if the goal is to solely generate a GHZ state whereas method (ii) is favorable if the gate is part of a complex algorithm. In general an algorithm requires operations with positive and negative values of the rotation angles for the available operations. For the resonant $R_\phi(\theta)$ operation both signs of θ can be realized by changing the phase of the light field since $e^{-i(-\theta)S_\phi} = e^{-i(-\theta)S_{\phi+\pi}}$ which is not possible for MS operations as $S_\phi^2 = S_{\phi+\pi}^2$. The sign of the rotation of the MS operation angle can only be adjusted by choosing the sign of the detuning δ [14]. However, performing MS operations with positive and negative detunings results in a more complex setup for generating the required RF signals and also a considerable overhead in calibrating the operation. Therefore it can be favorable to implement negative θ by performing $MS_\phi(\pi - |\theta|)$ which works for any odd number of ions whereas for an even number of ions, an additional $R_\phi(\pi)$ operation is required [14]. With this approach the quality of operations with negative rotation angles is reduced but the experimental overhead is avoided.

2.1.3 Tools beyond coherent operations

In general, any quantum computer requires non-reversible and therefore also non-coherent operations for state initialization and measurements[8]. For example, quantum error correction protocols rely on controlled non-coherent operations within an algorithm to remove information on the error from the system similar to state initialization. Furthermore, the robustness of a quantum state against noise can be analyzed by exposing it to a well defined amount of phase or amplitude damping [28]. Surprisingly, it has been shown theoretically that non-coherent operations can serve as a resource for quantum information [14, 15, 16]. Naturally, these ideas can only be implemented if controlled non-coherent operations are available in the system. Mathematically, these non-reversible operations are described by a trace-preserving completely positive map $E(\rho)$ acting on a density matrix rather than unitary operations acting on pure states. The action of such a map is described by $E(\rho) = \sum_k E_k^\dagger \rho E_k$ with Kraus operators E_k fulfilling $\sum_k E_k E_k = 1$ [8]. In our system two different variations of these controlled dissipative processes are available [17]: The archetype of a controlled non-coherent optical process is optical pumping. We can perform optical pumping on individual qubits inside the register with the following sequence as shown in figure 4b): (i) Partially transfer the population from $|D\rangle$ to $|S'\rangle$ with probability γ, and (ii) optical pumping from $|S'\rangle$ to $|S\rangle$ analogous to the qubit initialization. The partial population transfer is performed by a coherent rotation with an angle θ on the transition $4S_{1/2}(m_j = +1/2) \leftrightarrow 3D_{5/2}(m_j = -1/2)$ which leads to $\gamma = \sin^2(\theta)$. This reset process can be described as controlled amplitude damping on an individual qubit where the map affecting the qubit is shown in table 1. Note that the information in the qubit states is not affected as the optical pumping light couples to neither of the original qubit states. For a full population transfer ($\gamma = 1$) the procedure acts as a deterministic reinitialization of an individual qubit inside a register as required for repetitive quantum error correction [18].

Furthermore an alternative implementation of optical pumping can be used to generate controlled phase damping. This process preserves the populations in the respective qubit states but destroys the coherences between them with probability γ: (i) The information residing in state $|D\rangle$ of all qubits is protected by transferring it to the $|S\rangle = 4S_{1/2}(m_j = +1/2)$ state before the reset step. (ii) On the qubit to be damped, the population from $|S\rangle$ is partially transferred into the $|D\rangle = 3D_{5/2}(m_j = -5/2)$ state with probability γ. Here, the partial population transfer is

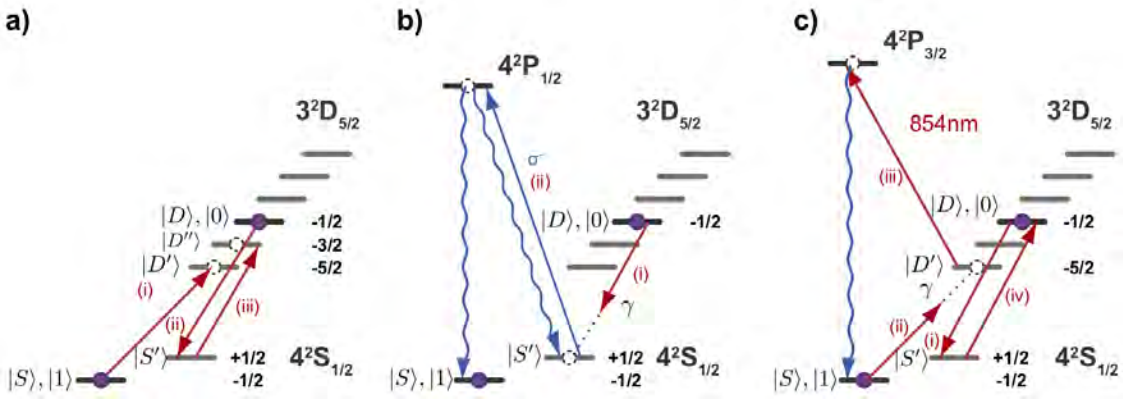

Figure 4: a) The process to decouple individual qubits: (i) The population from $|S\rangle$ is transferred to $|D\rangle$. (ii) The population from $|D\rangle$ is transferred to $|S\rangle$ and subsequently to (iii) $|D\rangle$. b) Controlled phase damping with strength γ utilizing light at 854nm. (i) Population from $|D\rangle$ is hidden in the $|S\rangle$ state. (ii) The population from $|S\rangle$ is partially brought to $|D\rangle$ and (iii) shining in light at 854 nm depletes the $3D_{5/2}$ via $4P_{3/2}$ and finally (iv) the population is brought from $|S\rangle$ back to $|D\rangle$. (c) Implementing controlled amplitude damping using the 397 σ beam. (i) Transferring the population from $|D\rangle$ to $|S\rangle$. (ii) Optical pumping of $|S\rangle$ using light at 397nm.

performed by a coherent rotation on the transition $4S_{1/2}(m_j = -1/2) \leftrightarrow 3D_{5/2}(m_j = -5/2)$ (iii) Shining light resonant with the $3D_{5/2} \leftrightarrow 4P_{3/2}$ transition at 854nm onto the ions depletes this level to $|S\rangle$. (iv) Transferring $|S\rangle$ back to $|D\rangle$ restores the initial populations, the coherence of the qubit has been destroyed with probability γ. The schematic of this process is shown in figure 4c) and the resulting map can be found in table 1. Our system furthermore allows measuring a single qubit without affecting idling qubits in the same ion string. For this, all spectator ions need to be decoupled from the detection light. This is realized by transferring the population from the $|S\rangle$ state to the $|D\rangle = 3D_{5/2}(m_j = -5/2)$ state. Applying light on the detection transition measures the state of the ion of interest while preserving the quantum information encoded in the hidden qubits. This information can be used to perform conditional quantum operations as needed for teleportation experiments [7] or quantum non-demolition measurements [19]. It should be noted, that the operations forming our implementable set of gates shown in table 1 allow the realization of any completely positive map, which corresponds to a Markovian process [19, 20, 21]. In order to faithfully estimate the resulting fidelity of an implemented algorithm, a complete numerical simulation of the physical system has to be performed. However, a crude estimation can be performed assuming a fidelity of 99.5% for non-entangling operations and $\{98, 97, 95, 93, 90\}$% for the MS operations on a string of $\{2, 3, 4, 5, 6\}$ ions [36]. The fidelity of the entire algorithm is then estimated by simply multiplying the fidelities of the required operations.

2.1.4 The linear Paul trap

In this section we give an overview of the experimental setup of our ion-trap quantum information processor. First, we describe in detail the ion trap, the optical setup and the laser sources. Then we concentrate on the experiment control system and techniques to infer the state of the qubit register.

Name	Addressed/global	Ideal operation
AC-Stark shift pulses	addressed	$S_z^{(i)}(\theta) = e^{-i\theta/2\sigma_Z^{(i)}}$
Collective resonant operations	collective non-entangling	$S_\phi(\theta) = e^{-i\theta/2S_\phi}$
Mølmer-Sørensen	collective entangling	$MS_\phi(\theta) = e^{-i\theta/2S_\phi^2}$
Phase damping	addressed non-coherent	$E_0^p = \begin{bmatrix} 1 & 0 \\ 0 & \sqrt{1-\gamma} \end{bmatrix}$ $E_1^p = \begin{bmatrix} 0 & 0 \\ 0 & \sqrt{\gamma} \end{bmatrix}$
Amplitude damping	addressed non-coherent	$E_0^a = \begin{bmatrix} 1 & 0 \\ 0 & \sqrt{1-\gamma} \end{bmatrix}$ $E_1^a = \begin{bmatrix} 0 & 0 \\ \sqrt{\gamma} & 0 \end{bmatrix}$
Single-qubit measurement	addressed non-coherent	Projection onto $\|0\rangle\langle 0\|$ or $\|1\rangle\langle 1\|$

Table 1: The extended set of operations in our ion trap QC. This set of operations allows us to implement any possible Markovian process.

The trap in our experimental system is a macroscopic linear Paul trap with dimensions as shown in figure 5 [2]. The trap is usually operated at a radial motional frequency of 3MHz and an axial motional frequency of 1MHz. These trapping parameters are slightly adjusted with respect to the number of ions in the string to prevent overlap of the frequencies from different motional modes of all transitions. In order to minimize magnetic field fluctuations, the apparatus is enclosed in a magnetic shield (75x75x125 cm) that attenuates the amplitude of an external magnetic at frequencies above 20 Hz by more than 50dB. The trap exhibits heating rates of 70ms per phonon at an axial trap frequency of 1MHz. Micromotion for a single ion can be compensated with the aid of two compensation electrodes. The remaining micromotion creates sidebands at the trap frequency which can be observed in an ion spectrum on the qubit transition. The strength of the excess micromotion is described by the modulation index β of these sidebands where in our setup a modulation index of $\beta \leq 1\%$ is observed [22, 23].

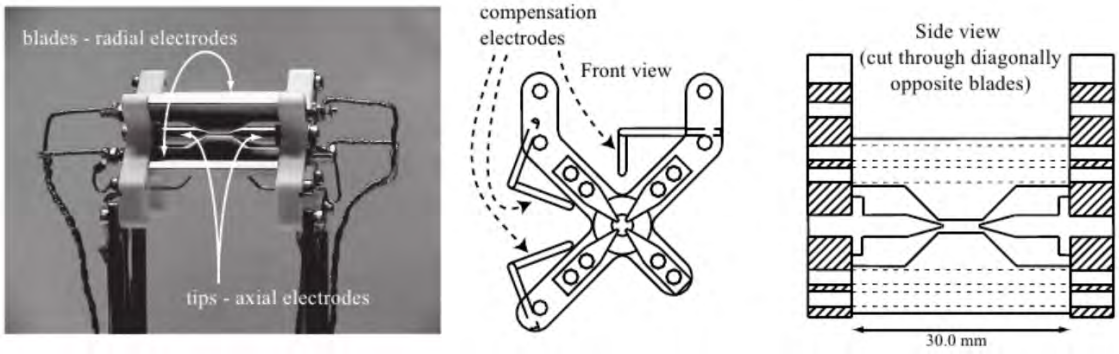

Figure 5: Schematic drawing of the linear Paul trap used in our experiment. The distance between the endcaps is 5mm whereas the distance between the radio-frequency blades is 1.6mm.

Transition	Wavelength	Usage	Linewidth
$4S_{1/2} \leftrightarrow 4P_{1/2}$	397nm	Doppler cooling, optical pumping and detection	$\leq$1MHz
$4S_{1/2} \leftrightarrow 3D_{5/2}$	729nm	Sideband cooling and qubit manipulation	$\leq$20Hz
$3D_{3/2} \leftrightarrow 4P_{1/2}$	866nm	Repumping for detection	$\leq$1MHz
$3D_{1/2} \leftrightarrow 4P_{3/2}$	854nm	Quenching for Sideband cooling and qubit reset	$\leq$1MHz
neutral calcium	422nm	Photoionization first stage	-
neutral calcium	375nm	Photoionization second stage	-

Table 2: Laser wavelengths needed for a Ca + ion trap experiment. The lasers are stabilized to a reference cavity with the Pound-Drever-Hall locking technique except for the photoionization lasers which are not actively stabilized.

2.1.5 Optical setup

A quantum information processor with $^{40}Ca^{+}$ requires multiple laser sources, listed in table 2, to prepare, manipulate and measure the quantum state of the ions. The ions are generated from a neutral atom beam with a two-step photo-ionization process requiring laser sources at 422nm and 375nm. Manipulating the state of the qubits is done with a Titanium-Sapphire laser at 729nm on the $4S_{1/2} \leftrightarrow 3D_{5/2}$ qubit transition and its setup as described in reference [24]. The laser has a linewidth of below 20Hz and the relative intensity fluctuations are in the range of 1.5% [24].

The laser sources sources reside on different optical tables than the vacuum vessel housing the trap, and thus the light is transferred between different tables with optical fibers. The optical access to the trap itself is constrained by the surrounding octagon vacuum vessel which is sketched in figure 6 including the available beams with their respective directions. The 397nm light is required for multiple tasks and thus multiple beams are required: one beam for Doppler-cooling and detection, another beam for optical pumping (labeled Pumping σ), and two beams for Raman sideband-cooling (labeled Raman σ, Raman π). In particular, the beams used for optical pumping need to be aligned with the magnetic field generated by the coils as indicated in figure 6. In practice it is favorable to adjust the orientation of the magnetic field with respect to the light beam since the magnetic field can be adjusted without moving any mechanical part. The beams of the 866nm and 854nm laser are overlapped with the 397nm detection beam in a single-mode photonic crystal fiber.

In order to implement our set of operations, the 729nm light needs to be applied to the ions from two different optical ports: (i) the addressed beam which is a tightly focused beam illuminating only a single ion and (ii) the global beam which is a wide beam that illuminates all ions with an approximately homogeneous light intensity. The angle between the global beam and the axial trap axis is 22.5° which leads to a Lamb-Dicke parameter of $\eta_{glob} = 6\%$ [40]. The width of the beam is chosen so that the light intensity shows variations of less than 2% over the entire ion string. Considering that the ions are arranged in a linear crystal, it is advantageous to use an elliptical shape for the global beam to achieve higher light intensities at the position of the ions. The elongated axis of the beam has typically a diameter of 100μm which is sufficient for ion strings with up to 8 ions. For larger ion strings, the beam size needs to be enlarged which increases the required time for performing collective operations. The angle between the addressed beam and the trap axis is 22.5° so that there the Lamb-Dicke parameter is smaller $\eta_{add} = 2.5\%$. The addressed beam needs

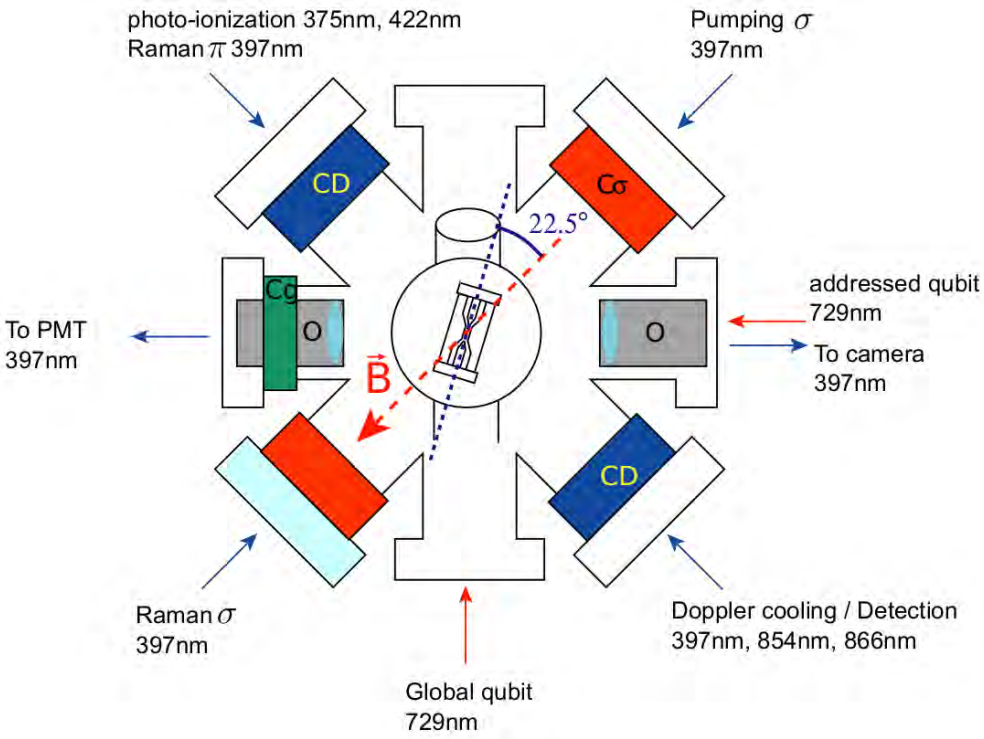

Figure 6: Overview of the alignment of the various laser beams, the coils generating the magnetic field and the trap with respect to the vacuum vessel.

to be able to resolve the individual ions in the string which means that the beam size needs to be smaller than the inter-ion distance of approximately 5μm. This small beam size is realized with the aid of a custom high numerical aperture objective situated in an inverted viewport as sketched in figure7a). Additionally, the beam has to be rapidly switched between the ions which is realized with an electro-optical deflector (EOD). The switching speed depends on the capacitance of the EOD and the output impedance of the driving high voltage amplifier. Figure 7b) shows the voltage on the EOD during a switching event between two neighboring ions which demonstrated that a switching event requires approximately 15μs. Experience has shown that a delay between the switching event and the next light pulse of 30μs is sufficient to switch between arbitrary ions in a string of up to 8 ions. Note that the voltage ramp measured at the EOD can only serve as an indicator for the position of the laser beam but does not provide information about the settling time of the laser light phase at the position of the ion. It was observed that the phase of the light field keeps changing for more than 100μs after a switching event. However, this does not affect the qubit operations for our set of operations as the AC-Stark shift does not depend on the phase of the light field as described in section 1.

2.1.6 Measuring individual ions within a quantum register

As described in section 1, measuring the quantum state of the ions is performed by counting single photons on the $4S_{1/2} \leftrightarrow 4P_{1/2}$ transition. We use high numerical aperture objectives located in an inverted viewport to reduce the distance between the ion and the objective as shown in figure 6.

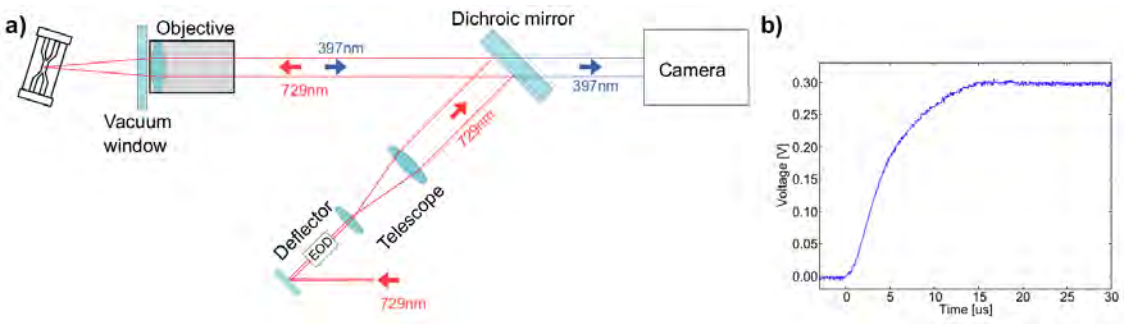

Figure 7: a) Optical setup for the addressing beam setup. b) Time dependence of the voltage on the EOD switching between two neighboring ions. After approximately 15s the voltage settles and thus the switching process is finished.

Two detection channels are available: one with a photo-multiplier-tube (PMT) and another with an electron multiplying CCD camera. The PMT integrates the photons over its sensitive area and thus cannot infer any spatial information on the ions. The number of detected photon counts depends on the number of bright ions as is indicated in the histogram of PMT counts shown in figure 8. By setting appropriate thresholds it is then possible to determine the number of ions found in the $4S_{1/2} = |0\rangle$ state which is sufficient information to perform permutationally invariant state tomography [25] or to determine the fidelity of a multi-qubit GHZ state [26].

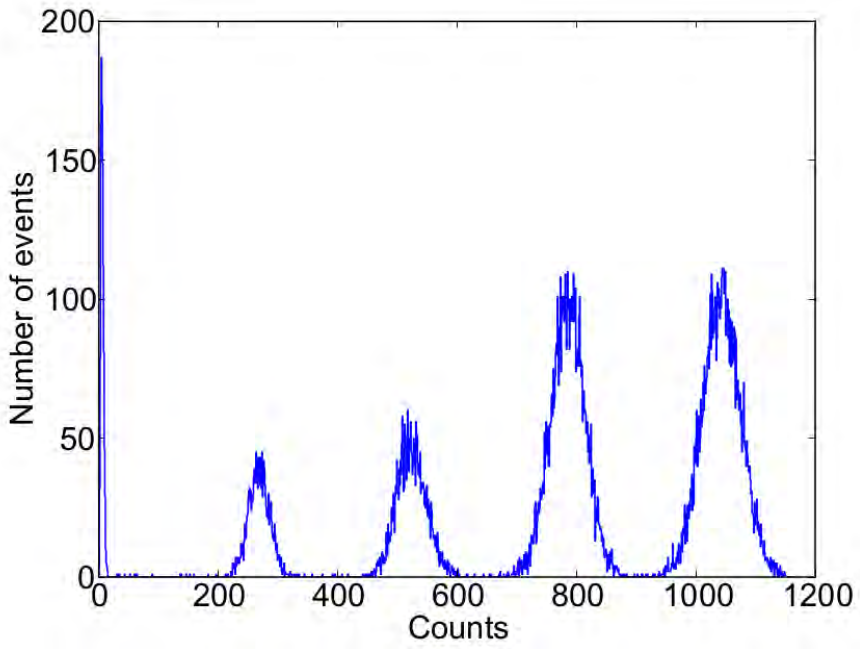

Figure 8: Histogram of counted pulses from the PMT for a 4 ion string. The histogram is derived 21200 measurements with a detection time of 5ms.

In contrast, the CCD camera is able to resolve the spatial information of the detected light and

is thus able to determine the state of each ion in the string separately. It uses the same objective as for generating the addressed 729nm beam where the beam at 729nm and the detected light at 397nm are separated by a dichroic mirror as sketched in figure 7a). The analysis of the camera data is performed in five steps: (i) A camera image is taken with an exposure time of 7ms. The value of each pixel corresponds to the number of detected photons. (ii) For further analysis, a limited region of interest (ROI) around the ions position of the whole camera image is used. For a register of 4 ions the ROI consists of 35x5 pixels but the ROI size needs to be adjusted to the length of the ion string. (iii) The pixel values are summed over the y-axis of the ROI-image to get the brightness information along the ion string. (iv) This brightness distribution is then compared to pre-calculated distributions which are generated from a reference image where all ions are bright. From this reference image, the position and brightness distribution of each ion are determined. The state of the ion string is then inferred by comparing the summed pixel values with the pre-calculated distributions of each possible outcome by calculating the mean squared error χ^2. Finally (v) the state with the smallest mean squared error is chosen to be the most likely state. Two examples of this analysis procedure are shown in figure 9. Note that this method is not scalable as the number of pre-calculated distributions grows exponentially with the number of ions. However recent work on state detection in trapped ion system promises efficient detection schemes [27].

2.1.7 Errors in the qubit memory

In general, errors affecting a qubit memory are described by a combination of phase damping and amplitude damping [8]. In optical qubits, amplitude damping corresponds to decay from the excited to the ground state whereas phase damping destroys the phase of a superposition state but does not alter the population of the qubit. The lifetime of the excited qubit is a fundamental property of the ion species and gives an upper limit to the storage time of a quantum memory encoded in an optical qubit. In the experiment, the lifetime of the excited state can be reduced due to residual light fields depleting the $3D_{5/2}$ state via another state, or by collisions with background gas particles. This possible error source can be investigated by confirming that the time constant of the exponential decay from the $3D_{5/2}$ state is close to the natural lifetime of $1.168(7)$s [28]. In our setup, we find a lifetime of $_1 = 1.13(5)$s [17]. The second noise type, phase damping, is usually investigated with Ramsey spectroscopy which determines the coherence properties of a superposition state [2]. There, the qubit is initially prepared in an equal superposition of the two computational states by a $R_0(\pi/2)$ rotation. After a certain storage time, a second rotation $R_\pi(\pi/2)$ is applied that ideally maps the qubit back into the state $|1\rangle$. If the phase ϕ of the second pulse $R_\pi(\pi/2)$ is varied with respect to the first pulse, the probability of being in state $|1\rangle$ is an oscillation dependent on ϕ. If the coherence of the state is decreased due to phase damping, the second mapping pulse cannot reach the basis states anymore which is observed as a decrease in the amplitude of the oscillation. This loss of contrast corresponds directly to the remaining phase coherence of the superposition which naturally decreases with increasing storage time.

In our system, phase damping is predominantly caused by fluctuations between the frequency of the qubit transition and the driving field. The two main contributions are (i) laser frequency fluctuations and (ii) fluctuations in the magnetic field which translate into fluctuations of the qubit transition frequency. It is then possible to distinguish the contributions by investigating the coherence decay on multiple transitions between different Zeeman substates of the $4S_{1/2}$ and $3D_{5/2}$

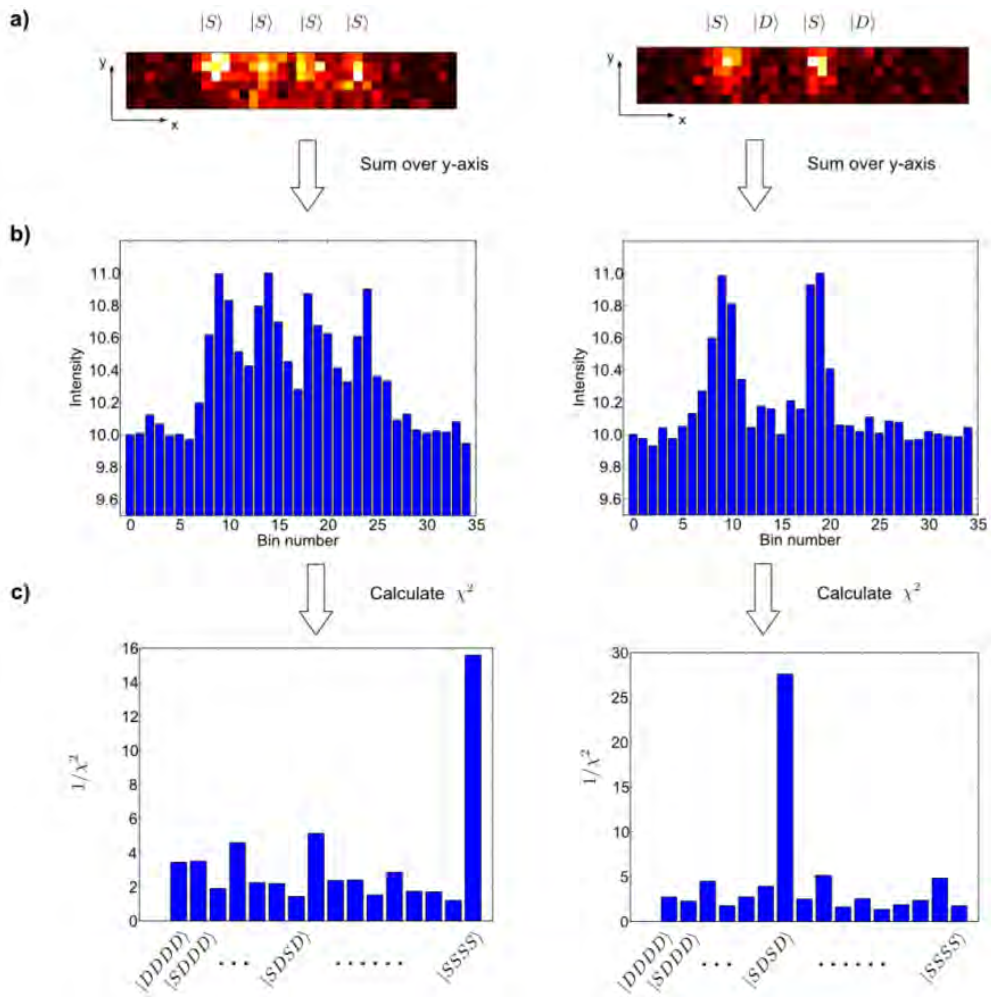

Figure 9: Schematic illustration of the camera detection in a 4 ion register. (a) False color image of the region of interest. (b) Brightness information after summation over the y-axis of the image. (c) $1/\chi^2$ of the sum with generated data for every possible state. The peak corresponds to the most likely state. In this case index 6 (15), which corresponds to the state $|SDSD\rangle(|SSSS\rangle)$, is the most likely state.

levels because they show different susceptibility to the magnetic field due to different Lande g factors. In figure 10a) the blue rectangles represent the coherence decay on the $4S_{1/2}(m_j = -1/2) \leftrightarrow 3D_{5/2}(m_j = -1/2)$ transition which is least sensitive to fluctuations in the magnetic field. The green diamonds show the coherence decay for the $4S_{1/2}(m_j = -1/2) \leftrightarrow 3D_{5/2}(m_j = -5/2)$ which has approximately 5 times higher sensitivity to fluctuations of the magnetic field [23, 29]. Note that both transitions show effectively the same coherence decay for storage times up to 1ms. This suggests that for typical experiments where the coherent manipulation is shorter than 1ms, the main source for dephasing are laser-frequency fluctuations.

The phase damping process can be theoretically described by a model that applies random phase- flips with a certain probability p to multiple copies of the same state. The ensemble of

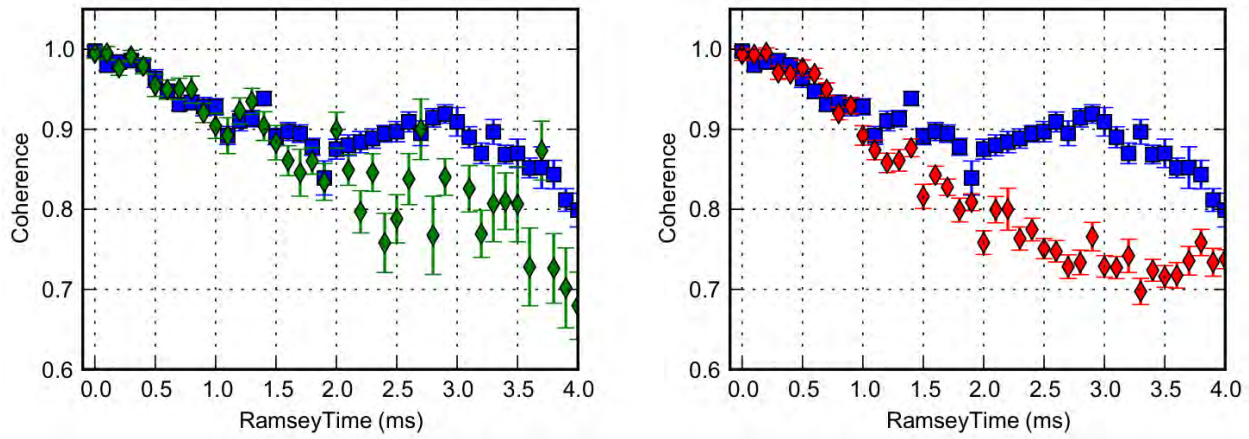

Figure 10: a) Ramsey contrast decay on two transitions with different sensitivity to the magnetic field fluctuations. Blue squares indicate the less sensitive $4S_{1/2}(m_j = -1/2) \leftrightarrow 3D_{5/2}(m_j = -1/2)$ transition whereas green diamonds correspond to the $4S_{1/2}(m_j = -1/2) \leftrightarrow 3D_{5/2}(m_j = -5/2)$ transition. b) Ramsey contrast decay on the transition which is least sensitive to magnetic field fluctuations, without (blue squares) and with (red diamonds) spin echo.

all states is then described by a density matrix whose off-diagonal elements are affected by the phase damping as $\rho_{i,j} \longrightarrow \rho_{i,j}(1-2p)$. This model of a phase-flip rate is close to the concept of a bit-flip rate used in classical computer science and is therefore widely used in theoretical works on quantum information [8]. However, a physical model for phase damping describes the phase-flip probability as a function of the information storage time. In order to do so, one has to find a noise-model describing temporal correlations of the noise source. The most straightforward noise model assumes temporally uncorrelated noise which leads to an exponential decay of the coherence characterized by the transversal coherence time $_2$ and therefore to off-diagonal elements $_{i,j} = _{i,j}e^{-t/_2}$ [30]. This description is used in most quantum computing models where the noise can be fully characterized by the amplitude damping timescale $_1$ and the phase coherence time $_2$ [8]. In most physical systems, technical noise is temporally correlated and thus this simple model of uncorrelated phase noise does not apply [26]. In particular the coherence decay in our system deviates notably from an exponential decay as can be seen in figure 10a). This effect can be amplified with the aid of a well known method to enhance the storage time of a quantum memory known as the spin echo technique. There, the basis states are swapped at half the storage time which reverses the phase evolution and thus cancels fluctuations provided their timescale is longer than the storage time. However, it is possible that the performance with a single echo is worse than the original register if this condition is not satisfied. This effect is demonstrated in figure 10b) where the coherence with spin echo (red diamonds) is worse than without echo (blue squares). There exist more sophisticated methods to enhance the qubit storage time which are able to take temporal correlations into account. A formal description of this techniques is known as dynamical decoupling which has already been demonstrated in various physical systems [31, 32, 33, 34]. For a given noise spectrum an optimal pattern of echo pulses can be determined to maximize the phase coherence. Interestingly, one can use this technique to determine the spectral noise density from multiple coherence decays with varying number of echos [34, 35].

In our system the noise from the laser and magnetic fields are almost identical over the entire register and therefore the phase noise can be modeled affecting the entire register simultaneously. This correlation leads to a faster loss of coherence between states with large total energy difference [26]. On the other hand, this spatial correlation enables decoherence free subspaces (DFS) which are not affected by dephasing. The DFS consists of states where acquiring an equal phase on all qubits leads only to a global phase of the state and thus to no dephasing. For example, a single logical qubit can be encoded in two physical qubits as $|0_l\rangle = |01\rangle + |10\rangle$ and $|1_l\rangle = |01\rangle|10\rangle$ respectively. The two logical states have identical total energy difference and thus form a DFS, where a universal set of operations with two logical qubits has been demonstrated in our system [36]. However, it is not clear how well the concept of a DFS can be extended to larger register sizes, and thus we show the coherence decay of an 8-qubit DFS state of the form $|00001111\rangle + e^i|11110000\rangle$ in figure 11. The state is generated by preparing the qubit register in the state $|00001111\rangle$ and performing a $MS_{\phi=0}(\pi/2)$ operation. If the DFS is also present for 8 ions, the loss of coherence should correspond to the spontaneous decay of the $3D_{5/2}$ state resulting in an exponential decay of the coherence with timescale $\tau = \tau_1/n$ where $n = 4$ is the number of excited ions. This is illustrated in figure 11 showing the measured coherence decay and the expected decay, assuming only spontaneous decay. Furthermore, the spontaneous decay can be eliminated by encoding the qubit in the two substates of the $4S_{1/2}$ level. The red squares in figure 11 show no noticeable decay during a storage time of 200ms where limitations of the experiment control system (and PhD students) prevent investigating longer storage times. The storage time limit of this DFS is then given by fluctuations in the magnetic field gradient and is expected to be in the 30s regime [37].

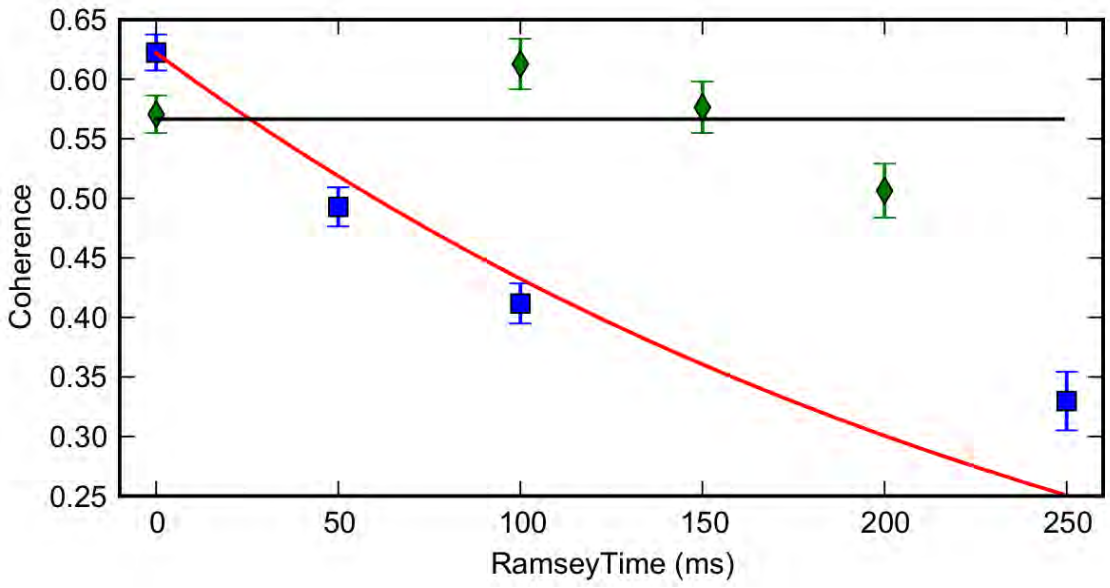

Figure 11: Coherence as a function of the qubit storage time of an 8 qubit DFS state encoded in the optical qubit (blue squares) and the ground-state qubit (green diamonds) eliminating amplitude damping decay. The solid lines represent the expected decay for both qubit types.

2.1.8 Errors during the coherent manipulation

Errors occurring during the coherent manipulation of the quantum information are mainly due to (i) laser intensity fluctuations (ii) crosstalk and (iii) the limited coherence of the motional mode.

Intensity fluctuations of the laser light manipulating the ions lead to a fluctuating Rabi frequency and thus decrease the fidelity of the operations. Measuring the fluctuations of the light field with a photo diode indicates that the fluctuations have relevant timescales on the order of seconds to minutes. We assume therefore that the major sources are (i) fluctuations of the coupling efficiency into a single-mode optical fiber, (ii) thermal effects in acousto-optical devices, (iii) polarization drifts in the fiber, which translate into a varying intensity after polarization defining optics, and (iv) beam pointing instability of the laser light with respect to the ion. These intensity fluctuations can be measured directly on the ions by inserting AC-Stark shift operations with varying length into a Ramsey experiment as sketched in figure 12a). The AC-Stark shift operations translate intensity fluctuations directly into phase fluctuations and thus the same Ramsey techniques as for characterizing phase-noise can be used to measure them. The timescale of the intensity fluctuations is slow compared to the required time for taking 100 repetitions of the sequence nd thus they cause excess fluctuations of the measured excitation probabilities rather than a coherence decay.

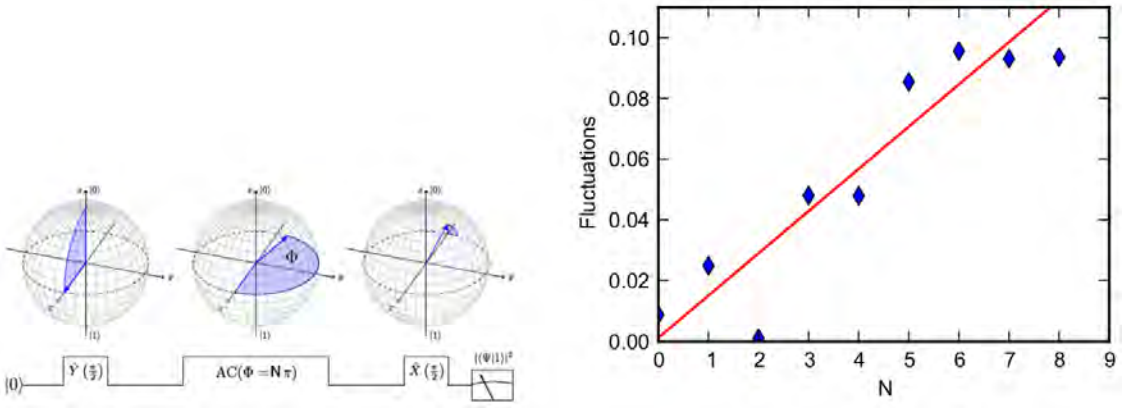

Figure 12: a) Measurement scheme for the slow intensity fluctuations with Ramsey type experiments. Multiple (N -times) rotations around the z-axis of the Bloch sphere are introduced into a Ramsey experiment translating intensity fluctuations into additional noise on the excitation probability. b) Measured state probability fluctuations Δp for multiple N where the slope is fitted to be $0.013(1)$ leading to effective intensity fluctuations of $\Delta I/I_N = 0.41(6)\%$.

These excess fluctuations can be determined by comparing the standard deviation of the measured data with the expected projection noise $\Delta p^2 = \Delta^2_{proj} + \Delta^2_{excess}$. This excess noise in the state probability can be translated into fluctuations of the rotation angle via error propagation. We choose the rotation angle to be $\theta = N\pi$ with N being an integer yielding $\Delta\theta/\theta = \Delta p_{excess}/\pi N$ and perform this analysis up to $N = 8$. The measured state probability fluctuations are then analyzed with a linear fit as shown in figure 12b). From this, the relative fluctuations of the rotation angles are determined which are directly equivalent to the relative fluctuation of the Rabi frequency $\Delta\theta/\theta = \Delta\Omega/\Omega$. For the AC-Stark shift operations the Rabi frequency is directly proportional to the laser intensity yielding $\Delta\Omega/\Omega = \Delta I/I$. From the fitted data we can identify the average laser

fluctuations to be $\Delta\langle I/I\rangle_N = 0.41(6)\%$.

An error source that affects the register when performing addressed single-qubit operations is crosstalk where due to the finite width of the addressing laser, along with the desired ion, also its neighboring ions are affected. This addressing error is characterized by the ratio of the Rabi frequency of the addressed ion i to the Rabi frequencies the neighboring ion $j : i, j = \Omega_i/\Omega_j$. The addressed operation, when addressing ion i, can then be described by $S_z^{(i)}(\theta) = e^{(i\theta\sum_j \sigma_z^{(i)}\epsilon_{i,j})}$ where ϵ is the addressing matrix describing the crosstalk. The magnitude of the error can then be bounded by the maximum off-diagonal element of this matrix $\epsilon_{max} = max_{i\neq j}\epsilon_{i,j}$. In figure 13 an example of excessive crosstalk in a three ion register is shown with $\epsilon_{max} = 22/121 = 18\%$. . Typically, the maximum crosstalk on the addressed AC-Stark operations is $\epsilon_{max} \leq 3\%$ for up to 8 ions where crosstalk between more distant ions is typically smaller than 10^3 . Note that this error is coherent, and thus can be undone if the whole addressing matrix is known. Thus, the compensation of the crosstalk can be integrated into the numerical optimization algorithm generating the sequence of operations if the crosstalk is constant over time.

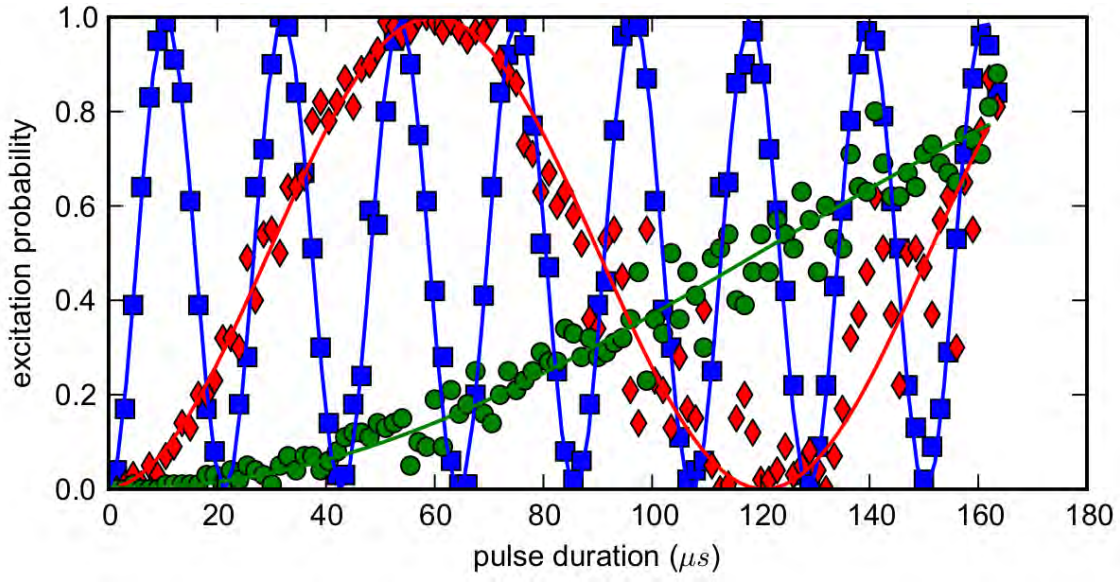

Figure 13: Illustration of the crosstalk between neighboring qubits where the middle ion (blue rectangles) is addressed. The fitted Rabi oscillation periods are 22μs for the addressed ion 2, 121μs for ion 1 (red diamonds), and 464s for ion 3 (green circles).

The presented error sources affect both, entangling as well as non-entangling operations. A loss of coherence on the motional mode does not affect non-entangling operations. However, the entangling MS operation require coherences between different motional states which can be decreased by (i) fluctuations of the static voltages defining the trap frequencies and (ii) heating of the ion string. The coherence time of the motional mode can be determined by performing a Ramsey type experiment which is only sensitive to the phase between two different motional states. This is possible by using a superposition of two motional states $1/\sqrt{2}(|S,0\rangle + |S,1\rangle)$ instead of a superposition of the electronic state $1/\sqrt{2}(|S\rangle + |D\rangle)$ [61]. The motional coherence can then be measured analogous to the qubit storage time and yields an exponential decay with time constant

$\tau_{motion} = 110(20)$ms. This coherence time is sufficiently long to allow high fidelity operations [11].

2.2 Innsbruck II: Scalable System for Trapped Ion Quantum Computation

One of the main challenges for ion-trap based quantum computation are:

- the long turn-around times for any changes to the chamber or trap (usually on the order of more than 2 weeks)
- ideally a vacuum exceeding UHV specifications,
- the sensitivity to magnetic field fluctuations, and
- mechanical vibrations (and thus motion of the ion with respect to the light field), limiting the coherence time of the system,

Within the SS system, we overcome all of these challenges by use of a flow-cryostat based on liquid helium, combined with both a rigid framework for the chamber, as well as mechanical decoupling of vibrations. Here, the cryostat with copper heatshields serves as a magnetic shield and at the same time creates an ideal vacuum on the timescale of a few days only.

2.2.1 Choice of the cryostat

There are four different types of cryostats available:

- Gifford-McMahon (closed-cycle cryostat)
- Pulse Tube (closed-cycle cryostat)
- Flow Cryostat (wet cryostat)
- Bath Cryostat (wet cryostat)

For our choice of the cryostat, the main criteria were magnetic fields (fluctuations should be in the order of 1 μm or less) and vibrations caused by the cryostat (the peak-to-peak vibrations should be about the size of the wavepacket of an ion in the trap, or smaller). Closed-cycle cryostats work with electricity. When we inquired with the companies which produce such cryostats, such as Cryomech or Janis, they told us one has to expect magnetic field fluctuations about 100 mGauss in a distance of 1m from the cryostat. We planed not to separate the cold finger of the cryostat too much from our trapping region. Hence, we would have to cope with fluctuations higher then 100 mGauss, which would correspond of line shifts of more than 100 kHz of Ca- or Sr-quadropule transition. One cannot place a mu-metal around a Gifford-McMahon cryostat, but with a Pulse Tube cryostat it is possible to separate the cold head from the cold finger. One can then wrap mu-metal around the cold head and thereby shield its magnetic field. In contrast to closed cycle systems, wet systems do not produce any magnetic fields.

When we inquired with the companies like Cryomech or Janis, they told us expect about 10-100 μm of vibrations with closed-cycle cryostats and about 1μm of vibrations with a wet system.

But that obviously depends on how the cryostat is mounted. Regardless of the choice of the cryostat that we will need vibration isolation to reduce the vibrations into the nanometer-regime. Additionally, closed-cycle cryostats produce a lot of noise in the lab, even if one places the required compressor outside the lab.

That left us with the choice between a flow cryostat and a bath cryostat, although both wet systems require us to get liquid helium every other week. But wet systems do not produce magnetic field fluctuations and produces less vibrations in the vacuum chamber. - All of these points so far could be full-filled with a Pulse Tube cryostat with magnetic shielding and a very good vibration isolation. - What would be a major undertaking is to cancel or dampen all noise in the lab produced by the Pulse Tube cryostat. For information on how sensitive our optical system is to noise, please refer to Chapter 2.2.3.

In a flow cryostat the temperature is tunable by tuning the flux of the coolant. In a bath cryostat, one always cools with the full power (and coolant consumption) and can only heat certain parts of the cryostat to get to higher temperatures. Hence, we chose to work with a flow cryostat.

2.2.2 Heat shields and reduction of the thermal load

Figure 14: View of the opened vacuum chamber of the phase 2 setup from the bottom. On the outside, one can see the vacuum chamber. The two silver rings on the inside are the two heat shields, which are made of silver-plated copper. The inner shield has a much thicker wall for better magnetic shielding.

In order to reduce the consumption of liquid helium, we planed on using not just one heat shield but two. The second heat stage uses the exhausted helium from the inner stage to cool it to about 100 K. Since the outer heat shield completely surrounds the inner heat shield, it will reduce the heat load due to black-body-radiation significantly. This leads to a considerable reduction of the liquid helium consumption. Additionally, we had all parts of the cryostat polished and silver-plated. Gold-plating would have reduced the thermal load even further, but was too expensive[1]. Figure 14

[1]We planed on heating the cryostat for better vacuum at room temperature already. If one heats up copper with a

shows the phase 2 setup, where one can see the vacuum chamber and the two silver-plated heat shields, ready to receive a trap in the inner heat shield.

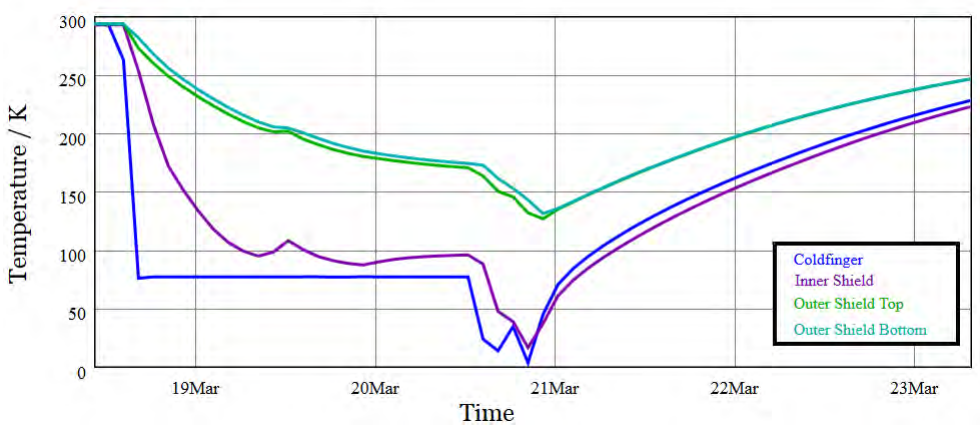

Figure 15: Temperature of the SQIP cryostat over time. It takes about half a day to cool the inner shield down to liquid nitrogen temperatures. But it takes another day to have the outer shield in thermal equilibrium. And it takes several days without heating before cryostat is back at room temperature.

In Figure 15, one can see a cool-down and heat-up cycle of the SQIP-cryostat in Innsbruck. In order to save liquid helium, we always cool down with liquid nitrogen first. It takes about half a day to cool down the inner shield to low temperatures with liquid nitrogen. But it takes a day and a half to get the outer shield into thermal equilibrium as well. These time constants are so long because we have to cool down a total of more than 20 kg of copper in our vacuum chamber. From the liquid nitrogen temperatures, it only takes two to three hours to cool down to liquid helium temperatures (the heat capacity of metals in that temperature regime is very low). After the cooldown, we stop the flow of liquid helium. One can see that it takes more than two and a half days, before the cryostat had reached room temperature because our thermal isolation is working so well.

In order to minimize the liquid helium consumption, we will operate our setup at the condensation temperature of hydrogen (21.5 K). There, the collision rate with background gas is so low that we are not limited by vacuum pressure and the consumption is about half a liter of liquid helium per hour. Should experiments require lower temperatures for instance for lower heating rates, better magnetic shielding, or better vacuum, one will have to face higher consumptions. Unfortunately, we do not know how much of that half liter per hour is caused by the dewar and the transfer line and how much is caused by our cryostat.

Should we not be forced to work with liquid helium[2], we could work with liquid nitrogen as well. The consumption of liquid nitrogen is about half a liter per hour. But when working with

thin film of gold on top, the gold will diffuse in the copper. Hence, one would need several μm of gold to not have everything diffuse, which would be very expensive. But the price difference between polishing and polishing with several μm of silver on top was not significant. Thus we had our cryostat silver-plated.

[2]meaning the background collision due to a higher vacuum pressure, when working with liquid nitrogen, will not limit our experiments

liquid nitrogen, we attribute at least half our consumption to our nitrogen dewar and the transfer line.

2.2.3 Vibrations

As already mentioned in Chapter 2.2.1, we aim for vibrations that are in the order of the size of the wavepacket of an ion in the trap, about 30 nm [3], but the boiling liquid in the coldfinger of the cryostat will cause vibrations in the order of 1 μm. Hence, we need vibration isolation. We decided to implement a decoupling scheme used for example in gravitational wave detection [38]. At room temperature, as part of the vacuum chamber, we are using a membrane bellow to decouple the vibrations, as can be seen in Figure 16.

Figure 16: Vibrational decoupling at the vacuum chamber is done with a membrane bellow. The freely shaking coldfinger is resting on top of gray rubber pieces which absorb the vibrations.

Initially, we planed to attach the cryostat to the ceiling and have the rest of the chamber standing on the optical table. However the floating of the optical table would cause more movement than any vibration caused by the boiling liquid in the coldfinger. Hence, we decided to support the freely shaking coldfinger with pieces of rubber which absorb vibrations of that magnitude very well.

In vacuum, we are mounting that part of the cryostat, in which the ion trap is located, as rigidly as possible without causing too much thermal load. We did Solidworks simulations on how rigid such a mount would be and how much thermal load it would cause. In the end, we used a hexapod structure, shown in Figure 17, between room temperature and the outer shield.

Unfortunately, there was not enough space reduce the diameter of the ring, where the rods are attached, when connecting the outer shield and the inner shield. Then the hexapod structure is not that rigid anymore. Therefore, we chose a hollow cylinder with a wall thickness of only 0.5 mm to connect the outer shield and the inner shield.

To thermally connect the rigidly mounted part with the ion trap and the coldfinger, we used thin wires of thermally well-conducting copper. There is a tradeoff between how many wires one uses to get a better thermal contact and how much the cryostat will shake. For convenience, we preassembled these pieces outside vacuum. Figure 18 shows such an assembly, where the top ring

[3] assuming Ca with a trap frequency of a about 1 MHz

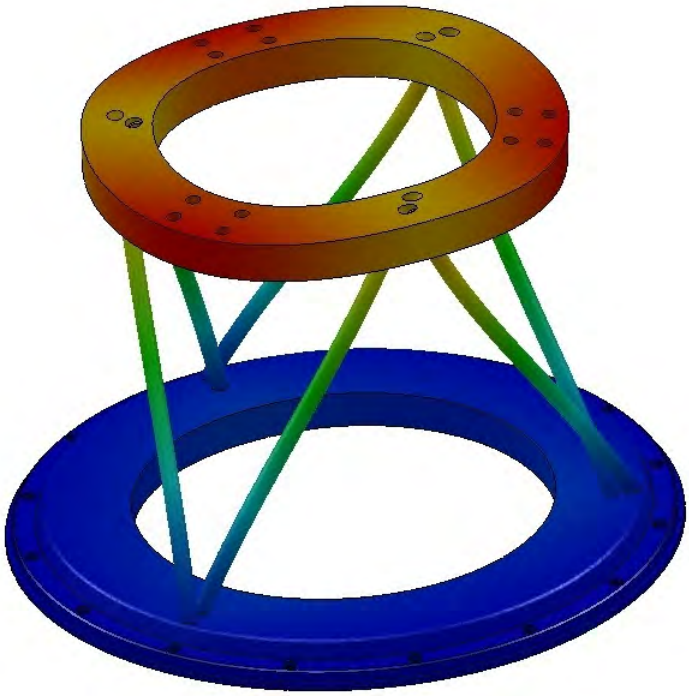

Figure 17: The hexapod structure used as a mount between room temperature and outer shield. This picture is a simulation how the hexapod would deform if a horizontal force were applied.

will be screwed to the coldfinger part and the bottom ring will be screwed to the rigidly mounted part of the cryostat.

In the phase 3 setup, all the materials of all screws and washers were chosen such that each screwed connection would get tighter the colder the cryostat gets.

Additionally, we installed aluminium bars on our table to prevent a movement of the vacuum chamber with respect to the optical table on which the cryostat is mounted. This setup can be seen in Figure 19.

When we measured the vibrations of our cryo system, we used a Michelson Interferometer, as can be seen in Figure 20. Since our cryostat has somewhat the form of a pendulum, the vibrations in the vertical direction are much lower than the two horizontal ones. Hence, we measured the vibrations only horizontally and had two of these interferometers placed around our cryostat to measure the vibrations along the trap axis and perpendicular to it, along the addressing beam axis.

The measurement procedure is as follows. Without the AOM in one arm, we can only measure vibrations smaller than half the wavelength of the used coherent laser light. With the frequency offset in one arm due to the AOM, one will detect a beat and the distance information lies in the argument of the detected sine. For convenience, we mixed the signal down get a resulting beat signal around a couple of kHz. This was then recorded in an oscilloscope. With data processing, one could extrapolate the argument of the sine and hence the length difference between the two arms. We had two flip mirrors as references on the optical table around the cryostat, a mirror glued to the vacuum chamber, and a mirror in the inner shield. We could measure the differential movement between any combination.

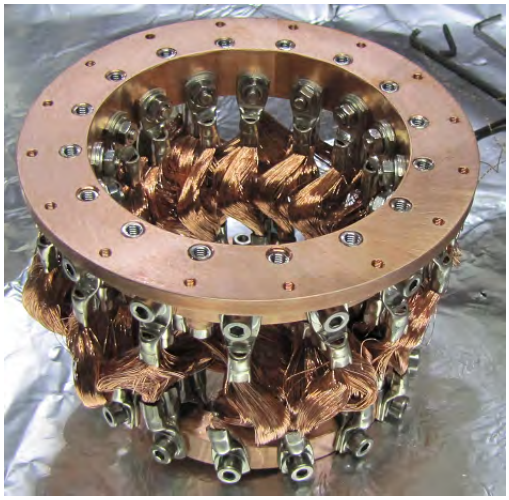

Figure 18: The vibration decoupling elements. The top and the bottom part are only connected via very thin copper wires. The bottom part is then screwed to the rigidly mounted part of the cryostat, and the top part to the freely shaking part with the coldfinger. The more copper wires one uses, the better the thermal contact but the worse the vibrational decoupling.

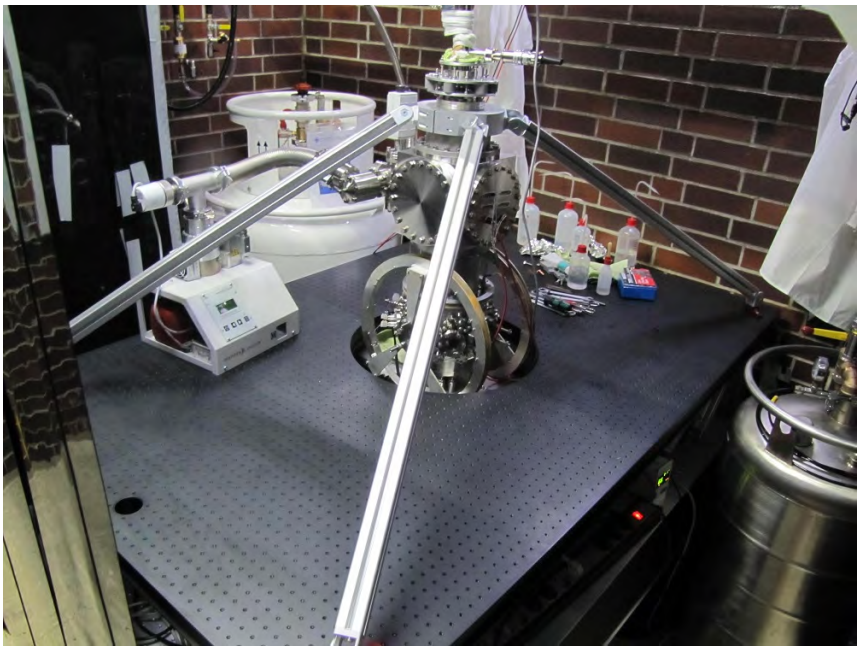

Figure 19: The optical table in the SQIP-lab: in the center, one can see the vacuum chamber with the cryostat rigidly mounted to the table with additional aluminium bars to suppress vibrations in the setup. On left side in the back, one can see the white helium dewar from Cryo Anlagenbau.

There are several components that one could vary in the environment, such as

- covering or uncovering the beam path (air turbulence)

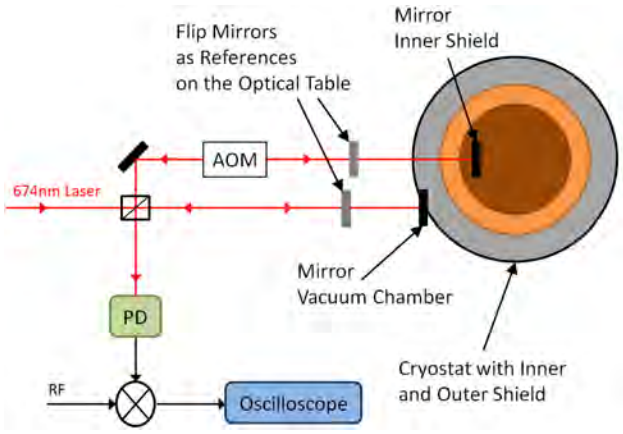

Figure 20: The vibrational measurement setup was a Michelson interferometer with an AOM in one arm for a frequency offset in detection. We had two flip mirrors as references on the optical table around the cryostat, a mirror glued to the vacuum chamber, and a mirror in the inner shield. We measured the differential movement between any combination.

- turning the fan filter unit above the experiment on or off
- floating the optical table
- turning the cryostat on or off

In Figure 21, one can see the characterization of the vibrations. The vibrations are mainly due to disturbances in the air and noise in the lab. The vibrations without noise and a floating table are comparable to the size of the wavepacket of the ion in the trap. - We measured peak-to-peak vibrations in the order of 20-25 nm at liquid nitrogen temperatures.

We want to stress here how important it is to have no air flow on the optical table and absolutely no noise in the lab. Otherwise, one will end up with several 100 nm of vibrations!

After these measurements, we did a long term measurement and started using liquid helium. The results of the vibration measurements can be seen in Figure 21. As we later found out, the vacuum of our transfer line was poor. Hence, we had to use a very high flow to even cool down to 20 K. One can see that the vibrations got less when cooling down from room temperature to liquid nitrogen temperatures, which was what we expected because of the thermal tightening of the screws. But when cooling down to liquid helium, the vibrations increased again. We attribute this behavior to the very high flux of liquid helium. But even peak-to-peak vibrations of 50 nm shown in Figure 21 f) are still acceptable to us.

One thing worth mentioning is that we also obtained information about the eigen frequencies of our system. They can be directly seen in Figure 21 f). Our inner shield vibrates with 31 Hz, our outer shield with 14 Hz, and the vacuum chamber between 90 and 100 Hz.

Since our vibration measurements show only vibration amplitudes in the size of the wavepacket of the ion in the ion trap, we think we will not be limited by the vibrations of our cryostat. - Should future experiments last several seconds and require absolute phase stability of the light, one will have to find a way to stabilize the phase of the light at the position of the ions. We think that the drift over ± 100 nm on the time scale of seconds as observed in Figure 21 a) are due to the

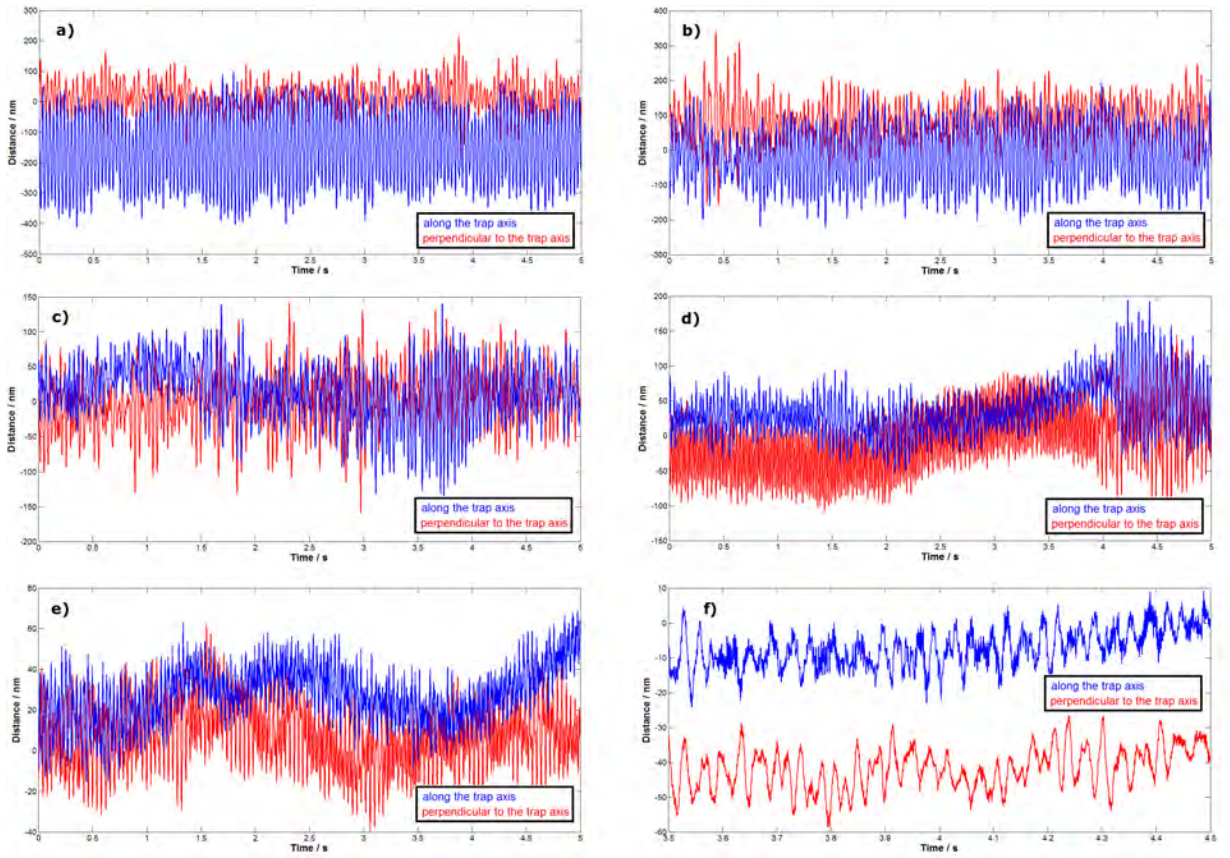

Figure 21: Vibrational measurements between the optical table and the inner shield to analyze what causes the most vibrations. In a), the beam path was not covered, the fan filter unit above the table was on, the optical table was not floating, and the cryostat was off. In b), we covered the beam path and could reduced the measured length differences. We assume, they are due to disturbances in the air. In c), we additionally switched of the fan filter unit and decreased the vibrations. We assume it was the noise of the fan filter unit that caused these vibrations. In d), we then floated the optical table. The vibration amplitude is now about 50 nm peak-to-peak, so in the order of the size of the wavepacket of the ion in the ion trap. In e), we switched on the cryostat and measured when the cryostat was still warm. We could not observe an increase in vibrations due to the cryostat. In f), we measured the vibrations when having cooled down with liquid nitrogen.

stabilization by floating of the table. This stabilization tilts the table slightly, which causes our cryostat to tilt, which causes the drift that we observed.

2.2.4 Magnetic shielding

A prominent source of decoherence in optical qubits are fluctuations in magnetic fields. The SQIP team has taken great care to minimize magnetic field fluctuations inside the cryostat. Traditionally, μ-metal sheets are used for attenuation of such fluctuations. Such shielding is typically bulky and incommodious. In the SQIP cryostat, the inner heat shield, as described in Section 2.2.2 doubles as a way to attenuate magnetic fields without the need for μ-metal. The copper heat shield is two

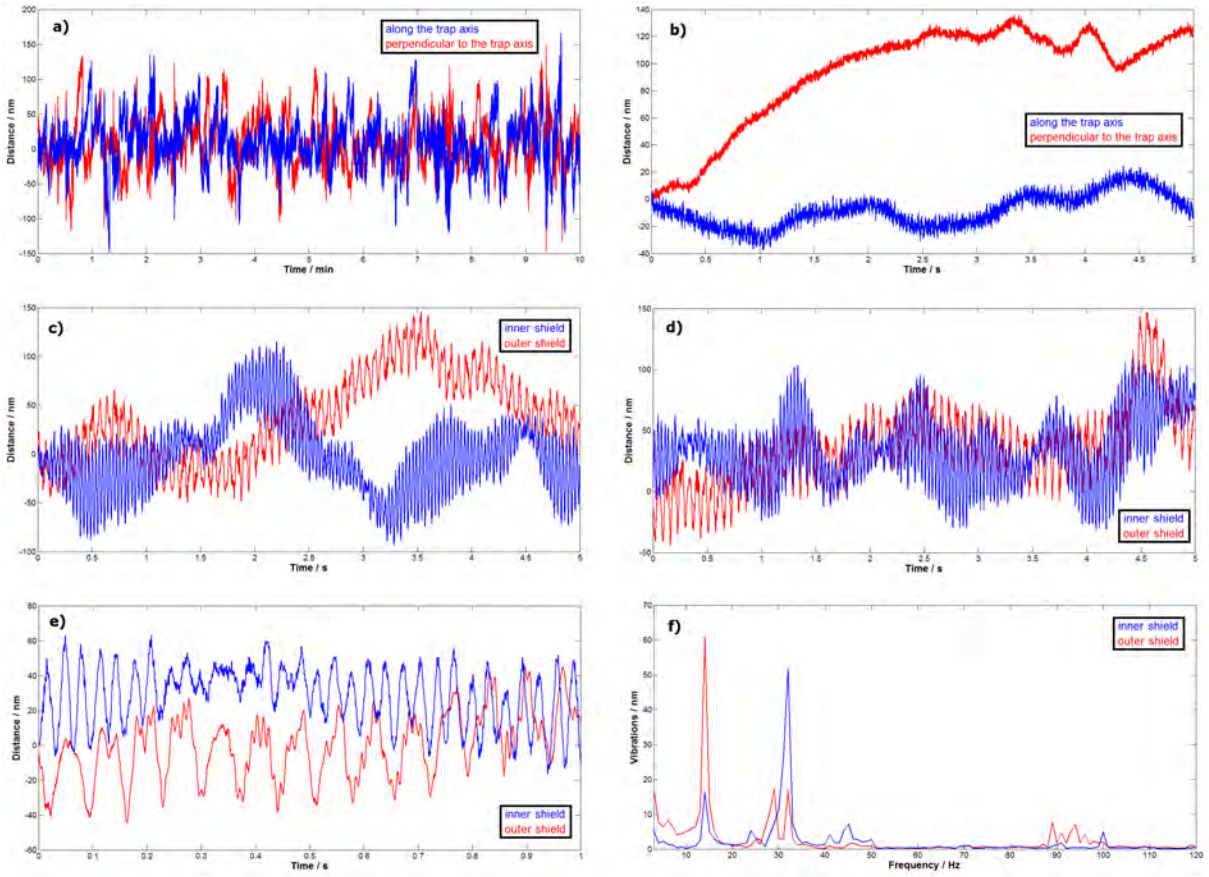

Figure 22: In a), we analyzed long term drifts over 10min. One can clearly see, no significant drifts occurred during the measurement. We attribute the drifts on the second scale over ± 100 nm to the movement cause by the stabilization of the floating table. But mainly, we characterized the vibrations, when cooling with liquid helium. In b), we measured how much the vacuum chamber is drifting with respect to the optical table. Since we have seen that the vibrations of the inner shield are similar for both directions, we switch the target for one measurement from the inner shield to the outer shield. In c), we measured how much the heat shields are shaking compared to the vacuum chamber. d) shows how much the heat shields are shaking with respect to the optical table. e) is a zoom of d), and f) is the Fourier-transform of e). We want to emphasize here, that the flux was very high during these measurements. Under normal conditions, we expect at maximum 30nm peak-to-peak vibrations.

centimeters thick. The penetration depth δ of electromagnetic fields is given by:

$$\delta = \sqrt{\frac{2\rho}{\omega\mu}}, \tag{1}$$

with ρ the resistivity of the copper, ω the field frequency, and $\mu = \mu_r\mu_0 \approx \mu_0$ the copper's permeability. Electromagnetic field attenuation is then determined by the Beer-Lambert law, $I = I_0 \exp(-d/\delta)$, with I and I_0 the input and output intensities, and d the thickness of the material. Filling in the figures, this in itself does not boast a high attenuation for relevant frequencies (50

Hz and higher). However, when considering that copper's resistivity drops by a few orders of magnitude when operating at cryostatic temperatures, it is apparent that the attenuation becomes substantial (ie. 85 dB at 50 Hz for temperatures below 10 K)

In SQIPs phase 3 cryostat design the copper heat shield has been designed in such a way that Eddy currents can flow freely in the plane perpendicular to the principal magnetic field axis. In practice, this means that instead of having a lid at the bottom of the inner shield, as in the phase 2 set-up, it is made to open from the side, so that the seam does not interfere with the Eddy currents.

Magnetic field attenuation of the new SQIP cryostat design has been tested. During these measurements it has been noted that there was a leak in the cryostat. This limited our pressure, and it is questionable to what extent this has limited the cooling power of the cryostat. Furthermore, it has later been determined that the vacuum inside of the liquid Helium transfer line was not optimal, which may also have influenced the cooling power. Hence, the measurements taken so far do not necessarily represent the best case scenario.

Set-up: Magnetic fields have been detected using a Honeywell HMC 1022 Magnetic sensor. It has been placed inside the inner shield, roughly where the trap would be located. Measurements are done in the vertical, and two horizontal directions (the latter two orientated perpendicular and parallel to the primary magnetization axis, provided by coils in Helmholtz configuration). One of the wires, part of the wheatstone bridge of the vertical measurement, had a short to ground inside the cryostat. An attempted fix outside the cryostat allowed us to do measurements in the vertical direction at room temperature, but ensuing difficulties kept us from further measuring vertical attenuation at lower temperatures. However, since the attenuation in the vertical direction at room temperature was comparable to the horizontal attenuation, we are confident that it will behave similarly at lower temperatures. Furthermore, the attenuation in the direction along the axis of the Helmholtz coils is the figure of interest, as this represents the quantization axis. The other two are mainly for comparison. The magnetic field inside the chamber due to a DC current is, for the three different coils

- Helmholtz: 0.0909 A $\rightarrow$ 1 Gauss
- Horizontal: 0.51 A $\rightarrow$ 1 Gauss
- Vertical: 0.36 A $\rightarrow$ 1 Gauss

An attenuation measurement consists of applying an AC current to coils, respective to the orientation that we are interested in. The amplitude of the current is monitored on an oscilloscope. The frequency and amplitude are tunable. The frequency ranges from minimally 0.01 Hz, to maximally 200 Hz, with a focus on frequencies around 50 Hz. The response of the magnetic field sensor is amplified and offset, if necessary, and monitored on an oscilloscope. The signal can be amplified by a known gain of 11.5 or 11.5^2. The value of interest is the ratio between the amplitudes of the magnetic field response (with gain correction) and the input current. We assume that at sufficiently low frequencies, around 0.01 Hz, the magnetic field response is in the $\omega \rightarrow 0$ limit, and the field/current ratio can be taken as a reference point, i.e. 0 dB attenuation.

Attenuation has been measured for various temperatures of the inner heat shield, ranging from room temperature down to 15 K. During the cooling cycles associated with these measurements, we have checked and adjusted the cooling efficiency of our cryostat. In the best case, the inner shield has been cooled to 15 K. However, it was later discovered that the liquid helium transfer

line was not operating efficiently. With a functional transfer line, we expect that the temperature can be reduced to below 10 K.

Measurement results: We have measured the time constant of the reaction of a magnetic field due to a step in current, for various inner shield temperatures. The results are displayed in table 3.

Table 3: Response time constant for a step in external magnetic field, for different inner shield temperatures

T_{inner} K	τ (s)	τ (s)	τ (s)
294	0.024	0.020	0.025
98	0.090	-	-
40	0.96	0.67	-
19	2.8	1.7	-
15	2.9	1.9	-

As mentioned, the vertical component of the magnetic field sensor shorted while cooling down. As a result, we have no data for the field response time in the vertical direction below room temperature.

Figures 23(a) and 23(b) show magnetic field attenuation as a function of applied magnetic field frequency, for several different temperatures of the cryostat inner shield. Since magnetic fields at 50 Hz are expected to be the primary source of potentially harmful noise in our lab, the most interesting point of the curves are around this frequency, marked by the dotted line. The trend towards higher attenuation at lower temperatures is clear. At high attenuation, above 50 dB, the signal-to-noise ratio became very low, making the determination of amplitude less trustworthy. The Fourier transform of the waveform of this signal was also analyzed, and the peak-height ratio of current-to-magnetic field was recorded at the relevant frequency. These are depicted by the circular data points in the graph.

Attenuation due to the skin effect scales with $\exp -d/\delta \propto \exp\left(-\sqrt{\omega}\right)$. Therefore, in theory, the curves should continue descending after the initial dropoff. At an attenuation of about 50 dB this no longer seems to be the case, which we attribute to the limit of our detector's resolution. In this range, magnetic field noise pick-up through other sources outside the chamber can start interfering with our data. However, if our set-up behaves according to theory, and we extrapolate the curves, we find that at an inner shield temperature of 14 K, the magnetic field attenuation at 50 Hz is well above 80 dB.

The plots in Figure 24 compare Helmholtz versus horizontal configuration data. At high temperatures, the attenuation due to the two horizontal configurations is nearly identical. The skin depth is limited by the resistivity of the copper, which is more or less identical in all orientations. At lower temperatures, resistivity of copper decreases, and defects such as the connecting edge of the inner shield become non-negligible. The design of the inner shield is such that Eddy currents due to magnetic fields in the Helmholtz axis flow unrestricted, while currents around the perpendicular horizontal direction are restricted by the inner shield lid. At low copper resistivity (i.e. low temperature) the difference as a result of this design is more apparent.

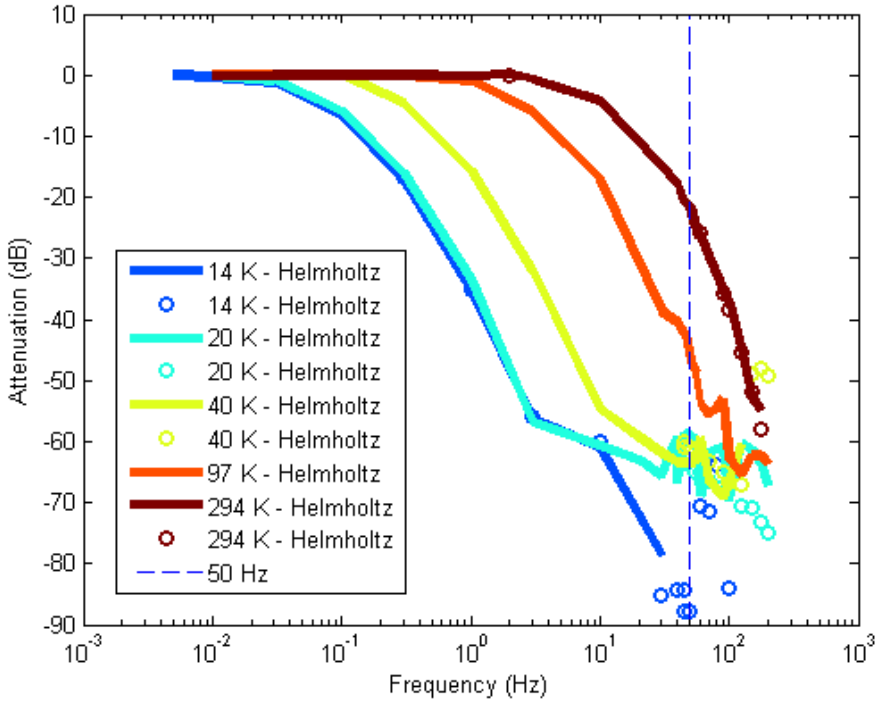

(a)

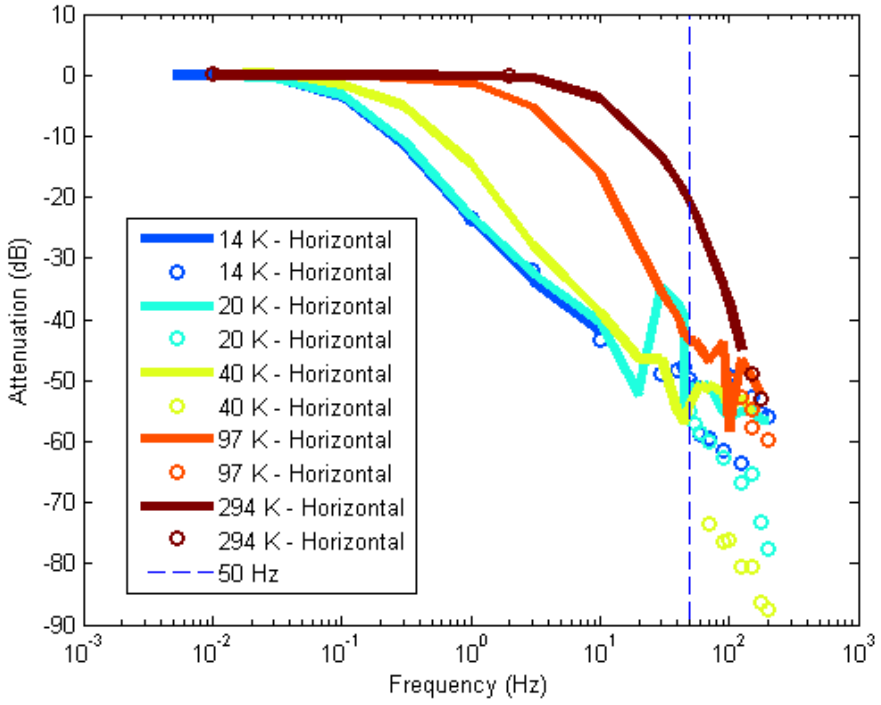

(b)

Figure 23: Magnetic field attenuation of the cryostat as function of frequency, for various temperatures of the inner shields. Data is shown for fields along a) the quantization axis (provided by the Helmholtz coils), and b) the horizontal direction perpendicular to the quantization axis.

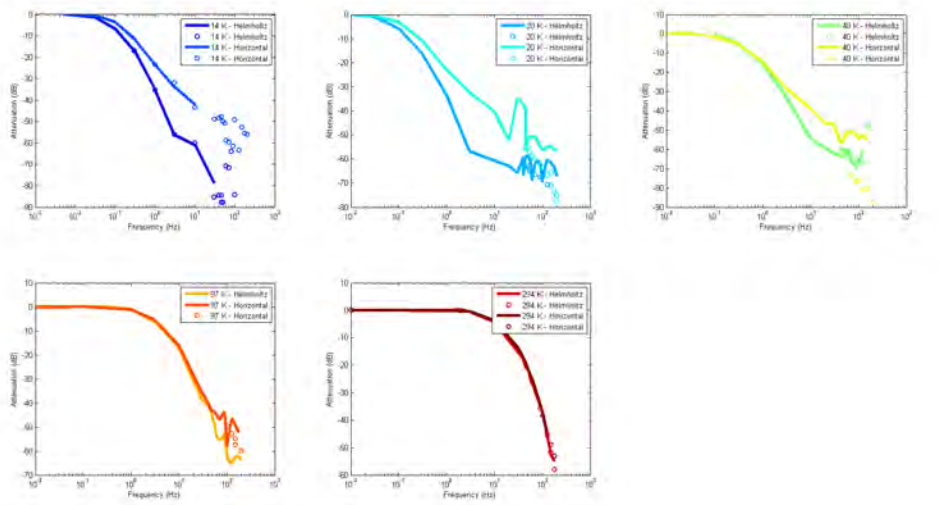

Figure 24: Comparison of attenuation along and perpendicular to the quantization axis

2.2.5 Optical access in the cryostat

Good shielding against magnetic fields dictate small holes in the heat shields. But single ion addressing capability requires a high numerical aperture (NA), hence large diameter holes. Addressing capability with NA = 0.25 would require a hole with a diameter of about 70 mm, when the lens is placed outside the heat shield. Such a big hole in the inner shield would decrease magnetic shielding significantly. Therefore, we decided to put the lenses in vacuum in the inner shield. We are using standard Thorlabs 1/2" aspheres with a focal length of 25 mm. The lenses are held by a copper holder which should only create tensions with a radial symmetry. Hence, we should not expect birefringence effects in the lenses, when they are cooled down. These lenses each have a numerical aperture of 0.25 and are used for single ion addressing as well as detection. The setup can be seen in Figure 25.

The single ion addressing requires holes with a diameter of 12 mm in the inner shield, resulting in a beam waist of about 600 nm. All other beams have holes with a diameter of only 8 mm. That was the tradeoff that we had to make between magnetic shielding and optical access.

We have to minimize our dark counts during detection. We made sure that along the detection beam there can be no reflections back towards the inner shield that could illuminate the trap and thereby cause dark counts on the PMTs[4].

2.2.6 Lasers

We lock all lasers but the photo ionization with a Pound-Drever-Hall scheme. For the qubit-lasers, we implemented a two-stage locking scheme, which consists of two Pound-Drever-Hall locks and can be seen in Figure 26. In this scheme, the laser diode is first locked to a medium finesse cavity.

[4]The beam has to pass through AR-coated glass at the viewport and the pieces of glass at each heat shield. Although the glass is always AR-coated, one has to expect backreflections, which might hit the trap and cause dark-counts in our detectors.

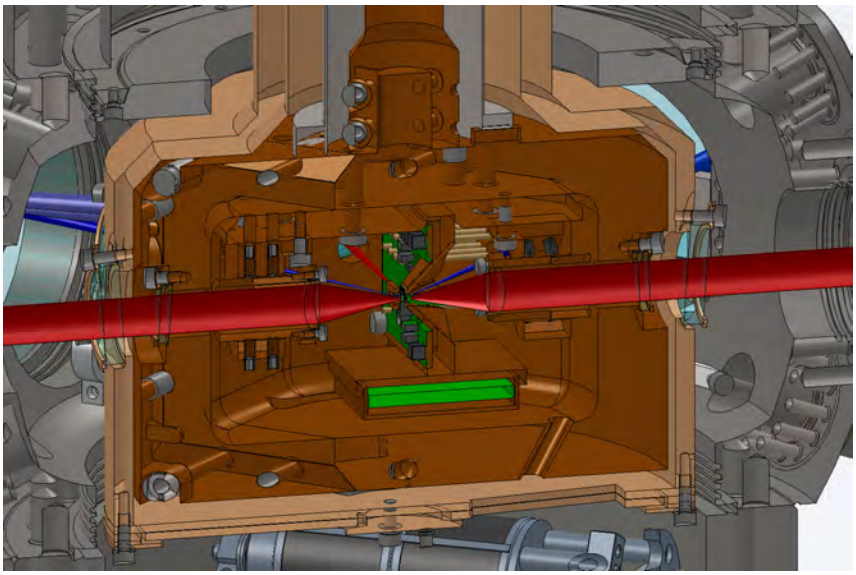

Figure 25: Cut through the drawing of the SQIP-cryostat. The big red rays symbolize the beam path for single ion addressing. One can see two lenses inside inner shield (the darker brown part of the setup). They each have a NA=0.25 and are used for single ion addressing and detection.

This results in a linewidth between 1 kHz and 10 kHz. We can then use an AOM to lock the laser light onto a high finesse cavity. This allows for line widths of less than 10 Hz, independent of the natural linewidth of the laser diode.

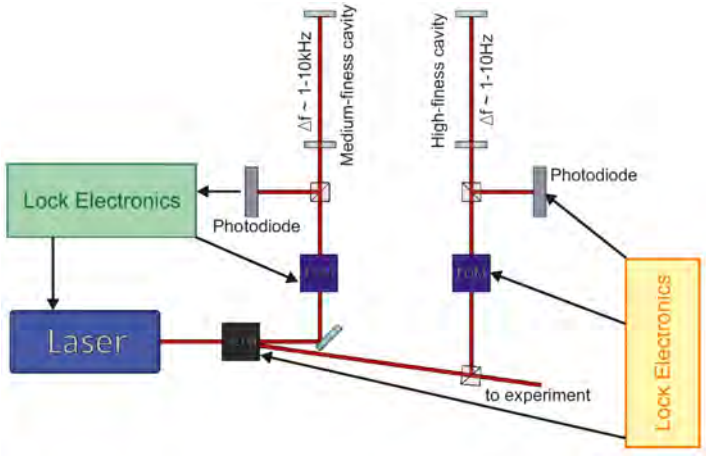

Figure 26: The locking scheme for our high finesse locks. We lock the laser to a medium finesse cavity. This results in a linewidth between 1 kHz and 10 kHz. We can then lock the laser to the high finesse cavity with an AOM by modulating its frequency. This second lock does not depend on the natural linewidth of the laser diode but is only limited by electronics and the high finesse cavity.

All lasers are locked[5] and are ready to use, see Table 4.

Table 4: Lasers used in the SQIP-lab in Innsbruck

Name	Species	Function	Frequency / THz	Locked
375	Ca	Photo Ionization	795-799	-
423	Ca	Photo Ionization	709.0788	-
397	Ca	Doppler Cooling and Detection	755.2228	yes
729	Ca	Qubit Laser	411.042129	yes
854	Ca	Repumper	350.8626	yes
866	Ca	Repumper	345.9999	yes
405	Sr	Photo Ionization	739-740	-
461	Sr	Photo Ionization	650.5038	-
422	Sr	Doppler Cooling and Detection	710.9623	yes
674	Sr	Qubit Laser	444.77904	yes[6]
1033	Sr	Repumper	290.2125	yes
1092	Sr	Repumper	274.5890	yes

2.2.7 Narrow linewidth laser system

The narrow linewidth laser system is based on the commercial diode laser TA pro from Toptica. A two step Pound-Drever-Hall locking scheme was chosen. In a first step the laser is locked to the prestabilization cavity with a finesse of approximately 5500. The error signal from the first locking step is fed back to the diode lasers current and the piezoelectric crystal of the diode lasers external cavity. The final locking step uses an AOM[7] as a noise eater to stabilize the laser to the high finesse cavity. Both the cavity housing and the spacer are commercially available from Stable Laser Systems[8] while the mirrors are manufactured by Advanced Thin Films. With a cavity ring-down measurement the finesse was measured to be approximately 240000. Advantages of this two step scheme is a broader capturing range and less sensitivity to environmental influences as vibrations or acoustics.

For the prestabilization step commercial electronics[9] are used, while a self made fiber noise cancellation (FNC) PCB is used for the lock to the high finesse cavity. The regulation range of the FNC board is limited to a couple of tens of kHz. In order to keep the output frequency of the FNC board within that range, drifts of the prestabilization cavity have to be compensated. This is done by measuring the output frequency of the FNC board with a field programmable gate array (FPGA) and applying feedback to a piezoelectric crystal, which holds one of the mirrors of the prestabilization cavity.

A stable reference laser[10] is used to characterize the SQIP laser system. To quantify the short term performance of the laser system, the beat note between the reference laser and the SQIP laser

[5]The 674 nm laser is only locked the medium finesse lock so far.
[7]Gooch & Housego AOMO 3080-120
[8]SLS 6300 with spherical spacer
[9]Toptica FALC 110
[10]Coherent 899

system is analyzed with a spectrum analyzer[11]. In Fig. 27 a) the SQIP laser is only locked to the prestabilization cavity. The linewidth of the central feature is 5.67(3) kHz, the servorbumps are approximately 45 dB below the carrier. In Fig. 27 b) the laser is locked to the high finesse cavity. This second locking step reduces the linewidth to 1.58(2) Hz.

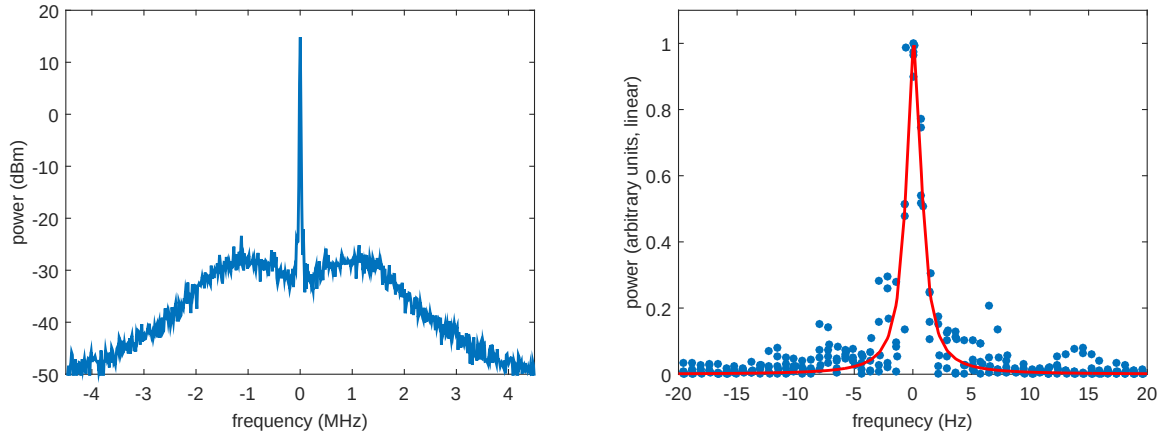

(a) (b)

Figure 27: Beat note of the SQIP laser with a stable reference laser. a) The SQIP laser is only locked to the prestabilization cavity. The resolution of the measurement is 100 Hz, averaging over 20 measurements is applied. b) With the final locking step the linewidth was reduced to 1.58(2) Hz. The resolution of the measurement is 1 Hz, averaging over 5 measurements is applied.

To measure the long term stability of the laser the beat note was measured over approximately 2.5 hours. The frequency of the beat note was counted with a self made, FPGA-based frequency counter. The Allan deviation calculated from this measurement is shown in Fig. 28.

2.2.8 Electronics

Real-Time-Sequencer: The real-time-sequencer is based on the same FPGA as in the off-the-shelf system in Chapter 2.1. The sequencer can be seen in Figure 29. That means it has a 10 ns timing resolution. But the new setup's sequencer can control up to 16 smart DDSs (the current box can only hold 9), whereas the old sequencer could only control 2 smart DDSs. In the new version, all IOs are galvanically isolated from the box. Hence, one cannot build ground-loops with the new sequencer by controlling devices in various parts of the lab.

Bus System: In the new SQIP lab in Innsbruck, we intend to control between 40 and 50 RF-sources, 30 to 40 analog voltages (besides the ones for the trap), and 30 to 40 digital signals. We are using DDSs for RF-sources, but unfortunately, that many DDSs are beyond the capability of our real-time-sequencer. Fortunately, we have electronics for a bus system in Innsbruck based on the ideas and work of Florian Schreck. The bus system, which can be seen in Figure 30, is a digital parallel bus which can provide galvanic isolation through so called bus-driver cards. The digital signals can then reach racks in which one can plug DDS, analog cards, or digital outputs

[11] Rohde & Schwarz FSV-3

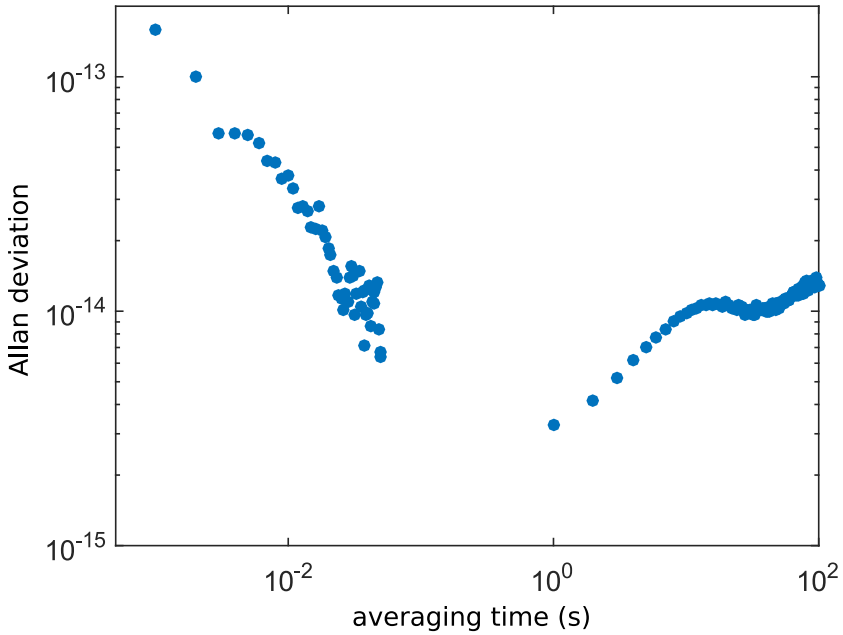

Figure 28: Allan deviation of the beat note between the SQIP laser and a stable reference laser. The measurement was carried out over a period of approximately 2.5 hours.

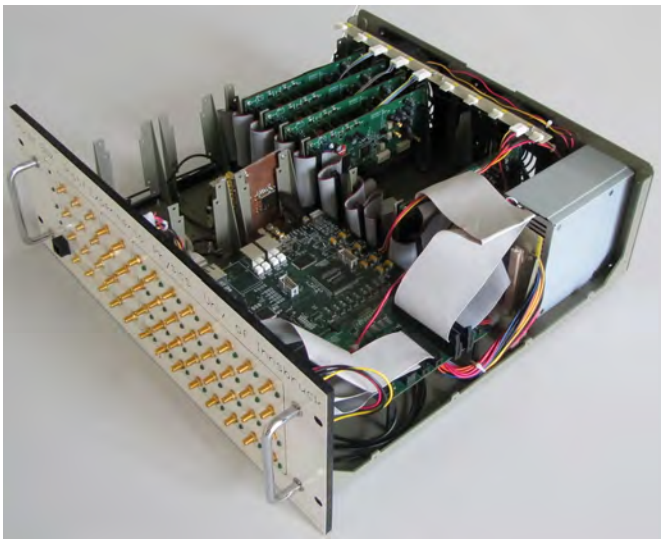

Figure 29: The new real-time-sequencer in the SQIP-lab in Innsbruck. It has a timing resolution of 10 ns and all IOs galvanically isolated.

to generate the desired signals. All these signals can locally be generated where they are required. This limits ground-loops in the lab.

The timing-resolution for the bus system is 1 μs. During the course of this MQCO-project, we developed an FPGA-based sequencer for this bus system. This sequencer allows us to control the

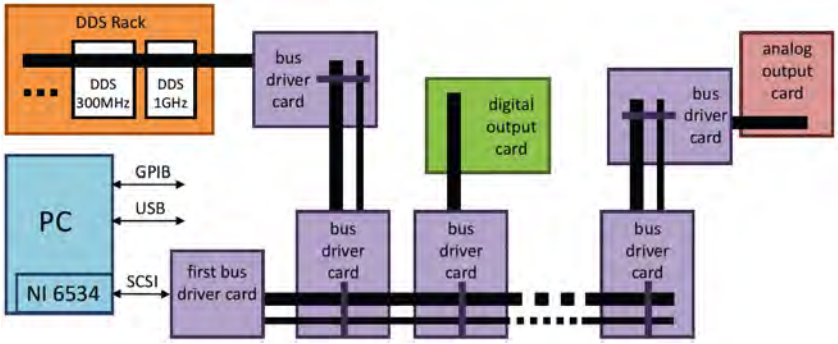

Figure 30: The bus system is a digital parallel bus which can provide galvanic isolation for different racks of electronic equipment, such as DDSs, analog outputs, and digital outputs.

bus in real-time during one measurement cycle. Thus, we are able to control all lasers related to dipole-transition with this bus sequencer. Only the quadrupole lasers are controlled and manipulated with our standard real-time-sequencer. The advantage is that we do not need to attenuate the RF with an RF-switch to turn light of a dipole laser on and off. But we can really program the DDS to output 0 Hz. Additionally, we can change parameters during one measurement, such as chirps, which we could not do with our old system. However, the DDSs controlled by the bus system do not allow for phase coherent switching.

DAC-Box: We are using a DAC box provided by the Mainz-team, refered to as Bertha, to control the voltages of our segmented traps. The documentation on this can be found in Chapter 3.4.

Counter Card : We developed an FPGA-counter to allow for detection of ion states, and micromotion. It will also allow us to implement a fast detection scheme based on statistical methods.

2.2.9 Resonator

We did a case study on how to effectively build a resonator for ion traps with a high voltage gain, a small volume inside a shield. One of these resonators can be seen in Figure 31.

In our case study, we tried several types of coils: a PCB coil completely produced with PCB-production methods, a normal coil made of a wire, and a spiral coil made of a high-temperature-superconductor. The highest voltage gain that we measured was higher than 90. The details will be found in a publication that we are currently working on.

2.3 Ion-transport at the University of Mainz

The task of the UMZ node within the SQIP project was to develop hardware, software and methodology for ion shuttling operations in segmented ion traps, and to demonstrate such operations. The required hardware, i.e. fast multichannel arbitrary waveform generators, has been successfully developed, characterized and produced in series, see Sec. 3.4.1. It has been used to demonstrate fast shuttling, see Sec. 5.1 in a multilayer planar trap, see Sec. 3.1.1. Protocols for fast ion separation have been developed 5.1 and demonstrated. These shuttling operations have been used together with elementary quantum logic operations to demonstrate the distribution of entangled qubits in

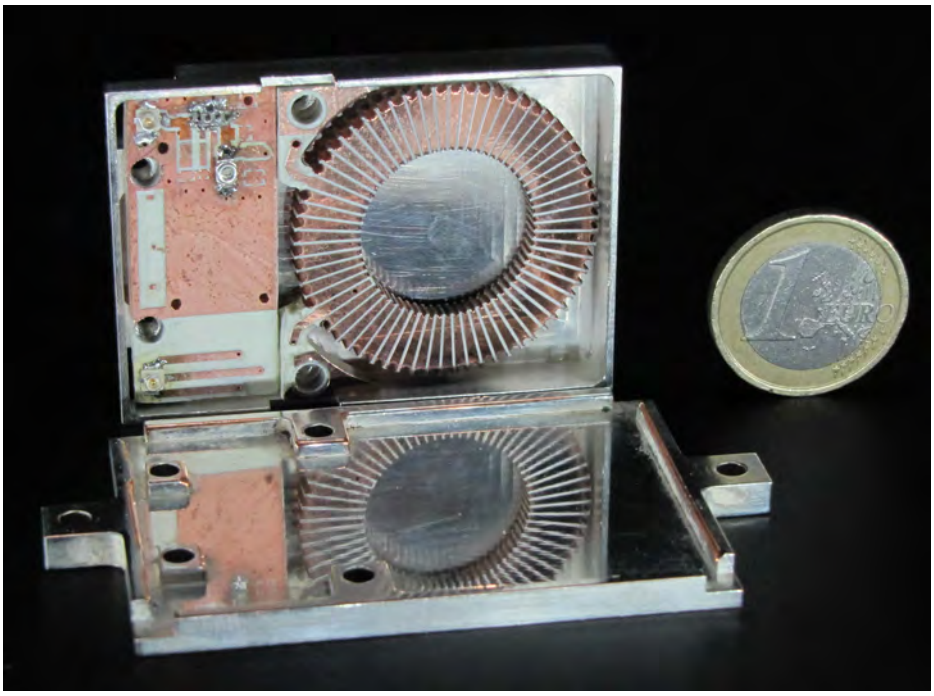

Figure 31: The RLC-resonator built with a PCB coil (right) and the matching network (left) in a silver-plated copper shield. The dimensions of the shielded resonator are 57mm x 40mm x 10.2mm.

a scalable architecture as shown in Sec. 5.2. Finally, next generations traps (Sec. 3.1.2) and waveform generators (Sec. 3.4.2) have been developed, produced and tested.

2.4 Surface trap treatment at the University of Berkeley

UCB's task within the SQIP consortium was to develop high quality surface traps, and deliver them to partner institutions for testing. Additionally, the aim was to understand and reduce anomalous heating. Towards these goals, UCB fabricated surface traps at the Berkeley Nanolab using different approaches, as discussed in Sec. 3.1.3. These traps were delivered and successfully tested at MIT and UIBK. A surface science chamber was built that allows ion trapping capability while including surface science tools. These tools were used for characterization of the trap surfaces (Sec. 3.2). Various trap treatments were investigated with the objective to reduce anomalous heating due to electric field noise from surfaces. With one such treatment, a two orders of magnitude reduction of the anomalous heating was achieved (Sec. 3.3). The observed heating was low enough to allow for the first time for fault-tolerant quantum computing in a scalable room temperature surface trap.

2.5 Quantum interfaces between ions and photons at the MIT

MIT's project within the SQIP team was to develop a strongly coupled ion-photon system, with the aim of demonstrating high fidelity transfer between ion and photon quantum states. At the start of this program the main outstanding challenge was in designing a cavity compatible with a scalable

surface trap architecture. The initial design for this incorporated an out-of-plane cavity using the trap substrate as the bottom mirror of the cavity. This design would provide a minimum distance between ion and mirror, a key parameter in optimizing strong coupling. While we did successfully fabricate and test such a trap at cryogenic temperature [39] we ran into fabrication issues with similar room temperature traps, as discussed in Sec. 3.1.5. To mitigate these fabrication issues we decided to switch to a sandia cavity trap which could similarly incorporate a mirror just bellow the trap surface, details are in Sec. 3.1.6. We have also looked into incorporating an in-plane cavity in Sandia's High Optical Access (HOA) trap, see Sec. 3.1.7. In Addition to investigating designs which minimize cavity-mode volume, we have investigated the properties of blue/UV coatings in vacuum. Specifically looking at how to prevent, mitigate, or recover the increased optical loss which incurs in vacuum. We were able to identify solutions to prevent this loss from occurring, and to recover in-situ mirrors which may have already suffered this loss [40] , see Sec. 3.6.

3 Hardware and accompaning procedures developed within the project

3.1 Ion traps for quantum information processing

3.1.1 UMZ multilayer planar trap Mk I

For conducting shuttling experiments, we have designed, fabricated and employed a new multilayer planar trap. While the fabrication technology has been mostly similar to previous designs [41, 42], however our previously used trap featured a complex geometry with a tapered zone, giving rise to strong axial micromotion, which had detrimental effects on Doppler cooling and shuttling experiments. The new trap was design with uniform geometry, i.e. 32 segments of the same size arranged along a straight axis. Furthermore, we added electrodes behind the rf rails for micromotion compensation along the radial direction which was previously not accessible. This trap was successfully put to operation. We indeed found a substantially reduced axial micromotion amplitude. However, the heating rates on the axial mode of vibration were by a factor of about 10 larger as compared to the previous trap, and display an astonishingly large variation of factors of up to 5 along the trap axis. This trap has been used to successfully design protocols for fast ion separation, cf. Sec. 5.1, and long-range distribution of entangled qubits.

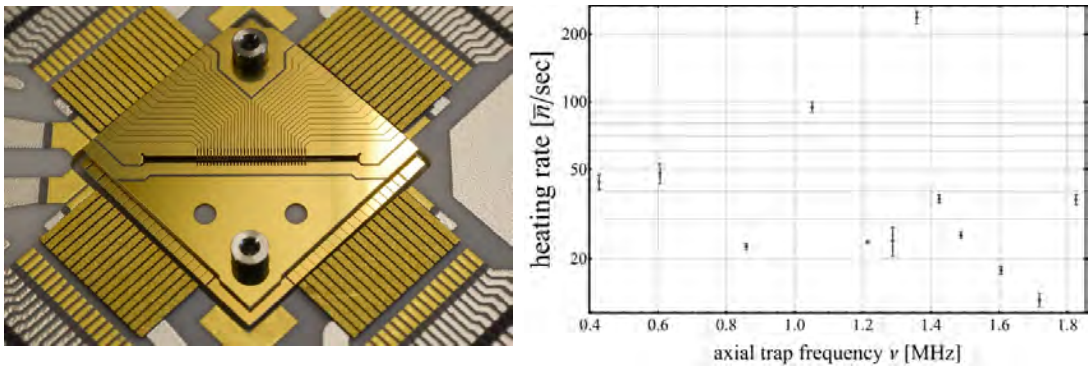

Figure 32: UMZ thick-film trap: A picture of the new multilayer planar thick-film trap is shown at the left. The trap is mounted on the filterboard. On each edge, the capacitor array can be seen. The dc electrodes are bonded directly onto the top surface of the capacitors. The rf leads and bondpads are at the left. The screws fixing the stack can be seen on top and bottom of the trap. They are surrounded by ground planes. The two holes on the lower part serves as vias for the ground connection. The plot at the right shows the measured heating rate in phonons per second versus the axial trap frequency. As no systematic behavior is seen, we conclude the the heating is mainly caused by technical noise.

3.1.2 UMZ multilayer planar trap Mk II - thick-film surface

Due to the unsatisfactory performance of the trap described in Sec. 3.1.1, we designed, built and employed a multilayer planar trap based on a new fabrication technology in phase III. While the

geometry is rather similar, we added a fabrication step where we deposited an additional 8μm gold layer on the electrode surfaces by means of electroplating [43]. Furthermore, we abandoned gluing the trap stack in favor of screwing it. This has led to an improved background pressure in the 10^{-11} mbar range, which strongly reduced trap loss and crystal melting events as compared to before. We find heating rates as low as 9 phonons/s for $^{40}Ca^{+}$ ions at an axial trap frequency of 1.7 MHz. As we do not see any proper power law behavior of the heating rate with respect to the trap frequency, and a strong dependence on the electrical wiring, we conclude that the heating is predominantly caused by technical noise rather than by the surface. Moreover, we observe stable trapping of longer chains of up to 6 ions for a single-segment axial trap potential, which has been limited to 2-3 ion before.

3.1.3 UCB surface traps : lithographic fabrication

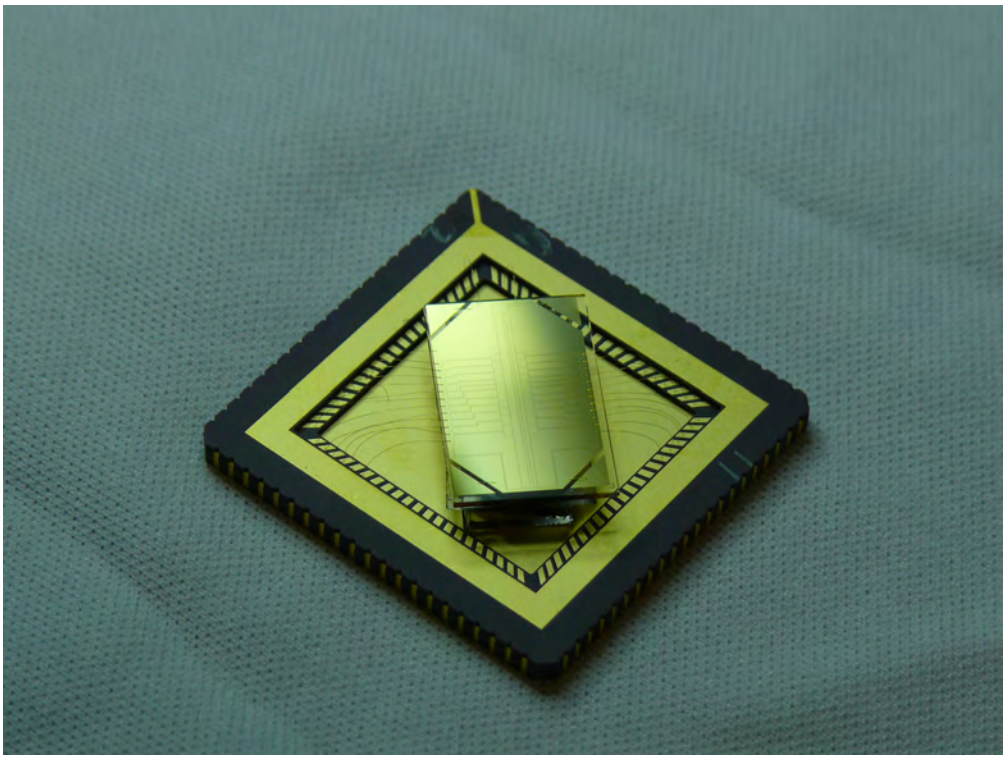

Figure 33: A gold surface trap fabricated at UCB.

At UCB, we developed three different trap fabrication methods, all with the main focus of yielding robust and cost effecive traps with fast turn-around times. Robustness and fast turn-around were very important for our work on removing and understanding electric field noise stemming from the metallic surfaces. The traps had to withstand harsh treatment such as Ar-ion milling as well as extreme temperature differences to alter the surface.

The first method was based on lithography on quartz. In such a trap, we successfully loaded ions in collaboration with MIT in a cryogenic environment. Those measurements showed that already a thin Gold film of 500 nm is sufficient for good trap performance, at least at low temperatures. The lithographic technique is easy to implement, however, it has the disadvantage that the

electrode gaps can easily charge because they are not recessed. Therefore, we developed a method to etch a quartz substrate with SF_6. We etched between 30 and 35 μm deep trenches with gaps between electrodes of between 10 and 12 μm, roughly an aspect ratio 3:1. Using angle evaporation on these, we successfully evaporated Gold, Copper, Palladium, and Platinum on three different traps. An example trap is shown in Fig. 33, mounted and wire-bonded to a chip-carrier.

3.1.4 Translume - surface traps with slot for high NA

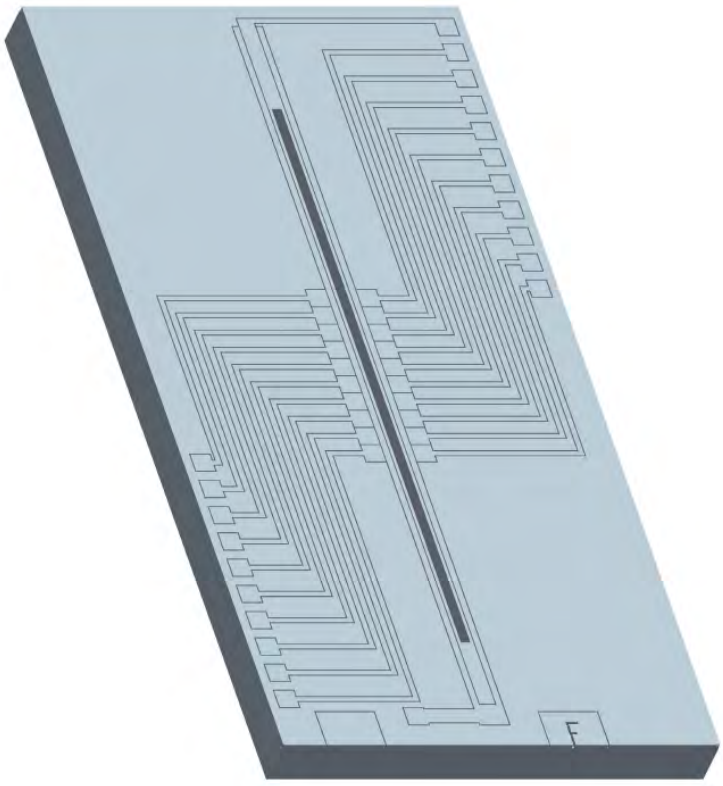

Figure 34: Design of a surface trap with a slit in the middle for tight laser focusing.

It soon became clear that the main challenge with these surface traps would be to provide optical access allowing for a sufficient focus of 1 μm as required for single ion addressing.

Therefore, we designed a narrow trap thus allowing for a tighter beam focus and less light scatter. A theoretical analysis showed that focusing a laser beam at 729 nm to a waist of 1μm would have been possible but very challenging. If the laser was to be sent parallel to the trap surface, the trap edge could not be further away from the center than four times the ion height. This left hardly enough space for RF electrodes, DC electrodes and connections. While our design accommodated all boundary conditions, the situation was non-ideal as the wiring of the DC electrodes would have significant influences on the trapping potential.

Therefore, we pursued an alternative strategy by manufacturing a slit in the trap center allowing the laser light to be sent in from the back-side (Fig. 34). We contacted several companies specializing in quartz etching to pursue this third method. Translume and Smart System Technology responded positively and both claimed that they could produce the required quartz substrates

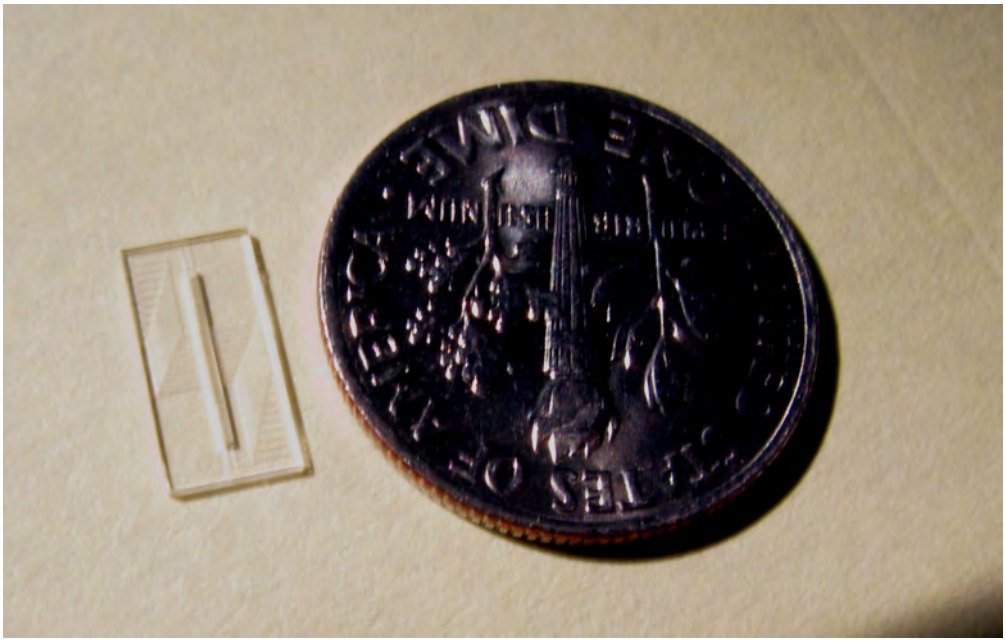

Figure 35: Surface trap with electrodes laser etched on a quartz substrate by Translume Inc.

with turn-around times on the order of one month. We chose to work with Translume. Traps were successfully produced and tested at UC Berkeley as well as Innsbruck. The slit allows laser access and, in fact, for the same laser geometry as the Mainz trap. Thus, this design enables easy switching between the 3D and planar trap design.

For the surface studies, we settled on a Cu-Al elecrodes. Aluminum allows us to evaporate thick films (1 μm) while keeping the costs reasonable. A final copper layer protects the aluminum from oxidation. For the Innsbruck traps, however, we used the more conservative approach, *i.e.* gold.

3.1.5 MIT Mirror trap

Our generation 1 design for the cavity-ion system was to micro-fabricate the ion trap directly on a high reflectivity mirror. Which is about as close as a mirror can be placed to the ion in a planar trap geometry. Our initial concerns for this design was the effect the exposed dielectric would have on the trapping potential, We explored those concerns demonstrating stable trapping for extended periods of time, measured heating rates comparable to fully metallized traps, and used the ion image to determine the trapping height. [1]

Despite our success in these cryogenic measurements, we ran into a number of fabrication issues in getting traps to work at room temperature. The main issue being breakdown voltages of $<$100 V, too low to trap with. While debugging the problem we did find that the problem was unique to our room temperature setups with one trap being tested both at room temperature and cryogenic temperature having breakdown voltages of 90 V and 300 V respectively. While we did not definitively resolve this issue, we believe we identified a small amount of metal residue in the gaps to be the cause of problem. We eventually installed a trap with a breakdown voltage of 200 V, which showed unusual properties during its roughly 1 year of use. The trap required

steadily increasing compensation voltages for the course of the year and trapping lifetime steadily decreased to a few minutes of bright lifetime in the end.

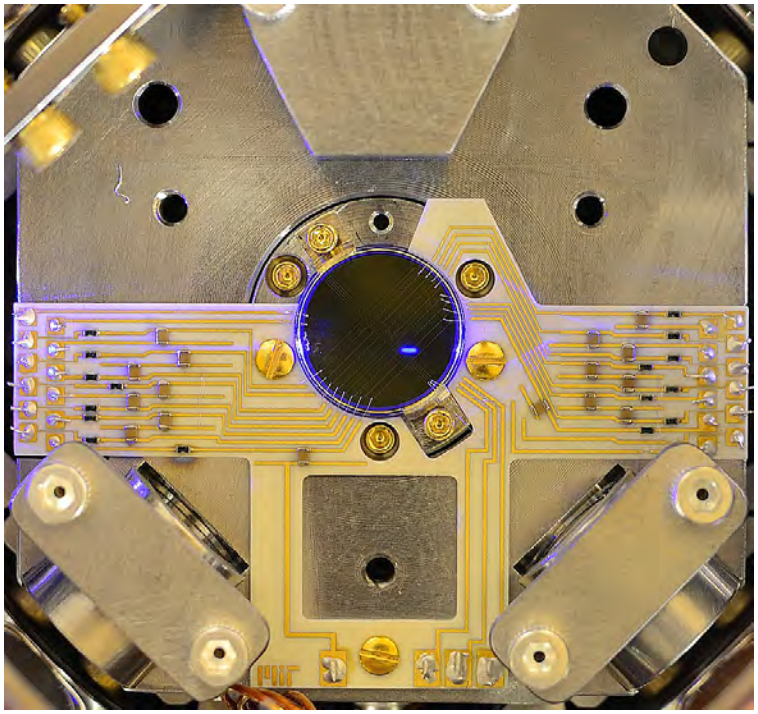

Figure 36: gold electrodes on top of a high reflectivity mirror

3.1.6 Sandia cavity trap

Due to complications in our fabrication procedure and the mentioned success in groups using devices from Sandia and GTRI we decided to modify our system to incorporate one of these designs. The natural choice for us was the Sandia cavity trap due to its similarity to our original design, with a backside cut-out allowing a mirror to be placed nearly at the trap surface. We received our first live traps at the 2013 IARPA review meeting and was subsequently installed. This has been our main trap in the lab for debugging and testing the rest of the control system.

3.1.7 Sandia HOA trap

While testing the Sandia cavity trap one immediate limitation we realized was the amount of light clipping on the trap edges, making single ion addressing impractical and would also be a major limitation in imaging the ion once a vertical cavity was installed. For these reasons we decided to design a cavity compatible with the HOA trap. With the high NA of the HOA trap, both in plane and through the trap, we could have both a tight cavity-mode while maintaining a high collection efficiency for imaging. The cavity axis is chosen to be in-plane, leaving the out-of-plane direction open for the tighter requirements of imaging and addressing.

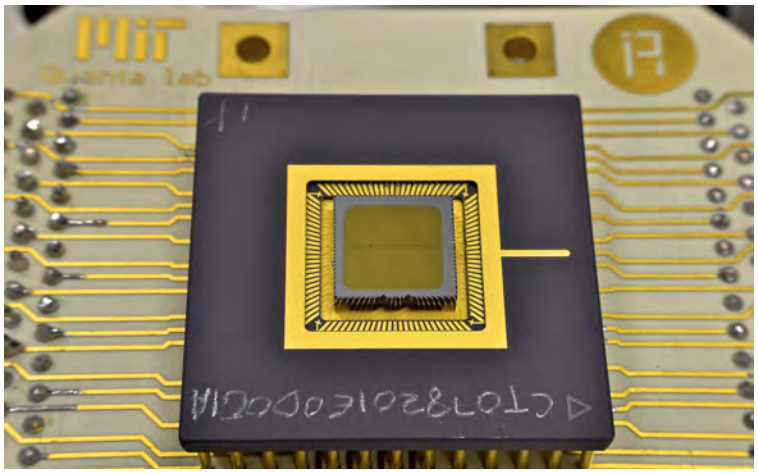

Figure 37: Sandia's cavity trap

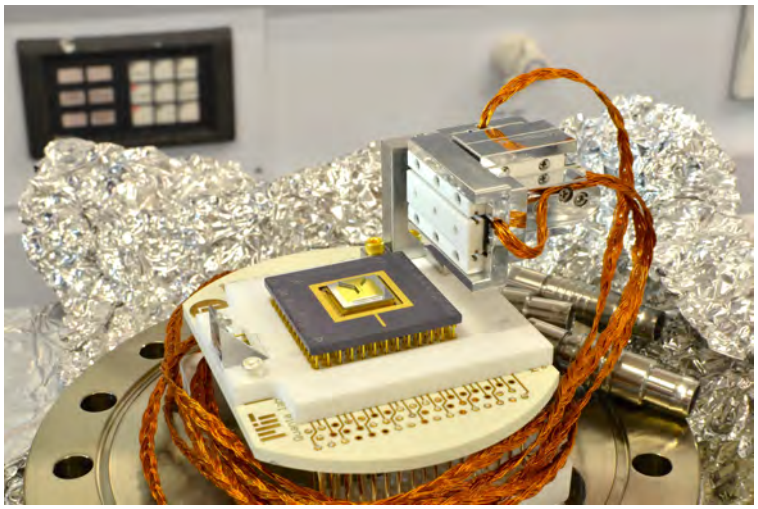

Figure 38: Sandia's High optical access trap, version 2

3.2 Surface trap characterisation

3.2.1 Identifying and tackling noise : surface vs. technical

One of the most important aspects of obtaining low motional heating is to reduce electronic noise sufficiently. The main problem is that measuring voltage noise at the required level of a few $\mathrm{nV}/\sqrt{\mathrm{Hz}}$ is quite some challenge, in particular, since the relevant electrodes are in UHV connected with long cables. Those long cables lead to pick-up of environmental electromagnetic interference.

We used the frequency spectrum of the electric field noise probed with the ion to gain insight into whether we are limited by electronic noise or not. Spikes in the spectrum as observed in early measurements are a clear indication of electronic noise for instance introduced by ground loops. Another method we used was to measure the heating rate at various locations in the trap. If surface noise is dominating, one expects that the heating rate does not change as a function of the ion position. However, technical noise should be most prominent if the ion is trapped between two electrodes or near a particularly poorly filtered electrode.

We also developed a method to measure heating rates normal and parallel to the trap surface [44]. For surface noise, one expects a ratio of two between the two heating rates, however, technical noise is highly polarized and much larger ratios are expected. We could show that the trap under investigation was not limited by electronic noise for motional heating parallel to the trap surface and that for the normal direction electronic and surface noise contributed about equally. Thus, it seems that with proper grounding, filtering and removing switching power supplies as much as possible, one can achieve low enough technical noise to be limited by surface noise.

However, after surface treatment, we observed that this is not sufficient [45]. In particular, we found that enclosing the whole apparatus in a Faraday cage with a measured EMI (electromagnetic interference) suppression of 30 dB at 1 MHz, reduced the heating rate by about one order of magnitude. This demonstrates that EMI can indeed be a serious problem and needs to be managed, especially when aiming at ultra-low motional heating as required for QIP. For the second generation, we thus added filter capacitors next to the trap as well as an in-vacuum faraday cage.

3.2.2 Dephasing of ion motion near a surface

For any type of operation that uses motional states for transfer of quantum information, it is imperative to maintain phase coherence during the entire duration of the process. Therefore, we started to monitor the frequency stability of the trap. For this we established a novel method exciting the ion motion via modulating the radiation pressure from a cooling laser at the trap frequency. We read out the excitation amplitude conveniently at the sideband. Separating the excitation into two pulses, we could very efficiently monitor trap frequencies in a Ramsey-type experiment. Our experiments establish phase coherence of a couple of milliseconds.

We measured the phase coherence of the axial motion between 600 to 1300 kHz axial trap frequency. The coherence time (T_ϕ) is compatible with a linear scaling of the coherence time with the trap frequency (see Fig. 39). We modeled the noise as comprising of two specific regions: a white noise part for low frequencies which rolls over to a 1/f spectrum at a cut-off frequency. Using this, we deduced the lower frequency cut-off of the 1/f part to be 5 Hz. Thus, at an ion-surface distance of 50 μm, stability of the trapping potentials should not be a limitation to typical gate times.

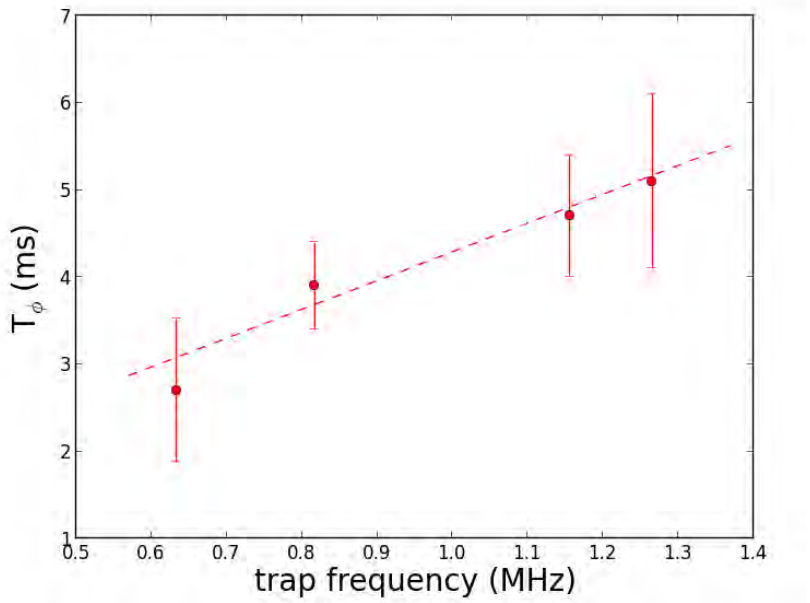

Figure 39: Dephasing time of the coherence of the ion motion near a surface trap at different trap frequencies.

3.2.3 Auger

We used Auger electron spectroscopy extensively to gather information on the elemental coverage of the surfaces of our traps. As discussed in detail in Sec. 3.3.1, we were able to monitor by this procedure how a surface initially contaminated with monolayers of carbon and oxygen could be cleaned. We could then correlate such coverage to the motional heating of a single trapped ion.

3.2.4 Fourier Transform Infrared Spectroscopy

The presence of high mass hydrocarbons in residual gas spectra inside an ultrahigh vacuum chamber has been suspected for sometime [46], and also observed by us [45]. Such hydrocarbon chains can be potential sources of fluctuating dipoles on surfaces and are therefore important to identify. With this in mind, we undertook Fourier Transform Infrared (FTIR) Spectroscopic probing of typical trap surfaces. To improve the signal to noise, it was apparent that polarization dependent reflection absorption spectroscopy would be necessary. For this, two sets of measurements are taken, one each with an S-polarized and the other with a P-polarized probe IR beam reflecting off the surface. Both sets will display absorption signals from atmospheric species such as carbon-dioxide and water vapor infrared transitions. However, only the P-polarized beam is sensitive to surface adsorbates at the monolayer level. Subtracting these two polarization spectra from each other will therefore leave a strong signal from the IR transition of the surface contaminant. We currently do such modulation by means of a wire-grid polarizer.

We noticed that even with pristine trap surfaces we observe a small signal at around 2900 cm^{-1} which typically is from C-H bonds on the surface. By contaminating this surface with isopropanol we have noticed this signal get stronger, thereby indicating the cleaning methods as a possible

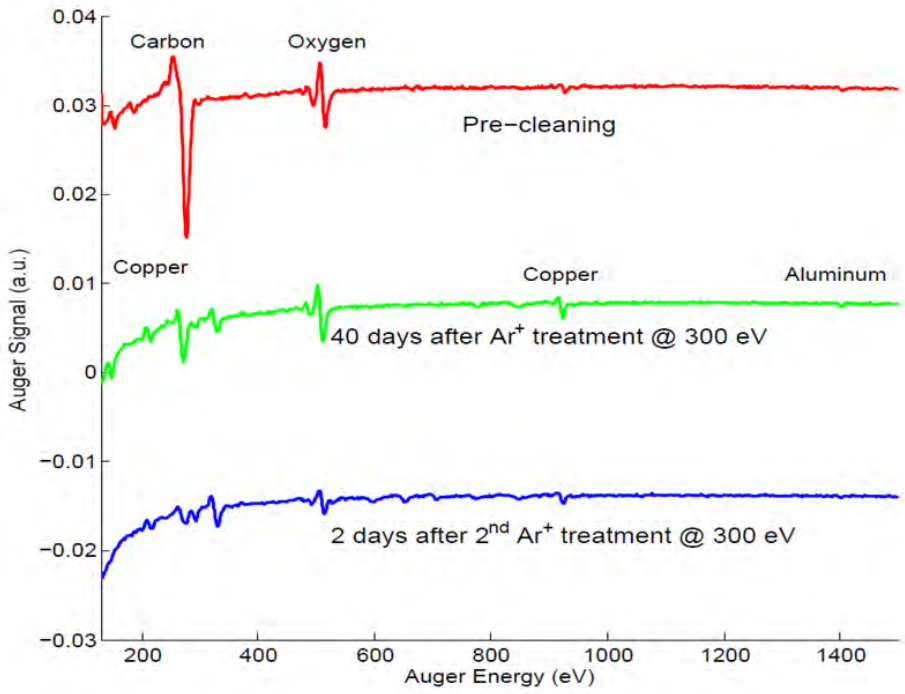

Figure 40: Auger spectra of a Cu-Al trap surface at different states after an Argon ion treatment.

origin of this signal. However, since 'dirt' on any of the optical elements might also lead to part of this signal, we decided to investigate this issue. To do this we sent the IR beam directly into the detector, keeping all the mirrors but without bouncing it off the trap surface. We looked at the P-S polarization difference signal, which is sensitive to only surface species. However, we found no C-H bond signal. This eliminates any 'dirt' contamination of the surfaces of our optical elements as the origin of the signal. We also tested whether we can detect changes of the surface contamination due to bake-out. We performed three bakes with gold traps. We did not notice any changes of the chemical composition of the contaminant due to bakes up to 200 ^{o}C. However, we detected a change which is compatible with an increased amount of O-H bonds.

We also have an experiment underway to probe the effect of near UV light on the IR spectrum due to surface monolayers. The aim is to investigate if photoionization lasers hitting trap electrodes cause any changes to the surface adsorbates thereby influencing the noise behavior.

3.3 Trap treatment

3.3.1 Argon ion milling

We have made numerous investigations into the technique of Argon-ion sputtering to clean the surfaces of ion traps. We implemented the first Argon-ion cleaning on a Cu-Al trap, and found a substantial reduction in heating rates. Of interest is the change in frequency scaling of the heating rates from the pre-cleaning behavior, pointing to a different noise mechanism limiting the heating rate. These low heating rates persisted for nearly 40 days (Fig. 41). We then did another cleaning step and observed no further improvement in heating. By monitoring the surface via Auger

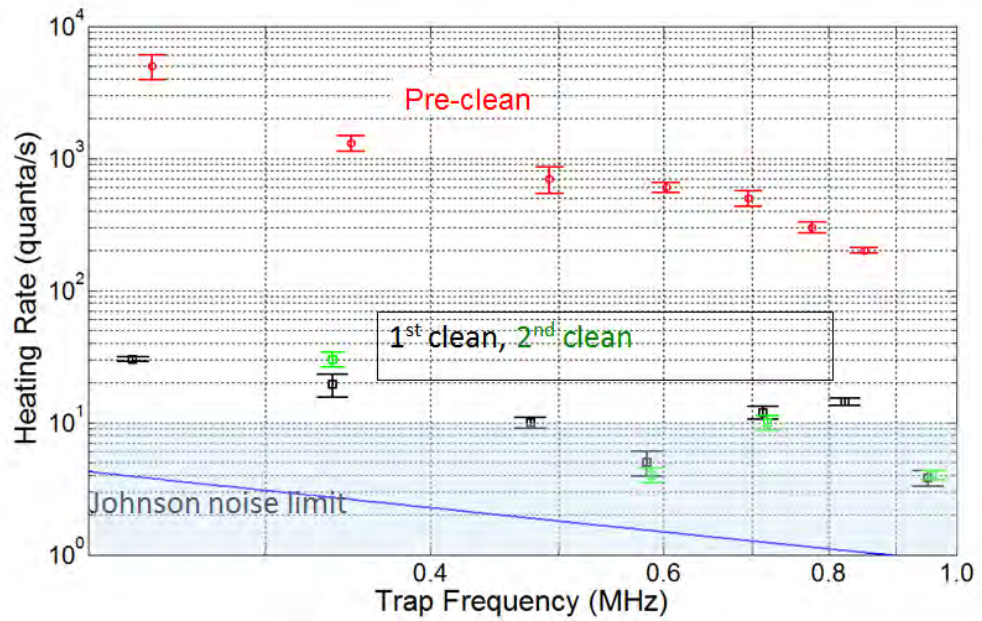

Figure 41: Heating rates and frequency scaling before and after Argon-ion milling a Cu-Al surface trap.

spectroscopy after each of these steps (Fig. 40), we deduced that the surface does not need to be atomically clean to reach very low levels of electric field noise. However at the end of the second Argon-ion cleaning, severe shorts of some of the trap electrodes to ground appeared. These shorts ranged from a few Ohms to 100 $k\Omega$. We were still able to trap, but the heating rates were unusually high.

The following Ar^+ cleaning tests on a new aluminum-copper surface trap aimed to test the methods and gain more understanding of the contaminants on the surface that may be responsible for the motional heating. The first treatment was for only one minute, and the Auger spectra showed a slight change in the elemental surface. The heating rates did not improve after this short treatment. The second cleaning was for 5 minutes, which reduced the carbon coverage by 25%, but the heating rates remained the same. After this, we increased the Argon cleaning time to 10 minutes and found that carbon had completely disappeared from the surface. This final cleaning stage however led to the development of shorts rendering four of our electrodes unusable.

Thus, in summary, while Argon cleaning can lead to low heating rate surface traps, enough to reach Molmer-Sorensen gate fidelities at the 10^{-4} level, it is not a preferable method due to the damage it causes.

3.3.2 UV light exposure

To test if ultraviolet light can destroy electric-field noise causing sources from a surface, we ran a series of tests with a UV light around 172 nm. We exposed the trap for 10 minutes and 60 minutes, and measured each time the heating rates at trap frequencies ranging from 300 to 1200 kHz. We only found minimal change on the order of one standard deviation as compared to the untreated trap.

Next, we systematically tried three different cleaning recipes. First, we irradiated the trap with UV light at 172 nm for 8 h, secondly we added Oxygen at the 10^{-4} mbar level while irradiating with UV light (1 h), and third, we tried in-situ Oxygen-plasma cleaning (0.5 h). After recovering a vacuum on the order of 1E-10 mbar, (about 2-4 days after each cleaning procedure), we measured the heating rates. We found very similar heating rates ($\sim$2 phonons/s @ 1 MHz) for all cleaning trials. In addition, we took Auger spectra after each cleaning trial. The spectra showed only small changes of the Carbon and Oxygen contaminations, however, with gold being present at all times indicating that the contamination layer cannot be very thick. A potential explanation for this is that carbon in the background pressure re-coats the traps after the cleaning procedure. Indeed in the residual gas analyzer spectra, hydrocarbons with masses between 13 and 27 AMU, CO and CO_2 appear together with H_2 as the dominant contaminants present in vacuum.

In summary, we found UV treatment of a trap surface to not affect ion motional heating, and only result in insignificant changes to the carbon and oxygen elemental coverage as determined by Auger spectroscopy.

3.3.3 Trap annealing

We began a process of developing a trap set-up that allowed for annealing experiments. The new trap mount was designed to withstand temperatures up to 1300 K, well above the melting point of gold. For initial testing, we set up an annealing oven using a quartz lamp. We successfully annealed electroplated gold traps. One interesting observation was that the traps take significant damage already above 700 K, far below the melting point of gold at 1300 K. Next, we designed a quartz heater element that was the same size as a trap and could be placed directly underneath the trap. In addition, it was thermally isolated from the chip holder. Also, we designed new filter board based on quartz which would allow us to heat the center of the apparatus to much higher temperatures. A test showed that we could get the trap glowing red, however, the thermocouple detached during the test. After these tests, we used this assembly in the main SQIP chamber. We annealed a trap to try to alter the surface properties via heat induced diffusion. We raised the heaters temperature to about 400 C for 10 minutes. However, this did not result in any change in the motional heating rates. A side effect of running the heater was a worsening of the vacuum pressure with ion lifetimes now reduced to 2 minutes. A full bake-out of the chamber was required to recover necessary pressures for trapping.

The heater plate design was also tested in another chamber and we found that the heater broke before the temperatures could be ramped to anywhere near annealing temperatures. For this reason we decided to use a more reliable commercial heater: a button heater from Heatwave Labs with pre-welded connectors. The button heater was placed directly underneath the trap with a redesigned trap holder. To test the new heater, we mounted an old surface trap directly on top of the heater and placed them inside the surface science equipped chamber. The goal was to first calibrate the heater as the manufacturer supplied specifications lacked sufficient information. For this, we placed a thermocouple directly on the trap and measured the heaters characteristic input-power versus temperature behaviour up to 650 ^{o}C. We also confirmed that the chip holder was sufficiently thermally isolated.

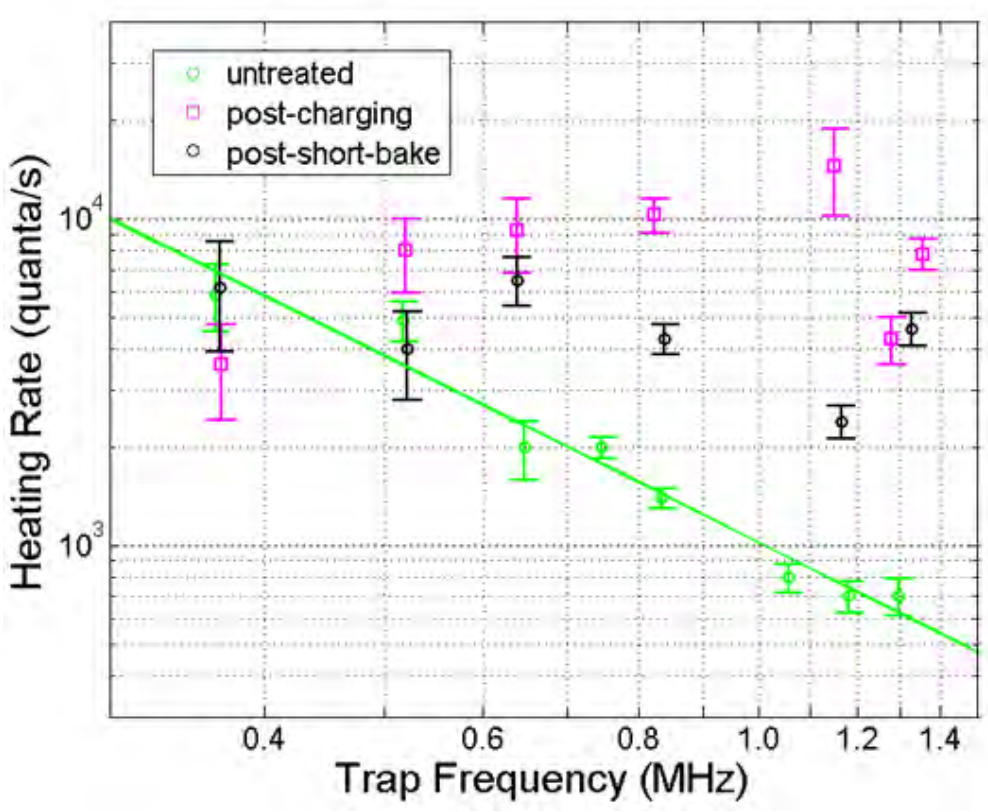

Figure 42: Heating rates and frequency scaling before and after laser charging a 50 um Al-Cu surface trap. A fit (straight line) to the untreated trap's heating rates gives a frequency scaling of $\dot{\bar{n}} \propto f^{1.9(0.2)}$.

3.3.4 Trap charging

We studied how laser light hitting the trap affects the observed heating. Grazing about 0.1 mW of 375 nm light along the trap, increased the heating rate by about a factor of two to 3 quanta/ms. We also made preliminary measurements where the light impinges normal to the surface yielding heating rates about 15 quanta/ms. At the same time, we saw moderate charging displacing the ion by about 1-2 micrometers, however, the axial trap frequency is altered by 20 % at 1 MHz. Furthermore, we observed that switching off all voltages (even disconnecting all DACs and shorting the pins to ground), the ion was trapped reliably within 5 micron of the original trapping position with an axial trap frequency on the order of a few hundred kHz. Finally, the heating rate increased even in the absence of light by about one order of magnitude to about 10-20 quanta/ms. This behavior remained unaltered even after letting the trap rest for four days. We next decided to check whether the trap is indeed charged with free charges or whether some change of the workfunction took place by laser induced chemistry. For this we rotated the trap towards the Auger unit and ran the Auger filament at 2 kV. After about 10 h of running the filament, we trapped again. Interestingly, we observed that the charging disappeared almost entirely. However, the heating rate remained strongly altered. In particular, we observed almost no dependency of the heating rate on the trap frequency. In particular, at trap frequencies at around 400 kHz the heating rates before laser exposure and after were within their error bars identical, while at 1 MHz the heating rates differed by one order of magnitude (Fig. 42). We measured then heating rates and found that they had decreased as compared to before the bake but are still higher than before laser exposure. Furthermore, instead of being independent on the secular frequency f, they dropped now with $\dot{\bar{n}} \propto f^{0.6}$. Naively, the bake had reverted some of the damage due to the laser exposure.

3.4 Electronics

Shuttling operations in segmented micro ion traps require arbitrary waveform generators capable of simultaneously supplying many trap electrodes with arbitrary voltage waveforms [47, 48]. Ideally, the analog sampling rate should be faster than the relevant trap frequencies, and the necessity of keeping the ions in the Lamb-Dicke regime sets stringent requirement on the signal characteristics in terms of noise level and suppression of digital artifacts. Such hardware is not commercially available. A particular challenge for such arbitrary waveform generators is the proper separation of digital and analog signals. Active data lines and clock signals can lead to electric pickup over a large bandwidth at the output lines. A further problem for high-speed digital-to-analog converters (DACs) is the occurrence of *glitches*: Upon a voltage update, charges are moved within the digital registers of the DAC, which leads to a spike on the output signal, which is quantified by the glitch impulse area, i.e. the time integral of the voltage spike. This quantity scales with the number of bits which are to be flipped for the update. Measurement reveals that without additional filtering, a single glitch can excite on the order of 20 phonons at trap frequencies in the 1 MHz range, such that it is crucial to employ low-pass filters with carefully chosen parameters in order to avoid uncontrolled excitation.

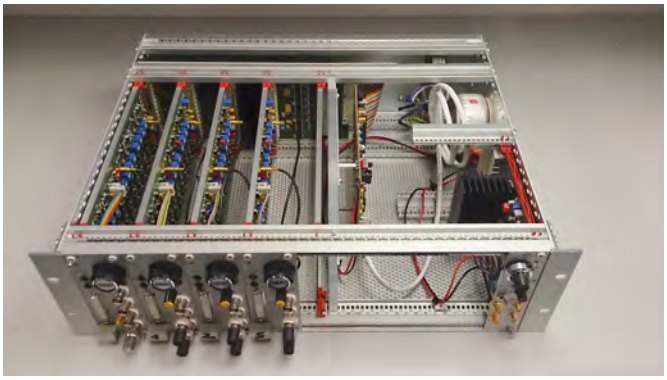

Figure 43: Fast multichannel arbitrary waveform generator Mk I: The picture shows a device fully equipped with four analog output boards (left), each having 2x12 output channels supplied by three quad-DACs. Right to the DAC boards, behind a shielding plate, the FPGA board is placed. At the right, the power supply can be seen, as well as an additional board allowing for joint triggering sequences to the ac-line and the trap rf-drive.

3.4.1 Fast multichannel arbitrary waveform generator Mk I

We developed, built, tested and employed a fast multichannel arbitrary waveform generator fulfilling the requirements listed above in phase I. The resulting device consists of a Virtex V FPGA acting as a FIFO buffer for digital waveform data supplied via ethernet, and output stages consisting of quad DACs. It is capable of individually supplying up to 48 electrode pairs comprising one segment. A differential voltage is internally added and subtracted from the signals, resulting in two signals for the two electrodes of one segment. For each segment, the compensation voltage can be derived from three different sources: i) An external input; ii) an internally generated voltage controlled by a potentiometer at the front panel; iii) two different DAC outputs, which are then not available for supply of trap electrodes. The analog update rate is depending on the segments which are to be updated. The fastest update rate possible is 400 ns, simultaneous update of all channels is possible at 1600 ns. This drawback can be partially mitigated by careful assignment of the output channels to the trap segments. An interesting feature of this device is to change sample times in steps of 20 ns beyond the minimum update time, which allows for timings which resolve typical trap oscillation periods. Furthermore, wait intervals can be inserted into the sequences, such that control on different timescales can be exerted without excessive memory requirements. The FPGA and auxiliary digital components are accommodated on a commercial mini-module installed on a homemade baseboard. The FPGA signals are routed to up to four homemade printed circuit boards, each bearing three quad DACs. The digital signals run on a backplane board, where digital isolators provide galvanic separation between the FPGA electronics and the analog output stages. On the DAC boards, great care has been taken to keep areas where digital and analog signal run separate. Because of these measures, the noise characteristics were found to be sufficient for the shuttling experiments reported in Sec. 5.1. Up to 16 digital FPGA signals can be routed to output connectors on the front panel, such that the device can also be employed to supply e.g. rf switches for laser control. Moreover, we developed an accessory boards which allows for joint triggering

of experiment sequences on the ac mains and the trap rf drive. Several of these devices have been built, one of these has been delivered to the SS lab at UIBK.

Table 5: List of relevant characteristics of the fast multichannel arbitrary waveform generators.

Specification	**Unit**	Mk I	Mk II
DAC	-	DAC8814	AD5541A
DAC resolution	bit	16	16
Amplifier	-	TLE2037	AD8510
Output range	V	± 10	± 40
Slew rate	V/μs	6	12
Temperature coefficient	ppm/°C	3	3
Max glitch impulse	nV·s	32	13
Analog update time	ns	400-1600	400
Analog channels	-	4x12	4x16
Compensation feature	-	y	n
FPGA	-	XILINX Virtex V	XILINX XC7Z020

3.4.2 Fast multichannel arbitrary waveform generator Mk II

In terms of scalability, the use of quad DACs in the MK I device represents a limitation. We therefore started the development of a Mk II device overcoming these limitations in phase II. The architectural fundamental change is thus employing single DACs rather than quad DACs for independent supply of each trap electrode. This in turn requires more digital signal lines, which gives rise to the necessity of changing from a 64 bit to a 128 bit architecture. We thus had to replace the Virtex V FPGA platform by Xilinx Zync system-on-a-chip. The resulting device will be able to supply 4x16 trap electrodes. We abandoned the concept of jointly supplying the electrodes pertaining to one segment, in order to allow for ion swapping operations. This also makes the feature of on-board switching of different compensation sources obsolete, which represents an advantage as end-users are not confronted with partially disassembling devices and manipulate on-board elements, preventing the risk of damage. The key requirement was a guaranteed simultaneous analog update time of 400 ns, which is achieved by overclocking the DACs. Concerning the other key specifications such as slew rate and glitch impulse area, the Mk II device outperforms the Mk I, see Table 5. So far, both analog and digital hardware have been designed, and a prototype device has been built and extensively tested. We are currently within serial production, one of the resulting devices will be delivered to the UIBK lab.

3.4.3 Low pass filters

As mentioned above, it is critical to filter all analog signal lines at a cutoff frequency significantly below the trap frequency to prevent the glitches arising from voltage updates from exciting undesired ion motion. One the one hand, the filters should be placed as close to the actual trap electrodes as possible, but on the other hand it is desirable to be able to change between filters

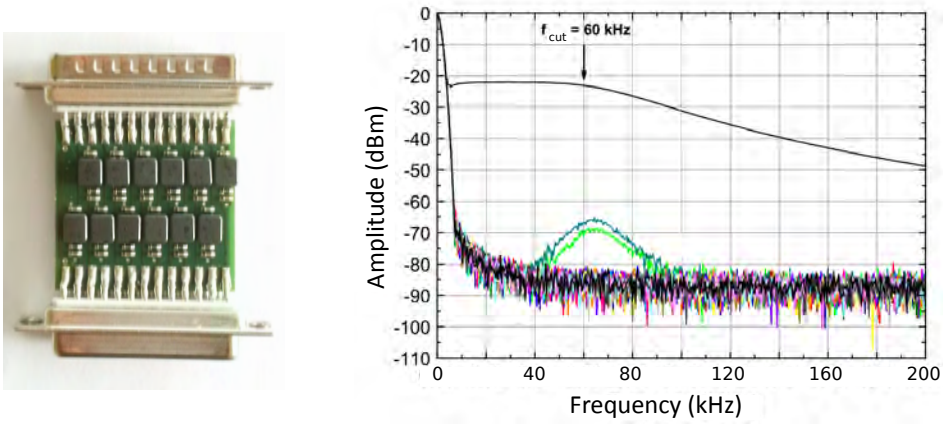

Figure 44: Low pass filter boards: The left image shows a filter board with sub-D connectors, bearing 24 low-pass filtered signal lines. The black rectangular components are shielded inductors, which have minimal inductive coupling. The plot at the right shows results of a frequency-domain measurement of the crosstalk of one channel. Signifcant crosstalk can only be seen for two neighboring channels, at frequencies around the cutoff. The suppression is about 40 dB.

with different cutoff frequencies. We thus developed compact filter boxes bearing custom made boards with sub-D 25 input and output connectors, each bearing 24 second-order Π-type filters, each consisting of two capacitors and one inductor. These can be directly plugged to the respective connectors at the vacuum flange of the trap apparatus. Typical cutoff frequencies range between 30 and 300 kHz, yielding a satisfactory tradeoff between attainable shuttling speed and glitch suppression. The latter is typically about 40 dB at axial trap frequencies in the range between 1 and 2 MHz. The LC-resonance at the cutoff frequency is damped due to the presence of a 50 Ω resistor at each analog output of the signal generator. The close packaging of inductors gives rise to inductive crosstalk. This behavior is not detrimental per se, as the electric feed-through between neighboring segments of the traps can be seen as an intrinsic, unavoidable crosstalk. However, the idea of pre-calculating complex shuttling waveforms using simulated electrostatic trap potentials (see Sec. 4.3) requires a near-ideal behavior of the system. We therefore compared different filters designs in terms of crosstalk, in particular a design with inductors arranged at 45° with respect to the neighboring ones to suppress inductive coupling, and a design using shielded, more bulky inductors arranged in parallel. The latter design showed a better crosstalk suppression, the results are shown in Fig. 44.

3.5 Shielding of TIQC experiments against environmental noise

3.5.1 Noise filtering via Faraday cage

Noise due to electric fields from electro-magnetic interference (EMI) can lead to motional heating by direct interaction with the ion or via coupling to the wires supplying the trap voltages. While surface noise usually dominates, we found that after surface cleaning, EMI noise becomes noticeable. Argon ion milling of a Cu-Al surface trap lowered the electric field noise as seen by the ion to $S_E \sim 10^{-11}\mathrm{V}^2/\mathrm{m}^2\mathrm{Hz}$. In order to shield the apparatus from EMI, we enclosed the entire vacuum chamber at UCB in an aluminum Faraday cage. This cage suppresses external noise at 1 MHz by

30 dB as measured with a pickup coil placed inside the cage. Measurement of the ion heating rates after installing the cage showed an order of magnitude drop in the electric field noise.

3.5.2 Cryo-shielding against magnetic fields

In addition to motional heating, fluctuations in magnetic fields can induce phase shifts in qubit states, giving further cause to reduce EMI. The Faraday shielding described in the previous section is sufficient for minimizing heating rates (sensitive in the MHz regime). However, if one wants to preserve phase coherence on time scales of typical quantum computations, attenuation of lower frequencies is also required. In particular, 50/60 Hz noise, present in any lab, should be suppressed. Magnetic field attenuation can be improved by using thick copper shields. A further increase in attenuation can then be achieved by implementing such shields in a cryogenic environment. The resistivity of copper drops by orders of magnitude when working at liquid Helium temperatures, resulting in a decrease in penetration depth of electro-magnetic fields. As described in Section 2.2.4, we have experimentally shown that 50 Hz magnetic field noise is attenuated up to 85 dB using two centimeter thick copper walls at 15 K.

3.6 Preventing vacuum induced optical loss

One of the main challenges we investigated during this program was in maintaining and recovering high-finesse optical cavities for the blue/UV in vacuum. This has been an outstanding problem, preventing the more favorable S-P transitions from being utilized effectively in strongly coupled CQED systems. We found that the loss mechanism was only present for dielectric stacks with Ta_2O_5 as their surface layer, with SiO_2 surface layers showing no measurable loss increase. The incurred optical loss can then be reversed by flooding the chamber with oxygen at atmospheric pressure. However, this recovery process is slow, taking placing on a similar scale to the original decay (hundreds of hours). A more permanent solution was to either originally have designed the coating stack with a SiO_2 surface layer or sputter a thin layer of SiO_2 (1 nm) on top of a Ta_2O_5 surface layer. This has a small effect on the total reflectivity but reduces the loss rate by an order of magnitude.

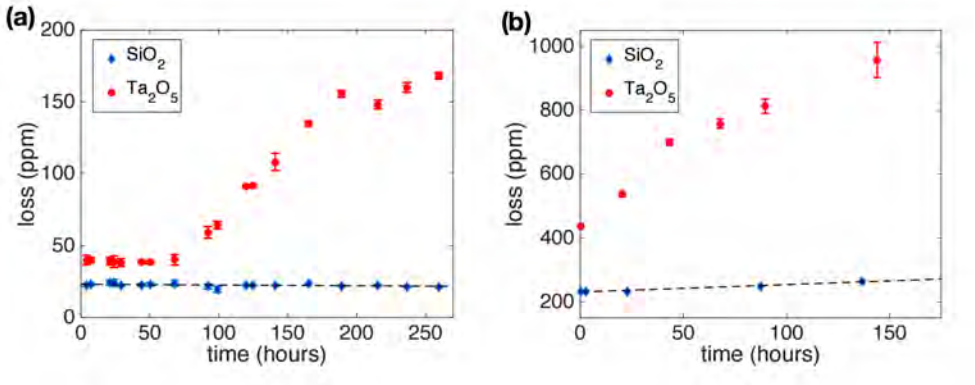

Figure 45: optical loss vs time for various top surface layers (a) Loss increase at 57°C for a Ta_2O_5 surface layer (red circles), and 110nm-thick SiO_2 surface layer (blue diamonds). (b) Loss at 100 °C for a Ta_2O_5 top layer (red circles) and a 1 nm-thick sputtered SiO_2 surface layer.

4 Software

4.1 From unitary operations to pulse sequences: Estebanizer

In order to implement any operation in a quantum information processing experiment, it is necessary to decompose it in terms of the quantum gates experimentally available. If the set of quantum gates provided by the experiment is rich enough, it will be possible to implement an arbitrary quantum unitary on the qubit register. Such a set of gates is known as *universal*.

A canonical universal set of gates consists of 2-qubit CNOT gates and arbitrary single qubit rotations; there exist deterministic algorithms that can provide near-optimal decompositions of unitaries in terms of these gates [8]. However, the most convenient set of gates depends heavily on the particular experimental implementation, and 2-qubit CNOT gates may not be the most efficient to implement in any given experiment. In particular, architectures like trapped ions[49, 50] or atom lattices[51] often have in their toolboxes high-fidelity N-qubit gates that can be applied to the whole qubit register. Implementing 2-qubit gates in terms of these would require refocusing or decoupling techniques. Therefore, to avoid this additional overhead, it is desirable to find direct decompositions of unitaries in terms of the global N-qubit gates.

A software solution has been developed in Innsbruck to find such decompositions of quantum unitaries, using a combination of analytical and numerical methods. The methods employed can be applied to many different physical implementations, such as optical trapped-ion qubits, hyperfine trapped-ion qubits or atom lattices.

A similar approach has been studied in [52], where optimal control techniques are used to derive pulse sequences for implementing quantum unitaries. However, the techniques presented there often lead to less-than-optimal sequences, since the algorithm starts with longer than needed sequences and then removes pulses, if possible. The algorithm presented here ensures, by design, that the least number possible of entangling gates is used. Another difference is the numerical optimization method proposed: in [52], simulated annealing is used to overcome local minima when carrying out numerical optimizations. This technique only brings an advantage for certain optimization landscapes. We propose here to use an optimization method that takes advantage of

the fact that the cost function and its gradient can be analytically calculated, which has shown to be more efficient in practice. In addition, whenever the unitary to be implemented is local, we have developed a deterministic analytic algorithm for finding optimal decompositions.

In most quantum information processing experiments, the most challenging and worst performing operations in terms of fidelity are entangling gates. Therefore, when looking for pulse sequence implementations it is a priority to minimize the number of entangling gates required. The simplest way to do this is by using layered pulse sequences, as shown in figure 46.

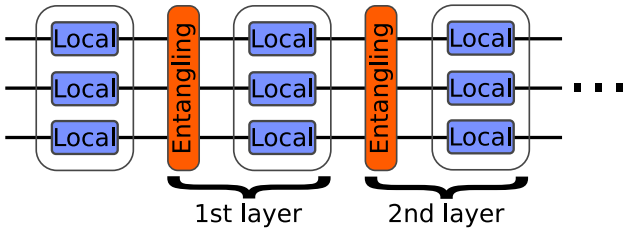

Figure 46: Sequence ansatz with layered local and entangling gates.

The number of entangling layers required for implementing a given unitary is unknown in advance. Therefore, the following algorithm is applied:

1. An ansatz sequence with N layers is proposed.
2. The parameters in the sequence (pulse lengths and phases) are numerically optimized.
3. If the sequence has converged to the desired unitary, stop. Otherwise increase N by 1 and go back to step (i).

A particular case of interest is when the action of the unitary only matters on certain input states. This happens, for instance, when one is interested in state preparation starting from some fixed input state. The unitary resulting from the compiled sequence only needs to be specified in a particular subspace of the input states, for example:

$$U_{\text{target}} = \begin{pmatrix} u_{11} & u_{12} & \vdots & \vdots \\ u_{21} & u_{22} & \text{free} & \text{free} \\ u_{31} & u_{32} & \vdots & \vdots \\ u_{41} & u_{42} & \vdots & \vdots \end{pmatrix} \tag{2}$$

A more general case than the previous is where the target unitary must be implemented for several subspaces with arbitrary relative phases. Suppose, for example, that one wants to measure some observable and perform feedback on the system based on the classical result of this measurement, as shown in figure 47. In this case the phase of the ancilla qubit after the gate is irrelevant, since it will be lost in the measurement. Therefore, the compiled sequence can be sought in such a way that it matches the desired unitary in the subspaces where qubit 4 is $|0\rangle$ or $|1\rangle$ separately,

allowing an arbitrary phase between them:

$$U_{\text{target}} = \begin{pmatrix} 1 & 0 & 0 & 0 & 0 & 0 & 0 & 0 \\ 0 & e^{i\phi} & 0 & 0 & 0 & 0 & 0 & 0 \\ 0 & 0 & 1 & 0 & 0 & 0 & 0 & 0 \\ 0 & 0 & 0 & e^{i\phi} & 0 & 0 & 0 & 0 \\ 0 & 0 & 0 & 0 & 1 & 0 & 0 & 0 \\ 0 & 0 & 0 & 0 & 0 & e^{i\phi} & 0 & 0 \\ 0 & 0 & 0 & 0 & 0 & 0 & 0 & 1 \\ 0 & 0 & 0 & 0 & 0 & 0 & e^{i\phi} & 0 \end{pmatrix} \tag{3}$$

Since there is one less constraint on the target unitary, a simpler implementation may be achieved.

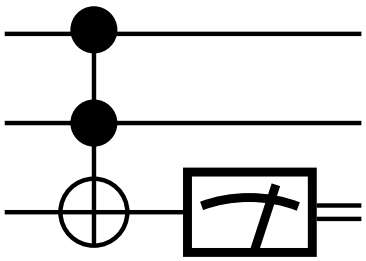

Figure 47: The phase of the ancilla qubit is irrelevant.

Owing to calibration errors, the operations experimentally applied might deviate from the intended ones in a systematic way. If it is possible to characterize the actual experimental operations being applied, then they should be taken into account for the compilation. One way to do this is:

1. Compile the target unitary in terms of the ideal gates.
2. Replace the ideal gates by the experimentally characterized ones.
3. Add as many local operations as needed to obtain the ideal target unitary.

As an example we show the action of a Toffoli gate on the 8 input logical states on figure 48. It can be seen that, by adding just two pulses, the output fidelity for each input state can increase by up to 20%. The sequence with 11 pulses is actually only an approximate correction to the uncorrected case. The exact correction requires 14 pulses, and actually yields a lower fidelity than the approximate one, since it requires more pulses and each of these has fidelities lower than 1.

4.2 TIQC-SPICE

As the capability and complexity of physical quantum systems grow, it quickly becomes essential to the design and implementation of new experiments to be able to effectively model their behavior and predict their performance. TIQC-SPICE is a simulation and analysis package for trapped-ion quantum computation developed in Python for this purpose. Along with the Estebanizer pulse compiling software (Sec. 4.1), it composes a comprehensive modeling system for designing, verifying, and optimizing TIQC experiments. A coarse block diagram for the overall system is shown in figure 49.

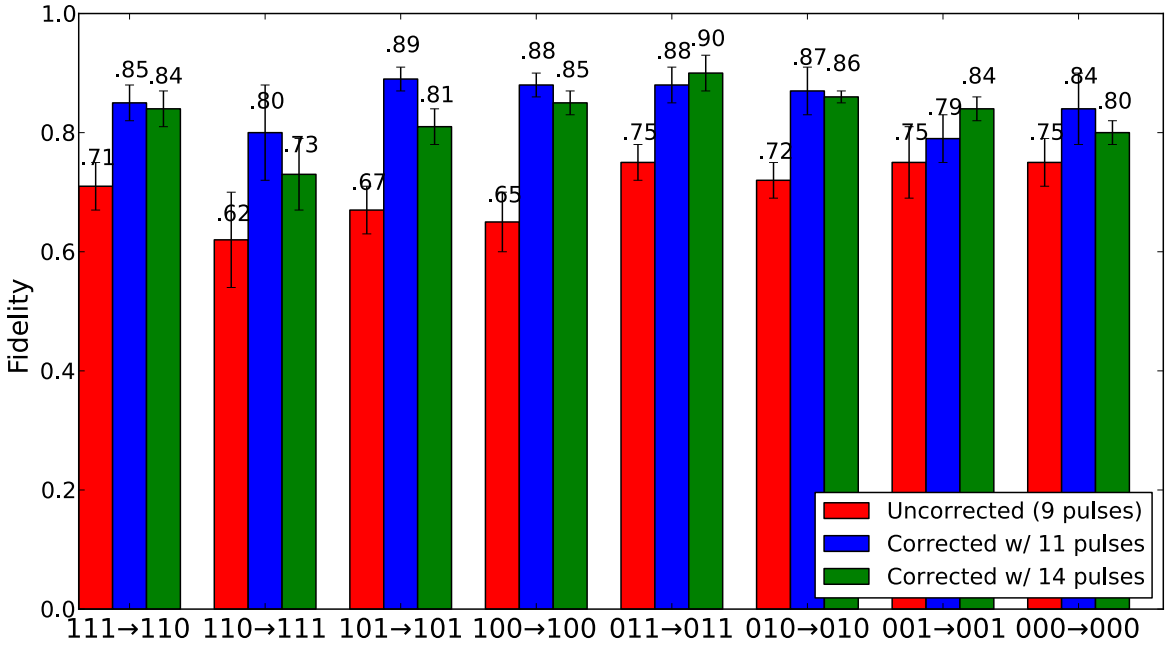

Figure 48: State fidelity for a Toffoli gate applied on the 8 canonical input states.

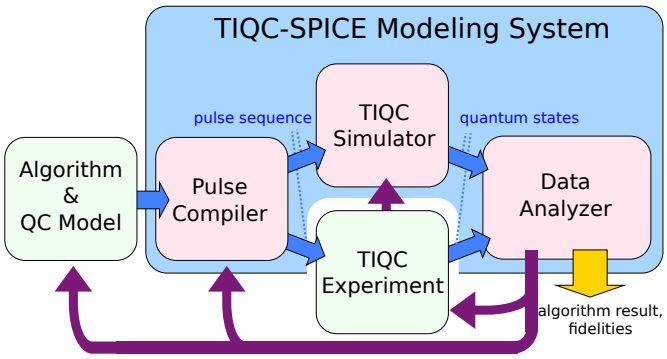

Figure 49: Block diagram of overall TIQC-SPICE modeling system (taken from [53]). Here, the Estebanizer software (Sec. 4.1) takes the place of the Pulse Compiler block. The TIQC Simulator (described here) and experiment result in quantum states, which are interpreted with incorporated Data Analyzer tools in order to find and compare results and fidelities and to provide feedback for optimizing systems, algorithms, and sequences.

The TIQC simulator utilizes numerical ODE and integration techniques in order to model the possibly non-unitary state evolution of a TIQC system in the presence of various static and dynamic sources of decoherence. The system state is described within a dimension-$(N+1)L^n$ Hilbert space, where N is the maximum number of phonons in the center-of-mass mode of the system, n is the number of ions, and L is the number of levels available to each ion (only $L = 2$ and $L = 3$ are implemented). The input to the system is in the form of a pulse sequence, from which the ideal time-dependent system Hamiltonian and corresponding unitary evolution is determined (the set of valid pulses is shown in table 6).

Pulse	**Description**
$R_{carrier}(\theta, \phi)$	Carrier pulse
$R_{blue}(\theta, \phi)$	Blue sideband pulse
$R_{ac}(\theta, \phi)$	AC stark pulse, approximates a Z-rotation
$R_{MS}(\theta, \phi)$	MS pulse; constructs a bichromatic Hamiltonian
$Delay(time)$	Represents the absence of a laser pulse
$Hide(ion)$	Move ion to or from the S'/D' hiding subspace
$MeasInit(ion)$	Perform in-sequence measurement and reinitialization of one ion

Table 6: Laser pulses available to specify a pulse sequence for determining the state evolution in the TIQC simulator (taken from [53]).

Static sources of decoherence are implemented via various randomized parameters affecting the input state of the system, while dynamic sources manifest themselves as randomized time-dependent perturbations to the system Hamiltonian or additional unitary or non-unitary operators inserted within the system's evolution [53]. Monte-Carlo techniques are then used to extract states and fidelities at points during and after the evolution. Each decoherence source is independently modeled and can be disabled or configured via experimentally-characterized system parameters. The currently implemented set of error sources and their corresponding parameters are listed in table 7.

Error parameter	**Description**	**Typical value**
$addressingerr$	Addressed beam overlap with neighboring ions	0.035
$addressingerr\_global$	Global beam non-uniformity	0.02
$heatingrate$	System heating rate	141000 μs/quanta
$coherencetime$	Dephasing: T_2 coherence time	5000 μs
$correlationtime$	Dephasing correlated exponentially to gaus. width	333 μs
$intensityfluct$	Fluctuations of qubit laser during pulse sequence	0.02
$stateiniterr$	Probability of error in initially preparing $\|S\rangle$ state	0.003
$specmodecoupling$	Coupling to spectator motional modes	0.02
$lifetime$	T_1 spontaneous decay rate (lifetime of $\|D\rangle$ state)	1168000 μs

Table 7: Decoherence models implemented in TIQC simulator, with their corresponding typical configuration parameters (derived from [53]).

The large Hilbert space (accounting for phonon states), necessity of numerical ODE solving

and integration for the time-dependent decoherence-affecting Hamiltonian, and Monte-Carlo sampling all come together to greatly limit the possible performance of a TIQC simulation engine (as should eventually be expected for any classical simulation of a quantum computer). To improve this performance, numerical calculations are vectorized and optimized for performance using the open-source Python NumPy and SciPy libraries. Further, because Python is an open platform, it is simple and economical to utilize parallelization to distribute the computational load over many computers. The simulator is therefore written such that individual Monte-Carlo simulation runs can be implemented and parallelized as unique threads (currently this is implemented using the ParallelPython package). Simulations of pulse sequences with ~ 100 pulses in a 5-qubit system (with 5-7 phonons) generally require time scales on the order of several hours. However, there remain various ways by which the simulator performance could likely be improved.

TIQC-SPICE has been an invaluable tool in crafting experimental demonstrations of quantum protocols. Paired with the Estabenizer pulse compiler, it provides a feedback mechanism in order to pick out quantum circuits and pulse sequences with decreased sensitivity to error. In implementing quantum protocols, it is an essential verification tool; for example, it was used to verify the theoretical success and predicted fidelities of the order finding and factoring experiments (Secs. 5.8 and 5.9).

4.3 Shuttling control software

Employing generic shuttling operations within computational sequences requires a unified, device-independent way for find suitable voltage waveform. Ideally, such software solution should allow for interfacing with a given experimental control software. Therefore, UMZ has started the development of an object-oriented software framework fulfilling these requirements. The derivation of voltage waveforms for a given shuttling operation in a segmented trap is very often addressed as an ill-posed inverse problem in the literature [54, 55]. However, due to the hyper-parametric nature of the regularization methods used to solve these problems, and the other constraints which have to be taken into account, this task practically turns into a general non-linear, non-local optimization problem. The core of our framework is therefore a templated, performance-optimized Nelder-Mead algorithm [56], which can be used for a given set of objects with an order relation and an algebra defined on them. The waveform derivation is broken down into three tasks: i) the information on the sequence of ion positions and desired trap frequencies is collected built input commands; ii) for each element of this sequence, a suitable voltage set is computed, where the difference with respect to the previous position set is also minimized; iii) based on the previous results, the optimum way of how the voltages vary with time is computed. Here, both the instantaneous and integral acceleration of the ions and the rates of change of the voltages are minimized.

So far, the object framework has been set up and steps i)-iii) have been tested for the case of shuttling a single ion by a distance of four trap segments of the trap described in Sec. 3.1.1. This scenario already bears some degree of complexity as maximum shuttling speed is to be traded against keeping the variation rates of the voltages below the hardware limits. The resulting waveforms are shown in Fig. 50.

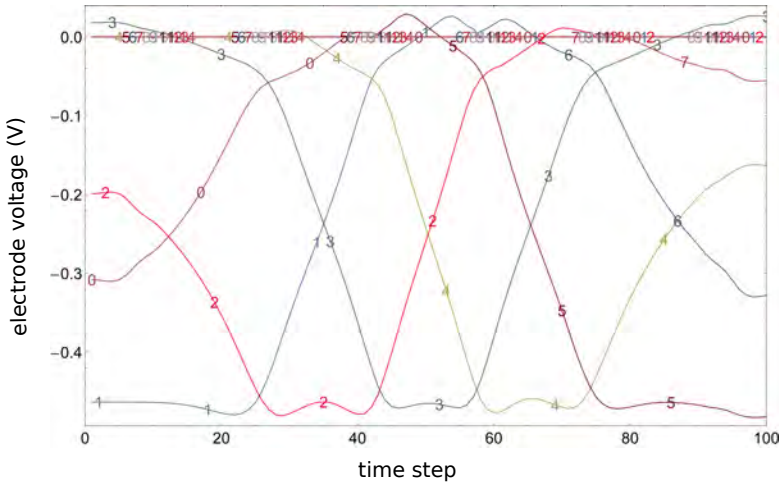

Figure 50: Voltage waveforms for shuttling a single ion by 4 segments along the tap axis. The voltages are calculated by the two-step optimization scheme explained in the text. The curves are labeled with the respective segment numbers. The nonuniform scaling along the time axis shows how the ion is smoothly accelerated and decelerated. Note that while the optimization includes 14 segments, only the segments near the ion position are used, i.e. biased to nonzero voltage.

5 Implemented Algorithms and Procedures

5.1 Ion shuttling operations

With the waveform generator we developed in phase I available (cf. Sec. 3.4.1), we demonstrated fast ion shuttling in the predecessor trap of the trap described in Sec. 3.1.1. A single groundstate cooled ion was shifted from the laser-ion interaction segment to the neighboring one, i.e. by a distance of 280 μm. Two protocols were established: One where identical shuttling to the initial segment was done after a variable delay time, and one where a voltage kick pulse was exerted after the first shuttle, and a very slow shuttle back was performed. In the first case, we were able to show that cancellation of the oscillatory excitation from the two shuttles can be accomplished by controlling the delay between these pulses on a 20 ns resolution, i.e. way below the trap period of about 800 ns. In the second case, we could demonstrate that suitable chosen kick parameters (delay, duration, amplitude) serve to cancel out the excitation from a single shuttle. We observe final excitation energies below 0.2 phonons, which is the thermal excitation after sideband cooling and therefore only an upper limit of the energy transfer [57]. Furthermore, we were able to show that the coherence of a spin-motion entangled state $|\uparrow\rangle|0\rangle + |\downarrow\rangle|1\rangle$ survives the huge phase space excursion during the fast shuttling. Similar results have been reported by the NIST group [58]

As a next step, we attempted to demonstrate separation of two ions [59] with similar methods, which turned out to be a much harder endeavor. Using intuitive voltage ramps as a starting point, we observed energy transfers which were too large to permit the quantification of these, which in turn makes optimization hard. The reason for these extreme excitations lies in the fact that the confinement strength becomes rather weak during the process (down to about 150 kHz in our case), which makes the ion prone to acceleration by background fields and to anomalous heating. We

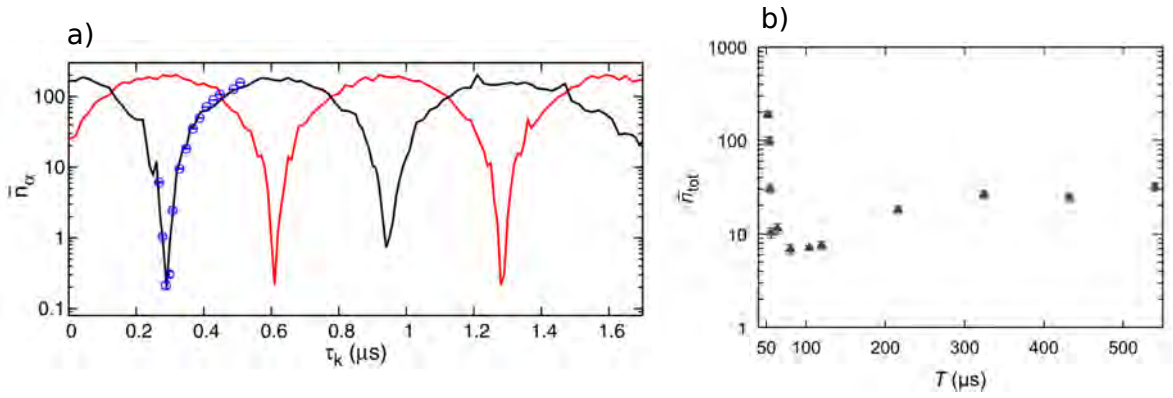

Figure 51: Main results for shuttling operations: **a)** shows the residual excitation in the form a mean phonon number pertaining to a coherent state after shuttling a single ion by 280 μm with about 4 μs. The values are measured with respect to the delay time before the de-excitation kick. The dot are pertaining to measurements where the mean phonon number is extracted from full Rabi oscillation data on blue, red and second red sidebands, and the solid line pertain to simplified measurements where only one specific pulse are was probed on each transition. The two curves were measured for different polarities of the voltage kick, and are therefore offset by 180°. **b)** shows the resulting total phonon number, inferred from Rabi oscillations on red and second red sideband, after separation of a two ion crystal. The Rabi oscillations were separately measured for each ion, such that the values represent the averaged excitation per ion. At short times, the excitation is of oscillatory nature and is due to rapid acceleration, whereas at long times it is of thermal nature, resulting from transient confinement at low effective trap frequencies.

therefore looked at the classical dynamics of the process in order to derive waveforms which mitigate these effects. It turned out that precise calibration of the background forces and the harmonic confinement parameters is ultimately required [60]. Using the calibration data in conjunction with the improved waveforms, we finally managed to obtain excitation that allow for determination of the motional excitation. We then developed and refined measurement and data evaluation methods that allow for efficient quantification of excitations of up to 1000 phonons/ion. With these tools at hand, we identified and used suitable control parameters to further optimize the process. The final result was an excitation level of down to 6 phonons/ion within 80 μs separation time, without additional de-excitation kicks [61]. Note that results reported from the NIST group [58] are better in terms of less excitation in less time, however this is partly due to the fact that much lighter $^{9}Be^{+}$ ions were employed.

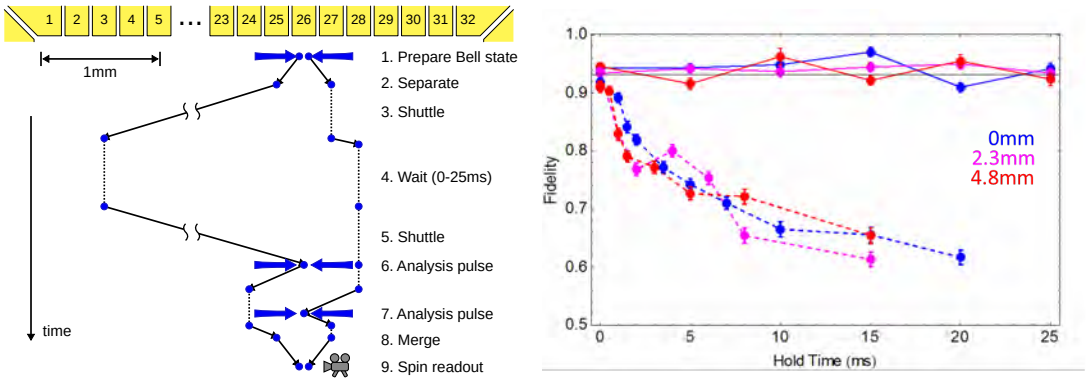

Figure 52: Long-range separation of entangled Bell states: The left panel shows the used experimental sequence, see text. The right panel shows the measured Bell state fidelity versus hold time for different maximum ion separations, for even Bell states (dashed) and odd Bell states (solid)

5.2 Distributing entanglement via ion-transport

In the trap described in Sec. 3.1.1, and with the waveform generator from Sec. 3.4.1, we have demonstrated the long-range distribution of entangled qubits in a scalable architecture, in order to provide a joint demonstration of basic building blocks for scalable quantum information processing. Two $^{40}Ca^{+}$ spin qubits have been entangled by means of a geometric phase gate mediated by spin dependent optical dipole forces, reaching Bell state fidelities of up to 95%. This is predominantly limited by SPAM errors and off-resonant excitation of spectator modes. After the gate, the ions are separated by means of the protocol described in Sec. 5.1, then one of the ions was shuttled to the adjacent end of the trap, by a distance of about 5 mm. After a variable hold time, the ion is shuttled back into the laser interaction region, where a qubit rotation is performed. Then, the other ion in moved into the interaction region, and another rotation is carried out. This way, we demonstrate full quantum state tomography with laser-based ion addressing. From the results, we see coherence decay on a timescale of a few ms for even Bell states, induced by magnetic field fluctuations. For odd Bell states, we do not see coherence decay irrespective of the ion separation for hold times of up to 20 ms. Probing at longer hold times was not possible so far due to increase

of SPAM errors with time. However, for odd Bell states, we do observe slow drifts of the Bell state phase, on the order of 30 Milligauss/(min·m), which on the one hand emphasizes the sensitivity of separated Bell states, one the other hand this drifting gradient represents a new decoherence source which is to be characterized and mitigated.

5.3 Topological Quantum Error Correction

In this section we review the basic background of the minimal 7-qubit topological color code that we have realized during the last period of the project. We then present in detail the various protocols that we have used to create (encode) the logical qubit in an optimized manner. We have demonstrated the error detection capabilities of the encoded logical qubit by measuring the complete error syndrome table. Furthermore the experimental implementation of the entire set of single-qubit Clifford gate operations acting on the logical qubit was demonstrated.

5.3.1 Preliminaries: Definition of the code and experimental toolbox

Definition of the logical qubit for the 7-qubit color code. Color codes are stabilizer quantum codes, that is, the code space is defined by a set of commuting stabilizer operators $\{S_i\}$ with eigenvalues ± 1. The code space is defined to be the $+1$-eigenspace of the set of stabilizers, that is, as the space of logical or encoded quantum states $|\psi\rangle_L$ such that $S_i|\psi\rangle_L = +|\psi\rangle_L$ for all i. The smallest fully functional 2D color code that encodes one logical qubit involves seven physical qubits (Fig. 53). The physical qubits are regarded as the vertices of a triangular planar code structure formed by three adjoined plaquettes. In color codes, there are two stabilizer operators associated with each plaquette, which for the minimal seven-qubit color code (Fig. 1A) results in the set of four-qubit X and Z-type operators

$$\begin{aligned} S_x^{(1)} &= X_1X_2X_3X_4, & S_z^{(1)} &= Z_1Z_2Z_3Z_4, \\ S_x^{(2)} &= X_2X_3X_5X_6, & S_z^{(2)} &= Z_2Z_3Z_5Z_6, \\ S_x^{(3)} &= X_3X_4X_6X_7, & S_z^{(3)} &= Z_3Z_4Z_6Z_7. \end{aligned} \tag{4}$$

Here, X_i, Y_i and Z_i denote the standard Pauli matrices acting on the i-th physical qubit with the computational basis states $|0\rangle$ and $|1\rangle$. These six stabilizers impose six independent constraints on the seven physical qubits and thus define a two-dimensional code space, which allows a single logical qubit to be encoded. The logical basis states $|0\rangle_L$ and $|1\rangle_L$ spanning the code space are entangled 7-qubit states and are the eigenstates of the logical operator $Z_L = Z_1Z_2Z_3Z_4Z_5Z_6Z_7$, where $Z_L|0\rangle_L = |0\rangle_L$ and $Z_L|1\rangle_L = -|1\rangle_L$ [62].

Encoding of physical qubits. All past and proposed experiments in this project are performed using a linear string of 7 $^{40}Ca^+$ ions confined in a Paul trap [49]. Each ion hosts a physical qubit, which is encoded in (meta)stable electronic states; more precisely, it is encoded and manipulated on the transition between the two electronic states $S_{1/2}(m_j = -1/2) = |1\rangle \rightarrow D_{5/2}(m_j = -1/2) = |0\rangle$, the latter having a radiative lifetime of about $1s$. A generic experimental cycle consists of the following sequence. (i) Initialization of all qubits in the electronic ground state $S_{1/2}(m_j = -1/2) = |1\rangle$ by optical pumping. (ii) Cooling the ion string to the motional ground state of the center-of-mass mode. (iii) Coherent operations on the $S_{1/2}(m_j = -1/2) \rightarrow D_{5/2}(m_j = -1/2)$ transition by a narrow linewidth laser at 729 nm. (iv) Detection of the final state by fluorescence

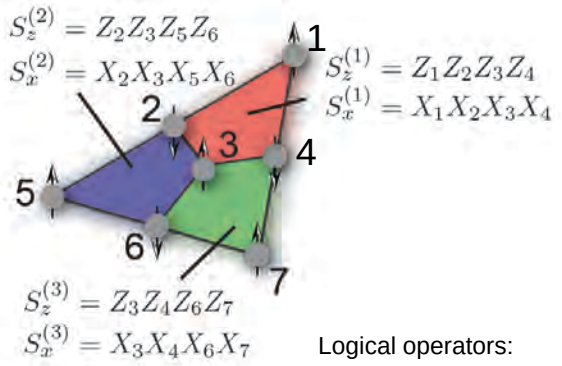

Logical operators:

$$\bar{Z} = \sigma_1^z\sigma_2^z\sigma_3^z\sigma_4^z\sigma_5^z\sigma_6^z\sigma_7^z \quad \bar{Z}|\bar{0}\rangle = |\bar{0}\rangle \quad \bar{Z}|\bar{1}\rangle = -|\bar{1}\rangle$$
$$\bar{X} = \sigma_1^x\sigma_2^x\sigma_3^x\sigma_4^x\sigma_5^x\sigma_6^x\sigma_7^x \quad \bar{X}|\bar{0}\rangle = |\bar{1}\rangle \quad \bar{X}|\bar{1}\rangle = |\bar{0}\rangle$$

Figure 53: **The topologically-encoded qubit:** One logical qubit is embedded in seven physical qubits forming a 2D tringular planar code structure of three plaquettes. The code space is defined via six stabilizer operators $S_x^{(i)}$ and $S_z^{(i)}$, each acting on a plaquette which involves four physical qubits. The code space is defined as the simultaneous +1 eigenspace of these six stabilizers. The two-fold degeneracy of the code space is lifted by introducing logical Z and X operators.

measurements, involving an electron shelving technique using a laser beam at 397 nm illuminating the whole ion string.

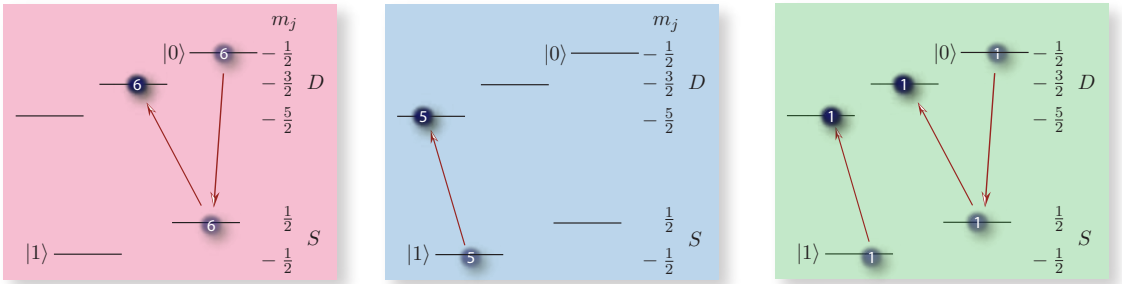

Figure 54: **Spectroscopic decoupling of physical qubits.** We ensure that only the qubits on a particular plaquette are affected by the entangling operation by applying spectroscopic decoupling pulses (DEC) to all other qubits. The quantum state of decoupled (or "hidden") qubits is coherently transferred from the $S_{1/2}(m_j = -1/2)$ and $D_{5/2}(m_j = -1/2)$ qubit states to the Zeeman"storage" states $\{D_{5/2}(m_j = -5/2), D_{5/2}(m_j = -3/2)\}$ by a sequence of up to 9 addressed single qubit rotations. The working principle of the decoupling and recoupling (REC) pulses is illustrated in Fig. 55 and described in detail in the main text.

Experimental unitary gate set. Within our setup, we realize a high-fidelity universal set of quantum operations consisting of single-ion phase shifts, collective rotations, and a collective entangling gate. To realize these operations, two different laser beams at 729 nm are used to

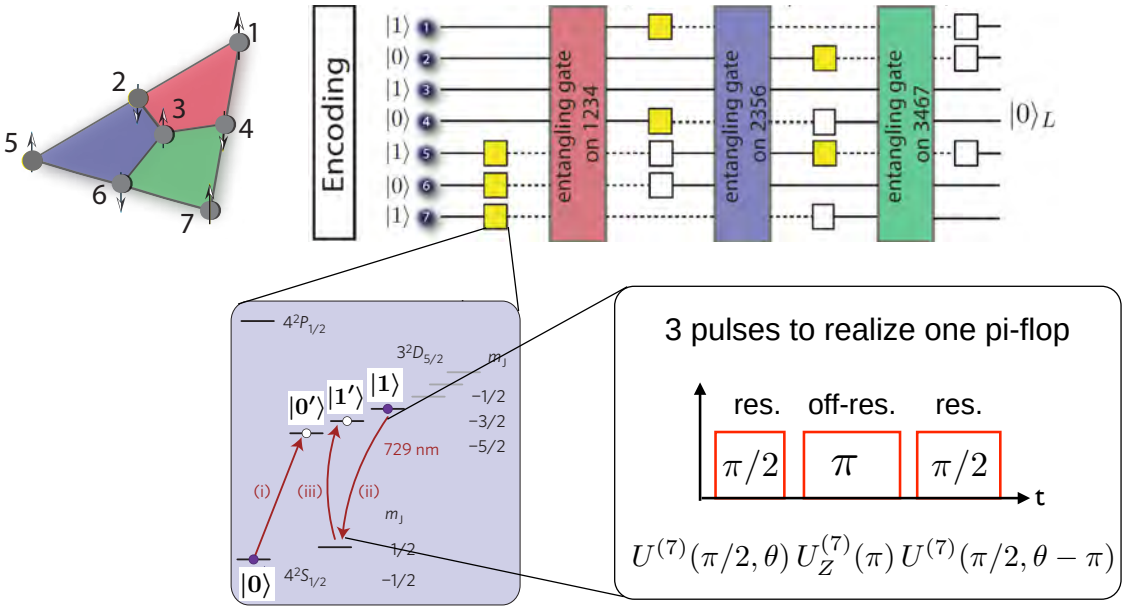

Figure 55: **Schematic sequence for state preparation:** The encoding of the logical state requires the generation of plaquette-wise entanglement of sets of 4 qubits belonging to each of the three plaquettes of the code. This encoding of the logical qubit is achieved by coherently mapping the input state $|1010101\rangle$ onto the logical state $|0\rangle_L$ using a quantum circuit that combines plaquette-wise entangling operations with de- and recoupling pulses (yellow and white squares, respectively). Dashed (solid) lines denote decoupled or inactive (recoupled or active) qubits. The de- and re-coupling pulses realize coherent transfer of electronic population from the computational basis states to a pair of elctronic states, where decoupled ions do not couple to the light from lasers acting on the qubit transition (MS gate). In order to minimize errors due to cross-talk between ions, that is, undesired exposure of neighboring ions to light from the addressed beam, we use a particular 3-pulse sequence to realize one coherent π-flop on the ion of interest—see text for details and alternative schemes.

perform coherent operations on the qubit transition. A spatially wide beam illuminating the whole ion string realizes collective operations of the form

$$U(\theta,\phi) = \exp\left(-i\frac{\theta}{2}\sum_i \left[\sin(\phi)Y_i + \cos(\phi)X_i\right]\right) \tag{5}$$

and a Mølmer-Sørensen-type entangling operation [10, 63]

$$MS(\theta,\phi) = \exp\left(-i\frac{\theta}{4}\left[\sum_i \sin(\phi)Y_i + \cos(\phi)X_i\right]^2\right). \tag{6}$$

Since the angle of incidence of the global beam with respect to the ion string is approximately 22.5°, the beam is shaped elliptically to illuminate all ions equally. The beam ellipticity is about

1:5 with a beam waist of $100\,\mu m$ in horizontal direction, which leads to an inhomogeneity of the coupling strength along the 7 ion string, measured by the Rabi-frequency, of about 1%. In addition, an addressing beam perpendicular to the ion string, focused to a beam waist of about $1.5\mu m$, is used to perform single-qubit rotations $U_Z^{(i)}(\theta) = \exp(-i\frac{\theta}{2}Z_i)$ on the i-th ion. This operation, corresponding to a rotation around the Z-axis in the Bloch-sphere picture, is carried out by detuning the laser beam about 20 MHz from the qubit transition, which effectively induces an AC-Stark shift [49]. The combination of the described gate operations realizes a universal set of gate operations [52, 14]. The addressing beam is also capable of inducing resonant operations of the form $U^{(i)}(\theta,\phi) = \exp(-i\frac{\theta}{2}\{\sin(\phi)Y_i + \cos(\phi)X_i\})$.

5.3.2 Protocol for spectroscopic decoupling of ions with address-error correction

Operating on subsets of ions: Spectroscopic decoupling of ions.

With the exception of the single-ion gates performed by the addressing beam, the experimental gates act collectively on all of the ions. The following techniques can be used to realize a unitary operation on a subset of the 7 ions.

1. *Shuttling ions* out of the laser focus: This technique, which is used by other groups such as the teams around Dave Wineland or Ferdinand Schmidt-Kaler is not available in our apparatus. The splitting, shuffling and merging of ion-strings requires segmented traps [64], while we currently have a bulk 3-D Paul trap installed. On the other hand, our trap show heating rates which is orders of magnitude lower compared to segmented 3-D traps and thus, for the moment, superior performance for the experimental realization and manipulation of the logical qubit.

2. *Beam shaping techniques:* Alternatively, one could in principle shape the beams, which in our setup illuminate the entire string as homogeneously as possible, in such a way that only a subset of the ions is exposed to the laser light. Possible approaches are to use several frequencies simultaneously on an acousto-optic deflector, MEMS devices as investigated at Duke by the team around Jungsang Kim, or spatial light-modulators that are commonly used in beamers, medical experiments (for instance for optical tweezers), and more recently also in AMO experiments (for instance by Antoine Browaeys in Paris). However, all of these techniques are still in their infancy with little to no automated routines for calibration, and generally provide very little longterm-stability.

3. *Refocusing techniques:* One can resort to refocusing techniques, as originally pioneered in NMR systems [65]. Here, partially entangling *global* entangling MS gate operations are interspersed with single-qubit AC Stark shifts, which eventually lead to an effective decoupling of (subsets of) ions from the entangling dynamics of the remaining ions (see, e.g., [14] for more information). As discussed below in more detail, the central tools for encoding the logical qubit are the entangling operations $MS(\pi/2, 0)$ acting on subsets of four out of seven qubits that correspond to one of the three plaquettes of the color code. However, decoupling 3 ions from the string of 7 ions using refocusing pulses requires a large overhead in terms of (partially entangling) MS gate operations and addressed, single-ion refocusing pulses. This is in principle possible (as demonstrated by our group in [66, 67]),

however, the increased number of partially entangling MS gates would lead to a substantial fidelity decrease.

4. *Spectroscopic decoupling of ions:* Thus, in this project we pursued an alternative approach, where we decouple ions *spectroscopically* from the dynamics induced by the global MS gate operation ("hiding"). To this end, we coherently transfer and store the quantum state of qubits to be hidden (e.g., 5, 6 and 7), encoded in the states $S_{1/2}(m_j = -1/2)$ and $D_{5/2}(m_j = -1/2)$, into a subset of the remaining (metastable) Zeeman levels. The key property of this approach is that it is a coherent process as opposed to, e.g., optical pumping between Zeeman levels, which would destroy the phase coherence of the individual physical qubits.

Spectroscopic decoupling with address-error correction. The coherent spectroscopic decoupling of an ion requires between one and three π-pulses between pairs of electronic levels (see Figure 54 for the three transitions involved). One π-pulse between a pair of levels can be realized by the following approaches:

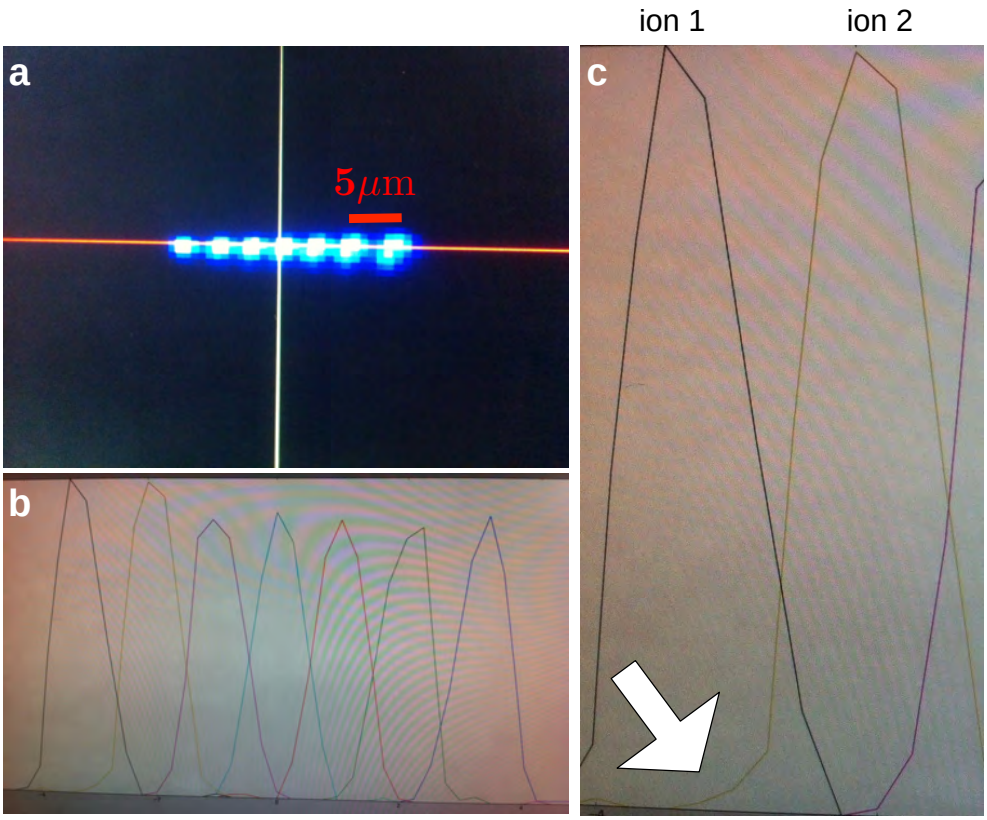

Figure 56: **(A) Fluorescence image of the 7-ion string.** (**B**) and (**C**) Spatial intensity profile of light for the addressed beam, which induces light-shift operations on individual ions. Residual light shifts on neighboring ions induce unwanted partial rotations on the neighboring ions. This effect can be largely reduced by using a composite pulse sequence for the spectroscopic decoupling and recoupling of ions. See Figure 55 and text for details.

1. *Addressed resonant laser (1 pulse)*: This population transfer could in principle also be performed by a single resonant $U^{(5)}(\pi, \theta)$ pulse. The advantage of this approach would be that it requires a minimal number of pulses, which are realized on resonance, each requiring a pulse length on the order of 20 μs. The disadvantage is that it induces the largest amount of errors on neighboring ions, due to crosstalk between the ions, as schematically shown in Figure 56. The reason is that the application of the addressed laser beam inevitably leads to small residual light intensities on the neighboring ions which should ideally be unaffected.

2. *Addressed light shift (addressed), sandwiched by two collective, global rotations (2 pulses), requiring in total 3 pulses:* Here, one realizes (i) a π-pulse on ion j by a collective $\pi/2$ rotation ($U(\pi/2, 0)$), followed by (ii) a π-light shift on the ion j that shall be decoupled ($U_Z^{(j)}(\pi)$), and finally (iii) the inverse of the first global rotation ($U(-\pi/2, 0)$). As a consequence, all ions but the j-ion ideally remain in their initial state, while the j-th ion undergoes the π-flop. The reason for splitting this up into 3 addressed pulses is to minimize errors on neighboring ions while realizing the decoupling operation on the target ion: This scheme is expected to induce less cross-talk errors on neighboring ions, as possible residual light shifts on neighboring ions in step (ii) are smaller due to the off-resonant application of this pulse. However, tests that we performed in the process of optimizing the sequence for state preparation of the logical qubit showed that this approach also led to considerable unwanted residual rotations on neighboring ions. The underlying effect is that if ions of the string that should ideally not be affected accumulate a dynamical phase shift in between the two global pulses (i) and (iii), the second global pulse (iii) will not exactly undo the effect of the first pulse (i).

3. *Addressed light shift (addressed), sandwiched by two addressed, local rotations on resonance (2 addressed spulses), requiring in total 3 addressed pulses:* The scheme essentially uses the same "sandwich" structure of three pulses as in the previous sequence, with the only difference that the first and third pulse ($\pm\pi/2$ rotations) are realized by the addressed beam. The advantage is that it minimizes the addressing-error $\epsilon = \Omega_{\text{neighbor}}/\Omega_{\text{target}}$ on the neighboring ions, which can be characterized by measuring the Rabi-frequencies of the neighboring ions and the target ion. For a seven-ion string with a minimal inter-ion distance of ≈ 3.5 μm at a trap frequency of about 1 MHz, the addressing error ϵ is about 5% on the ions located at the center of the chain. Contrary to the resonant pulse, the addressing error of the off-resonant AC-Stark pulses scale with ϵ^2, since the Rabi-frequency $\Omega^2/4\Delta$ scales quadratically with the Rabi frequency Ω for a given detuning Δ. Therefore the effectively induced error on the neighboring ions in the 3-pulse sequence also scales in leading order as ϵ^2, since errors induced by the two resonant $\pi/2$-pulses cancel out due to the phase shift of π.

   This scheme has the disadvantage that it requires a relatively large number of addressed pulses (up to 9 pulses for each de- or recoupling step), and thus increases the overall duration of the state preparation sequence. However, the advantage of minimizing addressing errors outweighed the disadvantage of longer sequences and is crucial to successfully encoding the logical qubit (see below). This is why spectroscopic decoupling (and recoupling) was realized by this last approach.

Further resource reduction in spectroscopic decoupling of ions.

Figure 54 (green subbox) shows the pulse sequence to spectroscopically decouple an ion j in an arbitrary computational state from the set of "active" ions. When the internal state of the physical state is known (e.g., during state preparation), the number of pulses can be reduced. For example, if the physical state is $|1\rangle$, then the two pulses required to decouple the (empty) $|0\rangle$ state can be omitted and so only the one pulse that coherently transfers $|1\rangle$ to the decoupled "parking" state is required. For example, the decoupling of qubits 5 and 6 (blue and red box) before the first entangling operation is realized as follows: The population of qubit 5 (initially entirely in state $S_{1/2}(m_j = -1/2)$) is transformed to the $D_{5/2}(m_j = -5/2)$ state via the composite pulse sequence of 3 coherent single-qubit operations, as described in the third scheme above: a resonant $\pi/2$-pulse $U^{(5)}(\pi/2, \theta)$ with arbitrary, but fixed phase θ on qubit 5, followed by a Z rotation $U_Z^{(5)}(\pi)$ and finally another resonant $U^{(5)}(\pi/2, \theta - \pi)$ rotation with phase $\theta - \pi$. As desired, effectively, this sequence realizes a π-flop (i.e. complete population transfer) between the computational basis state $S_{1/2}(m_j = -1/2)$ and the storage state $D_{5/2}(m_j = -5/2)$.

Similarly, spectroscopic decoupling of ions with population in the $D_{5/2}(m_j = -1/2)$ state is achieved by transfering the electronic population first to the $S_{1/2}(m_j = 1/2)$ ground state and subsequently to the $D_{5/2}(m_j = -3/2)$ state, as shown in the red box of Figure S1B. This sequence requires in total 6 single-qubit operations: $U^{(6)}(\pi/2, \theta)$, $U_Z^{(6)}(\pi)$ and $U^{(6)}(\pi/2, \theta - \pi)$ on the $D_{5/2}(m_j = -1/2) \rightarrow S_{1/2}$ transition, and a similar 3-pulse sequence on the $S_{1/2}(m_j = 1/2) \rightarrow D_{5/2}(m_j = -3/2)$ transition, respectively. Therefore, decoupling and also recoupling (REC) of one qubit with populations in (and coherences between) both computational basis states requires in total 9 single-qubit operations with a pulse length of about 10 μs per pulse.

5.3.3 Protocol for the encoding of the logical qubit

Encoding of the logical qubit.

Encoding of the logical qubit in the 7-qubit color code, requires the preparation of the 7 physical qubits in the simultaneous +1 eigenspace of the six stabilizer operators (see Eq. (4) and Fig. 53), which define the logical code space. There exist several qualitatively different protocols to achieve this goal:

1. The standard protocol (see e.g. [68]) for initial state preparation of stabilizer codes involves quantum non-demolition (QND) measurements of the stabilizer operators (or more precisely the generators of the code) via ancilla qubits. In the present case, to prepare the system in, e.g., the +1 eigenspace of the plaquette stabilizer $S_x^{(1)}$ would amount to mapping the projectors $\langle 0||0\rangle$ and $\langle 1||1\rangle$ on the ancilla qubit to $\langle 0||0\rangle(1 + S_x^1)/2$ and $\langle 1||1\rangle(1 - S_x^1)/2$ respectively, which requires a 5-qubit operation. A subsequent measurement of the ancilla projects the first four qubits onto the corresponding ± 1 eigenspace of $S_x^{(1)}$, where a correction needs to be applied if the $-$ outcome occurs. Subsequently, one needs to realize similar QND measurements of the other stabilizer operators to project the 7 qubits onto the desired code space. This state protocol by means of (many-body) QND measurements is exactly the same protocol that is also be used to realize QND measurements of the code's generators in order to deduce the error syndrome.

   Such QND-measurements of stabilizers require at least one additional physical qubit, i.e., 7+1 ions. The possibility to reliably measure in a QND manner a 4-qubit stabilizer via an ancillary qubit has been experimentally demonstrated previously in the group [66].

2. An alternative method to prepare a multi-qubit system in a combined +1 eigenspace of a set of stabilizers is by *dissipative stabilizer pumping*, which has been demonstrated in [66]. Here, the idea is to engineer dissipative multi-qubit dynamics in such a way that a system is – irrespectively of its initial state –"cooled" to a desired target state or target subspace (the code space). This approach requires at least one ancillary qubit, as well, and the typical fidelities of the dissipative processes are in practice considerably smaller than unitary quantum circuits that prepare the target states by standard unitary state preparation [66]. In this project, we therefore will not pursue this approach for the initialization of the logical qubit.

3. Unitary, deterministic state preparation: We have taken the approach to realize the initial preparation of the logical state $|0\rangle_L$ (encoding) deterministically by the quantum circuit shown. To prepare the system in the +1 eigenstate of all six stabilizers and the logical Z operators, first, the 7-ion system system is prepared in the product state $|1010101\rangle$, which satisfies the required three $\langle S_z^{(i)}\rangle = +1$ and $\langle Z_L\rangle = +1$ conditions. In three subsequent steps, plaquette-wise entangling operations are applied to also satisfy the three $\langle S_x^{(i)}\rangle = +1$ constraints. For each step, three of the seven physical qubits are spectroscopically decoupled prior to the application of the collective entangling gate. Subsequently, GHZ-like entanglement between the four qubits belonging to one plaquette of the triangular code is created with a fidelity of 88.8(5)%. The entire encoding sequence involves three collective entangling gates and on the order of 100 local single-qubit rotations, the latter resulting from the necessity to realize spectroscopic decoupling and recoupling of ions by means of composite pulse sequences, as explained above.

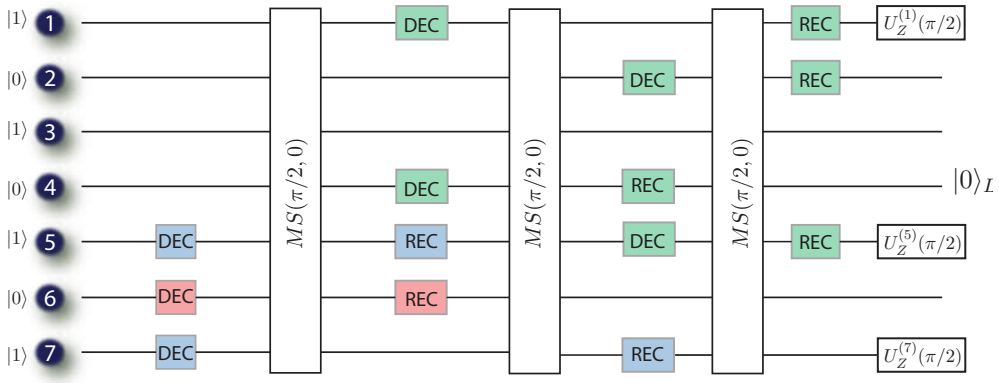

Figure 57: **Figure S1: Initialization of the logical qubit:** Circuit diagram of the encoding step, that is, the preparation of the 7-qubit system in the logical state $|0\rangle_L$. The encoding consists of three steps in which an entangling MS gate is applied to each of the three colored (red, green, blue) plaquettes consecutively in order to satisfy the $\langle S_x^{(i)}\rangle = +1$ constraints, where the 7 qubits are initially in the product state $|1010101\rangle$. We ensure that only the qubits in a particular plaquette are affected by the entangling operation by applying spectroscopic decoupling pulses (DEC) to all other qubits.

Encoding of the logical qubit: Details of the state preparation: The technique of spectroscopic decoupling described above has the advantage that the entangling operation, acting only

on the subset of 4 qubits, can be realized with a fidelity of 88.5(5)%, as determined by a 4-qubit state tomography of the created 4-qubit GHZ state, $(|0101\rangle + |1010\rangle)/\sqrt{2}$. Besides imperfections in the entangling operation, this value thus also includes the effect of small imperfections in the preparation of the initial product state $|1010\rangle$. The fidelity of the entangling operation on 4 out of 7 ions is substantially higher than the fidelity with which a 7-qubit GHZ state can be created by a global entangling operation (acting on all 7 ions). From population and parity measurements we estimate the fidelity for this 7-ion entangling operation to be about 84%.

The first step of the initialization of the 7-qubit system in the logical $|0\rangle_L$ state consists of converting the state of the 7 qubits, initialized by optical pumping in the state $|1111111\rangle$, into the state $|1010101\rangle$. This state fulfills the Z-type stabilizer constraints, as it is a +1 eigenstate of three $S_z^{(i)}$-stabilizers as well as of the logical operator Z_L. In the remaining three steps, the subsets of four qubits belonging to each of the three plaquettes of the code are sequentially entangled to also fulfill the stabilizer constraints imposed by the three operators $S_x^{(i)}$. This is achieved by spectroscopically decoupling the ions hosting inactive qubits (e.g., qubits 5, 6, and 7) not participating in the plaquette-wise entangling operation. The MS gate operation, applied to the remaining active qubits (e.g., qubits 1, 2, 3, and 4) creates the four-qubit GHZ-type entanglement. Under this operation, for instance in the first step the state $|1010101\rangle$ is mapped onto the superposition $|1010101\rangle \pm i|0101101\rangle$ (see e.g. [14]). To compensate for the $\pm\pi/2$ phase, we apply an AC Stark shift compensation pulse $U_Z^{(1)}(\pm\pi/2)$ on qubit 1 (note that this pulse can be delayed to the end since the first qubit does not participate in the entangling operations for the other plaquettes). The successful preparation of this intermediate state can be seen from the measurement of electronic populations in the $2^7 = 128$ computational basis states and the stabilizer operators, as shown in Fig. 58. Here, the data shows the two dominant expected populations, as well as the GHZ-type coherence as signaled by the non-vanishing expectation value of $S_x^{(1)}$. Similarly, the data show the appearance of the expected electronic populations and non-vanishing coherences $\langle S_x^{(2)}\rangle$ and $\langle S_x^{(3)}\rangle$ after repeating this step for the second (blue) and third (green) plaquettes respectively. After the third step and the application of the three phase compensation pulses the encoding of the system in the logical state $|0\rangle_L = |1010101\rangle + |0101101\rangle + |1100011\rangle + |0011011\rangle + |1001110\rangle + |0110110\rangle + |1111000\rangle + |0000000\rangle$ is signaled by positive (ideally +1) expectation values of all six stabilizers and the logical Z_L operator.

5.3.4 Protocol for optimized encoding of the logical qubit

In order to push up the fidelity of the preparation of the initial encoded logical state, we employed two techniques which allowed us (i) to reduce decoherence of the 7-qubit code *during* the actual sequence for state preparation (encoding), and (ii) to compensate systematic dynamical (single-ion) phase shifts that the 7-qubit accumulates during state preparation.

Dwelling in a Decoherence-Free Subspace (DFS) as long as possible. The described three-step sequence realizing plaquette-wise entangling operations to prepare the system in the state $|0\rangle_L$ works in principle by starting in any of the eight components of state $|0\rangle_L$. The advantage of choosing the initial input state $|1010101\rangle$ (instead of e.g. $|0000000\rangle$) is that for this initial state the 7-qubit state is during part of the encoding sequence in a decoherence-free subspace (DFS), in which the system is insensitive to global phase noise, as caused by magnetic field and laser fluctuations of the collective local rotations, which to leading order affect all ions in the same way.

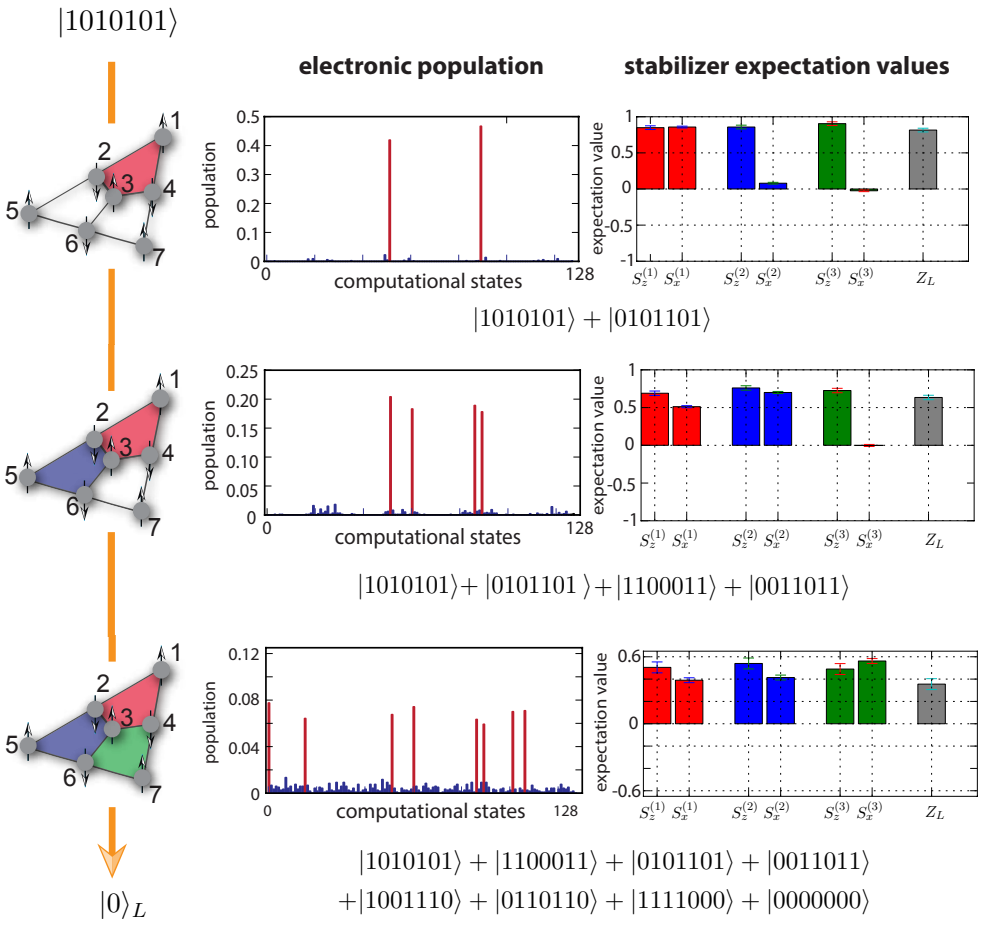

Figure 58: **Initialization of the logical qubit.** The step-wise encoding of the system in the logical state $|0\rangle_L$ is observed by measurements of the $2^7 = 128$ electronic populations in the computational basis states, as well as by the measured pattern of expectation values of the six stabilizers $\{S_z^{(1)}, S_z^{(2)}, S_z^{(3)}, S_x^{(1)}, S_x^{(2)}, S_x^{(3)}\}$ together with the logical stabilizer Z_L. The initial product state $|1010101\rangle$ is ideally a +1 eigenstate of all three $S_z^{(i)}$ stabilizers and of Z_L. **(A)** In the first step, GHZ-type entanglement is created between the four qubits belonging to the first (red) plaquette, which is signaled by the appearance of a non-vanishing, positive-valued $S_x^{(1)}$ expectation value. In the subsequent entangling steps acting on the second (blue) **(B)** and third (green) **(C)** plaquette, the system populates dominantly the expected four and eight computational basis states, and the created coherences show up in the non-zero expectation values of $S_x^{(2)}$ and $S_x^{(3)}$.

This type of noise constitutes one of the dominant noise sources in our setup [49]. Whereas the ideal quantum state after the second state (as given explicitly in Fig. S2B) still resides entirely in a DFS, the final state still benefits from partial protection with respect to the described global noise. This partial phase noise protection, in combination with the addressing-error-corrected decoupling and recoupling pulses as described above are essential to achieve the proper initialization of the system in the code space, despite the complexity and overall length of the complete encoding sequence.

A detailed analysis of the robustness properties of the state, both during the three state preparation steps (one for each plaquette of the code) as well as at the end of the state preparation, is ongoing work, with a manuscript currently in preparation. This manuscript will also contain experimental, unpublished data concerning the decay of coherences of the color code state at intermediate stages of the state preparation, and of logical (superposition) states after the state preparation.

Compensation of systematic phase shifts. The outlined DFS protection argument strictly speaking only holds if all ions reside in the computational subspace, as ions in states used for spectroscopical decoupling undergo different dephasing dynamics (e.g. due to different sensitivity to magnetic field fluctuations). In additional, even if ions stored in decoupling states do not undergo transitions, they still suffer dynamical phase shifts, in particular due to far-off-resonant coupling to other states, while the MS gate or global rotations are applied on the qubit transition. As a consequence, the intermediate states after the entangling operations on the plaquettes do not have a relative phase of +1. For example, the state after the first entangling operation, ideally ($|1010101\rangle + |0101101\rangle$) will have an unknown relative phase. Similarly, the state after the second operation which entangles the 4 qubits of the blue plaquette, will have three relative phases between its four components (see Figure 58 for the explicit expression), and the final encoded state seven relative phases between its eight components. The important observation is that these phases, though unknown, are systematic and fixed, as the preparation sequence with all its properties (duration and intensity of pulses, waiting times etc.) is essentially the same from run to run. Thus, they can be compensated for by light shift pulses on subsets of ions. The part of fluctuations in the dynamical relative phases, which varies on the short time scales from run to run, will lead to decoherence, which can (to first order) not be compensated by a set of phase shifts to the ions.

There are different strategies to compensate these systematic relative phases, so that all relative phases are equal to one, as required for the ideal target state $|0\rangle_L$:

1. The standard protocol is tracking of the phase shifts, as they build up from gate to gate (or after a certain number of gates) during the state preparation sequence, and undoing them at intermediate stages during the state preparation sequence. The relative phases can determined by Ramsey-type experiments, a technique that has been implemented in previous experiments by the experimental group of this project [69]. This technique is straightforward and a standard tool in the lab for the compensation of one relative phase (e.g. between the two components of a GHZ state). However, it quickly becomes tedious and impractical for more complex quantum states, such as the 7-qubit color code state prepared here, where up to seven relative phases have to be tracked.

2. We have thus developed and implemented in the experiment an alternative approach, which is based on the following observation: for the creation of plaquette-wise entanglement on the n-th plaquette via the MS gate, the relative phases in the state prepared in the previous $n-1$ entangling operations on the $n-1$ previous plaquettes do not matter. In other words, the application of arbitrary single-ion z-rotations commute with the entangling operation via the MS gate. Thus, one can take care of the phase compensation at the very end. We did this by an iterative approach, where we applied light shifts (varying over an interval of 2π) to one of the 7 ions. Similar to a Ramsey signal, this induces an oscillation in the expectation value of some of the stabilizer operators. We then fixed a compensation value for the AC Stark shift on this ion, such that the expectation value was maximized, irrespective of the other values. After applying this procedure about two times to all 7 ions, the 7 relative phases converge to

+1 and the stabilizer expectation assume their maximal values. Whereas this method works robustly for the 7 qubit system, we are currently investigating the scaling of this method to larger numbers of ions, as well as its robustness.

5.3.5 Protocol for quantum error detection

The realized 7-qubit code is the smallest CSS quantum error correcting code, which allows one to detect and correct an arbitrary error (bit flip, phase flip, and combinations thereof) on any of the 7 physical qubits. We investigated this property of correct identification of errors by means of the corresponding error syndrome experimentally after the encoding of the logical qubit. Here, we induced the errors at purpose. The errors are induced coherently by the corresponding Pauli operator X_i, Y_i or Z_i. The Z_i errors can be induced directly by a single AC Stark shift operation using the addressed beam (see Sec. 5.3.1), whereas the X_i and Y_i are realized by a combination of the collective local operations and single-ion Z_i operations.

Figure 59 shows a selection of three paradigmatic cases of single-qubit errors, the experimentally measured complete syndrome table (21 cases: an X, Y, or Z error on any of the 7 qubits) can be found in the supplemental material of Ref. 70. The experimental data clearly reveals the CSS character of the quantum code: Starting in $|0\rangle_L$ (Fig. 2A), single-qubit X (Z) errors manifest themselves as violations of Z-type (X-type) stabilizers only (Figs. 2B and C); the effect of single-qubit Y errors is equivalent to a combined X and Z error and is signaled by the simultaneous violation of the corresponding X and Z-type stabilizers (Fig. 2D).

For our experimental statistical uncertainties, the measured characteristic error syndromes can be perfectly assigned to the underlying induced single-qubit errors. To quantify the classification quality of the individual measured syndromes, we perform a Monte-Carlo based simulation of the measured fluorescence data. The idea is to sample the data set using a multinomial distribution and calculate for each sampled data the stabilizer pattern. For each of the simulated stabilizer patterns, the success of correctly assigning the observed error syndrome to the induced single-qubit error is quantified by calculating the classical trace distance between the sampled stabilizer distributions $S_i^{(sample)}$ and the 21 measured reference stabilizers $S_i^{(ref)}$ of Fig. 60. The trace distance D between the two classical distributions of the six stabilizer expectation values is given by

$$D = \sqrt{\sum_{i=1}^{6} \left[S_i^{(ref)} - S_i^{(sample)} \right]^2},$$

and yields $D = 0$ if the distributions are equal. The pattern of stabilizers, as generated by the Monte-Carlo method, is then associated to the reference syndrome for which the trace distance is minimal. Figure 60 shows the success rate of assigning the right error syndrome (e.g. for a Y-error on qubit 3) as a function of the number of measurement cycles n_{cycles}. The success rate is defined by the fraction of cases, in which the error syndrome has been correctly assigned to the corresponding single-qubit reference error syndrome, divided by the total number of attempts. It can be seen clearly that the success rate converges rapidly to 100% after about n_{cycles} = 20 measurement cycles. In the experimental measurements of the set of $S_x^{(i)}$ and $S_z^{(i)}$ stabilizers used for the error syndrome, we used 1000 cycles.

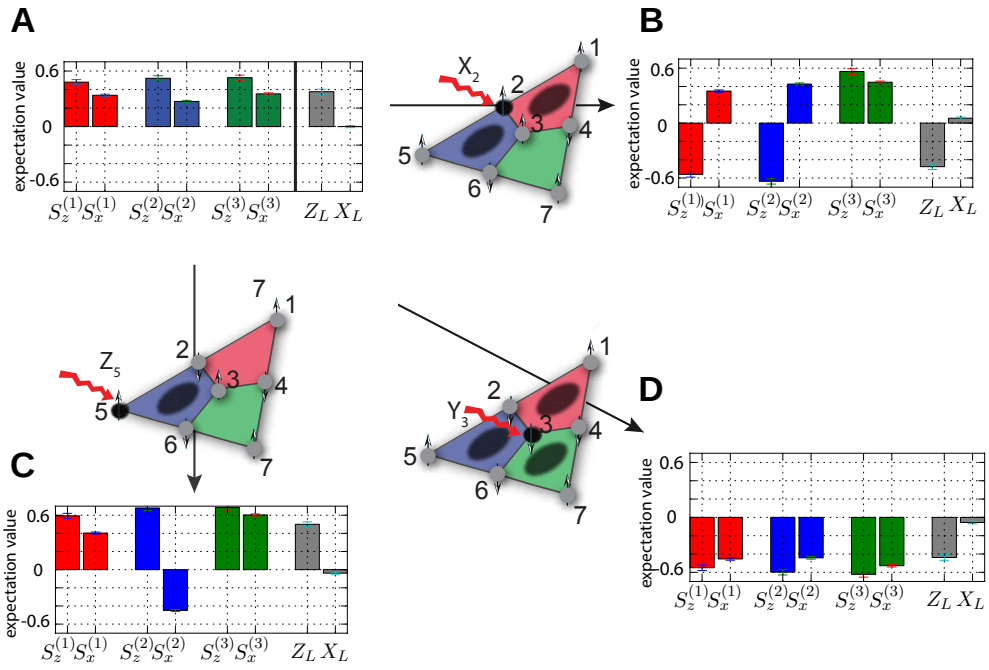

Figure 59: **Quantum error detection with the 7-qubit color code.** Shown is the effect of arbitrary single-qubit errors on the encoded logical qubit. (**A**) The initial logical state $|0\rangle_L$, prior to the occurrence of single-qubit errors, is reflected (i) by the error syndrome, in which all six $S_x^{(i)}$ and $S_z^{(i)}$ stabilizers are positive-valued, and (ii) by a positive (vanishing) expectation value of the logical operator Z_L (X_L). Single-qubit errors manifest themselves by a characteristic pattern of positive and negative stabilizer expectation values (error syndrome). (**B**) A bit flip error (red wiggled arrow) on qubit 2 affects the blue and red plaquettes (visualized by grey-shaded circles) and manifests itself by negative $S_z^{(1)}$ and $S_z^{(2)}$ expectation values and a Z_L sign flip. (**C**) A Z_5 phase flip error only affects the blue plaquette and results in a sign flip of $S_x^{(2)}$. (**D**) A Y_3 error – equivalent to a combined X_3 and Z_3 error – affects all three plaquettes and induces a sign change in all six stabilizers and Z_L.

5.3.6 Protocol for the implementation of encoded single-qubit Clifford gate operations

In topological color codes, quantum information is processed by logical gate operations acting directly within the code space [62, 71]. In contrast to Kitaev's surface code, the entire group of logical Clifford gates, generated by the elementary gate operations Z, X, the Hadamard H and the phase gate K,

$$H = \frac{1}{\sqrt{2}} \begin{pmatrix} 1 & 1 \\ 1 & -1 \end{pmatrix}, \qquad K = \begin{pmatrix} 1 & 0 \\ 0 & i \end{pmatrix}, \tag{7}$$

as well as the C-NOT gate for registers containing several logical qubits, can be realized transversally (see Figure 61) [62]. A universal set of gate operations can be obtained by this gate set by one additional non-Clifford gate. We will realize at a later stage of this project a T-gate, using 7+1 ions and the technique of magic state injection [72].

So far, we have implemented for the first time in any quantum computing experiment the entire

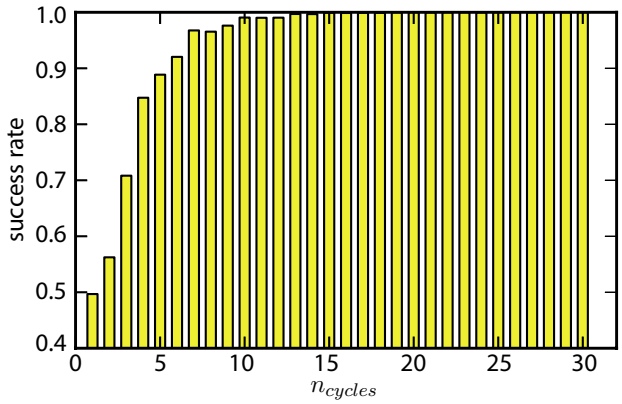

Figure 60: **Monte-Carlo simulation of the success rate to identify the right error syndrome for a given number of measurement cycles** n_{cycles}. The success rate converges rapidly towards 100% for $n_{cycles} > 20$ measurement cycles, implying that in these cases the error syndromes can be clearly distinguished and perfectly associated to the induced physical single-qubit error. The number of Monte-Carlo samples used to determine each data point is 5000.

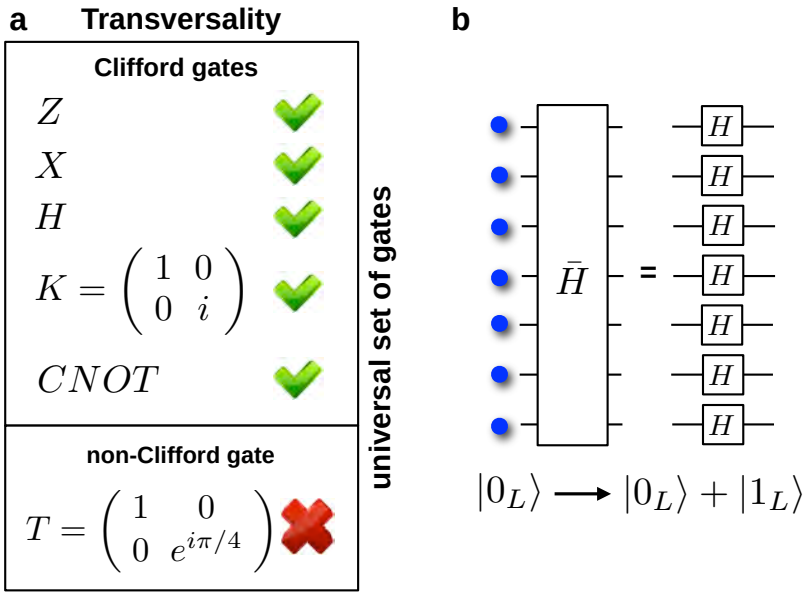

Figure 61: **Realization of logical gate operations in topological color codes. (A)** Topological 2D color codes allow one to realize the entire group of Clifford gate operations in a transversal way. A universal set of gates can be obtained by adding a non-Clifford gate, such as the T-gate to the set of Clifford gates. **(B)** Transversality amounts to a bit-wise application of the gate operations on all physical qubits, to achieve the corresponding operation on the logical level. We have implemented these operations by non-entangling global and single-ion rotations (see main text).

group of single qubit logical Clifford gates $Z_L = Z_1Z_2Z_3Z_4Z_5Z_6Z_7$,

$X_L = X_1X_2X_3X_4X_5X_6X_7$, $H_L = H_1H_2H_3H_4H_5H_6H_7$ and $K_L = K_1K_2K_3K_4K_5K_6K_7$. they commute with the six stabilizers (or generators) $S_x^{(i)}$ and $S_z^{(i)}$, i=1, 2, 3, of the code, as the logical operators share 4 physical qubits with each stabilizer operators. Thus, logical quantum states $|\psi\rangle_L$ remain within the code space under these logical operations. The logical Y_L operation is given by the sequential application of both an X_L and a Z_L operation, $Y_L = +iX_LZ_L = -Y_1Y_2Y_3Y_4Y_5Y_6Y_7$.

In the experiment, we realized these operations by a combination of single-ion and collective rotations. The logical Z_L-gate was implemented by single-ion Z rotations, $Z_L = \prod_{i=1}^{7} U_Z^{(i)}(\pi)$. The logical X_L is realized by a collective local rotation around the X-axis, $X_L = U(\pi, 0)$. We realized the logical Hadamard gate $H_L = H_1H_2H_3H_4H_5H_6H_7$ by a collective local Y rotation, followed by single-ion Z-rotations: $H_L = \prod_{i=1}^{7} U_Z^{(i)}(\pi)U(-\pi/2, \pi/2)$. Finally, we also implemented the logical phase or K_L gate in a transversal way. It is a distinguishing feature of 2D color codes (embedded in 4-8-8 lattices) that the latter codes enable a transversal implementation of the K_L gate operation [62], not requiring the technique of magic-state injection via an ancillary qubit [72] nor multi-qubit entangling operations such as, e.g. in the non-transversal 5-qubit code [8].

After initializing the logical qubit in the state $|0\rangle_L$, we prepared all six eigenstates of the logical operators X_L, Y_L and Z_L, which required quantum circuits consisting of up to three elementary logical Clifford gate operations (see Figure 62). The encoded qubit evolved as expected under the logical gate operations, as indicated by the characteristic changes in the pattern of X_L, Y_L and Z_L expectation values, and corroborated by quantum state fidelities within the code space of $\{95(2), 85(3), 87(2)\}\%$ of the experimental logical states $\{|0\rangle_L, |1\rangle_L$ and $|+_x\rangle_L = (|0\rangle_L + |1\rangle_L)/\sqrt{2}\}$ with the expected ideal states. Furthermore, the average values of the six stabilizers for each logical state are uncorrelated from the number of logical gate operations applied to prepare them (up to three). Thus, currently imperfections in the initial encoding dominate over errors induced by subsequently applied short Clifford gate sequences. This is a first indication of the high performance of the transversal logical Clifford gate operations, as compared to the encoding which involves numerous multi-qubit entangling and single-ion operations. We anticipate here that this behavior was confirmed by measured overlap with the code space of $\{34(1), 33(2), 39(2)\}\%$ for the states $\{|0\rangle_L, |1\rangle_L$ and $|+_x\rangle_L\}$.

We further explored the computational capabilities of the encoded qubit by executing a longer encoded quantum computation, which consists of up to 10 logical X_L gate operations applied to the system initially prepared in $|+_y\rangle_L$ (see Fig. 63A). Here, the logical qubit flips as expected between the Y_L eigenstates, as witnessed by alternating (vanishing) expectation values of the logical Y_L (X_L, Z_L) operator, accompanied by a moderate decay of the average stabilizer expectation values of only 3.8(5)% per logical gate operation, which is in quantitative agreement with the fidelities of our single-ion and collective local operations. More quantitatively, a weighted exponential fit of the form $A\exp(-n_{gate}/B)$, with n_{gate} the number of logical gates, into the $\langle Y_L\rangle$ expectation values yields a decay rate of the average expectation value of 3.8(5)% per gate. This decay is consistent with what we expect from the accuracy with which collective resonant π-rotations $U(\pi, 0)$ can be implemented on a string of 7 ions in our setup. A fidelity as high as about 99.6% of a single collective resonant π-rotation per ion would already lead to a fidelity loss of $\approx 3.8\%$ per gate operation. Here, two error sources dominate the measured fidelity loss per gate: (i) The relative intensity inhomogeneity of the global laser beam across the ion string ($\approx 1\%$), lowering the Rabi-frequencies at the ions located at the edge of the string; and (ii) thermal occupation of higher motional modes, which leads to decoherence of the global Rabi oscillations [49]. The application of the pulses for

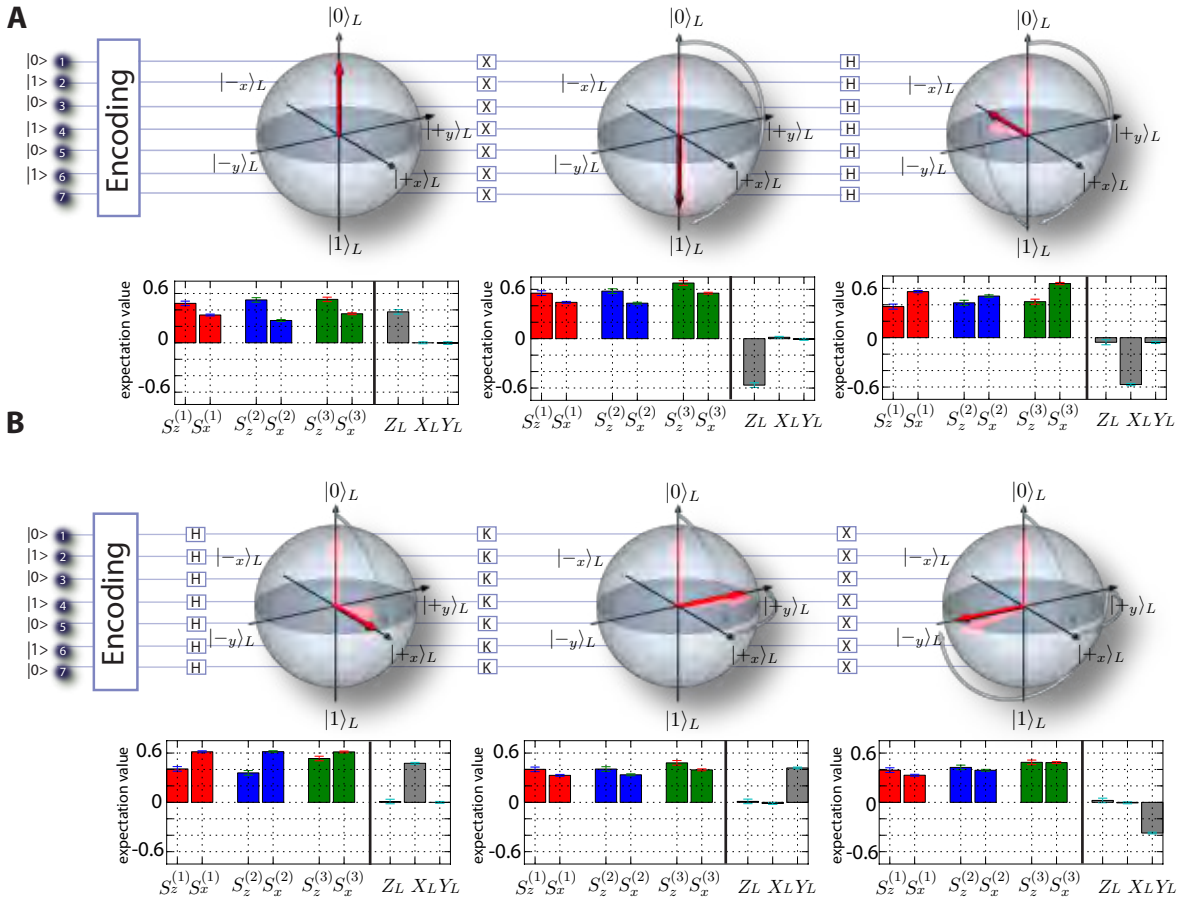

Figure 62: **Single qubit Clifford gate operations applied on a logical encoded qubit.** Starting from the logical $|0\rangle_L$ state, sequences of logical Clifford gate operations $\{X_L, H_L\}$ in **(A)** and $\{H_L, K_L, X_L\}$ in **(B)** are applied consecutively in a transversal way (i.e. bit-wise) to realize all six cardinal states $\{|0\rangle_L, |1\rangle_L, |-_x\rangle_L, |+_x\rangle_L, |+_y\rangle_L, |-_y\rangle_L\}$ of the logical space of the topologically encoded qubit. The dynamics under the applied gate operations is illustrated by rotations of the Bloch-vector (red arrow) on the logical Bloch-sphere as well as by the circuit diagram in the background. Each of the created logical states is characterized by the measured pattern of $S_x^{(i)}$ and $S_z^{(i)}$ stabilizers and the logical Bloch vector, with the three components given by the expectation values of the logical operators X_L, Y_Z and Z_L. The orientation of the logical Bloch vector changes as expected under the logical gate operations.

10 X_L gate operations is realized in a duration of 200μs. This is a factor of 18 shorter than the $1/e$ time of 3.6(6) ms on which logical coherences, as indicated by the expectation value $\langle X_L \rangle$, of the qubit initially prepared in $|+_x\rangle_L$, decay (Fig.S9)). The corresponding decay constant has been obtained by a weighted exponential fit into the $\langle X_L \rangle$ stabilizer expectation values. Thus, for the executed circuit of encoded quantum gates, imperfections in the logical Clifford gate operations dominate over the effect of the bare decoherence of the logical qubit.

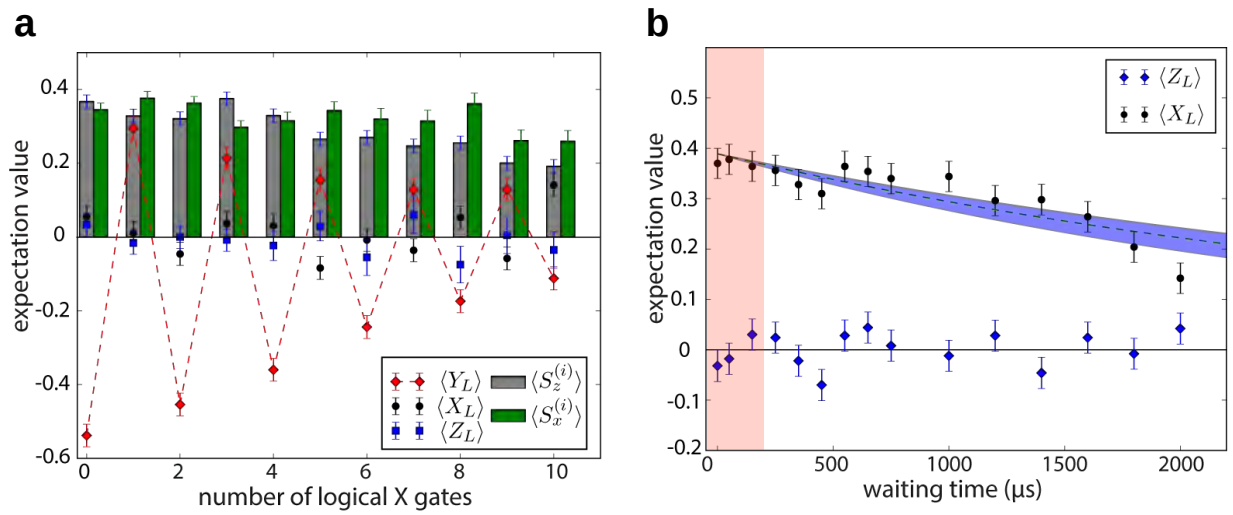

Figure 63: **Longer Clifford quantum computation on the encoded qubit: (A)** Repetitive application of logical quantum gate operations. First, we prepared the encoded $|-_y\rangle_L$ state by applying a H_L, K_L and X_L gate operation on the qubit initially prepared in the $|0\rangle_L$ state. Subsequently, flips between the logical $|+_y\rangle_L$ and $|-_y\rangle_L$ states were induced by consecutively applying logical X_L gate operations up to 10 times. The sign flip of the Y_L expectation value (red diamonds) after each step signals clearly the induced flips of the logical Bloch vector, whereas the expectation values of Z_L (blue squares) and X_L (black circles) are close to zero as expected (the average of $\{\langle Z_L\rangle, \langle X_L\rangle\}$ yields $\{0.01(1), -0.01(1)\}$). Average $S_z^{(i)}$ ($S_x^{(i)}$) stabilizer expectation values after each X_L gate are shown as grey (green) bars. **(B)** Characterization of the coherence of the logical qubit, initially prepared in the X_L eigenstate $|+_x\rangle_L$. A measurement of the decay of the X_L expectation value (black circles) as a function of time yields a $1/e$-time of 3.6(6)ms, while the Z_L expectation value (blue diamonds) remains zero as expected (on average 0.001(8)).

5.4 Fixed-point quantum search

Given an unsorted set containing N items, of which M are marked, the traditional version of Grover's quantum search algorithm [73] returns, with high probability, one of the marked items after $t^* \approx (\pi/4)\sqrt{\lambda}$ queries of an oracle function (where $\lambda = M/N$ is the density of marked items in the search space), representing a square-route speedup over the classical case. However, Grover's search is susceptible to "overcooking": after additional iterations, the success probability continues to oscillate as $p \approx \sin^2(t/\lambda)$, necessitating prior knowledge of M for a deterministic result. By contrast, the "fixed-point" Grover search algorithm [74] is immune to overcooking (while preserving the quantum speedup): the probability of measuring a marked item remains $p \geq 1 - \delta^2$ after any number of iterations $t \geq \log(2/\delta)/\sqrt{\lambda}$.

This significant result offers a unique experimental opportunity. The smallest possible demonstration of Grover's algorithm is the quantum search for a single item ($M = 1$) in a 2-qubit ($N = 4$) search space. Here, Grover's search predicts the measurement of the marked item with probability one after a single oracle call, whereas given a single classical query the success probability is 50%. The $N = 4$ quantum search has been successfully demonstrated in a variety of quantum

architectures [75, 76, 77, 78, 79] including trapped ions [80]. After a second query, however, the success probability of the traditional $N = 4$ Grover search returns to 25%, equivalent to a random guess. The fixed-point algorithm can then easily be distinguished: taking $\delta^2 = 0.1$, we find that the ultimate 90% probability of success is guaranteed after two oracle queries, still surpassing the classical success probability after two queries of 75%. A summary of the success probability of each algorithm for the four-item search after 0, 1, 2, and 3 queries is shown in Tab. 8.

Queries	*Grover*	*Fixed-point*	*Classical*
0:	25%	25%	25%
1:	100%	84%	50%
2:	25%	99%	75%
3:	25%	90%	100%

Table 8: Probability of success in returning a single marked item in a four-item search after increasing numbers of oracle queries, compared for the traditional Grover algorithm, the fixed-point algorithm, and a classical search.

To this end, we have constructed and simulated analytical pulse sequences for demonstrating the $N = 4$ fixed-point search on trapped ions. Here, the utility of our TIQC-SPICE simulation software (Sec. 4.2) was immediately apparent: in our initial iteration, our sequence seemed reasonable, but our simulations suggested fidelities too low to distinguish the search algorithms after two queries. We then reran the simulation iteratively with only a single source of error enabled, and isolated hiding and unhiding errors as the greatest contributor to our poor fidelities (we had been using hiding and unhiding pulses to simplify the pulse sequence for the Grover diffusion operator). Reconstructing a pulse sequence without intermediate hiding pulses, we re-simulated and found a minimum fidelity of 0.83 after two queries, corresponding to a 60% success probability.

5.5 Quantum modular arithmetic via Montgomery reduction and the quantum Fourier transform

A fundamental bottleneck in scaling up experimental demonstrations of Shor's algorithm has been the quantum implementation of reversible modular exponentiation via repeated modular multiplication. As described in Sec. 5.9, meaningful demonstrations of Shor's algorithm must include the reversible calculation of modular products. Though the algorithm does not presuppose a quantum speedup in implementing modular multiplication, it remains a classically challenging procedure, particularly in regards to the reversible execution of modular reduction (note that modular multiplication itself is only reversible in the case that the modulus and a multiplicand are co-prime, which happens to be the case by design in the factoring procedure).

Existing schemes for quantum products are far out of reach of the capabilities of current experimental hardware. Simplistic quantum procedures utilizing binary modular addition typically require many ancillary qubits and $\mathcal{O}(n^2)$ three-qubit gates [81, 82, 83] which tend to be particularly sensitive to decoherence and challenging to implement with elementary hardware operations. Moving arithmetic operations to quantum Fourier space eliminates the need for three-qubit gates and ancilla qubits, however requires $\mathcal{O}(n^3)$ two-qubit gates [84]. The best-case parallelized circuit

depth in these cases is $\mathcal{O}(n \log n)$ [83]. More efficient algorithms are plagued with high coefficients: for example a recent multiplier by Pavlidis and Gizopoulos requiring $9n + 2$ qubits, $800n^2$ gates achieving a linear depth of $1000n$ gates [85]. The requirements of each of these circuits is prohibitive in constructing experimental demonstrations of the factoring algorithm.

Classically, systems performing modular exponentiation under a large modulus often utilize Montgomery residue arithmetic [86, 87]. Montgomery techniques serve to simplify modular multiplication by ultimately replacing the integer division required for modular reduction with an additional conditioned multiplication, at the expense of an additional single-shot pre-calculation. Though the conditionality of the latter multiplication makes an efficient reversible variant of the procedure not immediately apparent, via a novel modification embedding the arithmetic within quantum Fourier transforms (QFTs) we have been able to devise a new circuit for modular multiplication based on Montgomery techniques achieving a circuit width of $2n + 2$ qubits, worst-case circuit size of $9n^2$ gates (with no three-qubit gates), and parallelized circuit depth of $26n$ gates; a vast improvement in complexity over existing circuits. Further, our circuit can be constructed with a minimal set algorithmic primitives (it is composed of a constant number of QFTs).

The low constants and coefficients in the characterization of our Montgomery multiplier make it directly applicable to smaller, experimentally realizable demonstrations of Shor's algorithm. It was immediately useful in constructing circuits and pulse sequences which could be used for demonstrating the quantum factoring of $N = 21$ in both a meaningful (as in the approach scales to large N) and experimentally reasonable way, and we believe it will likely be the basis of upcoming demonstrations of the factoring algorithm.

5.6 Planar ion trap computing architectures

Physical constraints and diminishing coherence ultimately impose limits on the scalability of computing in a single ion chain. The requirement of global beams and reliance on a shared motional state as a computational bus fundamentally limit the feasible size H of computational chains; in current systems, the coherence of entangling gates decreases prohibitively by around $H = 10$ ions [88]. Scalability and modularity therefore insist on systems which distribute quantum algorithms across multiple chains acting as independent quantum nodes. We consider then a "distributed linear chain" architectural extension to the linear chain model, in which n qubits are divided among W independent linear chains acting as "quantum co-processors", each containing H ions (so that $n = HW$).

As quantum algorithms necessarily involve entanglement generation across all of the involved qubits, these chains must communicate via some coherent coupling network, adding significant algorithmic and architectural overhead to the system. The primary proposed protocols for inter-chain entanglement are photonic interconnects [89] and, as described in Secs. 5.1 and 5.2, inter-chain shuttling [90]. The latter is currently significantly more efficient, with possible connection times on the order of $10\ \mu$s [57] compared to 5 to 250 ms [91] with ion-photon mapping. However, as a network architecture shuttling imposes two primary limitations: first, as qubits are passed physically, communication is limited by physical proximity (i.e. the network is limited to nearest-neighbor with dimension $d \leq 3$); second, only permutations of qubits can be performed between independent chains (i.e. no inter-chain entangling gates). In both cases, the architectural and topological consideration of this overhead will become exceedingly relevant as ion trap quantum computing systems advance. Particularly motivated by the recent successes and scalable potential of planar

CMOS ion traps [92], we have drawn from various innovations in classical computing architectures for insights into the efficient implementation of quantum algorithms in a two-dimensional distributed chain topologies.

5.6.1 Quantum Fourier transform as an algorithmic primitive

Our first insight was drawn from the design of classical processing systems. As the algorithmic overhead resulting from inter-chain entangling operations is strongly algorithm-dependent, we sought to narrow our focus to optimizing ion trap architectures to a particular set of powerful elementary algorithmic primitives as a quantum analog to a classical *instruction set architecture*, rather than the ability to efficiently perform any sequence of two- or three-qubit gates. Such primitives would ideally both be easily and regularly performed in a physical ion trap architecture and algorithmically powerful in terms of embedding important computational procedures efficiently.

Here, our quantum Fourier Montgomery product procedure motivates a larger architectural model: the quantum Fourier transform presents an ideal algorithmic primitive for larger quantum systems. In addition to its ubiquity in the formal construction of quantum algorithms, many of the complex classical logic or arithmetic operations usually relegated to "black boxes" in algorithm descriptions can be efficiently embedded within "generalized QFT" circuits (in which the interaction sequence of the QFT is maintained, but the individual rotation gates may be modified). The reversible execution of the latter computational procedures generally constitutes the bulk of the complexity in implementing quantum algorithms, as epitomized by modular multiplication in Shor's algorithm or the oracle function in Grover's.

In addition to the multiplication and modular arithmetic sequences exemplified by the Montgomery product, QFT-embeddable operations include linear-time n-controlled rotation gates [93], which form a powerful building block for general computational logic (as a particular example, the diffusion operator required by Grover's algorithm consists primarily of an n-qubit controlled-Z gate). The QFT, in turn, requires no three-qubit gates or ancillary qubits, and its $\mathcal{O}(n^2)$ two-qubit gates can be compactly parallelized into a linear-depth circuit, creating a framework for parallelizing a plethora of quantum algorithms. Further, the circuit for the parallelized QFT can be constructed recursively [94] and is highly regular, making it an ideal candidate for algorithm-dependent hardware optimization.

Within a linear ion chain, QFT-based algorithms can make significant use of the available global unitary operations. In particular, given an H-qubit linear chain, we have found analytical pulse sequence which performs up to $H-1$ unique controlled rotations sharing either a target or control qubit simultaneously with four global entangling gates (regardless of H). The H-qubit QFT can then be performed within a single chain with a total of $4H-4$ sequential entangling operations.

5.6.2 Quantum Fourier transform as a Clos network

Classically, intercommunication and shared hardware access in multi-processing systems rely on network topologies derived from switching network theory. This therefore seemed a reasonable starting point for formalizing the co-development of quantum algorithms and and ion trap architectures, and we began searching for ideal network architectures for performing the QFT.

As the QFT is composed of a controlled rotation between each possible pair of qubits, we first noticed that the particular set of interactions required by our QFT algorithmic primitive can be represented by the switching points of a classical crossbar network. Further, the signal paths within the crossbar present a particular sequence of interactions (where qubits interact and are swapped at the switch-points), so that the flat 2D form of the crossbar network can be interpreted as representing a (1D + time) nearest-neighbor QFT. The resulting sequence (shown in Fig. 64) is fully parallel, achieving linear circuit depth both in terms of interactions and swaps. However, while the linear depth of the nearest-neighbor sequence suggests that the first limitation of a shuttling architecture will not be detrimental in performing the QFT, the crossbar-QFT does require controlled-rotation operations to coincide with qubit-swaps (as is prohibited by a distributed chain shuttling architecture) and does not immediately extend to planar systems or gates with more than two qubits.

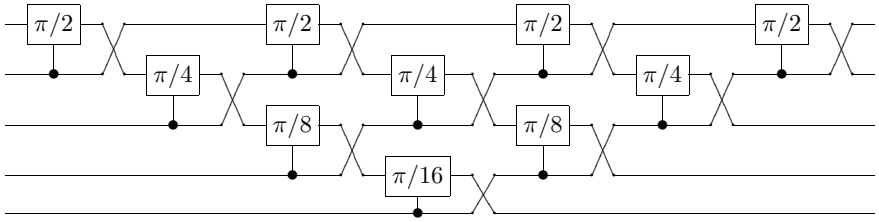

Figure 64: Quantum Fourier transform embedded in a classical crossbar network. Note that the operator only fills half of the crossbar–interaction points in the center are equivalently qubit swaps, resulting in a vertical reflection in the qubit paths (those at the top of the circuit shown).

The classical crossbar switch is the simplest example of a "nonblocking switching network", or a network which can be configured for every possible bijective mapping of input ports to output ports. It is also the most inefficient, requiring all n^2 switches to trivially connect each input to every possible output. This construction gives the network the additional property of being "fully broadcasting" (each output can be mapped to every possible *combination* of inputs). The broadcasting property of the crossbar network was essential to fully embedding the nearest-neighbor QFT, which requires that each qubit individually interact with every other qubit in the register (as represented by the network switch-points). However, the distributed chain architecture modifies this requirement in that any set of qubits sharing a chain can interact simultaneously, thereby decreasing the minimum number of gates to $\mathcal{O}(HW^2)$ (or equivalently $\mathcal{O}(n^2/H)$). Network architectures optimized for the QFT should therefore meet this decreased bound.

More efficient classical switching behavior is achieved with multi-stage networks, which require multiple successive switching layers but reduce the total number of required switching points. In particular, more efficient nonblocking switching networks can be constructed by decomposing the crossbar network into a 3-deep sequence of smaller crossbars in what is known as a *Clos network* [95]. An example of such a network is shown in Fig. 65. As is shown, Clos's insight was to show that such a decomposition preserves the original crossbar's nonblocking behavior as long as each crossbar in the middle layer is connected at least once to every crossbar of the outer two layers, and the number of crossbars in the middle layer $w \geq n/h$, where n is the total number of inputs to the network and h is maximum the number of inputs or outputs to a single crossbar in the outer layers. The Clos decomposition removes some of the redundancies that allow the broadcasting behavior of the single crossbar: at each stage, signals only enter one of the set of smaller

crossbars, and therefore only requires switches between it and other signals in that subnetwork.

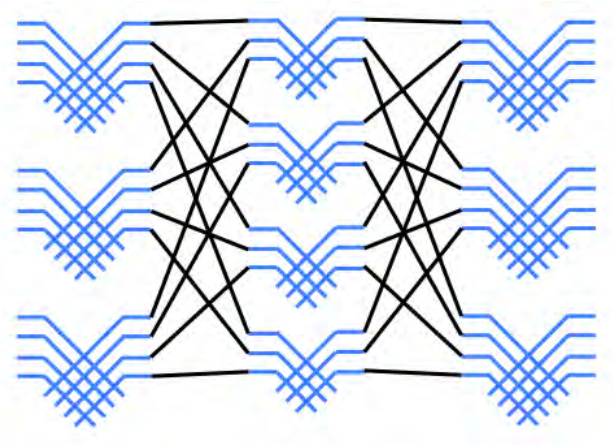

Figure 65: Classical three-stage Clos network, which decomposes a single crossbar into three sequential layers of smaller crossbar switches. Shown here, the outer crossbars have 4 inputs/outputs ($w = 4$), and so there are 4 inner layers with 3 inputs/outputs apiece ($h = 3$).

A unique feature of the Clos network is that the connections between layers of two-dimensional crossbars is naturally embedded in a third dimension by orienting sequential layers perpendicularly. In this way, the network seems like a natural extrapolation of the crossbar-QFT analogy to a planar distributed chain architecture: depending its orientation, the signal paths within a single sub-crossbar define either an interaction path within a single chain or perpendicular inter-chain shuttling sequence. Such a Clos-QFT construction turns out to be possible. Though we cannot interact qubits while they are swapped between chains, by appropriately relabeling qubits and only shuttling a subset $H_{shuttle}$ of the qubits in a given trap at a time, we can recover an identical crossbar interaction sequence. Further, it turns out that the redundancy reduction resulting from converting a crossbar network into a Clos network maps directly to the full-chain interaction points allowed by the distributed chain architecture. The resulting shuttling sequence has a total of $\mathcal{O}(n^2/H)$ and depth of $\mathcal{O}(n/H_{shuttle})$ shuttling steps, no more than the number and depth of quantum gates required to perform the QFT. If shuttling can be performed with speed and fidelity comparable to in-chain gates, we therefore find that, by assuming the QFT as our fundamental algorithmic primitive, the nearest-neighbor restrictions of a shuttling architecture are insignificant in performing quantum algorithms.

The Clos decomposition of a crossbar network is classically recursive: each smaller network can be decomposed until only 2-in-2-out crossbars remain, we arrive at a logarithmic-depth nonblocking network with $\mathcal{O}(n \log n)$ switch points. However, with each decomposition we complicate the interconnection mapping between crossbars, requiring an additional dimension to untangle the mapping into a nearest-neighbor mesh. Further, without adding $\mathcal{O}(n^2)$ ancilla qubits, the redundancy reduction of subsequent decompositions no longer maintains its analogy to a distributed chain architecture. This ultimately limits the Clos-QFT analogy; however, as we have shown, even at the single-decomposition level we arrive at a natural system for performing the QFT in a shuttling architecture without asymptotically increasing the algorithmic depth.

5.6.3 Single-instruction multiple data quantum Fourier transform

The hardware complexity necessary for parallelizing algorithms within a shuttling-based distributed-chain ion trap architecture remains prohibitive for scaling to larger systems: each unique shuttling pattern requires precise voltage waveforms to be computed and applied to many control electrodes, with the number of shuttling sites growing with the system size. Here, again, we look to classical computing architectures, particularly in terms of data parallelism. Classically, parallel computation structures are classified by Flynn's taxonomy into four primary classes [96]–single-instruction, single-data (*SISD*), single-instruction, multiple-data-stream (*SIMD*), multiple-instruction-stream, single-data-stream (*MISD*), and multiple-instruction, multiple-data-stream (*MIMD*).

Parallelizing the QFT primitive across multiple independent ion chains inherently implies performing simultaneous operations on multiple data streams (limiting our parallelization model to MIMD or SIMD). As constructed, the previously defined planar Clos-QFT (Sec. 5.6.2) is an example of MIMD–operations are both applied in parallel and unique to the particular chain, qubit, or shuttling zone. However, a SIMD shuttling protocol, in which only single global shuttling instructions are issued to the entire system, would offer a massive hardware simplification to an integrated shuttling-based TIQC system. Remarkable, it turns out that if we rearrange the initial location of the qubit register (simply implying a change of indices), we can modify the shuttling steps of the Clos-QFT such that they extend the entire system [97]. The resulting algorithm requires only two unique shuttling operations, which are alternated in order to create a combined qubit permutation which cycles through the entire QFT. Most importantly, it is identical in terms of circuit depth and number of in-chain gates, only increasing the number of individual qubit-shuttles by a constant factor of ~ 2 (as we can no longer leave certain shuttling zones out of a particular step) [97]. We have been referring to this result as the *SIMD-QFT*, and believe it will be a powerful tool in simplifying the design and construction of integrated TIQC systems (again paying particularly close attention to the potential quantum-computer-on-a-chip suggested by the development of CMOS ion traps [92]). Steps of a simple example of the SIMD-QFT, in which the number of simultaneously shuttled qubits $H_{shuttle} = 1$, is shown in Figs. 66, 67.

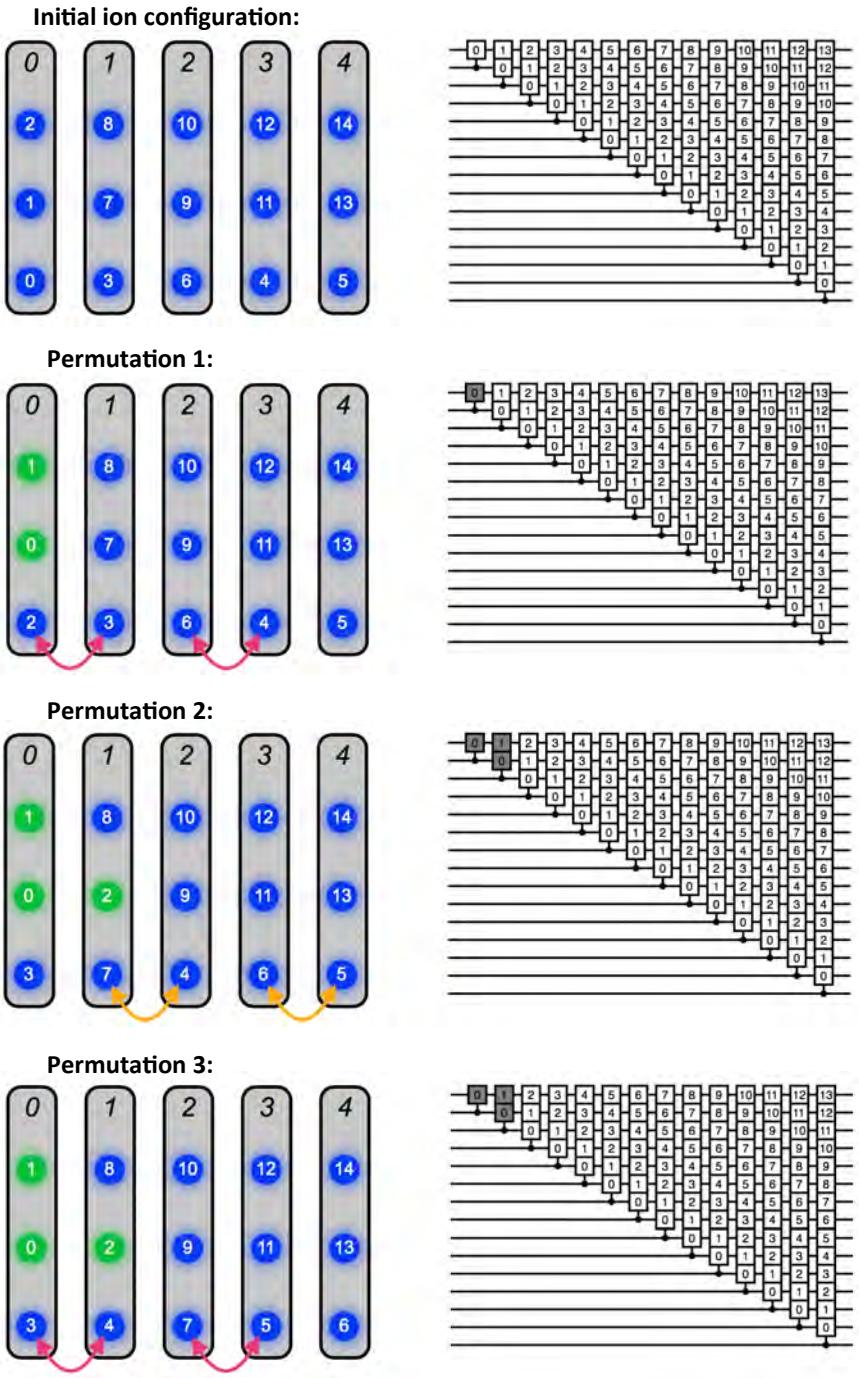

Figure 66: Steps 0-3 of a simple SIMD-QFT, in which only one ion per trap is shuttled at a time (from [97]). The two global shuttling operations are represented by the arrows connecting adjacent chains. Completed gates are greyed out in the circuit diagrams at right.

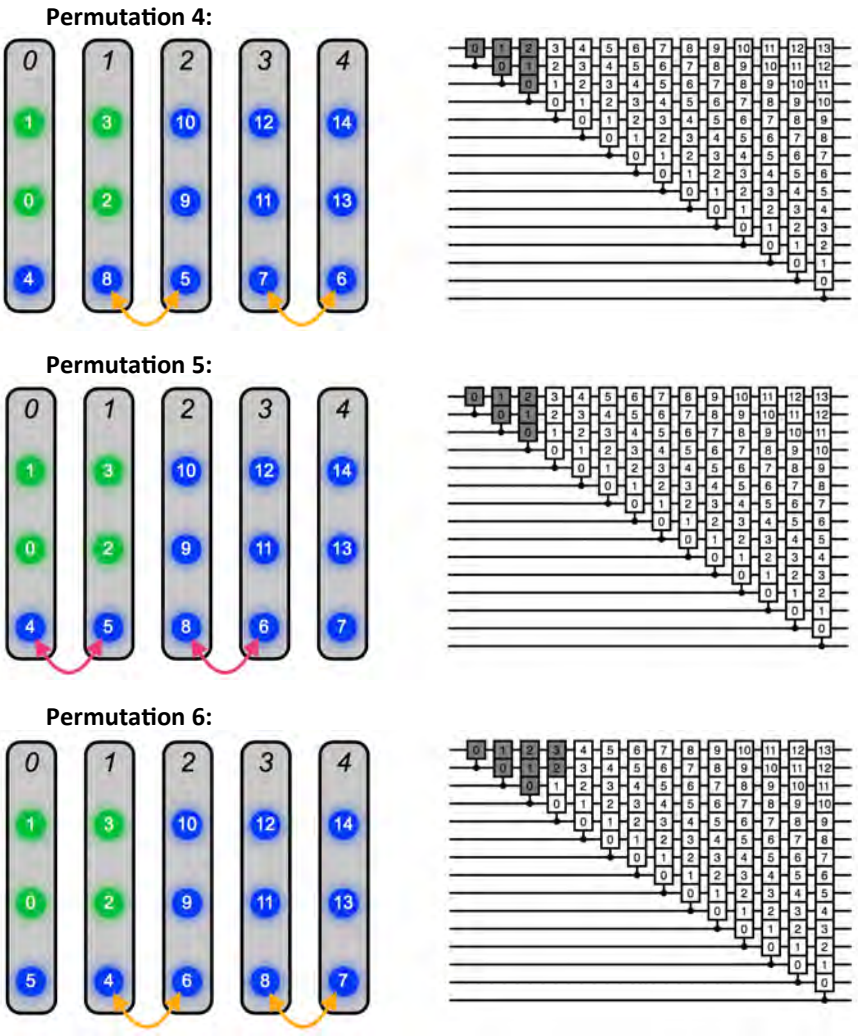

Figure 67: Steps 4-6 of a simple SIMD-QFT, in which only one ion per trap is shuttled at a time (from [97]). The two global shuttling operations are represented by the arrows connecting adjacent chains. Completed gates are greyed out in the circuit diagrams at right.

5.7 Semiclassical Quantum Fourier Transform and Kitaev's Vision

In the following we provide examples of how the available toolbox can be employed to realize various quantum algorithms where we focus on building blocks for a realization of Shors algorithm to factor a large integer numbers [98, 99]. The part of the algorithm that requires a QC is based on an order-finding algorithm which itself requires the QFT. This quantum analogue of the discrete Fourier transform maps a quantum state vector $|x\rangle = \sum_j x_j|j\rangle$, into the state $|y\rangle = \sum_k y_k|k\rangle$ where the vector $y = (y_1, ..., y_N) = F(x)$ is the classical discrete Fourier transform of $x = (x_1, ..., x_N)$ [99]. It is straightforward to translate this operation into a quantum circuit (see [99]) where an example for three qubits is shown in figure 68(a).

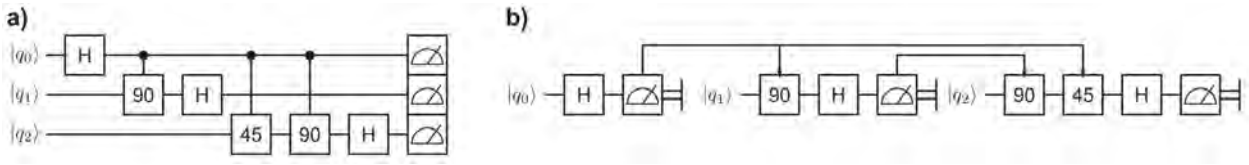

Figure 68: (a) Quantum circuit for a three qubit QFT algorithm. (b) Single-qubit Kitaev version of the QFT. The measurement outcome is stored in a classical memory which controls the subsequent single-qubit rotations.

The most straightforward (although not necessarily the most effective) way to implement the QFT is to realize directly the desired unitary using our available operations. With our optimization toolbox as described in section 4.1 we are able to find an optimized decomposition of the three-qubit QFT consisting of 18 operations. The smallest MS operation in the sequence is $\pi/16$ and thus the MS operations has to be optimized with this rotation angle. A maximally entangling operation is then implemented by applying this operation eight times subsequently. We benchmark the QFT by performing a full three-qubit quantum process tomography and find a process fidelity of 72% with the ideal QFT [100]. However, in order to find the best suited measure for the quality of an algorithm, one should consider how the quantum algorithm is embedded in the given problem. The QFT is almost exclusively used as the final building block of larger algorithms and then only the classical information of the final state is needed to determine the algorithms performance [101]. The quantum process fidelity is not the optimal measure to benchmark the performance of the QFT as it includes correlations that do not affect the outcome of the algorithm. One would rather choose a measure that utilizes the classical probabilities of the individual output states which can be described by a 2^N vector $p = (p_1, ..., p_{2^N})$. Such a measure is the squared statistical overlap (SSO) $S(p, q) = (\sum_i \sqrt{p_i q_i})^2$ which is the classical analogue of the quantum state fidelity [102]. An alternative suitable measure for the classical information is the statistical distinguishability $D(p, q) = 11/2 \sum_i |p_i - q_i|$, which is related to the quantum trace distance. These benchmarks are applied to a representative set of input states covering all possible periods. In [103], a QFT algorithm was benchmarked using five input states with different period and thus we use similar input states for comparability, as shown in table 9. The classical benchmarks yield on average an SSO of 87% which is considerably higher than the quantum process fidelity of 72%. Since the QFT is mainly used as the final block in an algorithm, it can be replaced by the semiclassical QFT that exchanges the quantum-controlled rotations by a measurement and a classically controlled rotation [101, 103]. This requires the measurement of each qubit to be performed before

Input state	Period	SSO	Distinguishability
$1/\sqrt{8}(\|111\rangle + \|110\rangle + \|000\rangle)$	1	77.1	77.1
$1/\sqrt{4}(\|110\rangle + \|100\rangle + \|010\rangle + \|000\rangle)$	2	78.0	73.3
$1/\sqrt{4}(\|110\rangle + \|100\rangle + \|011\rangle + \|000\rangle)$	3	90.4	86.4
$1/\sqrt{2}(\|011\rangle + \|000\rangle$	4	94.8	87.4
$\|000\rangle$	8	97.3	88.1

Table 9: Results for a fully coherent three qubit QFT.

Input state	Period	SSO	Distinguishability
$1/\sqrt{4}(\|000\rangle + \|100\rangle + \|010\rangle + \|111\rangle)$	2	99.5	94.5
$1/\sqrt{2}(\|100\rangle + \|000\rangle$	4	99.6	96.4
$\|000\rangle$	8	99.7	95.6

Table 10: Results for the semiclassical Kitaev single qubit QFT.

the operations that are controlled by this qubit. In figure 68 the time order of the measurements corresponds to qubit q_0, q_1, q_2 . A measurement furthermore destroys all quantum coherence on the qubit and thus it is possible to reuse the physical qubit and store the measurement outcome on a classical computer. This allows a semi-classical QFT to be performed on a single qubit as sketched in figure 68(b) which is known as the Kitaev QFT [104]. Note that it is not possible to generate an entangled input state with this version of the QFT and thus the Kitaev QFT is more restricted than the semi-classical QFT. Furthermore, the ability to measure and reset the qubit within the algorithm is required, which is possible with our extended set of operations. In ion-trap systems, in-sequence measurements notably disturb the motional state of the ion string and thus it is advisable to make the measurement as short as possible. In this case we chose a measurement duration of 150μs which still allows for a detection fidelity of 99% [105]. In order to achieve high fidelity operations after such a measurement it appears necessary to recool the COM mode with the Raman cooling technique as described in section 1. In the special case of the single-qubit QFT however only local operations are required after a measurement which can furthermore be implemented with the addressed beam. Due to the small LambDicke parameter, the quality of the single-qubit operations is not notably affected by the thermal occupation of the COM and the spectator modes after the measurements and thus recooling is not required. In table 10 the outcome for the single qubit QFT is shown for the non-entangled input states used before, leading to an average SSO of 99.6%. As expected, the single-qubit Kitaev QFT clearly performs better than the fully coherent QFT.

y	$\pi_1(y)$	$\pi_2(y)$	$\pi_3(y)$	$\pi_4(y)$
$\|0\rangle$	$\|0\rangle$	$\|1\rangle$	$\|0\rangle$	$\|3\rangle$
$\|1\rangle$	$\|3\rangle$	$\|0\rangle$	$\|3\rangle$	$\|0\rangle$
$\|2\rangle$	$\|2\rangle$	$\|3\rangle$	$\|1\rangle$	$\|1\rangle$
$\|3\rangle$	$\|1\rangle$	$\|2\rangle$	$\|2\rangle$	$\|2\rangle$
max(order)	2	2	3	4
No. of operations $\pi(y)$	11	10	23	24
No. of operations $\pi(y)^2$	-	-	17	10

Table 11: Representative unitary permutation operations for order 24 which were used as examples for the order-finding algorithm. The number of operations for applying the operation once and twice are also shown.

5.8 Implementing the Order-Finding Algorithm with Trapped Ions

One of the important algorithms that is compatible with the presented Kitaev single-qubit QFT is the order-finding algorithm which is able to determine the order of a permutation operation efficiently [18]. A permutation operation $\pi(y)$ has order k if $k-$times application of the operations results in the identity: $\pi(y)^k = y$, where y is a decimal representation of the n-qubit input state vector $|q_n ... q_0\rangle$. The algorithm splits the available quantum register in two parts: (i) a register where the permutation operation is applied and (ii) a QFT register that is initially prepared in an equal superposition state. The qubits from the QFT register control whether the permutation operations are applied. This operation is analogous to a CNOT operation where instead of the NOT operation the permutation operation is controlled. The kth qubit from the QFT register controls the permutation operations $\pi(y)^l$ with $l = 2^k$ as shown in figure 70(a).

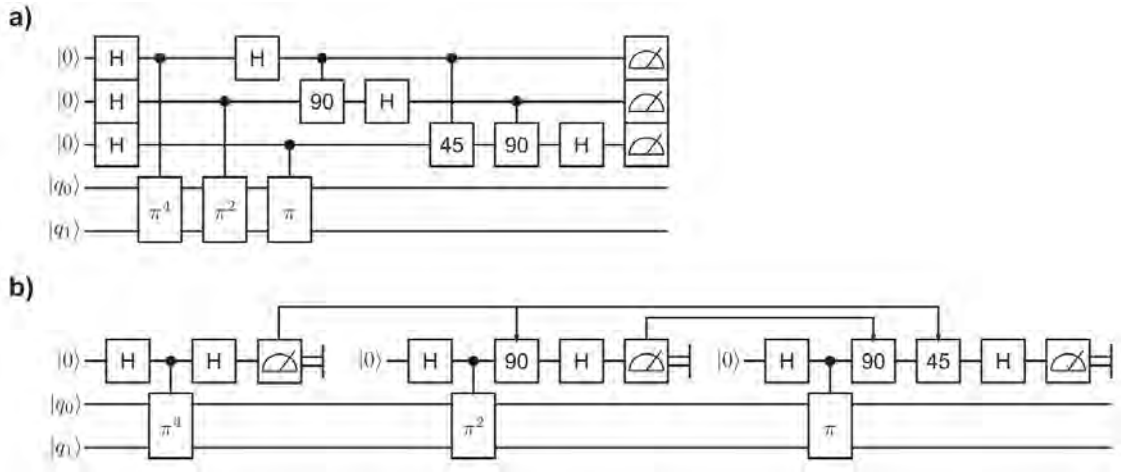

Figure 69: Order finding algorithm for a two qubit permutation operation in (a) fully coherent and (b) Kitaev version.

With this algorithm it is possible to use the single-qubit QFT to reduce the number of required qubits from 5 to 3 where the resulting quantum circuit is shown in figure 70(b). We seek to imple-

Order	Permutation operation	SSO	Distinguishability
1	$\pi_1(\|0\rangle)$	75.3(7)	75.3(7)1
2	$\pi_2(\|0\rangle)$	86.4(6)	86.5(6)
3	$\pi_3(\|1\rangle)$	85.9(6)	70.3(8)
4	$\pi_4(\|0\rangle)$	91.6(5)	90.7(6)

Table 12: Results for the semiclassical Kitaev order finding algorithm using the permutation operations defined in table 11.

ment the optimized order-finding algorithm using permutations on two qubits as a proof-of-concept experiment. The permutation operation is given by a unitary operation where we implemented the operations shown in table 11 which span orders from 2 to 4. It becomes clear that the order of the permutation can depend on the input state as, for example, $\pi_1(y)$ has order one for input states $y = |0\rangle, |2\rangle$ and order two for $y = |1\rangle, |3\rangle$. On the other hand, $\pi_2(y)$ shows order two regardless of the input state. The complexity of the algorithm depends on the investigated permutation operation, as the controlled permutation operations require entangling operations. The number of required operations for the individual permutation operations are presented in table 11 and the sequences of operations can be found in the appendix. In contrast to the single-ion QFT as presented above, the use of entangling operations after measuring the QFT qubit is required. This makes it necessary to recool the ion string within the sequence, where we employ the Raman recooling technique as described in section 2.1. We choose a recooling time of 800μs as this proved to provide a good balance between remaining excitation of the COM mode and additional phase damping due to the cooling time [105]. The output of the algorithm is again classical and thus the classical probabilities for measuring the state $|j\rangle$ are sufficient to infer the quality of the operation. Figure 20 shows the classical probabilities of the basis states for all permutation operations where the experimental results (blue bars) are compared with the expected ideal probabilities (red bars) and estimated probabilities from TIQC-SPICE simulations (green bars). Again the implementation is benchmarked with the classical SSO and distinguishability measures as presented in table 12 yielding an average SSO of 80.7%. The original problem is finding the correct permutation and therefore one could think of using a classical algorithm to find the most likely order for a given outcome.

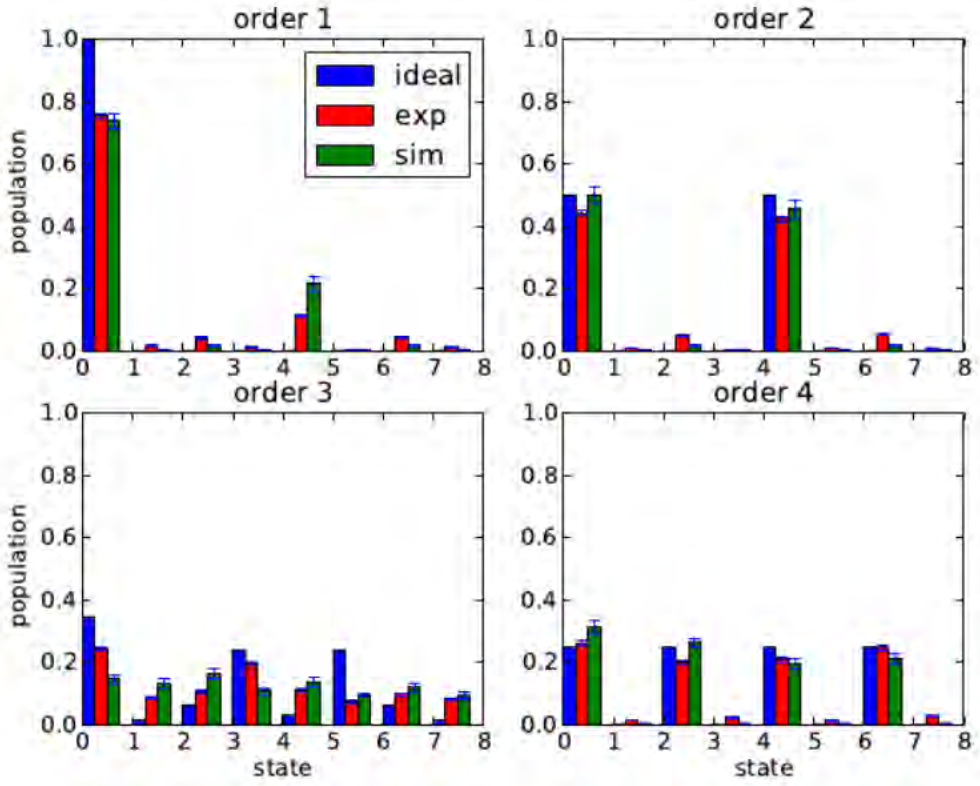

Figure 70: State probabilities for the order finding algorithm for the permutation operations $\pi_1..\pi_1$. The ideal probabilities (blue), experimental results (red) and predictions from a classical simulation (green) are shown.

5.9 Realizing Kitaev's Vision of Shor's algorithm

Shor's algorithm for factoring integers [98] is one of the examples where a quantum computer (QC) outperforms a classical computer. Experimentally its implementation is highly demanding as it requires both a sufficiently large quantum memory and high-fidelity control. Realizing Shor's algorithm [106, 104, 107, 108, 109, 110] represents proof for sufficient control of a quantum system such that it may also be used for quantum simulations or quantum-enhanced metrology, and brings us one step closer to harnessing the quantum world.

However, factorizing numbers is trivial if the factors are already known. A recent publication [111] illustrates that any realization of Shor's algorithm ought not be benchmarked by the number factorized but by the number of potential results the implementation can provide. In particular Ref. 111 shows that even an RSA-768 or N-20000 number used for cryptography can be factorized using only two qubits (and further optimized down to an unbiased coin-toss), providing that one knows the answer in advance. In the following we will present the first realization of Shor's algorithm in a potentially scalable system without relying on such prior knowledge of the factors. In particular, we run Shor's algorithm on 7 qubits using only 5 trapped ions. Here, implementing Kitaev's vision of qubit recycling reduces the memory-demand by a factor of 3 [112], while storing 2 qubits per ion facilitates the implementation. Our approach is supplemented by

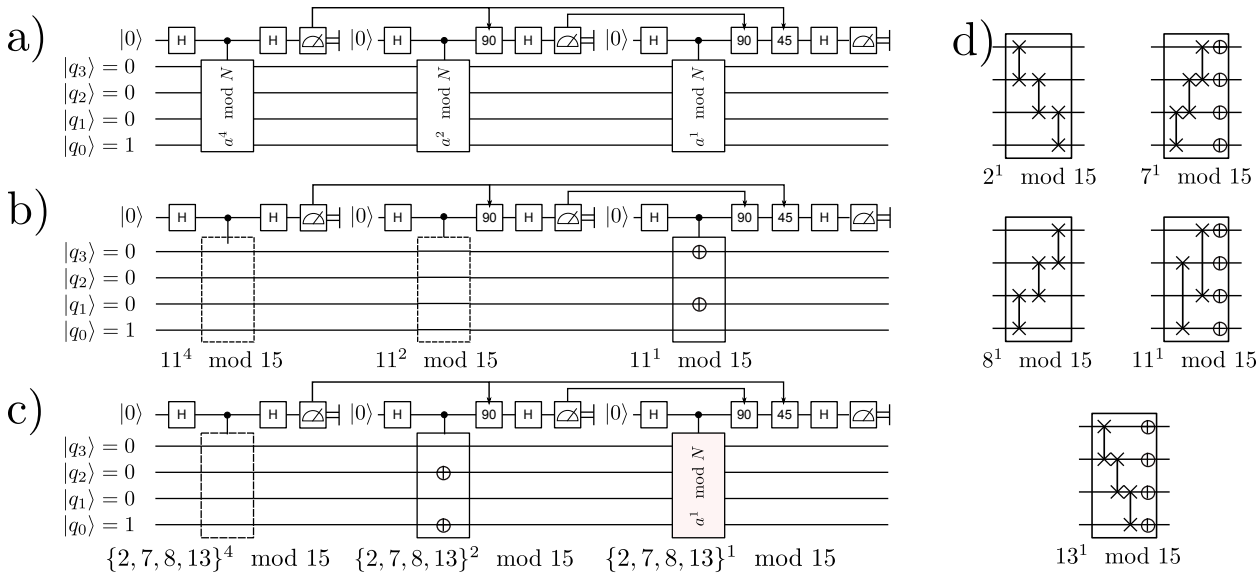

Figure 71: Circuit diagram of Shor's algorithm for factoring 15 based on Kitaev's approach for: a) a generic base a; and the specific circuit representations for the modular multipliers; b) The actual implementation for factoring 15 to base 11, optimised for the single input state it is subject to; c) Kitaev's approach to Shor's algorithm for the bases $\{2,7,8,13\}$: the optimised map of the first multiplier is identical in all 4 cases, the last multiplier is implemented with full modular multipliers as depicted in d); d) Circuit diagrams of the modular multipliers of the form $a \mod N$ for bases a=$\{2,7,8,11,13\}$.

in-sequence measurements, in-sequence recooling and feed-forward.

How does Shor's algorithm work? There is a classical recipe to find the factors of a large number. Assume the number we want to factor is $N = 15$. Pick a random number $a \in [2, N-1]$ (which we will call *base* in the following), say $a = 7$. Calculate the modular exponentiations $a^x \mod N$ for $x = 0, 1, 2...$ and find its period r: the first $x > 0$ such that $a^x \mod N = 1$. Given the period r, finding the factors requires calculating the greatest common divisor of $a^{r/2} \pm 1$ and N, which is classically efficient - for instance using Euclid's algorithm. For our example ($N = 15, a = 7$) the modular exponentiation yields 1, 7, 4, 13, 1, ..., which has period 4. The greatest common divisor of $a^{r/2} \pm 1 = 7^{4/2} \pm 1 = \{48, 50\}$ and $N = 15$ is $\{3, 5\}$, the non-trivial factors of N.

How can this recipe be implemented in a QC? A QC also has to calculate $a^x \mod N$ in a computational register for $x = 0, 1, 2...$ and then extract r. However, using the quantum Fourier-transform (QFT), this can be done with high probability in a single step (compared to r steps classically). Here, x is stored in a k qubits quantum register, or period-register, which is in a superposition of 0 to $2^k - 1$. The superposition in the period-register on its own does not provide a speedup compared to a classical computer. Measuring the period-register would collapse the state and only return a single value, say x_1, and the corresponding answer to $a^{x_1} \mod N$ in the computational register. However, if the QFT is applied to the period-register, the period of $a^x \mod N$ can be extracted with $\mathcal{O}(1)$ measurements.

What are the requirements and challenges to implement Shor's algorithm? First, we focus on

the period-register, to subsequently address modular exponentiation in the computational register. Factoring N, an $n = \lceil \log_2(N) \rceil$-bit number requires a minimum of n qubits in the computational register (to store the results of $a^x \mod N$) and generally about 2 n qubits in the period-register [99]. Thus even a seemingly simple example such as factoring 15 (an $n = 4$ -bit number), would require $3n = 12$ qubits when implemented in a very general way. These qubits then would have to be manipulated with high fidelity gates. Given current state-of-the-art control over quantum systems [113], such an approach likely yields unsatisfying performance. However, a fully quantum implementation is not really necessary. In Ref. 112 Kitaev noted that, if only the classical information of the QFT (such as the period r) is of interest, $2n$ qubits subject to a QFT can be replaced by a single qubit. This approach, however, requires in-sequence single-qubit readout, state reinitialization and feed-forward.

In the following, Kitaev's QFT will be referred to as KQFT$^{(M)}$. It replaces a QFT acting on M qubits with a semiclassical QFT acting repeatedly on a single qubit. Similar applications of Kitaev's approach to a semiclassical QFT in quantum algorithms have been investigated in Refs. 114, 115, 116. For the implementation of Shor's algorithm, Kitaev's approach provides a reduction from the previous n computational-qubits and $2n$ QFT qubits (in total $3n$ qubits) to only n computational-qubits and 1 KQFT$^{(2n)}$ qubit (in total $n + 1$ qubits).

A notably more challenging aspect than the QFT, and the second key-ingredient of Shor's algorithm, is the modular exponentiation:

(i) Considering Kitaev's approach (see Fig. 71), the input state $|1\rangle$ (in decimal representation) is subject to a conditional multiplication based on the most-significant bit k of the period register. At most there will be 2 results after this first step. The number of results for subsequent multiplications will increase exponentially with the number of steps. It follows that, for the very first step it is sufficient to implement an optimized operation that conditionally maps $|1\rangle \rightarrow |a^{2^k} \mod N\rangle$. Considering the importance of a high-fidelity multiplication (with its performance being fed-forward to all subsequent qubits), this efficient simplification improves the overall performance of experimental realizations.

(ii) With respect to all subsequent multiplications, implementing suitable maps rather than full multipliers will become exponentially more challenging, as the number of input states to be considered individually for the map optimisation grows exponentially with the number of qubits. It follows that after n steps, $2^n > N$ possible outcomes need to be considered - a numerical task as challenging as factoring N by classical means. Thus, controlled full modular multipliers need to be implemented, as we demonstrate in Fig. 72.

(iii) The very last multiplier allows one more simplification: Considering that the actual results of the modular exponentiation are not required for Shor's algorithm (as only the period encoded in the period-register is of interest), the last multiplier only has to create the correct amount of correlations between the period register and the computation register. Local operations after the conditional (entangling) operations may be discarded to facilitate the final multiplication without affecting the results of the implementation.

(iv) In rare cases, certain qubits do not partake at all in the computation. Thus, these qubits can be removed from the algorithm entirely.

The extensive application of these optimizations, often referred to as "compiled" implementations of Shor's algorithm, explain implementations of Shor's algorithm to factor 15 using only 3 qubits [107] (instead of minimally 5 qubits) or to factor 21 with only one qubit plus one qutrit [104] (instead of 6 qubits). In the following we will present the first realization of Shor's algorithm to

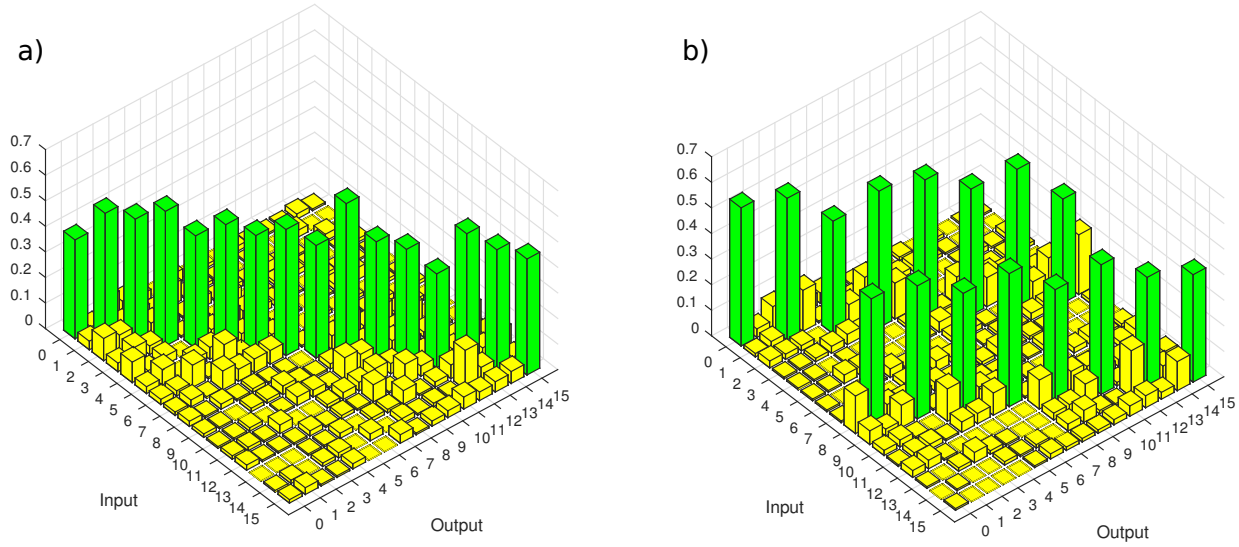

Figure 72: Experimentally obtained truthtable of the controlled 2 modular 15 multiplier: a) with the control-qubit being in state 0, the truthtable corresponds to the identity operation; b) when the control qubit triggers the multiplication, the truthtable illustrates the multiplication of the input state with 2 modular 15.

factor 15 employing the full, necessary Hilbert space of 5 qubits and implementing, for the first time, arithmetic operations in a QC, namely full modular multipliers (For the experimentally obtained truthtable of the multiplier $(2 \mod 15)$ please see Fig. 72 and supplementary material). Thus, our realization represents the first realization of a non-"compiled" Shor's algorithm. We will first explain Shor's algorithm to factor 15 (using bases a={2,7,8,11,13}) in a circuit model. Subsequently, we explain how this circuit model has been transferred to an ion-trap quantum computer, discuss the results, and address remaining questions.

Kitaev's approach requires in-sequence measurements, qubit-recycling to reset the measured qubit, feed-forward of gate settings based on previous measurement results, as well as numerous controlled quantum operations. We demonstrate all of these techniques in our realization of Shor's algorithm in an ion-trap quantum computer, with 5 $^{40}Ca^{+}$ ions in a linear Paul trap. The qubit is encoded in the ground state $S_{1/2}(m=-1/2)=|1\rangle$ and the metastable state $D_{5/2}(m=-1/2)=|0\rangle$. The universal set of quantum gates consists of the entangling Mølmer-Sørenson interaction [117], collective operations of the form $\exp(-i\frac{\theta}{2}S_\phi)$ with $S_\phi=\sum_i \sigma_\phi^{(i)}$, $\sigma_\phi^{(i)}=\cos(\phi)\sigma_x^{(i)}+\sin(\phi)\sigma_y^{(i)}$, $\sigma_{\{x,y\}}^{(i)}$ the Pauli operators of qubit i, $\theta=\Omega t$ determined by the Rabi frequency Ω and laser pulse duration t, ϕ determined by the relative phase between qubit and laser, and single qubit phase rotations induced by localized AC-Stark shifts (for more details please see the supplementary material and Ref. 118). An adaptation of the GRAPE algorithm [119] takes the unitary operations illustrated in Fig. 71 and derives a sequence of laser pulses equivalent to the desired quantum computation. This numerically demanding task can be simplified if the substituting operations (two-target C-NOT and C-SWAP operations) are optimized on their respective 3 qubits only and not on the entire 5 qubits. The problem with this approach is that the resulting sequence generally includes operations acting on all qubits. Implementing the optimized 3-qubit operations on a 5-ion string therefore requires decoupling of the remaining qubits from the computation space. We spectro-

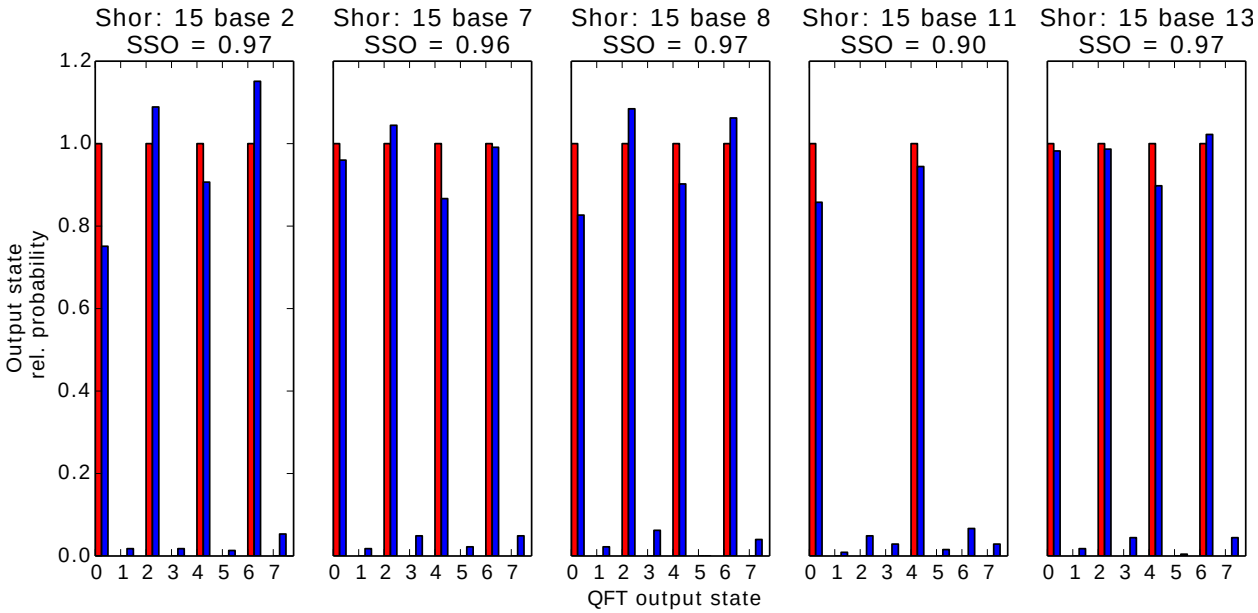

Figure 73: Results and correct order-asign probability for the different implementations to factor 15: a) 3-digit results (in decimal representation) of Shor's algorithm for the different bases. The ideal data (red) for periodicity $\{2, 4\}$ is superimposed on the raw data (blue). The squared statistical overlap is larger than 90% for all cases.

scopically decouple qubits by transferring any information from $|S\rangle \rightarrow |D'\rangle = D_{5/2}(m = -5/2)$ and $|D\rangle \rightarrow |S'\rangle = S_{1/2}(m = 1/2)$. Here, the subspace $\{|S'\rangle, |D'\rangle$ serves as a readily available quantum cache to store and retrieve quantum information in order to facilitate quantum computations. Finally, to complete the toolbox necessary for a Kitaev's approach to Shor's algorithm, we also implement single qubit readout (by encoding all other qubits in the $\{|D\rangle, |D'\rangle\}$ subspace and subsequent electron shelving [120] on the $S_{1/2} \leftrightarrow P_{1/2}$ transition), feed-forward (by storing counts detected during the single-qubit readout [121] in a classical register and subsequent conditional laser pulses) and state-reinitialization (using optical pumping for the ion, and Raman-cooling [30, 122] for the motional state of the ion string). The pulse sequences and additional information on the implementation on the modular multipliers are available as supplementary material.

The key differences of our implementation with respect to previous realizations of Shor's algorithm are: a) the entire quantum register is employed, without sparing qubits that don't partake in the calculation; b) besides the trivial first multiplication, full modular multipliers have been realized and applied; and c) Kitaev's originally proposed scheme was implemented with complete qubit recycling – doing both readout and reinitialization on the very same physical qubit. This is especially important for factoring 15 with base {2,7,8,13}, as at least two steps are required for the semiclassical QFT. In our realization we go beyond the minimal implementation of Shor's algorithm and not only employ all 5 qubits (plus additional storage qubits), but also include multiplication with up to the fourth power (although they correspond to the identity operation). This represents a more realistic attempt at a scalable implementation of Shor's algorithm as the entire qubit register remains subject to decoherence processes along the computation.

The measurement results for base {2,7,8,11,13} with periodicities {4,4,4,2,4} are shown in

Fig. 73. In order to quantify the performance of the implementation, previous realizations mainly focused on the squared statistical overlap (SSO) [103], the classical equivalent to the Uhlmann fidelity. While we achieved an SSO of {0.968(1), 0.964(1), 0.966(1), 0.901(1), 0.972(1)} for the case of a={2,7,8,11,13}, we argue that this does not answer the question of a user in front of the quantum computer "What is the periodicity?" Shor's algorithm allows one to deduce the periodicity with high probability from a single-shot measurement. The output state x of the QFT on k qubits suggests that the denominator of the term $\frac{x}{2^k}$ (after reduction) is the sought-after periodicity. For the realised examples, the probabilistic nature of Shor's algorithm becomes clear: the output state 0 never yields any information. For periodicity 4 (and 3 qubits in the period-register), the output state 4 suggests a fraction $\frac{4}{2^3} = \frac{1}{2}$, thus a periodicity of 2 and also fails. For peridocity 4, only the output states 2 and 6 allow to deduce the correct periodicity. In our realisations to base $\{2, 7, 8, 11, 13\}$, the probabilities to obtain output states that allow to deduce the correct periodicity are $\{56(2), 51(2), 54(2), 47(2), 50(2)\}\%$. Thus, a confidence that the correct periodicity is obtained at a level of more that 99%, requires to run the experiment about 8 times.

In summary, we have presented the first realization of Kitaev's vision to realize Shor's algorithm with 3-digit resolution to factor 15 using bases {2,7,8,11,13}. Here, a semiclassical QFT combined with single-qubit readout, feed-forward and qubit recycling was successfully employed. Compared to the traditional algorithm, the required number of qubits can thus be reduced by almost a factor of 3. Furthermore, the entire quantum register has been subject to the computation in a "black-box" fashion without classical precompilations. Employing the equivalent of a quantum cache by spectroscopic decoupling significantly facilitated the derivation of the necessary pulse sequences to achieve high-fidelity results. In the future, spectroscopic decoupling might be replaced by physically moving the qubits from the computational zone using segmented traps [64]. The obtained SSO was {0.968(1), 0.964(1), 0.966(1), 0.901(1), 0.972(1)} for bases {2,7,8,11,13}. Using single-shot evaluation, after only 8 measurements the correct periodicity can be found at a confidence of better than 99%.

Our investigations also reveal some open questions and problems for current and upcoming realizations of Shor's algorithm, which also apply to several other large-scale quantum algorithms of interest: While fault-tolerant quantum computation [123] is theoretically possible with sufficient register size and control, intermediate techniques and solutions for medium-sized quantum computers and quantum control are still missing. Another challenging aspect for scaling up the implementation of Shor's algorithm experimentally is finding system-specific implementations of suitable pulse sequences to realize the modular exponentiation operation. The presented operations were constructed from classical circuits, while the unitary operations and pulse sequences were obtained by the computationally demanding GRAPE algorithm which is infeasible for larger systems. A general and efficient recipe for decomposing the operations into standard unitary operators and then into pulse sequences is still work in progress. One possible approach would be to start from the smallest unit, a modular adder, from which a modular multiplicator can be built, which then serves as building block for modular exponentiation. How this will be done efficiently, including system-specific optimizations remains an open question.

6 Summary

This report provides a detailed overview about technological developments with respect to ion-trap based technologies, system integration, new algorithmic designs as well as implementation of quantum algorithms within the SQIP consortium. As such, all points of the phase 3 test-plan have been addressed:

1. Read-out of individual ions within an ion-string has been demonstrated with fidelities better than 99% (with respect to the distinguishability of the respective Poisson distributions of the count rates) during various algorithms.

2. Given the fidelity of hiding better than 99%, no detrimental effect of in-sequence readout can be obtained (see, for instance, Fig. 74).

3. T_1 has been repetitively checked, both for individual ions as well as ion-strings, and was confirmed to be in agreement with the literature values.

4. T_2 times vary between about 30 ms to 100 ms, depending on minor additional noise sources in the lab. However, the coherence of multi-qubit states may notably differ from these number, depending on their overlap with either a decoherence-free subspace on the GHZ state.

5. Simultaneous application of local operations on ion-strings is routinely performed using the global beam, as described in Sec. 2.1.2.

6. Using variations of the Estebanizer, parallel application of both entangling as well as local operations using refocusing techniques have been demonstrated within the framework of the topological qubit implementation [70] and the realizations of Shor's algorithm.

7. The employed techniques are described through this report.

8. A single-qubit gate, while initializing neighboring qubits, was a standard-procedure both during the realization of repetitive quantum error correction [18] as well as the Shor algorithm.

9. During these operations, we implemented addressed gate operations on single ions within the complete string - as required for universal quantum computation.

10. In similar terms, the realization of Shor's required us to perform two-qubit (actually, three-qubit) operations while initializing one neighboring qubit.

11. Finally, these multi-qubit operations were dependent on the superposition of neighboring qubits, whose coherence had to be maintained during the operations.

12. UMZ successfully demonstrated the splitting of entangled ions up to 5 mm apart - three-orders of magnitude wider separated than during usual ion-trap experiments.

13. All of the above experiments have been accompanied with characterization measurements, determining that, still, magnetic field fluctuations and the residual linewidth on the quadrupole

laser represent the main, incoherent limitations for quantum-information processing experiments. Here, the changes in the SS phase 3 setup provide an interesting solution to overcome magnetic field fluctuations. The final limitation, the laser operating the resonant transition, could be overcome by Raman-gates implemented on the ground-state.

14. In total, we find that the overall performance can be well predicted from the multiplication of the performance of the individual components, as we demonstrate upon investigating the performance of the different modular multipliers of Shor's algorithm. As such, the system, despite dominant correlated dephasing, seems to be recently well described (for sufficiently complex algorithms) by a depolarizing noise channel.

15. The above statement illustrates that, while we can verify correlated dephasing on small scales, the overall performance of the system (unsurprisingly) can be well mimicked by depolarizing noise. However, whether than depolarizing noise is macro- or microscopic (here, with similar or individual strength levels), can not be reliably distinguished yet.

16. Our implementations are all referenced to the GPS signal, generally with several gate operations acting in parallel (via global interactions and refocusing) on the entire register.

17. With respect to various algorithms, the system capabilities described in this report have resulted in the realization of the Order-finding algorithm [124], Shor's algorithm, repetitive quantum error-correction [18], measurement-reversal [105], paired with various procedures to characterize the system.

18. In total, the provided research results in the statement that all tasks with respect to the phase 3 test plan have been successfully addressed.

7 List of Publications

1. N. Dandiilidis et al., "Fabrication and heating rate study of microscopic surface electrode ion traps", New J. Phys. 13, 013032 (2011)

2. G. Huber et al., "A trapped ion local field probe", Appl. Phys. B 100, 725 (2010)

3. S. Wang et al., "Superconducting microfabricated ion traps", Appl. Phys. Lett. 97, 244102 (2010)

4. P. F. Herskind et al., "Microfabricated Surface Trap for Scalable Ion-Photon Interfaces", in Quantum Electronics and Laser Science Conference, OSA Technical Digest (2011)

5. T. Karin et al., "Transport of charged particles by adjusting rf voltage amplitudes", Applied Physics B: Lasers and Optics 106, 117 (2011)

6. T. Kim et al., "Surface-electrode ion trap with integrated light source", Appl. Phys. Lett. 98, 214103 (2011)

7. A. Walther et al., "Precision measurements in ion traps using slowly moving standing waves", Applied Physics B: Lasers and Optics 107, 1061 (2012)

8. T. Monz et al., "14-Qubit Entanglement: Creation and Coherence", Phys. Rev. Lett. 106, 130506 (2011)

9. P Schindler et al., "Experimental Repetitive Quantum Error Correction", Science 332, 1059 (2011)

10. P. F. Herskind et al., "Microfabricated surface ion trap on a high-finesse optical mirror", Optics Letters 36, 3045 (2011)

11. G. H. Low et al., "Finite geometry models of electric field noise form patch potentials in ion traps", Phys. Rev. A, 84, 053425 (2011)

12. S. Wang et al., "Laser-induced charging of microfabricated ion traps", J. of App. Phys. 110, 104901 (2011)

13. U.G. Poschinger et al., "Interaction of a Laser with a Qubit in Thermal Motion and its Application to Robust and Efficient Readout", Applied Physics B: Lasers and Optics 107, 1159 (2012)

14. A. M. Eltony et al., "Transparent ion trap with integrated photodetector", Appl. Phys. Lett. 102, 054106 (2013)

15. D. Nigg et al., "Experimental characterization of quantum dynamics through many-body interactions", Phys. Rev. Lett 110, 060403 (2013)

16. A. Walther et al., "Controlling Fast Transport of Cold Trapped Ions", Phys. Rev. Lett, 109, 080501 (2012)

17. P. Schindler et al., “Undoing a quantum measurement”, Phys. Rev. Lett 110, 070403 (2013)

18. T. Moroder et al., “Certifying Systematic Errors in Quantum Experiments”, Phys. Rev. Lett. 110, 180401 (2013)

19. D. Nigg et al., “Can different quantum state vectors correspond to the same physical state? An experimental test”, arxiv 1211.0942 (2012)

20. P. Schindler et al., “Quantum simulation of open-system dynamical maps with trapped ions”, Nature Physics 9, 361 (2013)

21. A. Stute et al., “Tunable ion-photon entanglement in an optical cavity”, Nature 485, 482 (2012) [This does not cite IARPA, was it done under MQCO? This is a mistake in the acknowledgements on our side. Philipp and I are not designated members of the CQED team, yet we helped them with the tomography and its evaluation. As such, we only noticed too late that IARPA was not credited in the (standard) acknowledgements statement of the CQED team.]

22. J. T. Barreiro et al., “Experimental multiparticle entanglement dynamics induced by decoherence”, Nature Physics 6, 943 (2010)

23. J. Welzel et al., “Designing spin-spin interactions with one and two dimensional ion crystals in planar micro traps”, The European Physical Journal D 65, 285 (2011)

24. A. Walther et al., “Single ion as a shot-noise-limited magnetic-field gradient probe”, Phys. Rev. A 83, 062329 (2011)

25. N. Daniilidis et al., “Quantum information processing with trapped electrons and superconducting electronics”, New J. Phys 15, 073017 (2013)

26. N. Daniilidis et al., “Probing surface electric field noise with a single ion”, Phys. Rev. B 89, 245435 (2014)

27. P. Schindler et al., “A quantum information processor with trapped ions”, New J. Phys. 15, 123012 (2013)

28. J. T. Barreiro et al., “Demonstration of genuine multipartite entanglement with device-independent witnesses”, Nature Physics 9, 559-562 (2013)

29. H. A. Fürst et al., “Controlling the transport of an ion: Classical and quantum mechanical solutions”, New J. Phys. 16, 075007 (2014)

30. F. Ziesel et al., “Experimental creation and analysis of displaced number states”, Journal of Physics B 46, 104008 (2013); appearing in special issue ”The 20th anniversary of quantum state engineering”

31. J. S. Pedernales et al., “Entanglement Measures in Ion-Trap Quantum Simulators without Full Tomography”, Phys. Rev. A 90, 012327 (2014)

32. D. Nigg et al., “Experimental Quantum Computations on a Topologically Encoded Qubit”, Science 18 vol. 345 no. 6194, 302–305 (2014)

33. H. Kaufmann et al., “Dynamics and control of fast ion crystal splitting in segmented Paul traps”, New J. Phys. 16, 073012 (2014)

34. Xiao-Jing Lu et al., “Fast shuttling of a trapped ion in the presence of noise”, Phys. Rev. A 89, 063414 (2014)

35. T. Ruster et al., “Experimental realization of fast ion separation in segmented Paul traps”, Phys. Rev. A 90, 033410 (2014)

36. A. Eltony et al., “Technologies for trapped-ion quantum information systems”, arXiv:1502.05739

37. P. Schindler et al., “Polarization of electric field noise near metallic surfaces”, Phys. Rev. A 92, 013414 (2015)

8 Supplementary Material: Kitaev's approach to Shor's algorithm

8.1 Pulse sequences

In the following, the pulse sequences employed in the experiment will be discussed in more detail. The nomenclature is as follows: The collective operations on the $S_{1/2}(m=-1/2) \leftrightarrow D_{5/2}(m=-1/2)$ transitions, addressing all ion-qubits, realize the unitary operation

$$R(\theta,\phi) = \exp(-i\frac{\pi}{2}\theta S_\phi)$$

with the collective spin operator

$$S_\phi = \sum_i \sigma_\phi^{(i)} = \sum_i \cos(\phi\pi)\sigma_x^{(i)} + \sin(\phi\pi)\sigma_y^{(i)}$$

based on the Pauli operators $\sigma_{\{x,y,z\}}^{(i)}$ acting on qubit qubit i. Here, the rotation angle θ is defined by $\theta = \frac{\Omega t}{\pi}$ with the Rabi frequency Ω and the laser pulse duration t. In this notation, a bit flip around σ_x corresponds to $R(1,0)$. The collective operations are supplemented by single-qubit phase shifts of the form

$$S_z(\theta,i) = \exp(-i\frac{\theta\pi}{2}\sigma_z^{(i)}).$$

The phase shift is realized by illuminating a single qubit with a tightly focused laser beam detuned -20 MHz from the carrier transition. Here, the induced AC-Stark shift Δ_{AC} implements the desired phase shift, with the rotation angle $\theta = \frac{\Delta_{AC}t}{\pi}$ depending on the pulse duration t. In combination, collective operations and single-qubit phase shifts allow to implement arbitrary local operations. A universal set of quantum gates, capable of implementing any desired unitary operation, can be realized by combining these arbitrary local operations with an entangling interaction. In our experiment, we employ the Mølmer-Sørenson (MS) interaction [117] to realize entangling operations of the form

$$MS(\theta) = \exp(-i\frac{\pi}{4}\theta S_x^2)$$

with $S_x = \sum \sigma_x^{(i)}$. Using this notation, the maximally entangling $MS(\frac{1}{2})$ operation applied onto the N-qubit state $|0\ldots0\rangle$ directly creates the N-qubit GHZ state.

8.2 Single-qubit measurement

Electron-shelving [120] on the $S_{1/2} \leftrightarrow P_{1/2}$ transition addresses, and thus projects, all qubits of the quantum register. For Kitaev's implementation, however, only one qubit ought to be measured. With collective illumination, this can nevertheless be achieved by transfering quantum information encoded in qubits that should not be measured into the D-state manifold. Here, the quantum information is protected against shelving light on the $S_{1/2} \leftrightarrow P_{1/2}$ transition - the ion will not scatter any photons. Using light resonant with the $S_{1/2}(m=-1/2) \leftrightarrow D_{5/2}(m=-5/2)$ transition (denoted by $R_2(\theta,\phi)$), a refocusing sequence of the form $R_2(0.5,0)\cdot S_z(1,i)\cdot R_2(0.5,0)$ efficiently encodes all but qubit i in $D_{5/2}(m=-1/2)$ and $D_{5/2}(m=-5/2)$. Subsequently, the entire quantum register may be subject to shelving light, yet only qubit i will be projected.

8.3 In-sequence detection and feed-forward

When all qubits that need to be protected against projection have been encoded in the $\{D_{5/2}(m = -1/2), D_{5/2}(m = -5/2)\}$ manifold, light at 397 nm resonant with the $S_{1/2} \leftrightarrow P_{1/2}$ transition state-dependently scatters photons an the remaining ion-qubits. The illumination time is set to 300 μs. A histogram of the photon counts detected at the photomultiplier tube is shown in Fig. 74. Using counter electronics with discriminator set at 4 counts within the detection window, the state D with a mean count rate of 0.24 counts/ms (or 0.07 counts within the detection window) and state S with a mean countrate of 48 counts/ms (or 14.4 counts in the detection window) can be distinguished with a confidence better than 99.8%. The boolean output of the discriminator is subsequently used in the electronics for state-dependent pulses and thus state-dependent operations.

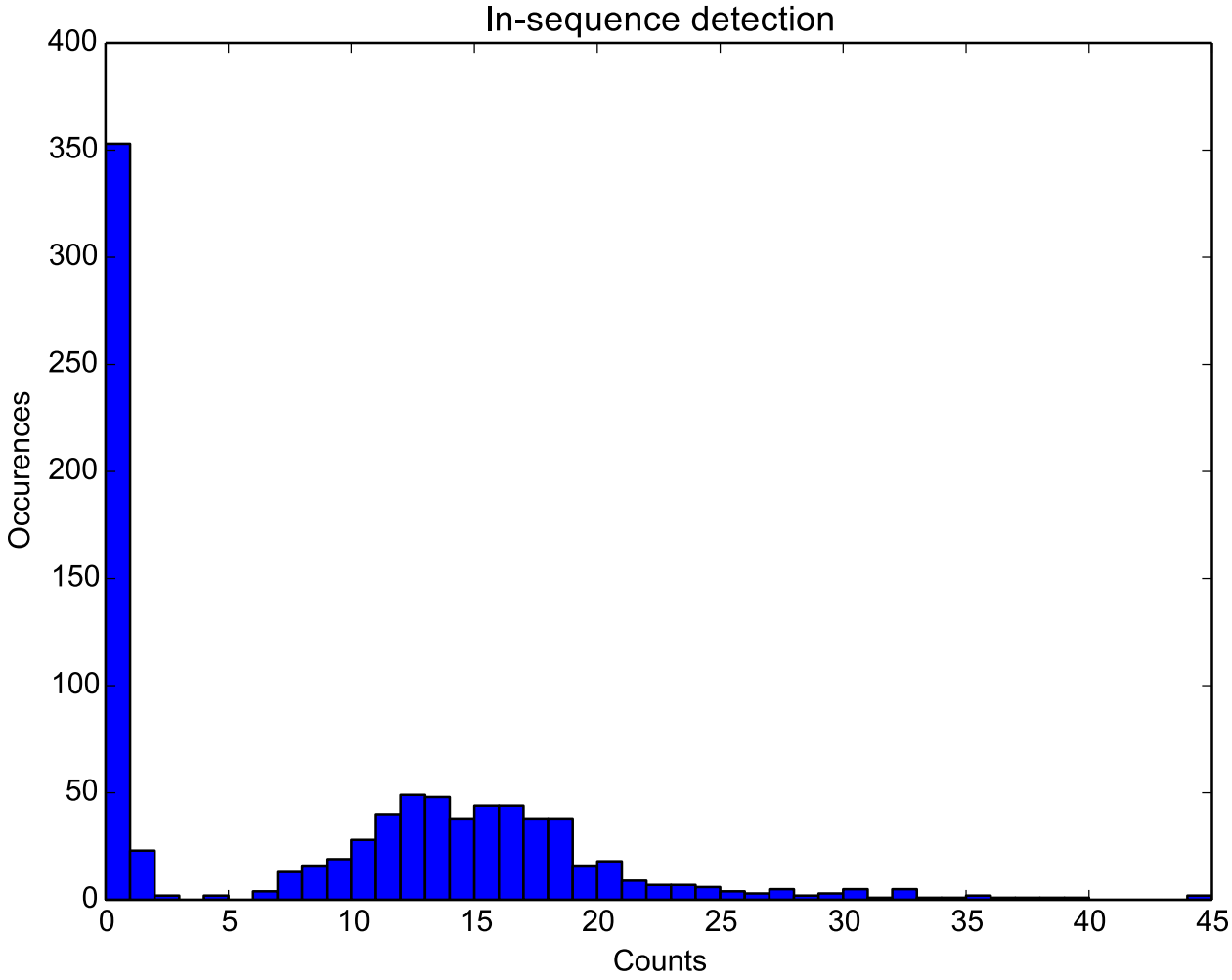

Figure 74: In-sequence photon-count histogram: Using a detection window of 300 μs, the photomultiplier tube collects on average 0.07 counts when the qubit is in state D and 14.4 counts when it is in state S. As can be seen in the figure, these two Poisson distributions are well distinguishable. Counts larger than 20 are an indication for sub-ideal hiding of other ions from the measurement process.

8.4 Recooling and Qubit-reset

Scattering photons during the detection window heats the ion-string and can lower the quality of subsequent quantum operations applied onto the register. Therefore recooling of the ion-string after the illumination with electron-shelving light is necessary. However, this recooling must not destroy any quantum information stored in the other qubits. Considering that the hidden quantum information is stored in the $D_{5/2}$ manifold, we employ 3-beam Raman-cooling [30, 122] in the $S_{1/2} \leftrightarrow P_{1/2}$ manifold. The Raman light-field, consisting of σ^+ and π light with respect to the quantization axis, is detuned by 1.5 GHz from the resonant $S_{1/2} \leftrightarrow P_{1/2}$ transition. The relative detuning between σ^+ and π is chosen such that it creates resonant coupling between $S_{1/2}(m = -1/2) \otimes |n\rangle \leftrightarrow S_{1/2}(m = 1/2) \otimes |n-1\rangle$, with $|n\rangle$ representing the quantized axial state of motion of the ion. The transfer is reset by resonant σ^- light. Raman cooling is employed for 500 μs. The qubit is reinitialized after cooling by an additional 50 μs of σ^- light. However, if the measured qubit was found to be in state D, neither does the measurement heat the ion string nor does the Raman cooling affect the register. Therefore the qubit is transferred from $D_{5/2}(m = -1/2)$ to $S_{1/2}(m = 1/2)$ (which was depleted by the previous 50 μs of σ^-). An additional pulse of σ^- light for 50 μs finally initializes the qubit, regardless whether it was projected into S or D. During the entire time when the qubit is subject to Raman cooling or initializing σ^- light, a repump laser at 866 nm is applied to prevent population trapping in the $D_{3/2}$ manifold due to spontaneous decay from the $P_{1/2}$ state to $D_{3/2}$.

8.5 Pulse sequence optimisation

For a sufficiently large Hilbert-space it will no longer be possible to directly optimize unitary operations acting on the entire register. Decomposing the necessary unitary operations into building blocks acting on smaller register sizes will allow one the use of optimized pulse sequences for large-scale quantum computation. From a methological point of view it may be preferred to physically decouple the qubits from any interactions (for instance by splitting and moving part of ion-qubit quantum register out of an interaction region, such as proposed in Ref. 64). However, given the technical requirements and challenges for splitting and moving ion-strings, we focus on spectroscopically decoupling certain ion-qubits from the interaction. In particular, we spectroscopically decouple an ion from subsequent interaction by transferring any quantum information from the $\{S_{1/2}(m = -1/2), D_{5/2}(m = -1/2)\}$ manifold to the $\{S_{1/2}(m = 1/2), D_{5/2}(m = -5/2)\}$ manifold using refocusing techniques on the $D_{5/2}(m = -1/2) \leftrightarrow S_{1/2}(m = 1/2)$ and $S_{1/2}(m = -1/2) \leftrightarrow D_{5/2}(m = -5/2)$ transitions. Using this approach, we optimise the controlled swap operation in a 3-qubit Hilbert space rather than a 5-qubit Hilbert space.

8.6 Controlled-SWAP

The controlled-SWAP operation, also known as Fredkin operation, plays a crucial role in the modular multiplication. For its implementation, however, we could not derive a pulse sequence that can incorporate an arbitrary number of spectator qubits (in the presented case, 2 spectator qubits in the computational register). However, using decoupling of spectator qubits, this additional requirement on the implementation is not necessary. Using pulse sequence optimization [119], we

obtained a sequence for the exact three-qubit case as shown in Tab. 13. In total the sequence consists of 18 pulses, including 4 MS interactions.

Pulse Nr.	Pulse	Pulse Nr.	Pulse
1	$R(1/2, 1/2)$	10	$R(1/2, 1)$
2	$S_z(3/2, 3)$	11	$S_z(1/4, 2)$
3	$MS(4/8)$	12	$S_z(3/2, 3)$
4	$S_z(3/2, 2)$	13	$MS(4/8)$
5	$S_z(1/2, 3)$	14	$S_z(3/2, 2)$
6	$R(3/4, 0)$	15	$S_z(3/2, 1)$
7	$MS(6/8)$	16	$R(1/2, 1)$
8	$S_z(3/2, 2)$	17	$S_z(3/2, 1)$
9	$MS(4/8)$	18	$S_z(3/2, 2)$

Table 13: Controlled SWAP operation: In a system of three ion-qubits, qubit 1 represents the control qubit and qubits $\{2, 3\}$ are to be swapped depending on the state of the first qubit. Note that this sequence only works for three-qubit systems. Spectator qubits would not experience the identity operation.

8.7 Four-Target Controlled-NOT

The modular multipliers $(7 \mod 15)$ and $(13 \mod 15)$ require, besides Fredkin operations, also CNOT operations acting on all qubits in the computational register Such an operation can be implemented (see Ref. 125(p.90, eq. 5.21)) with 2 MS operations plus local operations only - regardless of the size of the computational register. The respective sequence is shown in Tab. 14.

Pulse Nr.	Pulse	Pulse Nr.	Pulse
1	$R(1/2, 1)$	6	$MS(1/4)$
2	$S_z(3/2, 1)$	7	$R(3/4, 0)$
3	$MS(3/4)$	8	$S_z(3/2, 1)$
4	$R(5/4, 1)$	9	$R(1/2, 0)$
5	$S_z(1, 1)$		

Table 14: Four-target controlled NOT: Depending on the state of qubit one, the remaining four qubits $\{2\text{-}5\}$ are subject to a conditional NOT operation.

8.8 Two-Target Controlled-NOT

There exists an analytic solution to realize multi-target controlled-NOT operations in the presence of spectator qubits with the presented set of gates [125] - as required for the $\{2, 7, 8, 13\}^2 \mod 15$ multiplier. However, we find that performing decoupling of subsets of qubits of the quantum register prior to the application of the multi-target controlled-NOT operation presented above both facilitates the optimisation, and improves the performance of the realisation of a two-target controlled-NOT operation. Thus, the required two-target controlled-NOT operation is implemented via (i)

decoupling qubits 2 and 4, (ii) performing a multi-target controlled-not on all qubits with the first qubit acting as control, and (iii) recoupling of qubits 2 and 4.

8.9 Controlled Quantum Modular Multipliers

Based on the decomposition shown in Fig. 71d) and the respective pulse sequences outlined in the previous section, we investigate the performance of the building blocks as well as the respective conditional multipliers. In the following, the fidelities are defined as mean probabilities and standard deviations to observe the correct output state. The elements in the respective truthtables have been obtained as average over 200 repetitions.

- The Fredkin operation, controlled by qubit 1 and acting on qubits $\{35, 23, 34, 45\}$, yields fidelities of $\{76(4), 73(6), 72(4), 68(7)\}\%$. These numbers are consistent with MS gate interactions at a fidelity of 95% and local operations at a fidelity of 99.3%.
- The 4-target CNOT gate operates at a fidelity of $86(3)\%$.
- Considering the quality for modular multipliers of $(\{2, 4, 7, 8, 11, 13\} \mod 15)$, we find fidelities of $\{48(5), 40(5), 50(6), 46(5), 38(5)\}\%$. This performance is consistent with the multiplication of the performance of the individual building blocks: $\{37(6), 36(5), 37(6), 48(5), 36(5)\}\%$.

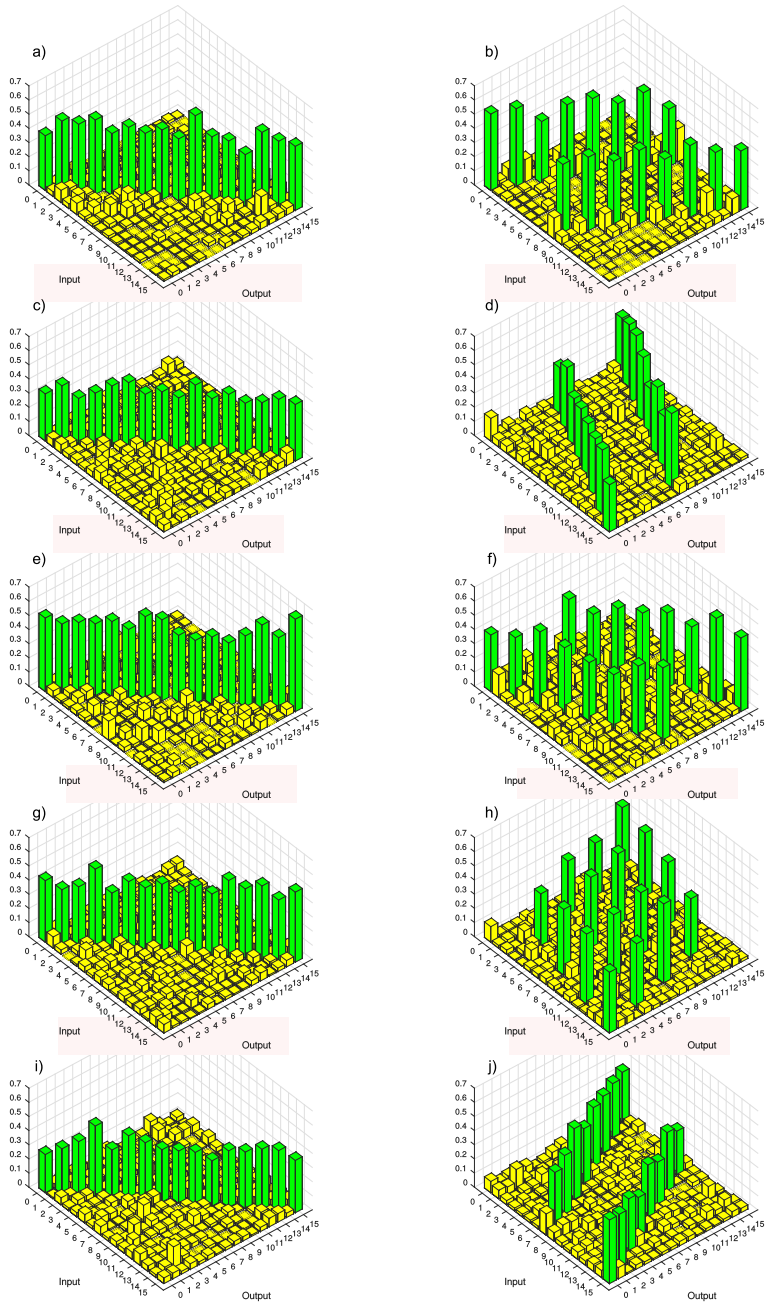

Figure 75: Controlled modular multipliers: While the full truthtables have been obtained, for improved accessibility only the subset of data for the computational register (in decimal basis) is presented for modular multipliers $(\{2, 7, 8, 11, 13\} \mod 15)$ where the control bit maps from $|0\rangle$ to $|0\rangle$ (a,c,e,g,i) as well as when $|1\rangle$ maps onto $|1\rangle$ (b,d,f,h,j). When the control qubit is in state $|0\rangle$, one expects to find the identity operation implemented, as shown in (a,c,e,g,i). If the control qubit is in state $|1\rangle$, the input state gets multiplied by $(\{2, 7, 8, 11, 13\}) \mod 15$. This behaviour is visually demonstrated as the output state increases in steps of $\{2, 7, 8, 11, 13\}$ until it reaches 15, where the output is then returned to its value modular 15.

9 References

[1] D. Wineland, Journal of Research of the National Institute of Standards and Technology 103 (1997).

[2] F. Schmidt-Kaler *et al.*, Journal of Physics B **36**, 626 (2003).

[3] C. Roos *et al.*, Physical Review Letters **83**, 7134716 (1999).

[4] J. Eschner *et al.*, J. Opt. Soc. Am. B **20**, 10031015 (2003).

[5] H. Rohde *et al.*, Journal of Optics B:Quantum and Semiclassical Optics **3**, 3441 (2001).

[6] I. Marzoli *et al.*, Phys. Rev. A **49**, 2771 (1994).

[7] M. Riebe *et al.*, New Journal of Physics **9**, 211 (2007).

[8] M. A. Nielsen and I. L. Chuang, *Quantum Computation and Quantum Information* (Cambridge University Press, 2000).

[9] J. Benhelm *et al.*, Nature Physics **4**, 463 (2008).

[10] K. Mølmer and A. Sørensen, Phys. Rev. Lett. **82**, 1835 (1999).

[11] A. Sørensen and K. Mølmer, Phys. Rev. A **62**, 022311 (2000).

[12] H. Haeffner *et al.*, Phys. Rev. Lett. **90**, 143602 (2003).

[13] G. Kirchmair *et al.*, New. J. of Phys. **11**, 023002 (2009).

[14] M. Müller, K. Hammerer, Y. Zhou, C. F. Roos, and P. Zoller, New J. Phys. **13**, 085007 (2011).

[15] F. Verstraete, M. Wolf, and C. Ignacio, Nature Physics **5**, 633 (2009).

[16] S. Diehl *et al.*, Nature Physics **4**, 878 (2008).

[17] D. Nigg *et al.*, Phys. Rev. Lett. **110**, 060403 (2013).

[18] P. Schindler *et al.*, Science **332**, 1059 (2011).

[19] D. Nigg *et al.*, Nature **470**, 486 (2011).

[20] G. Baggio, F. Ticozzi, and L. Viola, IEEE **470**, 486 (2012).

[21] S. Lloyd and L. Viola, Phys. Rev. A **65**, 010101 (2001).

[22] D. Berkeland *et al.*, Journal of Applied Physics **83**, 5020 (1998).

[23] M. Chwalla *et al.*, Phys. Rev. Lett. **102**, 023002 (1998).

[24] M. Chwalla, "Precision spectroscopy with $40^C a^+$ ions in a Paul trap,", 2009.

[25] G. Tóth *et al.*, Phys. Rev. Lett. **105**, 250403 (2010).

[26] T. Monz *et al.*, Phys. Rev. Lett. **106**, 130506 (2011).

[27] A. H. Burrell *et al.*, Phys. Rev. A **81**, 040302 (2010).

[28] P. A. Barton *et al.*, Phys. Rev. A **62**, 032503 (2000).

[29] G. Tommaseo *et al.*, The European Physical Journal D - Atomic, Molecular, Optical and Plasma Physics **25**, 113 (2003).

[30] D. J. Wineland *et al.*, Journal of Research of the National Institute of Standards and Technology **103**, 259 (1997).

[31] D. J. Szwer *et al.*, Journal of Physics B: Atomic, Molecular and Optical Physics **44**, 025501 (2011).

[32] Y. Sagi *et al.*, Phys. Rev. Lett. **105**, 053201 (2010).

[33] C. Barthel *et al.*, Phys. Rev. Lett. **105**, 266808 (2010).

[34] M. J. Biercuk *et al.*, Nature **558**, 9961000 (2009).

[35] J. Bylander *et al.*, Nature Physics **7**, 565570 (2011).

[36] T. Monz *et al.*, Phys. Rev. Lett. **103**, 565570 (2009).

[37] H. Haeffner *et al.*, .

[38] T. Tomaru *et al.*, Cryocoolers **13**, 695 (2005).

[39] P. F. Herskind *et al.*, Opt. Lett. **36**, 3045 (2011).

[40] D. Gangloff *et al.*, Opt. Express **23**, 18014 (2015).

[41] S. Schulz, U. Poschinger, K. Singer, and F. Schmidt-Kaler, Fortschr. Phys. **54**, 648 (2006).

[42] S. Schulz, U. Poschinger, F. Ziesel, and F. Schmidt-Kaler, New J. Phys. **10**, 045007 (2008).

[43] R. B. Blakestad, dissertation, University of Colorado, .

[44] P. Schindler, D. J. Gorman, N. Daniilidis, and H. Häffner, 1505.01237v1 (2015).

[45] N. Daniilidis *et al.*, Physical Review B **89**, 245435 (2014).

[46] D. A. Hite *et al.*, Phys Rev Lett **109**, 103001 (2012).

[47] R. Bowler, U. Warring, J. W. Britton, B. C. Sawyer, and J. Amini, Rev. Sci. Instrum **84**, (2013).

[48] M. T. Baig *et al.*, Rev. Sci. Instrum **84**, (2013).

[49] P. Schindler *et al.*, New Journal of Physics **15**, 123012 (2013).

[50] T. Harty *et al.*, Phys. Rev. Lett. **113**, 220501 (2014).

[51] T. Xia *et al.*, 1501.02041 (2015).

[52] V. Nebendahl, H. Häffner, and C. F. Roos, Phys. Rev. A **79**, 012312 (2009).

[53] S. X. Wang, Phd thesis, Department of Physics, Massachusetts Institute of Technology, 2012.

[54] R. B. Blakestad *et al.*, Phys. Rev. A **84**, 032314 (2011).

[55] K. Singer *et al.*, Review of Modern Physics **82**, 2609 (2010).

[56] J. A. Nelder and R. Mead, The Computer Journal **7**, 308 (1965).

[57] A. Walther *et al.*, Phys. Rev. Lett. **109**, 080501 (2012).

[58] R. Bowler *et al.*, Phys. Rev. Lett. **109**, 080502 (2012).

[59] M. A. Rowe *et al.*, Quantum Inf. and Comput. **2**, 257 (2002).

[60] H. Kaufmann, T. Ruster, C. T. Schmiegelow, F. Schmidt-Kaler, and U. G. Poschinger, New Journal of Physics **16**, 073012 (2014).

[61] T. Ruster *et al.*, Phys. Rev. A **90**, 033410 (2014).

[62] H. Bombin and M. A. Martin-Delgado, Phys. Rev. Lett. **97**, 180501 (2006).

[63] C. F. Roos, New J. Phys. **10**, 013002 (2008).

[64] D. Kielpinski, C. Monroe, and D. J. Wineland, Nature **417**, 709 (2002).

[65] L. M. K. Vandersypen and I. L. Chuang, Rev. Mod. Phys. **76**, 1037 (2005).

[66] J. Barreiro *et al.*, Nature **470**, 486 (2011).

[67] B. P. Lanyon *et al.*, Phys. Rev. Lett. **111**, 210501 (2013).

[68] E. Dennis, A. Kitaev, A. Landahl, and P. J., J. Math. Phys. **43**, 4452 (2002).

[69] T. Monz *et al.*, Physical Review Letters **102**, 040501+ (2009).

[70] D. Nigg *et al.*, Science **345**, 302 (2014).

[71] H. Bombin and M. Martin-Delgado, Phys. Rev. Lett. **98**, 160502 (2007).

[72] S. Bravyi and A. Kitaev, Phys. Rev. A **71**, 022316 (2005).

[73] L. K. Grover, in *Proceedings, 28th Annual ACM Symposium on the Theory of Computing (STOC)*, p. 8 (1996).

[74] T. J. Yoder, G. H. Low, and I. L. Chuang, Phys. Rev. Lett. **113**, 210501 (2014).

[75] I. L. Chuang, N. Gershenfeld, and M. Kubinec, Phys. Rev. Lett. **80**, 3408 (1998).

[76] J. A. Jones, M. Mosca, and R. H. Hansen, Nature **393**, 344 (1998).

[77] M. Anwar, D. Blazina, H. Carteret, S. Duckett, and J. Jones, Chemical Physics Letters **400**, 94 (2004).

[78] P. G. Kwiat, J. R. Mitchell, P. D. D. Schwindt, and A. G. White, Journal of Modern Optics **47**, 257 (2000).

[79] P. Walther *et al.*, Nature **434**, 169 (2005).

[80] K. A. Brickman *et al.*, Physical Review A - Atomic, Molecular, and Optical Physics **72**, 050306 (2005).

[81] C. Zalka, arXiv (1998).

[82] S. A. Cuccaro, T. G. Draper, S. A. Kutin, and D. P. Moulton, arXiv (2004).

[83] T. G. Draper, S. A. Kutin, E. M. Rains, and K. M. Svore, Quantum Information & Computation **6**, 351 (2006).

[84] S. Beauregard, Quantum Information & Computation **3**, 14 (2002).

[85] A. Pavlidis and D. Gizopoulos, Quantum Information & Computation **14**, 649 (2014).

[86] P. L. Montgomery, Mathematics of Computation **44**, 519 (1985).

[87] A. J. Menezes, S. A. Vanstone, and P. C. V. Oorschot, *Handbook of Applied Cryptography*, 1st ed. (CRC Press, Inc., Boca Raton, FL, USA, 1996).

[88] T. Monz *et al.*, Physical Review Letters **106**, 1 (2011).

[89] J. I. Cirac, P. Zoller, H. J. Kimble, and H. Mabuchi, Physical Review Letters **78**, 4 (1996).

[90] D. Kielpinski, C. Monroe, and D. J. Wineland, Nature **417**, 709 (2002).

[91] C. Monroe *et al.*, Physical Review A - Atomic, Molecular, and Optical Physics **89**, 022317 (2014).

[92] K. K. Mehta *et al.*, Applied Physics Letters **105**, (2014).

[93] M. Saeedi and M. Pedram, Physical Review A - Atomic, Molecular, and Optical Physics **87**, 062318 (2013).

[94] M. A. Nielson and I. L. Chuang, *Quantum Computation and Quantum Information* (Cambridge University Press, 2002), p. 700.

[95] C. Clos, Bell System Technical Journal **32**, 406 (1953).

[96] M. J. Flynn, IEEE Transactions on Computers **C-21**, 948 (1972).

[97] A. M. Eltony, Phd thesis, Department of Physics, Massachusetts Institute of Technology, 2015.

[98] P. W. Shor, Foundations of Computer Science, 1994 Proceedings., 35th Annual Symposium on pp. 124–134 (1994).

[99] M. A. Nielsen and I. L. Chuang, *Quantum Computation and Quantum Information (Cambridge Series on Information and the Natural Sciences)*, 1 ed. (Cambridge University Press, 2004).

[100] I. Chuang and M. A. Nielsen, J. Mod. Opt. **44**, 245567 (1997).

[101] R. B. Griffiths and C. S. Niu, Phys. Rev. Lett. **76**, 3228 (1996).

[102] C. A. Fuchs, arXiv:quant-ph/9601020 (1996).

[103] J. Chiaverini *et al.*, Science **308**, 997 (2005).

[104] E. Martin-Lopez *et al.*, Nat Photon advance online publication (2012).

[105] P. Schindler *et al.*, Phys. Rev. Lett. **110**, 070403 (2013).

[106] A. Politi, J. C. F. Matthews, and J. L. O'Brien, Science **325**, 1221 (2009).

[107] E. Lucero *et al.*, Nat Phys **8**, 719 (2012).

[108] C. Y. Lu, D. E. Browne, T. Yang, and J. W. Pan, Physical Review Letters **99**, 250504+ (2007).

[109] B. P. Lanyon *et al.*, Physical Review Letters **99**, 250505+ (2007).

[110] L. M. K. Vandersypen *et al.*, Nature **414**, 883 (2001).

[111] J. A. Smolin, G. Smith, and A. Vargo, Nature **499**, 163 (2013).

[112] Kitaev, quant-ph/9511026 (1995).

[113] K. Southwell, Quantum Coherence (Nature Insight), Nature **453**, 1003 (2008).

[114] R. B. Griffiths and C. S. Niu, Physical Review Letters **76**, 3228 (1996).

[115] S. Parker and M. B. Plenio, Physical Review Letters **85**, 3049 (2000).

[116] M. Mosca and A. Ekert, "The Hidden Subgroup Problem and Eigenvalue Estimation on a Quantum Computer," in *Quantum Computing and Quantum Communications*, Vol. 1509 of *Lecture Notes in Computer Science*, C. Williams, ed., (Springer Berlin Heidelberg, 1999), pp. 174–188.

[117] A. Sørensen and K. Mølmer, Phys. Rev. Lett. **82**, 1971 (1999).

[118] F. Schmidt-Kaler *et al.*, Appl. Phys. B **77**, 789 (2003).

[119] V. Nebendahl, H. Häffner, and C. F. Roos, Phys. Rev. A **79**, 012312 (2009).

[120] H. Dehmelt, Bull. Am. Phys. Soc. **20**, 60 (1975).

[121] M. Riebe *et al.*, Nature **429**, 734 (2004).

[122] I. Marzoli, J. Cirac, R. Blatt, and P. Zoller, Physical Review A **49**, 2771 (1994).

[123] P. W. Shor, in *Foundations of Computer Science, 1996. Proceedings., 37th Annual Symposium on*, **0**, 56 (IEEE, Los Alamitos, CA, USA, 1996).

[124] P. Schindler *et al.*, New Journal of Physics **15**, 123012+ (2013).

[125] V. Nebendahl, *Optimierung verschränkender Quantengatter für Experimente mit Ionenfallen* (Austria, 2008).

BAA #: IARPA-BAA-09-06

PROJECT #: W911NF-10-1-0284

Scalable Quantum Information Processing (SQIP) With Trapped Ions

Capstone activity: Final report

Principal Investigator:	Rainer BLATT
Phone:	0043 512 507 524 50
Fax:	0043 512 507 524 91
email:	rainer.blatt@uibk.ac.at
Institution:	Institute for Experimental Physics University of Innsbruck, Austria
Institution address:	Technikerstr. 25/4 6020 Innsbruck, Austria
Other Institutions:	Universität Mainz, Germany University of Berkeley, California, USA Massachussets Institute of Technology, USA

Reporting Period:	Aug 2015 - January 2016
Agency & Point of Contact:	IARPA, Dr. David Moehring

Contents

1 Introduction

The following report outlines the progress that has been made within the "Scalable Quantum Information Processing (SQIP) with Trapped Ions" capstone program. In particular it will emphasis on

- the two setups maintained and installed at the University of Innsbruck (UIBK) in Austria, lead by Rainer Blatt, focusing on quantum information processing - in particular the realization of quantum algorithms ,
- the team around Ferdinand Schmidt-Kaler at the University of Mainz (UMZ) working on distributed entanglement within an ion-trap via splitting and shuttling of ions without excess heating of the motional state,
- the group of Issac Chuang at the MIT in Boston working both on quantum algorithms as well as an ion-photon interface to connect distant ion-traps,
- supplemented by the team at the University of Berkeley/California (UCB), supervised by Hartmut Häffner, aiming at understanding and overcoming detrimental effects in surface-trap based quantum computation.

The report is divided into the acitvites carried out by the individual nodes.

2 UIBK activities

2.1 Commercial of the shelf system improvement

2.1.1 Single ion addressing error

The setup for single ion addressing in the COTSS setup is shown in Fig 1 The focus at the position of the ions can be measured by scanning the x-direction of lens L2 via the motorized translation stage and measuring the excitation probability of each single ion via the camera. In Fig 2(a) a typical scan of the lens L2 across a 3-ion crystal is shown.

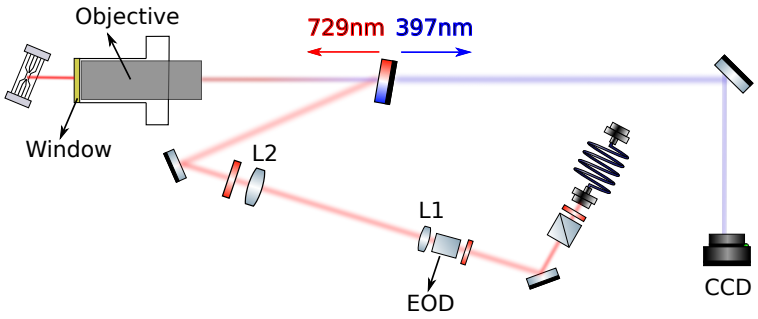

Figure 1: Schematic optical setup of the single ion addressing used in COTSS.

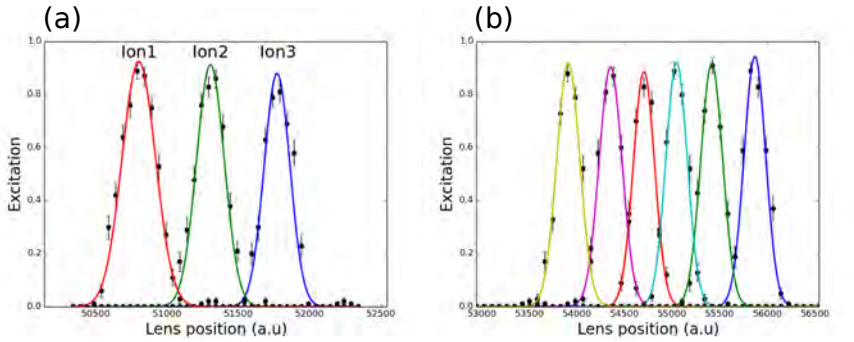

Figure 2: Excitation of the $4S_{1/2}(m_j = -1/2) \rightarrow 3D_{5/2}(m_j = -1/2)$ transition when scanning across a (a) three and (b) six-ion crystal with a focused laser beam. The excitation of the individual ions leads to the possibility of single-ion addressing. The measured beam waist at the focus is 1.6 μm.

It can be seen that each ion is excited in sequence by a gaussian-like excitation profile. The focus at the position of the ions can be measured via the width of the gaussian beam profile. Since the units of the abscissa is given by the step size of the motorized translation stage, the axis has to be calibrated by the known inter-ion distances. The waist of the beam at the focus is $\omega_0 = 1.6$ μm. Simulations with *Zemax* leads to a waist $\omega_{sim} = 1.3$ μm at the position of the focal point. In optical systems, the minimal achievable focus is given by the radius R_{airy} of the Airy disc, which arises by the diffraction from the aperture of an optical system. Here, with the used optical system

the minimum Airy disc radius $R_{airy} = \frac{1.22\lambda}{2NA} = 1.53$ μm, with the maximal numerical aperture $NA = 0.29$. A sinc-type regression function in to the data shown in Fig 2(a) leads to a radius $R_{airy} = 2.37$ μm. The measured radius is bigger than the diffraction limit, because the aperture of the EOD limits the initial beam waist and therefore we do not make use of the full aperture of the objective. Fig 2(ab) shows the addressing of a 6-ion crystal at a tip-voltage of 700 V on the $4S_{1/2}(m_j = -1/2) \rightarrow 3D_{5/2}(m_j = -1/2)$ transition.

By including the EOD, the same excitation pattern as in Fig. 2(a,b) can be measured when scanning the control-voltage of the EOD. Fig. 3(a) shows the excitation profile of the individual ions as a function of the control-voltage. Therefore, each ion can be addressed during the sequence by setting the corresponding EOD control-voltage. In Fig. 3(b) the third ion was addressed. The ratio of the Rabi frequencies of the addressed ion to the neighboring ions is around 3%. When implementing an algorithm in our system, the addressed operations are performed by σ_z rotations originating from AC-Stark shifts. The Rabi frequency there is proportional to the square of the resonant Rabi frequency and thus the effective addressing error for AC-Stark pulses is around $9 \cdot 10^{-4}$.

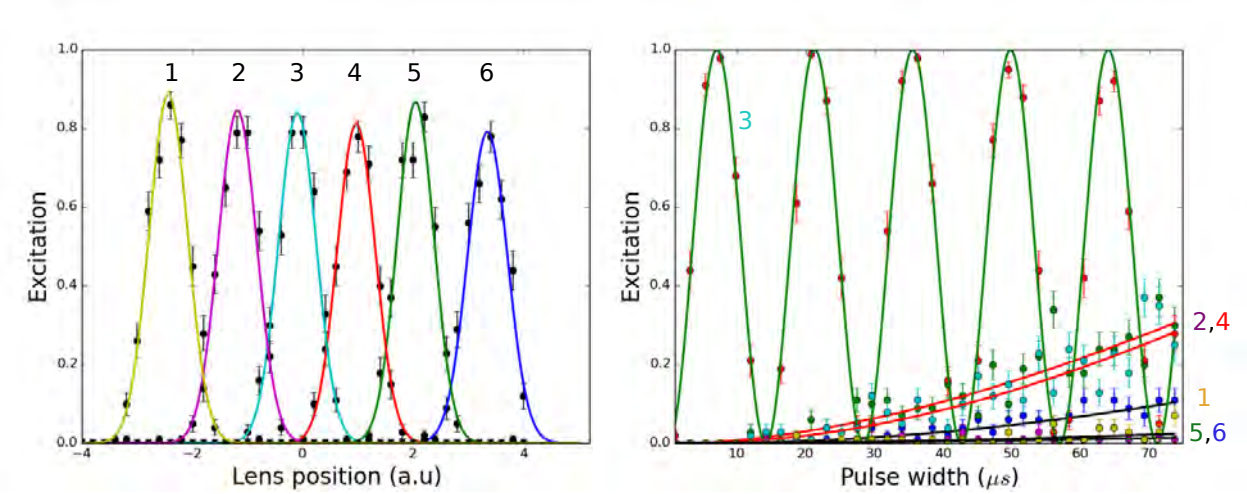

Figure 3: (a) Addressing profile of a six-ion crystal with a distance of about 3μm by scanning the voltage applied on the EOD. (b) Rabi oscillations on the third ion with crosstalk to the neighboring ions of about 3%.

2.1.2 Single qubit gate multiplexer

In the COTSS setup, we routinely use beam steering of the laser beam to address individual ions. This beam steering, can be realized by acousto-optics (AO)[16, 24, 11], electro-optical deflectors (EODs)[20, 19] or microelectromechanical (MEMS) mirrors[9]. The laser beam's spot size has to be smaller than the minimal ion-ion separation (3.5 μm) to suppress cross-talk between adjacent ions. This can be further helped by restricting local qubit rotations to R_z, which is realized via an AC-Stark shift and therefore depends on the electric field only in second order[19, 11]. The standard beam steering for the COTSS setup is an EOD, but in contrast to EODs, AO devices can

simultaneously produce more than one output beam when supplied with multiple radio frequencies simultaneously. In this way, arbitrary combinations of ions can be addressed at once (Figure 4.c).

Also, the time it takes to switch one such laser beam between any two beam positions is constant. It is given by the time $\tau_\mathrm{a} = D/v_\mathrm{a}$ at which an acoustic wavefront traveling at velocity v_a traverses the laser beam of diameter D inside an AO crystal. It depends on the acoustic mode and beam diameter chosen to operate the device. Here, deflectors (AODs) usually differ from modulators (AOMs) in their internal design and setup. AOMs are typically operated using a focused laser beam and use the crystal's fast longitudinal acoustic [001] mode in order to allow for rapid amplitude modulation. An AOD is operated using a collimated laser beam and often uses the crystal's transverse acoustic shear [110] mode, where v_a is about an order of magnitude slower in the commonly used material TeO_2[5].

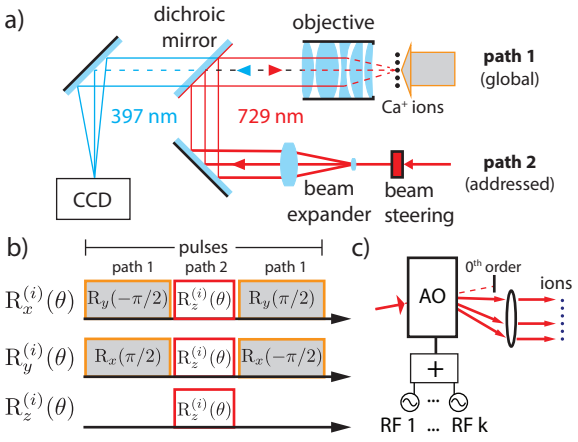

Figure 4: a) Exemplary optical setup for single ion addressing and detection[11]. b) Pulse sequences to implement single qubit rotations by angle θ on ion (i). The $\mathrm{R}_z^{(i)}$ rotation is realized by detuning the laser beam sufficiently far from the qubit transition to only induce an AC-Stark shift. c) Multiple radio frequencies (RF 1...k) applied to an acousto-optic device (AO) lead to k addressed beams that are imaged onto the ion string.

This choice is motivated by the central figure of merit for any kind of optical deflector: the number of resolvable spots $N = \Delta\phi/\Theta$ over the device's deflection range $\Delta\phi$, where $\Theta \propto \lambda/D$ is the angular spreading of a laser beam at wavelength λ (Rayleigh criterion). In AO devices the deflection range $\Delta\phi = \lambda\Delta f_\mathrm{AO}/v_\mathrm{a}$ is given by the ratio of the optical wavelength to the range of supported acoustic wavelengths, which is determined by the device's bandwidth Δf_AO. For a wavelength of $\lambda = 729$ nm, $\Delta f_\mathrm{AO} = 40$ MHz and $v_\mathrm{a} = 620m/s$ this range amounts to $\Delta\phi \sim 47$ mrad, which is much larger than that afforded by an EOD ($\lesssim 5$ mrad). As AODs commonly use a significantly larger crystal than AOMs, N can easily surpass values of 300 resolvable spots. In Figure 5 we use such an AOD[1] with the above parameters to implement single-site addressing in a register of up to 20 ionic qubits. In this case, switching a single beam between any two sites takes $\sim 12\mu s$ and yields pulses with $< 1\%$ intensity fluctuations. The reduced excitation probability and

[1]Gooch & Housego, model 45070-5-6.5DEG-633

correspondingly reduced coupling strength Ω on either side of Figure 5.a,b is due mostly to sub optimal beam focusing and, for the outermost ions, clipping on optical elements in the beam path. Figure 5.c further illustrates the capability to perform R_x rotations on all or a select number of ions simultaneously using the global or tightly-focused, AOD-steered beam(s).

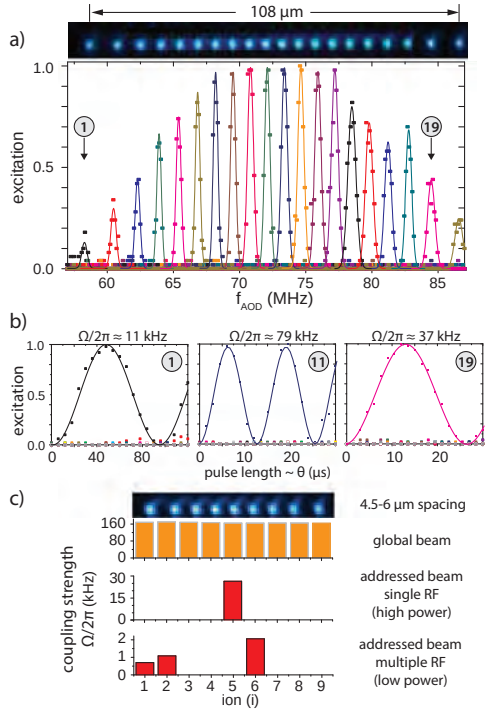

Figure 5: a) Scan of the radio frequency f_{AOD} encoding the position of a tightly focused laser beam ($1/e^2$ diameter $\sim$ $3\mu m$) directed onto a crystal of 20 ions, where the smallest inter-ion spacing is $\sim 5\mu m$. Plotted is the excitation probability from the initial $|\downarrow\rangle$ state to $|\uparrow\rangle$ following 100 repetitions of a $\mathrm{R}_x^{(i)}(\theta)$ sequence where θ is set to π for ion 11. b) Single-ion Rabi flops at frequency Ω observed under variation of the laser pulse length ($\propto \theta$) implementing the addressed $\mathrm{R}_z^{(i)}(\theta)$ rotation. All panels share the same laser power. c) Coupling strength (Rabi frequency) obtained in a 9 ion crystal using either the global beam for equal illumination or one or more single-site addressed beams simultaneously.

2.1.3 Temporal noise analysis

The optical qubit available in $^{40}Ca^{+}$ shows two dominant sources of decoherence, namely laser- and magnetic field fluctuations. Both error sources lead to a time variation of the qubit transition frequency and therefore lowering the coherence of the qubit. Here, the influence of the laser- and magnetic field stabilization performance on the coherence is discussed.

We are making use of Ramsey spectroscopy to characterize the coherence of our quantum system. There, for a given Ramsey time t_R, the probability of measuring the excited state $p_{|0\rangle}$ is given by $p_{|0\rangle} = 1/2(1 + C(t_R)\cos\phi)$, whereas the contrast $C(t_R)$ corresponds to the oscillation amplitude. Fig. 6 shows Ramsey contrast measurements using the spin echo technique on the $4S_{1/2}(m_j = -1/2) \rightarrow 3D_{5/2}(m_j = -1/2)$ transition for different settings of the laser feedback control loop. The blue diamonds correspond to the Ramsey contrast for the initial laser performance, which is qualitatively characterized by measuring the noise spectrum of the in-loop Pound-Drever-Hall error signal shown by the blue curve in the inset of Fig. 6. The Ramsey contrast pattern shows clearly a dip at a Ramsey time $t_R = 100\mu$s, which indicates dominant frequency components of the laser frequency in the region of ≈ 10 kHz. The coherence decay can be investigated theoretically assuming a certain laser spectrum $S(\omega)$ and fitting the resulting coherence $C(t)$ to the measured data points (blue diamonds). The temporal course of the decoherence for a Ramsey experiment including a spin echo sequence can be calculated by the following equation [19]:

$$C(t_R) = \exp\Big[-t_R^2 \int_0^\infty S(\omega)^2 \underbrace{\mathrm{sinc}(\omega t_R/4)^2 \sin(\omega t_R/4)^2 d\omega}_{g_{n=1}(\omega,t)}\Big] \tag{1}$$

with the power spectral density (PSD) $S(\omega)^2$ and a weighting function $g_{n=1}(\omega, t)$, where n specifies the number of interleaved spin echo pulses. For the noise spectrum $S(\omega)$ we assume a sum of a narrow Lorentzian profile around the laser center frequency $L(\omega) = \frac{\Gamma^2}{\Gamma^2+\omega^2}$, and multiple broad Gaussian profiles, representing the "servo-bumps": $G^{(\omega_0,\sigma)}(\omega) = \exp -(\omega - \omega_0)^2/\sigma^2$: In our specific setup, the noise is well described by 3 Gaussian profiles:

$$S(\omega) = a\Big[L(\omega) + b\, G^{(10kHz,4kHz)}(\omega) + c\, G^{(2.9kHz,30Hz)}(\omega) + d\, G^{(1kHz,200Hz)}(\omega)\Big], \tag{2}$$

where $G^{(10kHz,4kHz)}(\omega)$ corresponds to the dominant noise peak at around 10 kHz, which is indicated by the oscillating behavior, a narrow Peak at 2.9 kHz, which arises from the Etalon lock, and a peak at 1 kHz, which could be induced by acoustic noise and explains the contrast loss up to 1 ms. In Fig.6 the contrast decay according to equation 2 with the fitted parameters $[a = 36.5\ \sqrt{Hz}, \Gamma = 3\ Hz b = 5.3, c = 4.2, d = 1.5]$ is shown by the red curve. After optimizing the parameters of the feedback loop to the slow part of the intracavity electro optical modulator (EOM) with respect to the Piezo feedback, the noise spectral density around 10 kHz could be reduced by 20 dBm (green curve of the inset). The coherence decay measurement after the optimization (green diamonds) clearly indicates that the oscillation vanishes.

2.1.4 Cooling multiple modes simultaneously

Cooling using electromagnetically induced transparency (EIT) is an alternative ground state cooling technique for trapped ions. It is similar to Raman sideband cooling but the laser detunings are

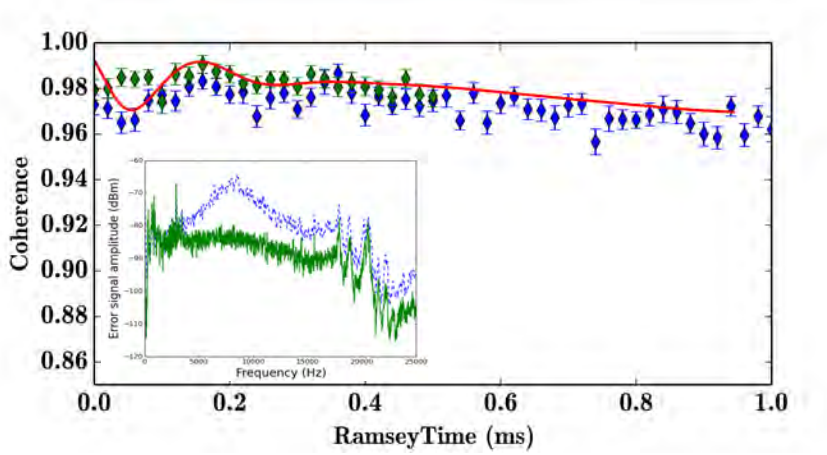

Figure 6: Measurement the coherence decay using the spin echo method for two different settings of the feedback loop electronics of the 729 nm laser. The blue and green curve of the inset show the noise spectrum of the in loop error PDH error signal and the blue (red) diamonds correspond to the coherence measurement respectively.

chosen in such a way that to first order the atomic system is pumped into a dark state which does not couple to the laser fields. Therefore, spontaneous photon emission rates are significantly lower than for Raman cooling, and so are the heating processes intrinsic to the laser cooling scheme. As a consequence, the cooling range of oscillation frequencies over which the ion motion is cooled close to the ground state can be made wider than with Raman cooling and higher cooling rates can be achieved.

EIT cooling requires a three-level Λ atomic system where the coupling of two ground states $|g\rangle$, $|f\rangle$ to one excited state $|e\rangle$ leads to coherent population trapping in a superposition of the two ground states that does not couple to the excited state. Figure 7(a) shows the basic EIT scheme: the $|g\rangle \leftrightarrow |e\rangle$ transition is driven by a laser beam blue-detuned by Δ and with a Rabi frequency Ω_σ, creating dressed states $|\tilde{g}\rangle$, $|\tilde{e}\rangle$ which are shifted by an amount

$$\delta = \frac{1}{2}\left(\sqrt{\Omega_\sigma^2 + \Delta^2} - |\Delta|\right) \tag{3}$$

from the bare states. The probe beam with detuning Δ_π and Rabi frequency $\Omega_\pi \ll \Omega_\sigma$ couples the second ground state $|f\rangle$ to the dressed states resulting in a Fano-like absorption profile (Fig. 7(c)). For $\Delta_\pi = \Delta$, the absorption becomes zero held at a fixed position in space. If, however, the atom is trapped in a harmonic trap with oscillation frequency ω, the ion can absorb light on vibrational sidebands of the transition (Fig. 7(b)). Setting the light shift of the dressing beam equal to the trap frequency, $\delta = \omega$ maximizes the absorption probability on the red sideband transition $|f, n\rangle \leftrightarrow |\tilde{g}, n-1\rangle$. For every absorption event the phonon number n decreases by one unit. At the same time, as the absorption on the carrier transition $|f, n\rangle \leftrightarrow |\tilde{g}, n\rangle$ vanishes, the only heating mechanism in the Lamb-Dicke regime is absorption on the blue sideband which however can be made much less likely than red sideband absorption (see inset of Fig. 7(c)).

The range of oscillation frequencies over which EIT cooling is efficient can be set by choosing the detuning Δ which in turn determines the decay rate of the dressed state $|\tilde{g}\rangle$. Similar to other

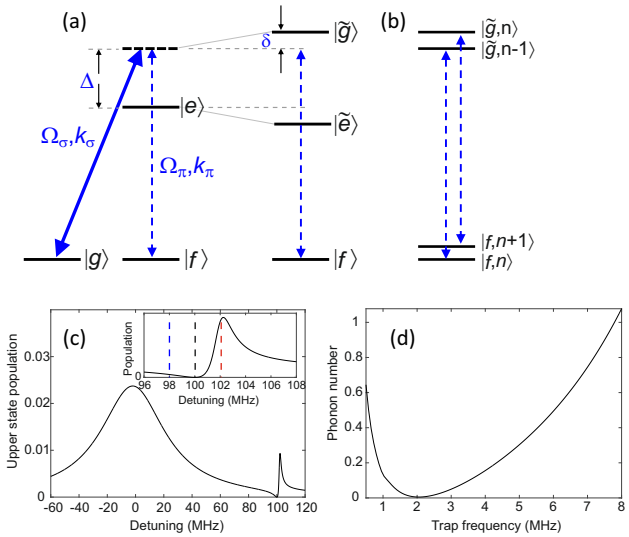

Figure 7: (a) EIT cooling can be implemented in a three-level-Λ system. One transition is driven by a strong, blue-detuned laser (Rabi frequency Ω_σ) creating dressed states. A weaker laser probes the resulting Fano-like absorption profile (shown in (c)) where the coupling to the dressed state $|\tilde{g}\rangle$ results in a narrow absorption feature. For a probe laser with a detuning equal to the one of the dressing laser, absorption on the carrier transition is suppressed in steady state, and absorption on the red sideband is much stronger than on the blue sideband (see (b) and dashed lines in the inset of (c)). (b) In the dressed state picture, absorption of the probe beam is possible on the red sideband transitions $|f, n\rangle \leftrightarrow |\tilde{g}, n-1\rangle$ or on the blue sideband transitions $|f, n+1\rangle \leftrightarrow |\tilde{g}, n\rangle$. (c) Fano-like absorption profile for the weak probe beam. As depicted in the inset, red sideband transitions have a high probability, blue sideband transitions have a low probability and carrier transitions are suppressed. (d) For the absorption profile shown in (c), cooling to the ground state can be achieved over a wide range of trap frequencies.

sideband cooling schemes, there is a trade-off between the lowest achievable temperatures and the cooling range. However, due to the suppression of carrier excitation, cooling close to the ground state can be achieved over a fairly large cooling range. An example of the achievable cooling range is shown in Fig. 7(d).

To characterize EIT cooling for larger ion crystals, measurements are taken using a crystal of nine ions with center-of-mass mode frequencies of $\{\omega_z, \omega_{r1}, \omega_{r2}\} = 2\pi\,\{0.50, 2.59, 2.76\}$ MHz and a crystal of eighteen ions with COM modes of $\{\omega_z, \omega_{r1}, \omega_{r2}\} = 2\pi\,\{0.21, 2.68, 2.71\}$ MHz. In experiments using long ion chains it is advantageous to use radial rather than axial modes as the linearity of the ion string can only be maintained by a reduction of the axial mode frequency. However, as the axial mode frequency decreases so does the speed at which gates between ions work. Furthermore, heating effects increase with decreasing motional frequency, reducing the time available for gate operations. Hence, it is beneficial to use the transversal modes and therefore, the core of the EIT cooling investigation lies on this part of the mode spectrum.

For the nine-ion crystal, all modes of the radial spectrum are cooled simultaneously. To achieve this, the light shift induced by the σ^+ light is centered roughly in the middle of the radial mode spectrum at 2.2 MHz. Optimization of the σ^+ polarization reduces unwanted light shifts due to the

wrong polarization components to 11 kHz. The intensity of the π polarized beam is set to induce a light shift of 90 kHz, about 24 times smaller than the coupling laser's intensity.

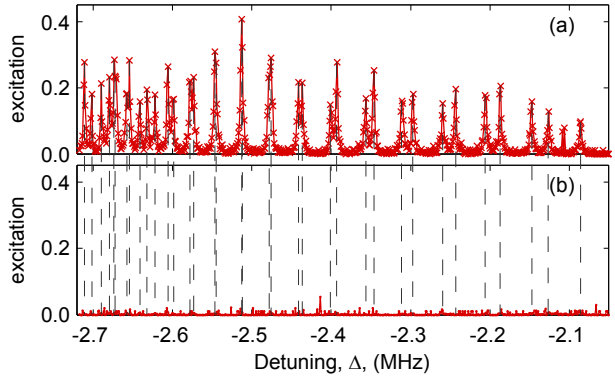

Figure 8: (a) Radial mode spectrum of a nine-ion crystal trapped in a linear Paul trap after Doppler cooling. (b) Radial mode spectrum of a nine-ion crystal after Doppler cooling and consecutive EIT cooling. The σ^+ induced light shift is set to 2.2 MHz and the cooling pulse is applied for 1 ms. Dashed lines between (a) and (b) serve to aid comparison of the spectra. As is clearly illustrated, the EIT cooling works on all radial modes, spread over a range of 1.2 MHz, simultaneously.

Fig. 8 compares the radial part of the spectrum for the nine-ion crystal (from 2.76 MHz to 1.53 MHz) after Doppler cooling only (Fig. 8 (a)) with a spectrum after the additional application of EIT cooling (Fig. 8 (b)). The data presented in Fig. 8 (b) were taken with a single EIT cooling pulse of 1 ms applied. A comparison of the Doppler cooled and the EIT cooled spectra clearly shows how well the cooling works. In the case of the nine-ion crystal, the complete range of radial modes, extending over a range of 1.2 MHz, is cooled simultaneously with only one setting for the EIT cooling beams.

Complete cooling of all modes simultaneously is also observed for the eighteen-ion crystal. This result is achieved by setting the induced light shift from the σ^+ beam to 2.3 MHz (roughly centered between the highest radial mode at 2.71 MHz and the lowest radial mode at 2.08 MHz), leading to an unwanted light shift of 18 kHz on the $\left|\mathrm{S}_{1/2}, m = 1/2\right\rangle$ level due to σ^- components. The intensity of the π beam is chosen to induce a light shift of 120 kHz, corresponding to an intensity about 19 times smaller for the cooling laser than for the coupling laser.
Fig. 9 shows the results from the measurements carried out on the radial part of the red-sideband spectrum for the eighteen-ion crystal. Fig. 9 (a) shows the spectrum for Doppler cooling only and Fig. 9 (b) for additional EIT cooling. The data presented in Fig. 9 (b) are measured with a single EIT cooling pulse of 1 ms applied. Also in the eighteen-ion case the complete set of radial modes, expanding over a range of 0.7 MHz, is cooled simultaneously with only one setting for the EIT cooling beams.

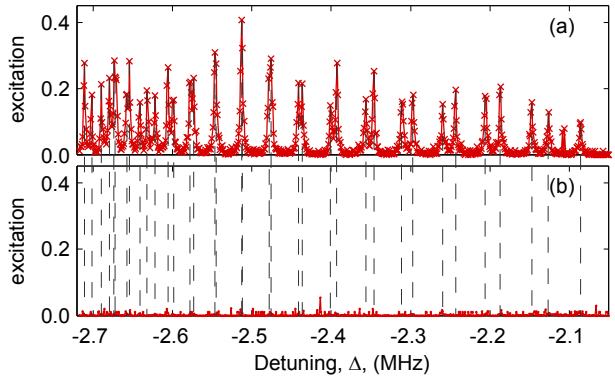

Figure 9: (a) Red-sideband radial mode spectrum for an eighteen-ion crystal after Doppler cooling only. (b) Red-sideband radial mode spectrum after Doppler cooling and consecutive EIT cooling. The σ^+ induced light shift is set to 2.3 MHz and the cooling pulse is applied for 1 ms. Dashed lines between (a) and (b) serve to aid comparison of the spectra. The data clearly demonstrate, that EIT cooling works on all radial modes spread over a range of 0.6 MHz simultaneously.

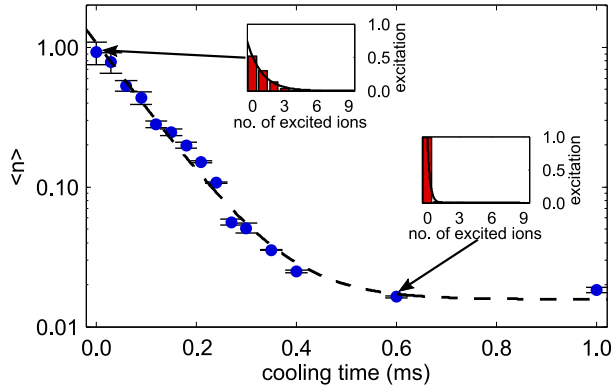

Figure 10: Cooling dynamics of the mode at 2.24 MHz of a nine-ion crystal. The ions are subject to Doppler cooling and EIT cooling, with a σ^+ induced light shift of 2.2 MHz for varying cooling duration. Subsequently, rapid adiabatic passage (RAP) maps the phonon number within the crystal to the electronic state of the ions, which is measured using an EMCCD camera. The histograms (insets) give the probability for observing a given number of excited ions (from no ions to nine ions) after various cooling times. The mean phonon number is derived from a thermal distribution fit to the data (solid line). To ensure that all data are equally included in the least-square fitting routine for the cooling rate, the logarithm of the commonly used exponential function is applied (dashed line) to yield a cooling rate of $(11.0 \pm 1.0)\ 10^3 \mathrm{s}^{-1}$.

2.2 Characterization of the scalable system

In this section we will characterize the qubit performance in the scalable system. This system is based on a slotted cryogenic surfacce trap fabricated by Translume and UCB.

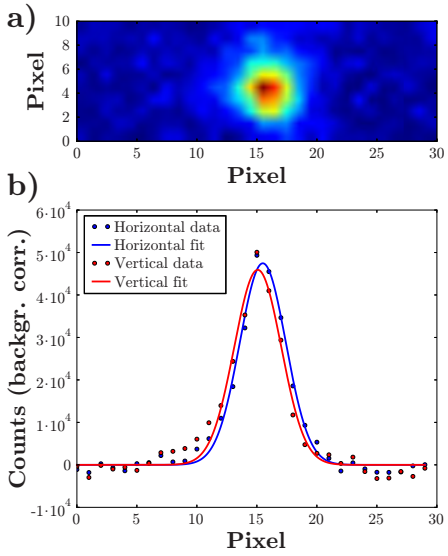

Figure 11: a) depicts a $^{40}Ca^{+}$ ion on the EMCCD camera. b) displays the averaged counts of the ion along a horizontal and vertical axis. The counts nicely represent Gaussian fits showing few aberrations in the detection optics.

Due to the non-evaporative getters from *SAES Getters*, we typically achieve pressures of below 10^{-8} mbar in the vacuum chamber at room temperature. At first, we cool for 24 to 36 hours with liquid nitrogen to reduce the liquid helium consumption during cool down. After switching to liquid helium, it usually takes a couple of hours to reach our typical operating temperatures of about 20 K.

At these temperatures, we can trap ions and our life-times are several hours, which is at the moment limited by the operation (changing trap voltages to unstable trapping parameters) but not by collisions with background gas. We can use an ion imagend onto the electron multiplying charge-coupled device (EMCCD) camera to characterize the detection optics, as done with a $^{40}Ca^{+}$ ion in Fig. 11. To characterize the detection optics, the sum over the rows (Fig. 11 a)) and columns (Fig. 11 b)) of the region of interest are in nice agreement with a Gaussian fit, from which we conclude that there are only weak aberrations in our detection optics.

Next, we characterized the qubit addressing capabilities of the NA $= 0.23$ lens. For this measurement, a $^{40}Ca^{+}$ ion as moved along the trap axis through the addressing beam and the Rabi flops for different positions were measured. From the Rabi frequency, the light intensity at one position along the trap axis can be determined. One obtains a plot of the intensity profile of the beam along the trap axis, as depicted in Fig. 12. The beam waist of 2.7 μm is sufficient for single ion addressing, but should be further improved by alignment outside the vacuum chamber.

In order to perform the first experiments later required for quantum information processing, we recorded Rabi flops on the carrier with a sideband cooled $^{40}Ca^{+}$ ion, shown in Fig. 13.

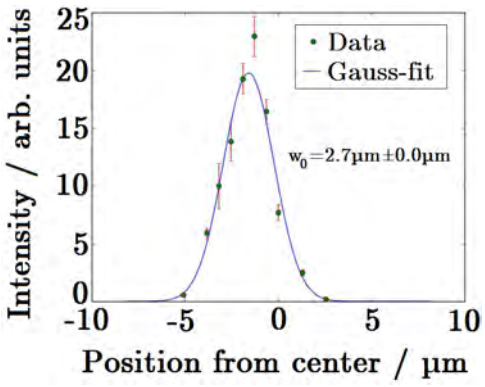

Figure 12: Test of our addressing optics. A single ion was moved along the trap axis through the addressing beam and the measured light intensity is measured, resulting in a beam waist w_0 of 2.7 μm.

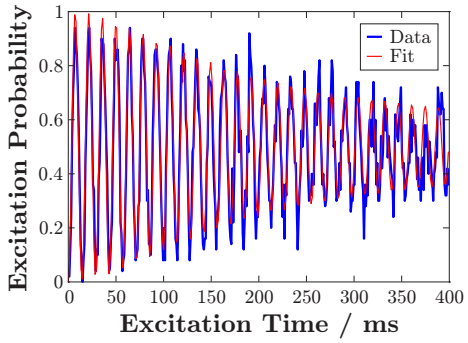

Figure 13: Rabi flops with a sideband cooled ion.

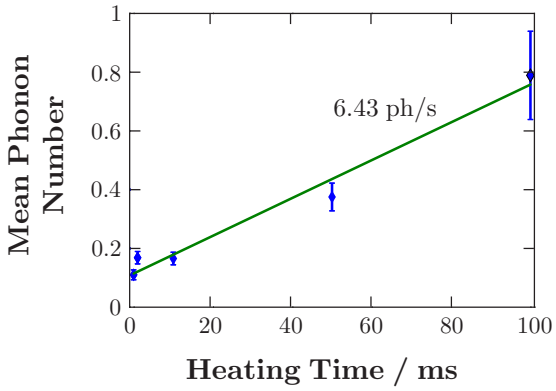

Figure 14: Axial heating rate measurement for a trap with an ion-electrode distance of 133 μm and a secular motion frequency of 1.1 MHz.

The heating rate of a trap in a setup is a rate of change of motional quanta of the secular motion frequencies of the trap in phonons per second. It is an important quantity for quantum information processing as phonons are used in entangling gates. Therefore, high heating rates limit the fidelity of entangling gates, and they are measured by measuring the mean phonon number after cooling and different wait times, as shown in Fig. 14. Our heating rate is 6.43 ph/s, which is about what one would expect from a trap with an electrode-ion distance of 113 μm and a secular motion frequency of 1.1 MHz at cryogenic temperatures.

Another important quantity in quantum information processing is the coherence time, which is shown in Fig. 15. The fit in our case was Gaussian, which suggests slow noise in the experiment was causing the decoherence.

2.3 Randomized benchmarking

The single-qubit Clifford group consists of 24 different operations out of which we randomly draw a sequence with up to 100 operations. The group is generated by the rotations

$$R_x(\theta) = e^{-i\frac{\theta}{2}\hat{\sigma}_x} \qquad R_y(\theta) = e^{-i\frac{\theta}{2}\hat{\sigma}_y} \qquad R_z(\theta) = e^{-i\frac{\theta}{2}\hat{\sigma}_z} \tag{4}$$

around the x, y and z-axis, where $\{\hat{\sigma}_x, \hat{\sigma}_y, \hat{\sigma}_z\}$ are the Pauli operators. At the beginning of each sequence, the qubit is initialized in the computational state $|1\rangle_z$. The rotations are implemented using integer multiples of $\pi/2$ for the rotation angle θ.The complete set of rotations used to generate each Clifford gate are shown in Table 2.3.

The operations that can be implemented with a resonant beam on a single ion are of the form:

$$R\text{car}(\theta, \phi) = e^{i\frac{\theta}{2}(cos(\phi)\hat{\sigma}_x + sin(\phi)\hat{\sigma}_y)} \tag{5}$$

We choose θ and ϕ out of the set $\{0, \pi/2, \pi, 3\pi/2\}$. Because there is no direct implementation of the rotation around $\hat{\sigma}_z$, we have to translate the computational gates from the Clifford-group (Table 2.3) into the operations stated in Eq. 5. Three physical gates are required to implement one $\hat{\sigma}_z$ gate. To minimize the dependence of the noise on the target gate (in order to make randomized benchmarking more reliable), we implement all operations from Table2.3 using three physical

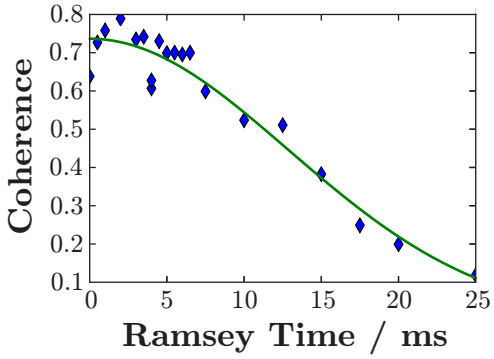

Figure 15: Ramsey experiment with an optical $^{40}Ca^{+}$ qubit in our setup. The coherence time is mainly limited by laser intensity fluctuations.

$R_z(0)$	$R_z(\pi/2)$	$R_z(\pi)$	$R_z(3\pi/2)$
$R_z(0).R_x(\pi)$	$R_z(\pi/2).R_x(\pi)$	$R_z(\pi).R_x(\pi)$	$R_z(3\pi/2).R_x(\pi)$
$R_x(0).R_y(\pi/2)$	$R_x(\pi/2).R_y(\pi/2)$	$R_x(\pi).R_y(\pi/2)$	$R_x(3\pi/2).R_y(\pi/2)$
$R_x(0).R_y(-\pi/2)$	$R_x(\pi/2).R_y(-\pi/2)$	$R_x(\pi).R_y(-\pi/2)$	$R_x(3\pi/2).R_y(-\pi/2)$
$R_y(0).R_x(-\pi/2)$	$R_y(\pi/2).R_x(-\pi/2)$	$R_y(\pi).R_x(-\pi/2)$	$R_y(3\pi/2).R_x(-\pi/2)$
$R_y(0).R_x(\pi/2)$	$R_y(\pi/2).R_x(\pi/2)$	$R_y(\pi).R_x(\pi/2)$	$R_y(3\pi/2).R_x(\pi/2)$

Table 1: The 24 elements of the Clifford-group are implemented using rotations around the X,Y,Z axes. The operations in each row map $|1\rangle_z$ to a fixed eigenstate of the Pauli-operators, with the different entries in the row introducing different relative phases to the orthogonal state.

operations. The identity operator is realized by a pause with the same duration as it would take for one of the other pulses.

An experimental run consists of (i) qubit reset, (ii) optical pumping to the $4S_{1/2}(m_F = -1/2)$ state, (iii) Doppler-cooling of all modes, (iv) sideband-cooling of the axial motion, (v) coherent manipulation and (vi) readout of the ion. Each sequence is repeated 100 times before the next random sequence is implemented. Here, it is important to choose the ideal final state to be $|0\rangle$ to be susceptible to initialization errors. If the target state would be the same as the initial state, $|1\rangle$ then errors during optical pumping (to the $4S_{1/2}(m_F = +1/2)$) would not be detected since the detection scheme does not discriminate between the two Zeeman-states of the $S_{1/2}$ state.

The length of the sequence is altered after each measured point to mitigate systematic effects of slow drifts in the system parameters. 27 different sequence lengths, with 50 random sequences for each sequence length. In total 1350 different sequences of Clifford gates were executed, with each repeated 100 times to estimate the survival probability $p_m(\vec{G})$. In order to determine the average gate fidelity for each Clifford operation (which consists of 3 physical operations), the decay constant p is determined by fitting the function:

$$P_0 = A\,p^m + B \tag{6}$$

to the measured excitation probabilities. Analyzing the experimental data shows that the specifics of the fitting procedures have a significant influence on the outcome. We used either the *raw data*, that is each data-point consisting of 100 cycles or *mean data* where the mean value of all measurements for a given sequence length is used. Another crucial aspect is the weighting of the measured data. For the *raw data* we performed an unweighted fit as well as a fit that was weighted according to the statistical uncertainty given by quantum projection noise. The *mean data* was weighted by the standard deviation of the outcomes of the different sequences for a given sequence length. Figure 16 shows the *raw data*, the *mean data* and the fitted model (eq 6). The resulting parameters are:

Data type	A	B	p
raw unweighted	0.569 ± 0.035	0.424 ± 0.036	0.991 ± 0.001
raw weighted	0.627 ± 0.044	0.384 ± 0.045	0.992 ± 0.001
mean weighted	0.560 ± 0.037	0.433 ± 0.038	0.991 ± 0.001

An alternative illustration of the data is shown in figures 17 and 18 where the distribution can be seen more clearly. Figure 18 highlights that the measured data shows a skewed distribution for

sequence length smaller than 10 Clifford operations.

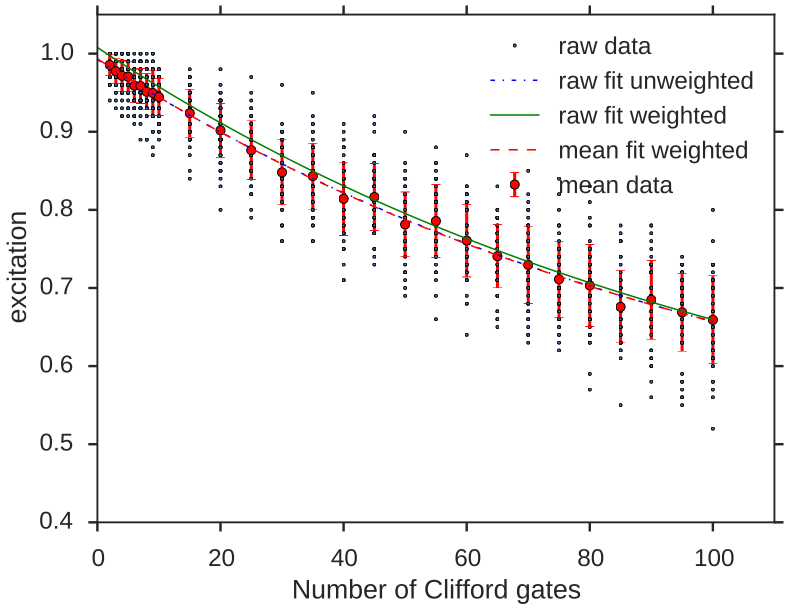

Figure 16: Excitation probability as a function of the sequence length. The solid lines indicate fits of the mean values weighted with the standard deviation (red dashed), the raw data unweighted (blue dash-dotted), and raw data weighted with quantum projection noise (green solid).

It can be seen that the weighted *raw data* fit is clearly deviating from the data points and also shows an unphysical negative value for the SPAM error. This shows that quantum projection noise is not a suitable model for data points with probabilities close to one. This means that the measured standard deviation for short sequences is dominated by variations in the fidelities between different implementations of sequences with the same length. The parameters estimated from *raw data* unweighted and *mean data* agree well and lead to a Clifford operation fidelity of 99.5(1)%. Assuming that all operations show the same infidelity, this corresponds to a single qubit fidelity of $p^{1/3} = 99.85(1)\%$.

The results of randomized benchmarking are only meaningful if following assumptions for the noise processes are met:

- The noise is Markovian
- The noise is gate-independent

The ARO/LPS project "Certified Topological Quantum Computation"[2] constructed a bound for the standard deviation of the measured randomized becnhmarking data. If the stated assumptions for the noise processes are met, following inequality holds:

$$\delta_1 \leq \frac{1}{\sqrt{qs}} \sqrt{(q-1)(m^2r^2 + 7mr^2/4) + P_0(1-P_0)} \; . \tag{7}$$

[2]Project #: W911NF-14-1-0103

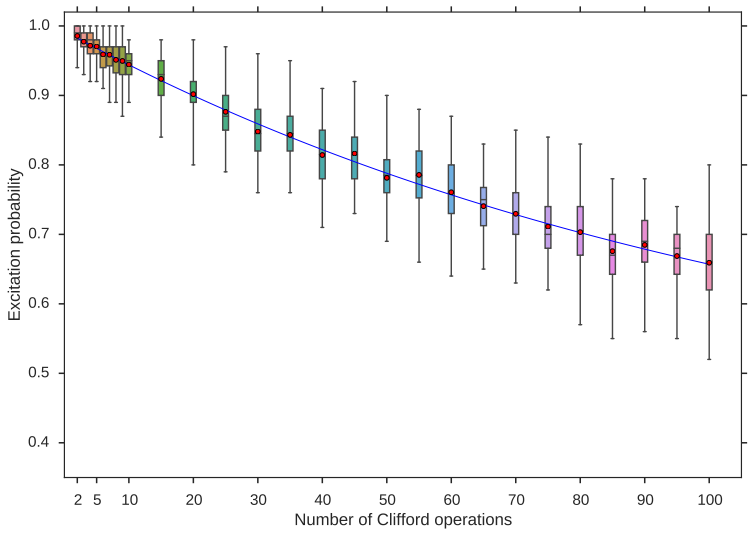

Figure 17: Excitation probability as a function of the sequence length. The blue solid line indicates a fit of the unweighted raw data. The boxes illustrate the distribution of the individual data points. The solid line inside the box indicates the median whereas the edges of the box correspond to the 75% and 25% quartiles. The whiskers show the maximum and minimum whereas the red dots indicate the mean values.

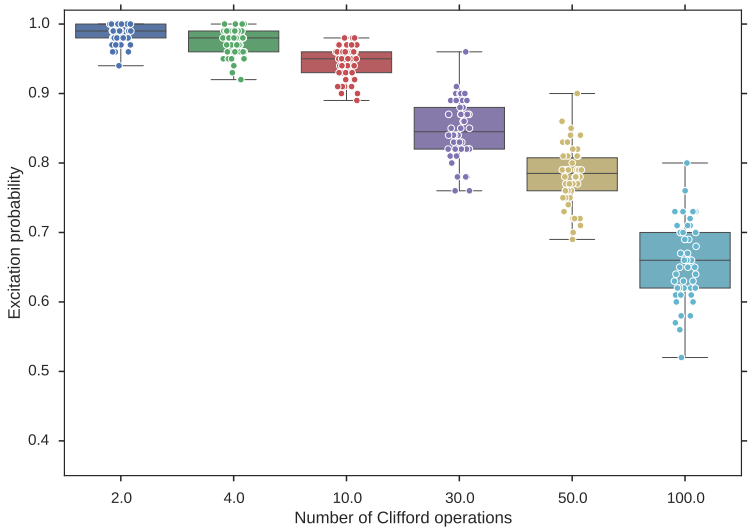

Figure 18: Excitation probability for selected sequence lengths. The boxes illustrate the distribution of the individual data points. The solid line inside the box indicates the median whereas the edges of the box correspond to the 75% and 25% quartiles. The whiskers show the maximum and minimum excitations. The individual data points are also shown.

Here, $r = (1-p)/2$ is the average gate infidelity, m is the sequence length and s and q are the number of random sequences and measurements per sequence respectively. A second, tighter bound is given by

$$\delta_2 \leq \frac{1}{\sqrt{qs}} \sqrt{\frac{3qmr^2}{4} + \frac{q}{12}\left(1 + 2(1-6r+18r^2)^m - 3(1-2r)^{2m}\right) + P_0(1-P_0)} \tag{8}$$

For the full set of measurements presented above, $r = (1-p)/2 = 0.0045$. In figure 19 we show the standard deviation of the measured data in comparison with the bound from equation 7 and the improved bound from equation 8, including the expected fluctuations from measurement projection noise. The four sub-figures indicate 10, 20, 30, and 50 random realizations s for each sequence length m. The increase of the violation of the bound with the number of random sequences per length shows that the experimental noise violates one of the assumptions of randomized benchmarking. From this we induce that the noise is gate-dependent or non-Markovian.

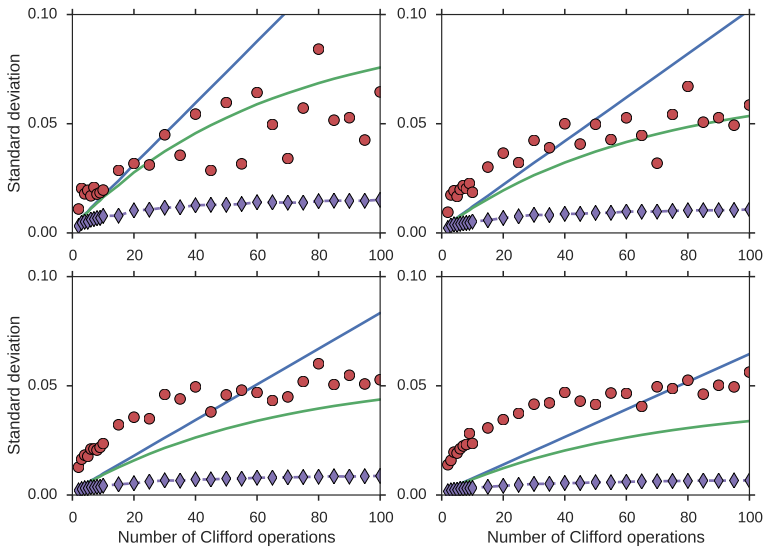

Figure 19: Standard deviation of the excitation probability as a function of the sequence length for 10, 20, 30, and 50 random realizations for each sequence length. The solid green line shows the bound from equation 7 including measurement projection noise; The solid blue line shows the improved bound from equation 8 including measurement projection noise. The red circles indicate the measured standard deviation whereas the purple diamonds correspond to the standard deviation expected from measurement projection noise.

3 UMZ activities

3.1 Transverse modes for entangling gates

A large part of the capstone activities at UMZ has been devoted to employing transverse vibrational modes as mediating modes for entangling gates. The main motivation for this comes from our previous finding that separation/merging operations with our current available technology result in motional excitations on the few phonon level, and they require a substantial calibration overhead [14, 18]. While anticipated improvements such as a larger voltage range of the next generation waveform generator 3.3, waveform correction [3] and improved shuttling protocols [17] are expected to decrease the obtained excitation energy, the problem that the trap frequency is strongly reduced while the axial confining potential is transformed from a single to a double well configuration will persist. Thus, it seems rather likely that even with all possible technological improvements, separation/merging will contribute excitations on the level of 0.1 to 1 phonons per ions, which will in turn deteriorate entangling gate fidelities in larger sequences with multiple shuttling and gate operations.

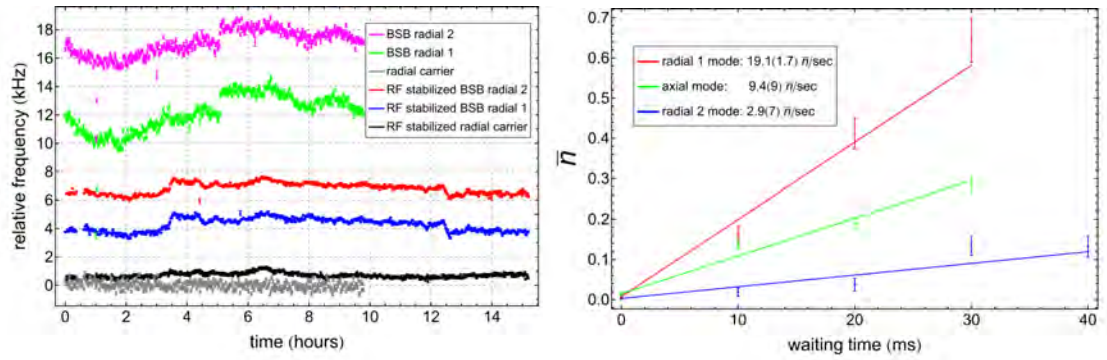

Figure 20: Transverse mode characteristics in UMZ planar multilayer trap: The left panel shows the results of spectroscopically tracking the transverse mode frequencies over one workday. The carrier is shown for reference in black (grey), and the radial sidebands in blue/red (green/magenta). The black/blue/red data is taken with active stabilization, while the grey/green/magenta is taken with a free running setting. The latter case shows increased fluctuations because the spectroscopy was not performed at the accuracy limit. The stabilized case displays significantly reduced drift, however jumps beyond the accuracy still occur. The right panel shows the result of heating rate measurements in terms of mean phonon number versus time, where the radial modes are shown in red/blue and the axial mode is shown in green.

The envisaged solution is therefore to employ transverse vibrational modes for gate operations, for making these resilient against axial motional excitations of up to some tens of phonons. Transverse modes however bear a number of additional technological challenges: First, in contrast to axial modes, the transverse mode frequencies depend on the trap drive rf voltage amplitude, which therefore has to be kept stable. Second, the transverse modes are affected by common-mode electrical noise on the dc trap segments, which is also not the case for the axial modes.

We started out by installing an active rf level stabilization system, which has already been developed and tested during MQCO [10], on the new apparatus bearing the thick-film multilayer planar trap. This system consisted of a two-diode rectifier which is installed at the capacitive divider tap-off of the helical resonator, where the output signal is low-pass filtered and fed to a PI servo. The servo signal is used as AM input of the signal generator used to generate the trap rf. This system was previously tested at the old apparatus hosting the thin-film tapered multilayer planar trap. While it was basically found to be operative, the spectroscopic resolution on the order of about 20 kHz was rather bad. On the new setup, we pushed the spectroscopic resolution to the limit of some 100 Hz, and observed that the stabilization system did not perform as expected. Drifts of several kHz during 1 h were seen, see Fig. 20. We figured out that the drift was predominantly due to temperature drifts of the rectifier diodes, we therefore installed a Peltier-based temperature controller on the rectifier. This led to reduced drifts, however drifts on the few-kHz level were still persisting. We identified the high-impedance low-level signal from the capacitive divider to be the most likely bottleneck, as it is most susceptible to electromagnetic interference. As a consequence, the design and manufacturing of an integrated solution is in progress, where a temperature stabilized unit comprised of an active rf buffer stage and a rectifier will be installed directly at the tap-off. For the time being, we proceeded with the situation that the transverse mode frequencies are stable below 1 kHz, and exhibit jumps of about 2 kHz of unclear origin two times during one day.

The heating rate on the transverse modes were measured, and were found to be strongly varying with respect to the electrical wiring of the entire dc system. The values range between few phonons/s and up to about 1000 phonons/s, additionally the ratio between the heating rates of the two modes is not constant. This makes clear that the predominant noise technical noise, which is also supported by the previous finding that no deterministic scaling behavior with respect to the mode frequency has been seen for the axial mode. After trying different cables and grounding topologies for the dc signals, and rearranging electrical equipment to keep cable lengths short, we achieved a situation where rather low heating rates were observed, see Table 3.1.

mode	heating rate (phonons/sec)	frequency (MHz)
axial	9	1.488
rad1	19	3.739
rad2	3	4.590

However, for the electrical configuration, we observed a substantial increase of the spectroscopic linewidth for the transverse modes, as compared to previous wirings with larger heating rates. We thus performed Ramsey measurements to assess fast fluctuations of these. For this, we first create spin superposition by pi/2 pulses as usual, and then do a pi pulse on the red sideband of the mode to be probed, resulting in a superposition of the number states with zero phonon and one phonon, with both components being in the same spin state. Thus, mode frequency fluctuations lead to phase accumulation of the superposition, whereas magnetic field fluctuations do not. After a variable wait time the sequence is applied in reversed order to map the accumulated phase to the spin, which is then read out. On the axial mode, the Ramsey contrast is lost within 5 ms. By contrast, on the high-frequency transverse mode total dephasing takes place within merely 200 μs. Repeating this measurement with ac-line triggering, we see a constant baseline of the Ramsey contrast, but a strong contrast modulation with a 100 μs period. We conclude that there is a strong

common ac-mains pickup on the dc trap segments, which has phase-stable high-frequency components from switching power supplies. To tackle that problem, we will add ground connections at different places, while testing both heating rates and mode coherence for each setting. Eventually we might enclose the entire trap apparatus including the waveform generator and rf hardware in a Faraday cage, as a consequence to the findings from the UCB node.
Finally, we realized an entangling geometric phase gate [15] on the lower-frequency transverse mode of a two-ion crystal. In comparison to gates on axial modes, the transverse mode gates are facilitated by the fact that the ion distance is no parameter which has to be adjusted, but the additional spectator modes leave more undesired entanglement to these, if not countered by proper pulse design [6]. Our first attempt to realize such a gate led to a fidelity in the 90% range, where the bottleneck is presumably due to the ac modulation of the mode frequencies.

3.2 Fast ion swapping

Scalable operation of trapped ion quantum processors, especially when employing a hybrid species approach, requires the capability for deterministic reordering of ion strings. In the past, microstructured trap with junctions of X- or Y-topology have been manufactured and tested [12, 2]. Shuttling across junctions however was found to be a rather complex operation, leading to excess excitation and timing overhead. An interesting alternative for this would be to employ the segmentation of the microtraps for deterministic ion crystal rotation, i.e. a swap operation. Such a process has already been demonstrated by UIBK in 2009, however without measurement of the final motional excitation of the ions.

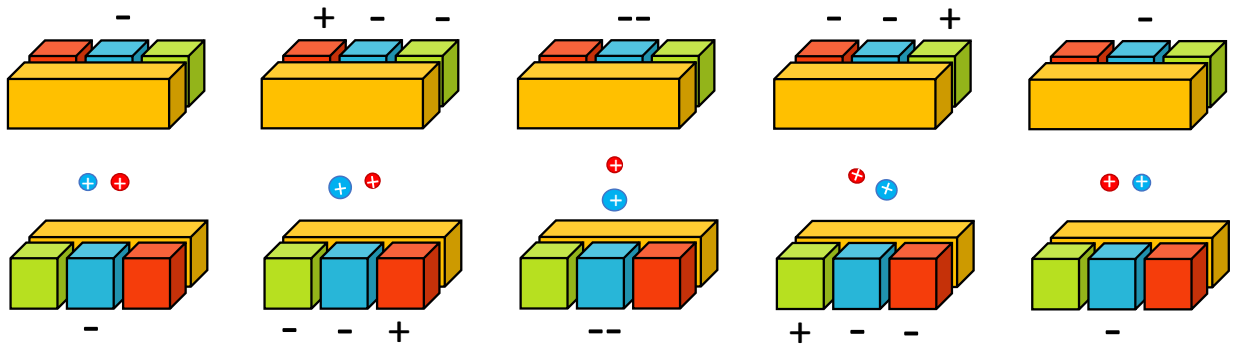

Figure 21: Ion crystal rotation: It is schematically shown how the voltages on the relevant segments are varied in time to rotate the two-ion crystal.

Within capstone, we have realized deterministic ion crystal rotation in the new thick-film planar multilayer trap. As illustrated in Fig. 21, the process requires only six trap electrodes, where the middle segment pair serves for axial confinement, and the outer electrodes generate diagonal symmetry breaking electric field for a smooth rotation of the potential ellipsoid. In the first step, the diagonal field is ramped up in order to rotate the axis of weakest confinement within the plane

defined be the trap axis and the dc electrodes. Then, the trapping voltage at the middle segments is increased, beyond the level at which the ion crystal smoothly crosses the structural transition to vertical alignment while the diagonal field is ramped down. The ramps are then applied in reverse, with opposite polarity of the diagonal field, such that the ion crystal ends up reordered. We found this process to work in the absence of Doppler cooling for process times ranging between 20 and 100 μs. The trap drive rf level had to be reduced in order to make the available dc voltage range of ± 10 V sufficient for crossing the alignment structural transition, such that the common-mode radial secular frequencies are $2\pi\times 4.3$ and $2\pi\times 3.3$ MHz rather than $2\pi\times 3.3$ and $2\pi\times 1.9$ MHz obtained for usual operation.
We have measured the residual excitation of all six secular modes of the two ion crystal after rotation by driving Rabi flops on motional sideband. As a result, we do not observe significant excitation contributed by the rotation on any of the secular modes for a total swapping time of 20 μs.

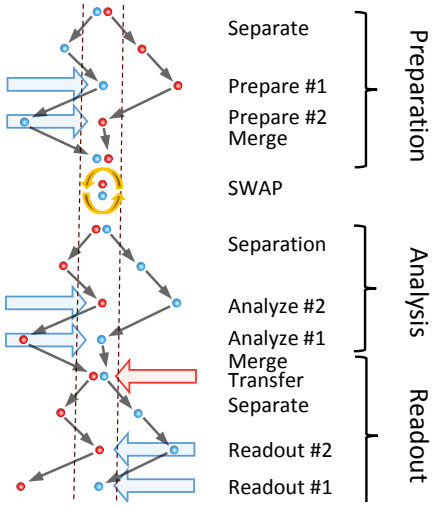

Figure 22: SWAP gate process tomography sequence: The plot shows how the two ions are shuttled within the segmented trap. The arrows indicate laser operations.

In order to verify that the swapping indeed takes places deterministically, and to demonstrate high-fidelity qubit operation in conjunction with different shuttling operations, we performed a full quantum process tomography of the SWAP-gate effectively mediated by the ion rotation [3]. The sequence is depicted in Fig. 22 and consists of building block for state preparation, analysis and readout. Each of these block starts with a two-ion crystal, which is split in order to move the ions sequentially into the laser interaction region. For preparation and analysis, qubit rotations are performed, while state dependent fluorescence is observed during readout. After the preparation, the ions are merged again and the swapping takes place. After the analysis part, another merging takes place, and electron shelving from $|\uparrow\rangle$ to the metastable $D_{5/2}$ state is done. The measurement consists of measurement of the nine different pairs of the Pauli operators $\{\sigma_z, \sigma_y, \sigma_x\}$ for each of

[3] It should be noted that ion rotation is not equivalent to s SWAP gate for *different* ion species, as demonstrated in [23]

the 16 possible pairs of the prepared states $\{|\uparrow\rangle, |\uparrow\rangle + i|\downarrow\rangle, |\uparrow\rangle - |\downarrow\rangle, |\downarrow\rangle\}$, i.e. in total 144 preparation/analysis settings. Each setting is probed 1000 times.

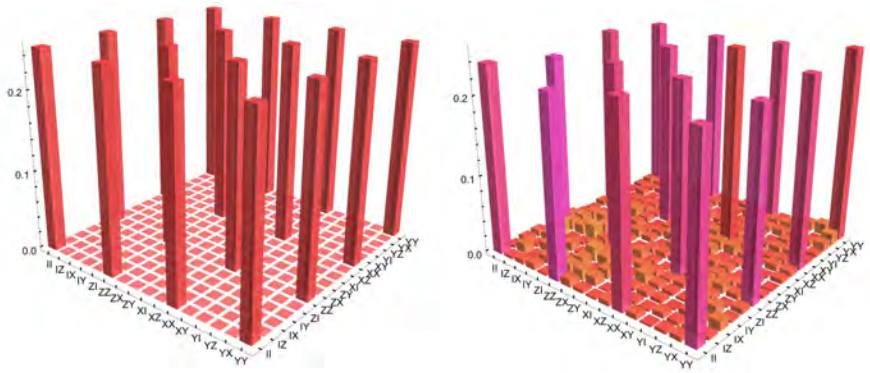

Figure 23: SWAP gate process tomography results: The left plot show the ideal χ-matrix of a SWAP gate, the right plot shows out measurement result

A crucial issue was found to be the qubit phase management in the inhomogeneous environment: The quantizing magnetic field determining the qubit transition frequency is varying along the trap axis, and therefore along the direction where the qubits are moved. In conjunction with shuttling, this leads to the pickup of additional phases, which are deterministic, but need to be properly accounted for. While this could in principle be done by performing Ramsey measurements on the qubits after the shuttling sequence without gates, this would require recalibration for each sequence modification and is therefore not desirable. Instead, we mapped out the Zeeman splitting inhomogeneity along the trap axis by employing Ramsey measurements of phase accumulation rates. We use this data together with position calibration data for the shuttling operations to *calculate* the expected phase accumulation for each qubit. These phases are used to correctly set the analysis pulse phases.

For each prepared state, we reconstruct the density matrix via linear inversion. From the obtained set of 16 density matrices, we reconstruct the process χ matrix, again via linear inversion. The results are shown in Fig. 23. Without(with) correction for state preparation and measurement (SPAM) errors, we obtain a mean process fidelity of 98.0(5)% (99.0(5)%), while the identity operation (no SWAP) yields values of 98.6(5)% (100.0(5)%). Thus, the main residual error source are SPAM errors. Beyond that, qubit decoherence due to magnetic field fluctuations clearly contributes, along with the limited accuracy of the phase calibration. Efforts are currently underway to attempt to disentangle these error sources.

As a conclusion, these measurements clearly demonstrate how two qubits are prepared, manipulated and read out within a complex sequence involving separation, merging, shuttling and rotation operations.

3.3 Next generation waveform generator

Within capstone, we have successfully completed the design, prototype manufacturing and testing of the successor device for our fast multichannel arbitrary waveform generator. The requirement of an improved device arises from the following reasons:

- The previous device is employing quad DACs, such that the achievable update rate depends on the set of electrode voltages to be updated. The strongly restricts the control of shuttling operations where several potential well are used.
- Ion crystal operations such as demonstrated in Sec. 3.2 require independent control of the adjacent electrodes comprising one pair, which is not directly possible with the previous device.
- The strong reduction of confinement during separation operation leads to motional excitation. It is beneficial to employ increased segment voltages for maximized residual confinement during this process, i.e. to increase to output voltage range significantly beyond ± 10 V.
- For the long time goal of establishing a control infrastructure comprising fully synchronized rf pulse synthesis, laser control, trap control and measurements, and even including in-sequence feedback, the FPGA platform used in the previous device is insufficient. Most prominently, the Virtex V FPGA was found rather unwieldy to control. The Zynq SoC platform used for the new design allows more rapid prototyping and improved design flexibility.

The design of the new device was started during the final period of MQCO, where the housing box including power supplies and backplane was conceived, the analog hardware was design and tested, and the programming of the Zynq SoC started. It was however found that the increased complexity of the new hardware led to sophisticated challenges concerning the timing constraints of the FPGA firmware. For different instances where the FPGA was programmed, strong glitches due to mis-set DAC bits were seen, randomly occurring at different rates. It was even observed that these effects depend on whether metal shields were installed around the DAC cards or not.
Within capstone, these issues were tackled by working out the correct timing constraints. As a result, we now have a prototype of the new waveform generator, which has 80 analog output lines at ± 40 V output range and uniform 400 ns update time, where all channels are fully synchronized. This device would be capable of controlling advanced traps such as the Sandia HOA trap, with independent control of almost all electrodes.

4 UCB activities

4.1 Annealing of traps

In order to explore the effects of heating the trap, we designed and installed a button heater beneath the trap substrate as illustrated in Figure 24. It allows for both heat treatment and ion trapping in the same apparatus. We demonstrated trapping in trap with nominally 100 μm ion-surface distance and measured a heating rate of 0.2 quanta/ms. This particular trap developed a short from the radio frequency electrode to ground, rendering it useless. Before removal from vacuum, we tested the

button heater and estimated a temperature at the surface of over 1000 °C. This process created new shorts on the trap and caused a clear visual difference in the heated area. We investigated this difference with SEM and found no structural difference in the areas of the trap.

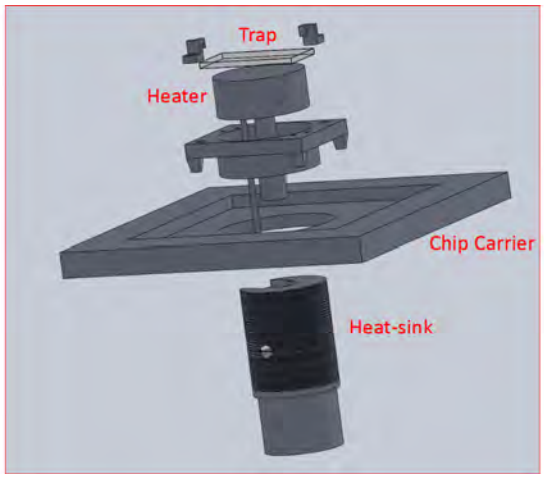

Figure 24: Schematic of the setup designed to anneal the trap with a commercial button heater. The clear trap substrate is shown above the button heater, with a heat sink on the bottom side of the chip carrier.

4.2 Robust trap designs

The purpose of the new trap design is to increase the robustness of the Argon cleaning process developed previously in the SQIP program. By bombarding the surface with Ar^+ ions at 300 eV, we remove the topmost layer of oxygen and carbon contaminants. After cleaning, heating rates are reduced by two orders of magnitude, but traps might no longer viable for continued experiments due to the high rate of shorting during cleaning. It is our hypothesis that a combination of dust and metal deposited in the trenches during cleaning are to blame for the shorts appearing. To mitigate the development of bridges between electrodes and ground, the new design features wider gaps (from 10 μm to 20 μm), as shown in Figure 25. We will also evaporate the traps at a 30° angle instead of 45° to reduce the amount of metal deposited initially into the trenches. We have received the new traps from Translume and will complete the fabrication process to begin testing in February.

4.3 Infrared Fourier-transform spectroscopy on surfaces

4.3.1 Experimental Setup

Auger spectroscopy identifies Carbon and Oxygen as the main contaminants. However, Auger spectroscopy cannot detect Hydrogen nor is it very sensitive to the chemical structure of the surface. Hence, it is unknown in which forms Carbon and Oxygen are bound to the electrode surface. One method of characterizing the Chemical composition is through Fourier Transform Infrared

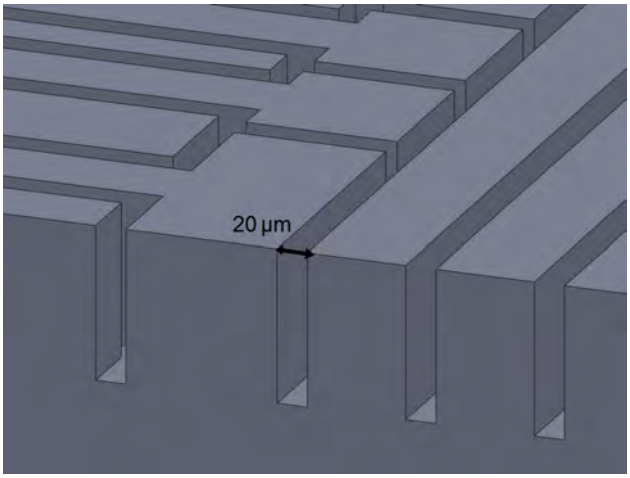

Figure 25: Design of the trap new trap with 20 μm gaps.

Spectroscopy (FTIR). Molecular bonds vibrate at specific frequencies, which correspond to particular vibrational energies, typically in the infrared (IR) regime. Exciting the sample with a broad beam of IR light, and analyzing the intensity of the output of a Michelson-Morley arrangement creates an interferogram. Fourier transformation of the signal as a function of the path length difference inside the Michelson-Morley interferometer creates a spectrum. It is then possible to map individual peaks to bonds and functional groups to construct a description of the molecular structure of the sample [7]. The keystone of our experiment is the Fourier Transform Infrared Spectrometer Bruker Tensor 27 FTIR. The spectrometer produces a broad IR beam, whose phase is modulated by a Michelson-Morley interferometer. We focus this light with a parabolic mirror onto the sample. The beam is aligned such that it grazes off of the trap surface at an angle on the order of 8.5° and is focused then with a second parabolic mirror on the a Mercury Cadmium Telluride detector. Using an automated wire-grid polarizer we can choose light polarized perpendicular (S) or parallel (P) to the sample surface.

4.3.2 Infrared Spectroscopy

To analyze the spectra, one typically compares the obtained signals to organic chemistry tables from references like the Spectral Database for Organic Compounds. Most signals are either "peaks" or "stretches", the latter being effectively broad peaks or collection of peaks. Consider Fig. 27: The primary region of interest in most FTIR spectra ranges from 4000 to 2500 cm^{-1} where single bond stretches are located. Common signals here include water, alcohol hydroxyls, alkanes, alkenes, and alkynes. The next region, from 2500 cm^{-1} to 2000 cm^{-1}, includes triple bonds typically found in the air between optical elements. From 2000 cm^{-1} to 1300 cm^{-1}, there are double bonds most of which include at least one carbon. Finally, from 1300 cm^{-1} to 400 cm^{-1}, there is the fingerprint region which is best analyzed in terms of its overall shape rather than its many challenging to resolve bonds that can range from complex rock and wag motions of alkanes to single bonds with uncommon elements.

Even the FTIR spectra of beams not interacting with the test sample show a rich variety of signals. To begin, the IR beam is not necessarily spectrally flat. Furthermore, the light passes

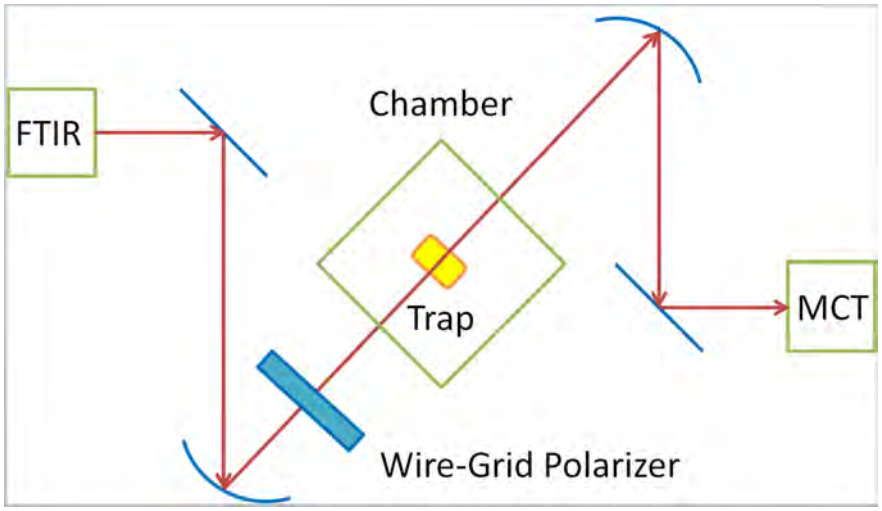

Figure 26: Optical setup displaying the FTIR and external instruments.

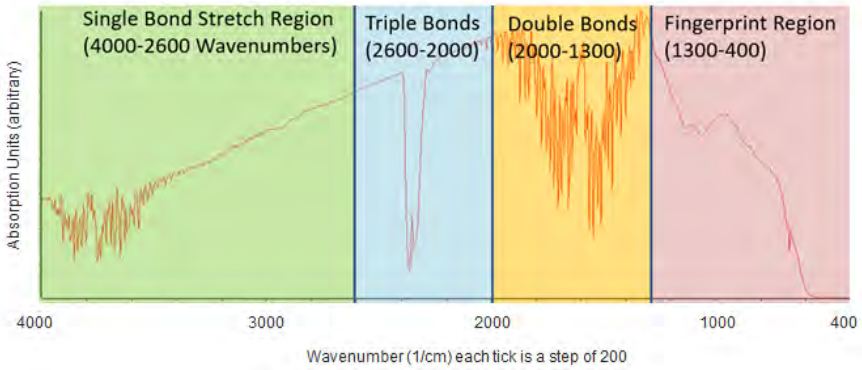

Figure 27: Common types of chemical bonds by region in IR spectra.

through atmosphere and can be absorbed by molecules contained in it. Similarly, the light passes through various optical elements that exhibit contamination. Hence, it is important to reference the spectra to a background to ensure the reliability of information extracted from parts of the spectra absorbed by the sample. The most straightforward method is to compare the spectra of the contaminated surface under study to that of an ideal perfectly clean one. Unfortunately, it is near impossible to obtain perfectly clean samples. Another interesting method for discerning surface absorption from other effects is to use the fact that most contaminants bound to the surface are either aligned perpendicular or parallel with respect to the surface. In particular, Grazing Angle Polarization Modulation (PM) takes advantage of this fact by alternating between perpendicular (S) and parallel (P) components, using one signal as the background for the other [4]. When grazing the surface, the P polarized light has a much greater surface interaction than the S polarized light due to interactions with the polarized molecular layer [8]. Note that the light impinges with a much larger angle onto all other optical surfaces such that the polarization sensitivity for those elements is very small. Furthermore, molecules in the gas phase are unpolarized and hence the method

reduces background fluctuations from the free beam propagation [22].

Fig. 28 displays the spectra of S and P polarized light, as well as their normalized difference. Most of the noise matches the noise in the background spectra, leaving some small peaks and the traps fingerprint. Zooming in on specific regions to analyze certain peaks, one can already observe some peaks, such as the carbon double bond around 1700 cm^{-1}. There are also small fluctuations around the single and double bound water and carbon dioxide noise. This is caused by the background fluctuating in the time between data collection. While not present on this particular spectra, the carbon dioxide noise in the triple bond region is typically the most prone to this effect due to its relative strength.

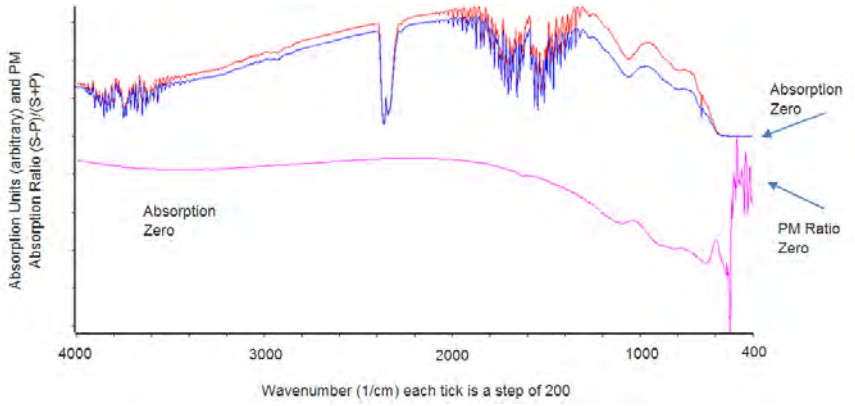

Figure 28: S polarized (red), P polarized (blue) and difference over sum (violet) of a typical spectra.

It may not be possible to precisely determine what the contamination is, but it is possible to comment on its molecular structure by identifying particular bonds. The data shows if it is contaminated and characterizes the contamination with its fingerprint. When performing experiments, one compares the spectra before and after various tests to check if there is any substantial change to the contamination, with spectra like those displayed in Fig. 29.

4.3.3 Investigating Surfaces

Each trap surface begins as a substrate that is manufactured elsewhere. Trap substrates are typically ordered from Translume and made of fused silica. Gold and copper-aluminum alloy are evaporated onto the substrate using a titanium adhesion layer in a clean room. After spending time stored in plastic containers and brief exposure to laboratory air, the surfaces are mounted inside a vacuum chamber. During the initial roughing pumping, variac-controlled heaters perform a bake-out (vacuum heat treatment) with heater tape to remove water from the surface of walls and carbon from inside them. Temperature remains below 200 °C to prevent developing leaks in the viewports.

Extreme care to keep all parts which go inside the vacuum chamber oil-free includes multi-step ultrasonic cleaning and wearing nitrile gloves while handling them. The trap surface itself should never get directly contacted to other tools except those for wire-bonding used to connect the trap electrically. All tools in close proximity are cleaned with isopropanol, which is kept away from the surface. However, any surface that has been exposed to the atmosphere is expected to have

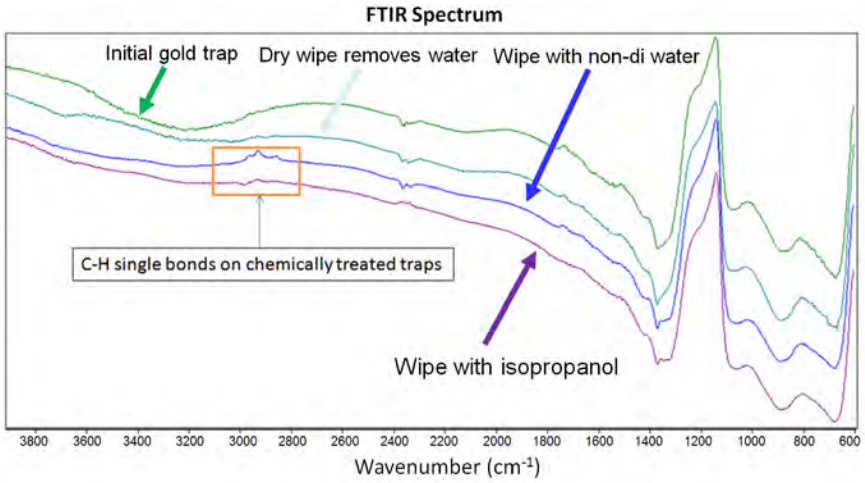

Figure 29: Difference over sum spectra of a surface subjected to various test. Most prominently, alkane bonds appear around 2900 cm^{-1}.

a covering of adsorbents at least several monolayers thick. Additionally, electrode materials that react with oxygen will have native oxide layers [1].

Before collecting data, one must be sure to avoid picking up polarization-dependent instrument noise. When the beam passes through the optics without grazing off of the trap, no polarization dependence is observed, demonstrating that only the surface contributes polarization dependent signals and noise. With grazing angle, there is some angular dependence on the polarization. The magnitude of polarization dependent signals increased with angle up until 90 degrees, as would be expected. In theory, the spectra should be a flat line with absorption peaks dropping down. However, in practice we observe a drift in the signal during the scans. This is caused by imperfect positioning of the interferogram mirror and can be removed by referencing a background collected with the same imperfection. Apart from the drift, the following features are present: From 4000 cm^{-1} to 3400 cm^{-1} there are peaks that typically correspond to water noise from humidity in the air and condensation on our optics. From 2400 to 2200 cm^{-1}, a pair of strong peaks corresponds to the instrument's carbon dioxide noise [21]. The entire double bond region here is clouded by water and carbon dioxide signals as well. Due to the complex nature of the fingerprint region, one can typically at best use it to recognize that surfaces are contaminated and distinguish between them, as each contamination will have a different fingerprint. Most of the spectra vanish below 600 cm^{-1} so that region is not included.

In addition to the fingerprint regions shown in Fig. 30, some single bonds and the aforementioned instrument noise are relevant to analysis. Of the single bonds present, most are alkanes, which would be expected for alkanethiol contamination, especially on metal surfaces [8-11]. There is a distinct lack of alkene, alkyne, carboxyl, and other common bonds in any spectra. When hydroxyl bonds are present, they are most likely to be water on the surface in addition to typical water noise from our instruments and optics. Despite their relative intensity, the bonds of the fingerprint region are too numerous and close together to resolve. Some fingerprints include stretches consistent with alkane wag and rock, while others have a broad signal centered around 1200 cm^{-1} that can be associated with plasmon resonance [13].

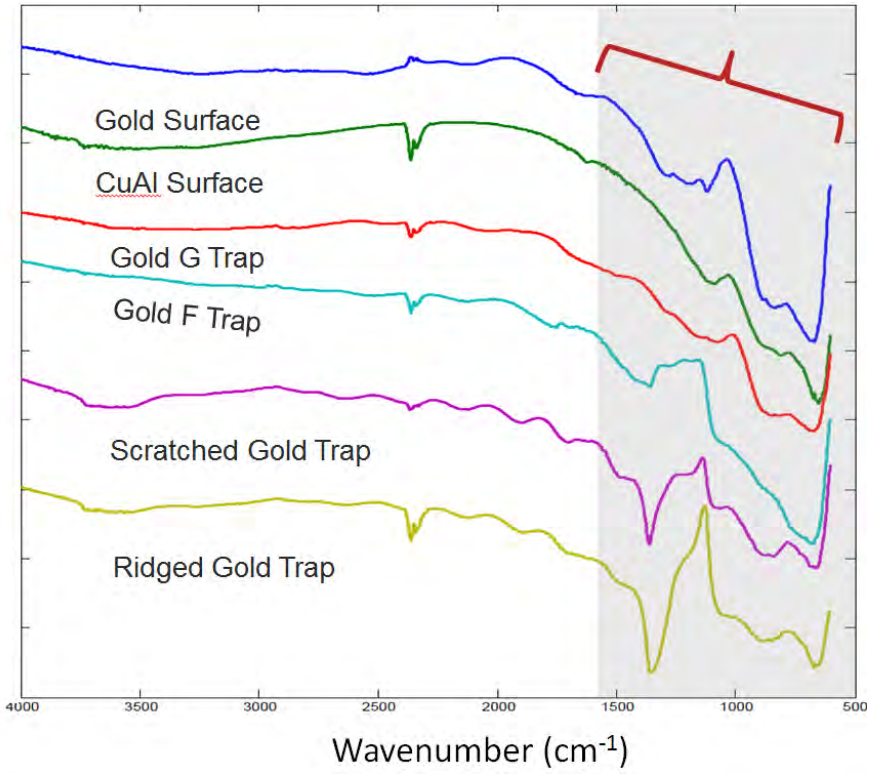

Figure 30: All surfaces tested are uniquely dirty. All traps exhibit some degree of noise around 2400 cm^{-1} due to fluctuation in carbon dioxide signals due to the instruments exposure to air. The majority of each characteristic spectrum is dominated by a unique fingerprint region.

The spectra change with the addition and removal of isopropanol, acetone, distilled water, and ordinary water, as expected. Each temporarily adds specific peaks which can then be removed through mechanical abrasion by cloth with wet isopropanol to observe the original spectra. The addition of isopropanol, acetone, and non-dilute water leave complex spectra with numerous organic bonds. Drying and abrasion on any of these wet surfaces without isopropanol or on a surface with dried isopropanol was insufficient to completely return to the original spectra as shown in Fig. 31.

The instrument and environment noise also fluctuate in time. The 2400–2200 cm^{-1} peaks of carbon dioxide and all other noise drift differently from each other. The peaks in the triple bond region fluctuated both positively and negatively over time, crossing over zero on the scale of seconds to minutes. Over many minutes, the maximum positive or negative amplitude of the noise increase and continue to do so over a timescale of hours. For all other noise, the amplitude increases on average continuously and the P polarized spectra to drift as a whole in a similar manner as the prior type of noise. Overall, retaking the background between samples on reasonable timescale can suppress these sources of noise.

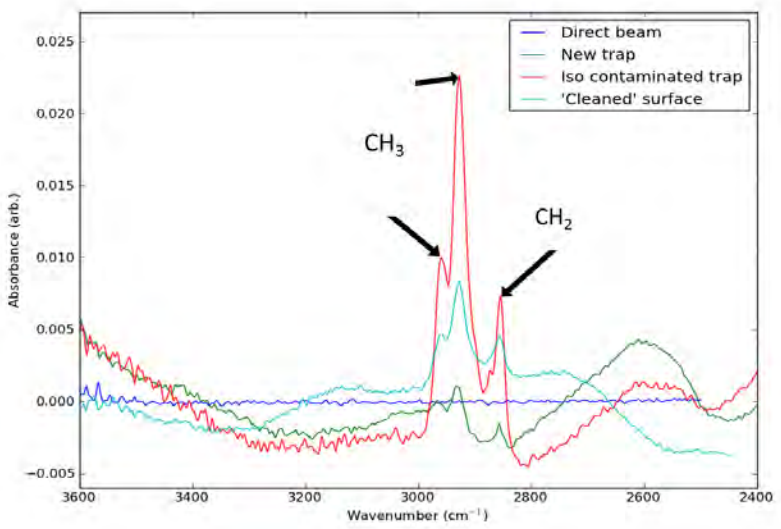

Figure 31: Changes to the alkane bond region due to controlled isopropanol contamination and removal. Direct beam without grazing angle (blue), new clean gold trap (green), same trap with isopropanol contamination (red), and trap after surface cleaned" (cyan).

4.3.4 Tests for Change in Contamination

The goal of the measurements is to identify the chemical compositions of whatever is on the surfaces and determine how they change under in-vacuum heat treatment, blue laser light, and in situ ultraviolet radiation exposure. Before a trap can be used as intended, it must bake in a vacuum chamber and it is often exposed to blue light and ultraviolet radiation prior to and between experiments.

To be relevant to observations found with trapped ions, this study mimics the steps taken to prepare the traps to understand how the steps affect the trap surface. Ion trappers commonly use blue laser and ultraviolet radiation, which may also create or change the molecular structures. For the UV tests, we attach a UV LED on top of the substrate. For laser tests, replace the top flange with a visible light viewport and shine light directly in from above. These sources are 375 nm coherent light and a UV LED emitting light near 290 nm.

Beyond the expected changes caused by intentional contamination of alcohols and waters, no other tests make a substantial difference to trap spectra. Over three weeks of heat treatment in vacuum creates no substantial has been detected. Similarly, no effects from shining blue laser at 375 nm for days were detectable. Finally, we could also detect no changes after exposing the samples to UV radiation at 290 nm in vacuum. However, the unique initial contamination prior to the tests are unmodified by these processes. Most of this contamination is due to long alkane chains (carbon-hydrogen bonds). There is a distinct lack of carbon-carbon bonds despite the fact that most organic molecules display them.

It is quite possible that the equipment and methods are not sensitive enough to detect minute changes to the spectra. Meaningful signals may be obscured by water and carbon dioxide signals.

However, the observed signals, particularly in the fingerprint region, are very strong and indicate that the trap surfaces are heavily contaminated.

4.3.5 Summary

We use PM-FTIR spectroscopy to investigate contamination on Au and Cu-Al surfaces Each surface had a unique spectra corresponding to some organic deposition. Abrasion, wet Isopropanol wiping, sonication, heat, UV, and laser treatments were able to affect the spectra significantly. Hence, we conclude that while the surfaces are strongly contaminated the methods discussed above are not suitable to change the surface composition substantially.

5 MIT activities

5.1 μ-Cavity HOA system

Capstone activities at MIT have focused on assembling and characterizing a ion-photon interface, with the aim of coherent coupling between them. The goal being to merge the long-range coherent coupling protocols developed in the neutral atom community with the local control demonstrated within trapped ions. The design chosen was to integrate an optical cavity with Sandia's high optical access (HOA) trap. This particular trap geometry offered two axes with very large numerical aperture (NA), across the trap isthmus with an NA=0.11 and through the central slot with an NA=0.25. Perfect for the requirements of providing an axis for a strong-coupling regime optical cavity, as well as an axis for single ion addressing and high NA light collection.

The assembled system, shown in figure 5.1, consists of a high finesse optical cavity across the HOA isthmus. Both mirrors are mounted on a flexure stage which in turn in mounted on a 3-axis slip-stick stage. The flexure stage allows for high bandwidth piezo modulation of the mirrors, $> 10kHz$, while also providing distance and shielding of the piezo voltages from the ions. The 3-axis stage, allows in-situ alignment to any trapping zone within the HOA's 'Quantum' region and provides the option of removing the cavity completely from the trapping area allowing us to debug and study charging effects on the mirror substrates.

Optical access is maintained through the flexure stage in the regions around the mirrors the NA is > 0.25 commensurate with the back-side slot and drops to just 0.15 between the mirrors. A global axial beam enters across the trap surface, and A right angle mirror serves to provide an exit path for the cavity beam. In addition, the right angle mirror serves to block the oven-flux from direct line-of-sight to the cavity mirrors.

5.2 Mirror substrate preparation

A large part of the assembly process was spent preparing the mirror substrates. These were fabricated and coated early on in the MQCO program and required significant machining to make them compatible with the HOA-cavity design. In particular, a $\sim 200\mu$m step was cut into each substrate to allow the mirror centers to be placed $< 68\ \mu$m from the trap surface and allowing the beam to traverse and exit the mirror substrate without clipping on the substrate edge. The step, shown in figure 5.2, cuts into the usable mirror diameter just 6-7 beam radii from the mirror center

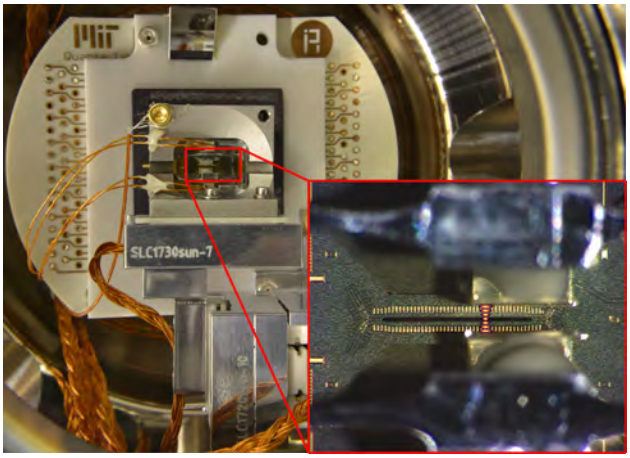

(40-60 μm). We were able to show no measurable increase in scattering loss or birefringence. This suggests that for future designs, with high-speed cnc milling and polishing, more complex substrate geometries could be utilized.

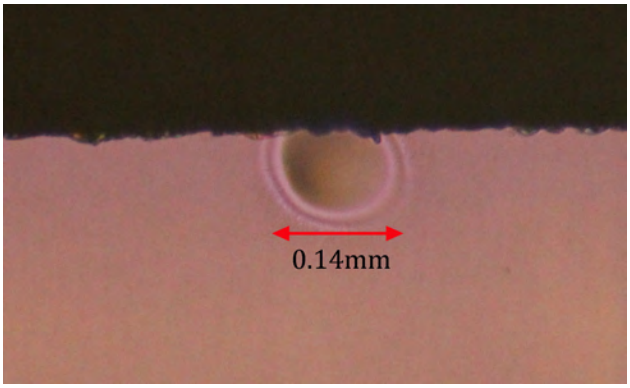

The cuts were made with with a Disco DAD3240 die saw at MIT's Microsystems technologies laboratory. The step was made by cutting part way (400-1000 μm) through the mirror-side of the substrate. Then flipping the substrate and aligning to the partial cut plus a 200 μm offset before making a through-cut. This process allowed for a maximum step size of roughly the blade width (200 μm). This process allowed us to make cuts with 1-5 μm accuracy relative to the mirror centers. However, we found that chipping along the edges generally produced features O(5-10 μm) and so cuts were always over-sized, and the final dimensions were achieved by hand polishing the substrates afterward.

5.3 system characterization

After the cutting process, we characterized each mirror before selecting a pair for the system assembly. Mirror losses and birefringence were measured through cavity spectroscopy while applying 100-400MHz sidebands to the probe beam, easily resolved with the cavities 10-50MHz linewidth. For longer cavities with linewidths < 10MHz, we used ring-down spectroscopy with a 30ns (1/e) beam shutoff time.

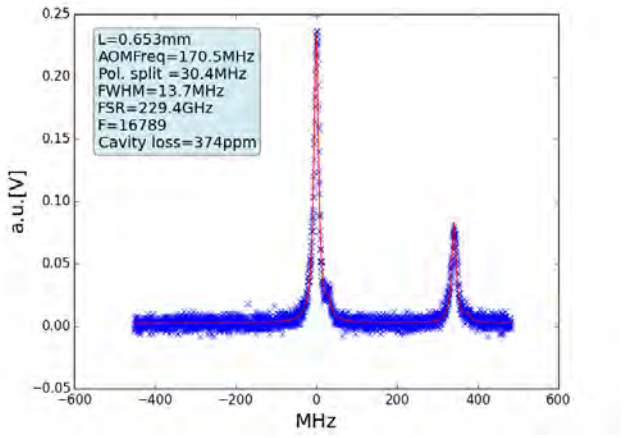

The mode volume of the cavity was determined using a combination of high-magnification imaging and clipping loss measurements. The length of the cavity was determined to within 5 μm using images of the cavity configuration using the mirror substrate as a calibration for the imaging magnification. And the cavity-mode waist was determined by inserting a razor into the cavity while measuring cavity losses and fitting the profile to a model of hard-edge clipping. From these measurements we were able to determine the assembled cavity to have a path length of 0.65mm, a mode-waist of 6.3 μm.

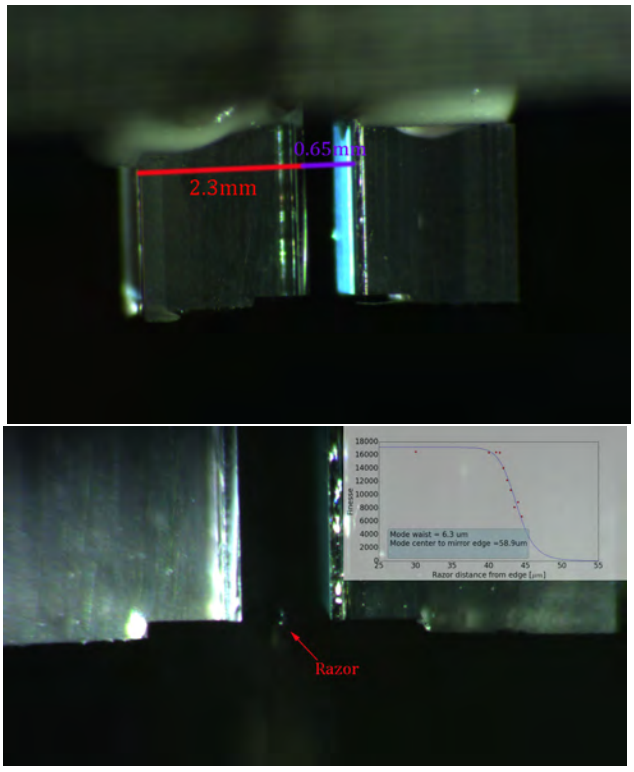

In addition to the mode-waist, by moving the razor to the mirror edge we found the mode-center

to mirror edge distance to be 59 μm. This number being critical for the mirror pairs usability in the design, requiring that this distance be smaller than the trapping height above the HOA top metal surface (68 μm).

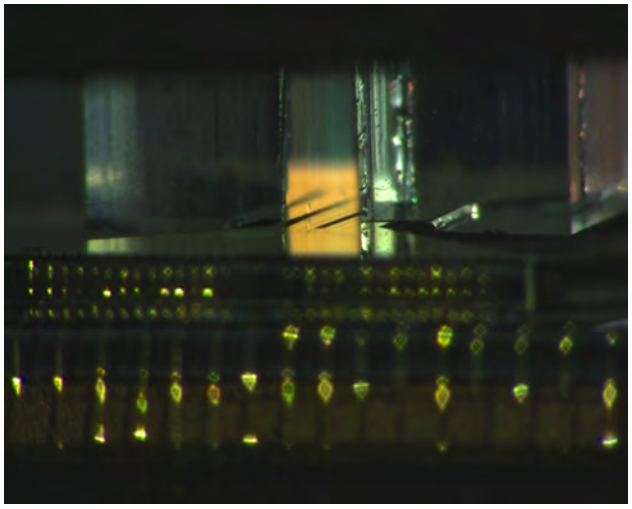

5.4 summary

After baking the assembled system, we found the cavity finesse dropped from 17000 to 7000. This increased loss is consistent with previous measurements for a first-time baked chamber. We believe after cleaning / replacing this mirror pair a similar loss would not occur during the second bake. In either case we intend to carry out measurements in the current system which is expected to have an effective cooperativity of ~ 5, and a cavity-ion coupling rate $g \approx 2\pi 32$MHz on the 408nm transition in strontium.

Currently, We've now trapped ion's in several zones within the loading arm of the HOA-1 trap but are awaiting shuttling solutions from Sandia to move ions into the linear-quantum region. On the cavity, We've realigned the experiment cavity with 408nm and finesse has been constant at 7000 for the last month. We are also setting up the 816nm beamline for stabilizing the cavity legnth. We hope to have our first cavity-ion coupling results within the next few weeks.

6 Milestones and Metrics

Table 2: SQIP Capstone Metrics

Nr	Milestones & Deliverables	Metric	Value / Comment
1.01	Lifetime and coherence of qubit	T_1, T_2	$T_1 = 1.1s\ T_2 = 80ms$
1.02	Test Markovianity via spin-echo	T_2 vs. $T_2^\star$	$T_2 = 37ms\ T_2^\star = 78ms$
1.03	Temporal noise analysis	Spectrum	See Sec.2.1.3
1.04	Suitable cooling methods	Cooling time, $\bar{n}$	Cooling rate $11 \cdot 10^3 s\ \bar{n} = 0.01$
1.05	Ion-light coupling stability	Rabi-decay	$\delta\Omega/\Omega = 2.5 \cdot 10^{-3}$
1.06	Randomized Benchmarking	Clifford-Fidelity	$F_{\text{single}} = 0.998(1)$
1.07	Micromotion compensation	Modulation index	< 0.1
1.08	Heating and stability of trap	$\dot{n}$, T_2^{trap}	$\dot{n}$ =3-15 phonons/s on radial modes,$T_2^{\text{trap}} \approx 1$ ms
1.09	Single-ion addressing	Addressing error	$\delta\Omega_{ac}/\Omega_{ac} = 9 \cdot 10^{-4}$
1.10	Single-qubit gate multiplexer	2-of-3 gate	See Sec.2.1.2
1.11	Addressing via string transport	Register size, addr. error	3 ions, below measure
1.12	Heating on split/merge	Δn	< 0.1 on both radial modes
1.13	Ion-cavity positioning	Stark-shift	In progress
1.14	Single-photon generation	Wave-paket	In progress
1.15	Cavity coupling constant	g	In progress
1.16	Spatial noise analysis	Correlation length	Bell state coherence observed up to 5 mm separation
1.17	PMT array with spatial resolution	3-qubit readout	In progress
1.18	Trap architecture for in-situ cleaning	Design	See Sec.4.2
1.19	In-situ trap heat treatment	$\dot{n}$	In progress
1.20	Final report		completed

Publications in refereed journals

1. Daniel Nigg, Thomas Monz, Philipp Schindler, Esteban A. Martinez, Markus Hennrich, Rainer Blatt, Matthew F. Pusey, Terry Rudolph and Jonathan Barrett; "Can different quantum state vectors correspond to the same physical state? An experimental test." New J. Phys. 18, 013007 (2015).

2. M. Palmero, S. Martnez-Garaot, U. G. Poschinger, A. Ruschhaupt and J. G. Muga. "Fast separation of two trapped ions" New J. Phys. 17, 093031 (2015)

3. Thomas Monz, Daniel Nigg, Esteban A. Martinez, Matthias F. Brandl, Philipp Schindler, Richard Rines, Shannon X. Wang, Isaac L. Chuang, Rainer Blatt "Realization of a scalable Shor algorithm", accepted at Science, to appear on March 4, 2016

Preprints

1. I. Talukdar, D. J. Gorman, N. Daniilidis, P. Schindler, S. Ebadi, H. Kaufmann, T. Zhang, H. Häffner, "Implications of surface noise for the motional coherence of trapped ions", arXiv:1511.04819 (2015)

2. Matthias F. Brandl, Philipp Schindler, Thomas Monz, Rainer Blatt, "Cryogenic resonator design for trapped ion experiments in Paul traps", arXiv:1601.06699 (2016)

3. Esteban A. Martinez, Thomas Monz, Daniel Nigg, Philipp Schindler, Rainer Blatt, "Compiling quantum algorithms for architectures with multi-qubit gates", arXiv:1601.06819 (2016)

7 References

[1] C. J. Powell A. W. Czanderna and T. E. Madey. *Specimen Handling, Preparation, and Treatments in Surface Characterization*, chapter Interpretation of Infrared Spectra, A Practical Approach. Kluwer Academic Publishers, New York, Boston, Dordrecht, London, Moscow, 2002.

[2] R. B. Blakestad, C. Ospelkaus, A. P. VanDevender, J. M. Amini, J. Britton, D. Leibfried, and D. J. Wineland. High-fidelity transport of trapped-ion qubits through an x-junction trap array. *Phys. Rev. Lett.*, 102:153002, Apr 2009.

[3] R. Bradford Blakestad. *Transport of Trapped-Ion Qubits within a Scalable Quantum Processor*. dissertation, University of Colorado.

[4] Desbat Bernard Pere Eve Buffeteau, Thierry and Jean Marie Turlet. *Progress in Fourier Transform Spectroscopy: Proceedings of the 10th International Conference, August 27 – September 1, 1995, Budapest, Hungary*, chapter Double Beam FT-IR Reflection Spectroscopy on Monolayers, pages 627–629. Springer Vienna, Vienna, 1997.

[5] I. C. Chang. Acousto-optic devices and applications. In Michael Bass, editor, *Handbook of Optics*, volume 2, chapter 12. McGraw-Hill, 2 edition, 1995.

[6] T. Choi, S. Debnath, T. A. Manning, C. Figgatt, Z.-X. Gong, L.-M. Duan, and C. Monroe. Optimal quantum control of multimode couplings between trapped ion qubits for scalable entanglement. *Phys. Rev. Lett.*, 112:190502, May 2014.

[7] J. Coates. Interpretation of infrared spectra, a practical approach.

[8] Robert Corn. Rapid-scan polarization-modulated fourier-transform infrared reflection absorption spectroscopy. *Hinds Instruments, Inc. Spring*, pages 1–4, 1996.

[9] S Crain, E Mount, S Baek, and J Kim. Individual addressing of trapped 171Yb+ ion qubits using a microelectromechanical systems-based beam steering system. *Applied Physics Letters*, 105(18):181115, November 2014.

[10] Marco Dillmann. *Stabilisierung der radialen Säakularfrequenzen gefangener Ionen in einer segmentierten Paul-Falle*. diploma thesis, University of Mainz, 2014.

[11] C. Hempel. PhD thesis, Universität Innsbruck, available online at `http://www.quantumoptics.at`, 2014.

[12] W. K. Hensinger, S. Olmschenk, D. Stick, D. Hucul, M. Yeo, M. Acton, L. Deslauriers, C. Monroe, and J. Rabchuk. T-junction ion trap array for two-dimensional ion shuttling, storage, and manipulation. *Applied Physics Letters*, 88(3), 2006.

[13] Claire E. Jordon, Brian L. Frey, Steven Kornguth, and Robert M. Corn. Characterization of poly-l-lysine adsorption onto alkanethiol-modified gold surfaces with polarization-modulation fourier transform infrared spectroscopy and surface plasmon resonance measurements. *Langmuir*, 10(10):3642–3648, 1994.

[14] H Kaufmann, T Ruster, C T Schmiegelow, F Schmidt-Kaler, and U G Poschinger. Dynamics and control of fast ion crystal splitting in segmented paul traps. *New Journal of Physics*, 16(7):073012, 2014.

[15] D. Leibfried, B. DeMarco, V. Meyer, D. Lucas, M. Barrett, J. Britton, W. M. Itano, B. Jelenkovic, C. Langer, T. Rosenband, and D. J. Wineland. Experimental demonstration of a robust, high-fidelity geometric two ion-qubit phase gate. *Nature*, 422:412, 2003.

[16] H C Nägerl, D Leibfried, H Rohde, G Thalhammer, J Eschner, Ferdinand Schmidt-Kaler, and Rainer Blatt. Laser addressing of individual ions in a linear ion trap. *Physical Review A*, 60(1):145–148, 1999.

[17] M Palmero, S Martínez-Garaot, U G Poschinger, A Ruschhaupt, and J G Muga. Fast separation of two trapped ions. *New Journal of Physics*, 17(9):093031, 2015.

[18] T. Ruster, C. Warschburger, H. Kaufmann, C. T. Schmiegelow, A. Walther, M. Hettrich, A. Pfister, V. Kaushal, F. Schmidt-Kaler, and U. G. Poschinger. Experimental realization of fast ion separation in segmented paul traps. *Phys. Rev. A*, 90:033410, Sep 2014.

[19] Philipp Schindler, Daniel Nigg, Thomas Monz, Julio T Barreiro, Esteban Martinez, Shannon X Wang, Stephan Quint, Matthias F Brandl, Volckmar Nebendahl, Christian F Roos, Michael Chwalla, Markus Hennrich, and Rainer Blatt. A quantum information processor with trapped ions. *New Journal of Physics*, 15(12):123012, December 2013.

[20] Ferdinand Schmidt-Kaler, Hartmut Häffner, Mark Riebe, Stephan Gulde, Gavin P T Lancaster, Thomas Deuschle, Christoph Becher, Christian F Roos, Jürgen Eschner, and Rainer Blatt. Realization of the Cirac–Zoller controlled-NOT quantum gate. *Nature*, 422:408–411, 2003.

[21] George Stanley. Bruker tensor 27 ft-ir and opus data collection program. v. 1.1. *Radboud University Nijmegen.*

[22] J. M. Turlet T. Buffeteau, B. Desbat. *Mikrochim. Acta [Wien]*, II:23–26, 1998.

[23] T. R. Tan, J. P. Gaebler, Y. Lin, Y. Wan, R. Bowler, D. Leibfried, and D. J. Wineland. Multi-element logic gates for trapped-ion qubits. *Nature*, 528:380, Dec 2015.

[24] D D Yavuz, P B Kulatunga, E Urban, T A Johnson, N Proite, T Henage, T G Walker, and M Saffman. Fast Ground State Manipulation of Neutral Atoms in Microscopic Optical Traps. *Physical Review Letters*, 96(6):063001, February 2006.